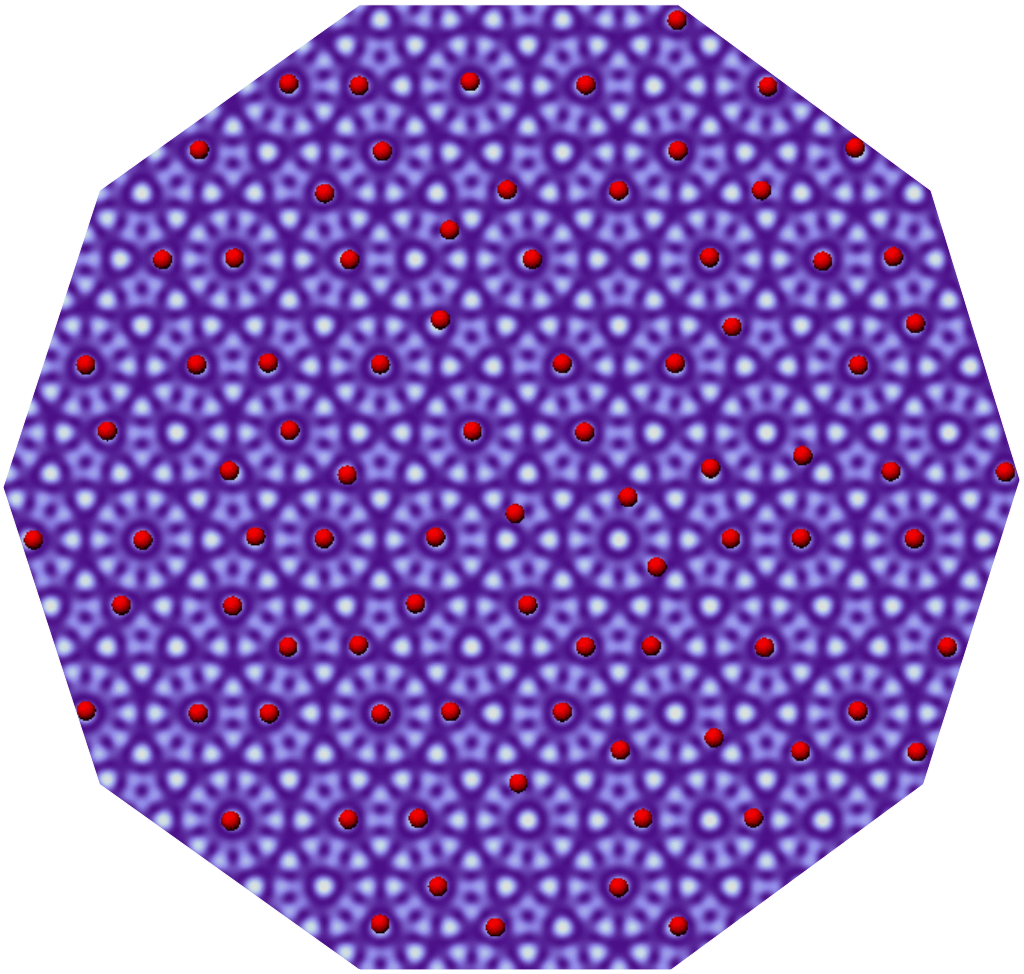

Michael Schmiedeberg

Colloidal particles on quasicrystalline substrates

Colloidal particles on quasicrystalline substrates

vorgelegt von
Diplom Physiker

Michael Schmiedeberg

geboren in Villingen-Schwenningen

Von der Fakultät II - Mathematik und Naturwissenschaften
der Technischen Universität Berlin

zur Erlangung des akademischen Grades
Doktor der Naturwissenschaften (Dr. rer. nat.)

genehmigte Dissertation

Promotionsausschuss:
Vorsitzender: Prof. Dr. Martin Schoen
Erster Berichter: Prof. Dr. Holger Stark
Zweite Berichterin: Prof. Dr. Sabine Klapp

Externer Berichter: Prof. Dr. Hartmut Löwen

Tag der wissenschaftlichen Aussprache: 24.7.2008

Berlin 2008

D 83

Contents

Chapter 1

Introduction

Quasicrystals are non-periodic solids that nevertheless exhibit long-range positional and orientational order. They can possess rotational point symmetries, such as five- or ten-fold rotational axes, that are not allowed in periodic crystals. Since their discovery [1] quasicrystals have caused much fascination, mainly because our understanding of what crystals are has had to change. Besides the non-crystallographic rotational symmetry, quasicrystals also show other physical properties that cannot exist in periodic crystals. Phasons, for example, are correlated global rearrangements of atoms that, like phonons, are hydrodynamic modes since they do not increase the free energy in the long-wavelength limit [2, 3]. Their different features are still a main topic and intensively discussed in the field [4]. In recent years, increasing research activities have been directed towards the question of how atoms order and move on quasicrystalline surfaces [5–19]. The goal of such studies is to understand and control the growth of quasicrystals and their exceptional material properties.

Colloidal suspensions are dispersions of micron-sized particles in a fluid. They are a well-known model system for statistical physics and for mimicking atomic systems. If subjected to a laser field, colloids are forced towards the region of highest laser intensity. Therefore a modulated light field can be used as an external potential acting on the particles. Unlike in atomic systems, the interactions between the colloids can be fine-tuned and by using video microscopy, the positions and movements of the particles can be observed in experiment. Leaving aside chemical details, colloidal suspensions in laser fields are therefore a very attractive system to study structural features of particle adsorbates on substrates.

In this work, we study the dynamics and the ordering of particles on quasicrystalline substrates. Using different simulation techniques, like Monte-Carlo or Brownian dynamics algorithms, as well as analytical theories, we determine the phase behavior and the motion of colloids confined to two dimensions in laser fields with one- or two-dimensional quasicrystalline symmetry. The one-dimensional potential is a sum of two incommensurable modulations in one direction and is constant in the other. The two-dimensional light field can be realized as the interference pattern of five laser beams and therefore exhibits decagonal symmetry (see figure 1.1).

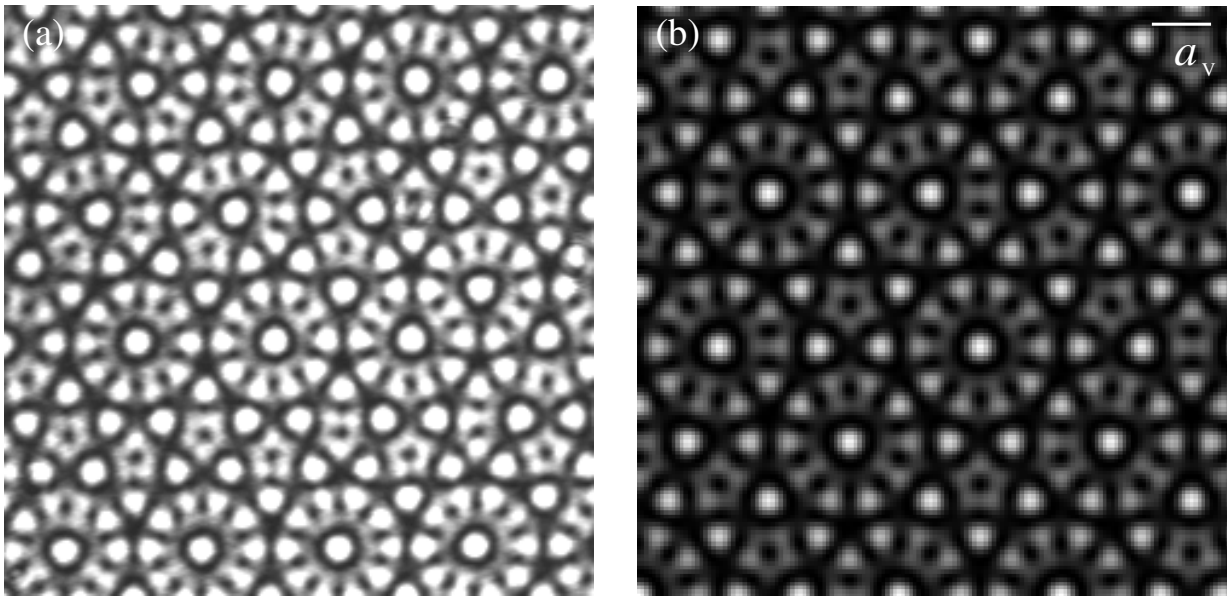

Figure 1.1: (a) Experimental realization of a laser intensity field with decagonal symmetry. Photo and experiment by J. Mikhael [20]. (b) Theoretically calculated grey-sale representation of the decagonal interference pattern of five laser beams. White parts indicate a high laser intensity corresponding to minima of the potential. The bar in the upper right corner marks the wave length $a_V = 2\pi/|\mathbf{G}_j|$ associated with the modulation vector $\mathbf{G}_j$ (see section 3.3).

The phase behavior of two dimensional systems, such as atomic monolayers on a surface, is known to be unique. Without an external potential, melting occurs in a two stage process due to the dissociation of different types of defects [21–27]. An external one or two-dimensional potential, if commensurable to the colloidal lattice structure, can stabilize or even induce triangular ordering [28], resulting in interesting non-trivial phase diagrams [29–32].

For colloidal particles in very weak quasicrystalline potentials, we find a triangular or a liquid phase depending on the two-particle interaction strength and the density. For very strong laser intensity, the system orders with the same symmetry as the substrate. However, when the strengths of the colloidal interaction and the substrate potential are comparable, we find interesting and unexpected new phases. The dynamics of particles in quasicrystalline potentials also reveals surprising phenomena, such as a frustrated non-periodic solid phase in the one-dimensional potential or a crossover from a subdiffusive regime at intermediate times to asymptotic diffusion for a single Brownian particle in the decagonal laser field.

Another advantage of considering colloidal suspensions in laser fields as a model system for particles in quasicrystalline potentials is that phasonic displacements, gradients, or drifts can easily be studied. We demonstrate how phasonic rearrangements can be induced by the laser field and how the motion of a single Brownian particle in a decagonal potential is affected by a phasonic drift.

This work is organized as follows: In chapter 2, we shortly introduce colloidal suspensions and demonstrate how light fields can be used to manipulate the particles. Chapter 3 gives an overview over history, properties, and construction methods of quasicrystals. Furthermore, we explain in detail how we determine the decagonal potential and introduce the phasonic degrees of freedom. We also shortly introduce examples of systems with induced decagonal symmetry, such as adatoms on the surface of quasicrystals. In chapter 4, the simulation techniques and their details are presented. We briefly summarize the most important theories of melting in two dimensions without any external potential in chapter 5. In chapter 6, colloidal suspensions in one dimensional laser fields are discussed. First, previous works and their results for periodic modulations are shortly introduced, then we present our results for the phase behavior and dynamics of colloids in a one-dimensional quasicrystalline potential. In chapter 7, the ordering in two-dimensional decagonal laser fields is analyzed, along with examples of induced phasonic rearrangements. In chapter 8, we study the dynamics of a single Brownian particle in a decagonal potential without or with phasonic drift. We also show how such a system can be used as a model system to study non-equilibrium path-ensemble averages. Finally, we conclude in chapter 9.

Chapter 2

Optical Matter

Colloids are widely used as a model system in statistical physics and often laser beams are employed to manipulate them. For example, colloidal ordering can be induced by modulated laser fields, which is called optical matter [33]. In this chapter, we first describe the properties of a charge-stabilized colloidal suspension and then explain how one can manipulate micron-sized particles with laser beams. Finally, we present some previous works done with 2D colloidal systems in laser fields.

2.1 Charge-stabilized colloidal suspensions

Colloidal systems consist of small particles dispersed in a continuous solution. Usually, colloids are about 0.01 to 10μm in diameter and therefore can show pronounced Brownian motion. Typical examples are solid particles in a liquid or gas, like paint or smoke, and drops dispersed in liquids or air as in milk or fog. Sometimes, air bubbles in liquids or solids, i.e., aqueous or solid foams, and even liquid or solid particles in solids, e.g., gelatin or glass mixtures, are also called colloidal systems. Here we consider spherical solid particles, usually consisting of plastic material (e.g., polystyrene) or glass, in a liquid solvent. Due to the attractive van der Waals interaction such colloids stick together and form clusters. To prevent aggregation and to stabilize the colloidal suspension, usually one of the two following mechanisms is chosen: In a sterically stabilized suspension surfactants or polymers are added. They adhere to the surface of the colloids and keep them at a large distance, where van der Waals interactions are small. As a consequence, clustering is prevented. In a charge-stabilized suspension, as we consider here, the colloids are charged and the sign of the charge is the same for all colloids. Therefore, there is a repulsive interaction caused by the Coulomb forces. Due to counter ions in the solvent that accumulate around a colloidal particle, the interaction is screened. It is given by the pair potential $\phi(r)$ according to the DLVO-theory [34, 35], named after Derjaguin, Landau, Verwey, and Overbeek:

$$\phi(r) = \frac{(Z^* e)^2}{4\pi\epsilon_0\epsilon_r} \left(\frac{e^{\kappa R}}{1+\kappa R} \right)^2 \frac{e^{-\kappa r}}{r}, \tag{2.1}$$

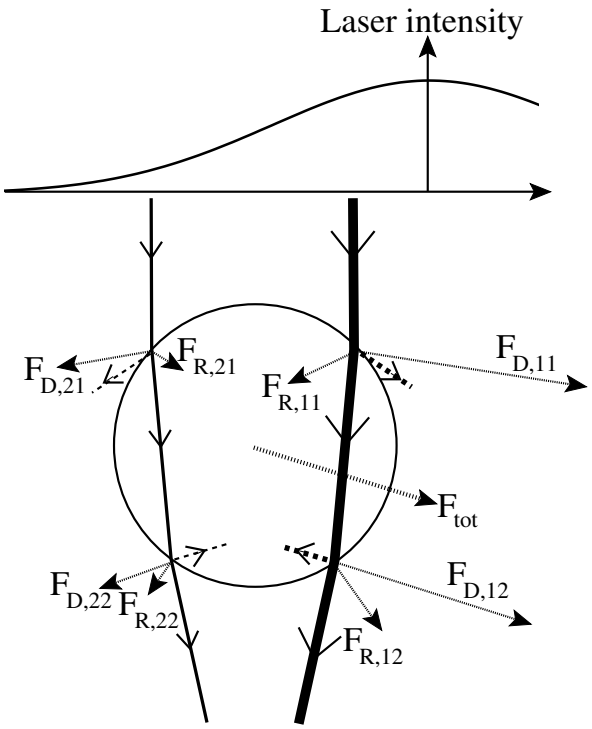

Figure 2.1: Colloidal particle in a laser beam with Gaussian intensity profile. The refraction of the light rays (full lines) lead to forces pointing in forward and outward direction. A small part of the rays is reflected (dashed lines). Because the rays closer to the beam center line are stronger, the total force acts in forward direction and towards the beam center line.

where r is the distance between two interacting colloids, R the radius of a colloid, Z^* its effective surface charge, ϵ_r the dielectric constant of water, and κ the inverse Debye screening length. Note that in our simulations we also do not allow the colloids to overlap, which corresponds to an additional excluded-volume interaction as for hard spheres. However, the mean particle distance and the screening length are usually much larger than the radius and therefore the excluded-volume interaction does not play an important role.

2.2 Optical tweezing

Inducing ordering in colloidal suspensions by modulated laser fields is based on the same phenomenon that is also responsible for optical tweezing, which is a widely used technique to manipulate micron-sized particles [36–38], but also viruses or bacteria [39], by laser beams. We therefore shortly introduce the principle of the optical tweezing effect and then explain how colloids are affected by laser fields.

We consider a colloidal particle in a laser beam with Gaussian intensity profile (see figure 2.1). Assuming that the refraction index of a colloid is higher than the one of the surrounding, light rays are refracted towards the center of the colloid. The deflections of

the rays lead to forces in outward forward direction (see forces $\mathbf{F}_{D,11}$, $\mathbf{F}_{D,12}$, $\mathbf{F}_{D,21}$, and $\mathbf{F}_{D,22}$ in figure 2.1). A small part of the rays is reflected at each interface leading to small additional forces mainly in forward direction ($\mathbf{F}_{R,11}$, $\mathbf{F}_{R,12}$, $\mathbf{F}_{R,21}$, and $\mathbf{F}_{R,22}$). If the colloidal particle is displaced out of the center of the beam, the forces acting on the side closer to the beam center line, i.e., $\mathbf{F}_{D,11}$, $\mathbf{F}_{D,12}$, $\mathbf{F}_{R,11}$, and $\mathbf{F}_{R,12}$, are much larger than those on the outside of the beam ($\mathbf{F}_{D,21}$, $\mathbf{F}_{D,22}$, $\mathbf{F}_{R,21}$, and $\mathbf{F}_{R,22}$). Therefore, the resulting total force $\mathbf{F}_{\text{tot}}$ acts in forward direction and towards the beam center, i.e., the colloid is forced back into the region of highest intensity. As a consequence, a laser beam can be used to trap and move around particles.

An alternative explanation of the optical tweezing phenomenon considers the energy of a dielectric particle in an electric field. Because the colloid has a higher dielectric constant than the surrounding medium, the free energy can be lowered by moving the particle into regions with a higher electric field, i.e., towards a higher laser intensity.

In an optical tweezer, the force is approximately proportional to the gradient of the laser intensity and is directed towards the highest intensities. Therefore, a colloid confined to a plane perpendicular to the beam can be considered to be in a potential that is proportional to the intensity of the light field, i.e., a particle in a Gaussian laser beam experiences a Gaussian potential. Correspondingly, a modulated laser field affects a two-dimensional colloidal suspension: The particles are forced towards the brightest spots of the laser pattern, which act as minima of a potential realized by the light-intensity distribution.

2.3 Previous works with colloids in laser fields

As shown in the previous subsection, modulated laser fields act as external potentials for colloidal suspensions. Such a set-up is widely used as a model system in statistical physics to study ordering or dynamics in external potentials (for a recent overview, see e.g. [40]). Here we present some examples of previous works with such systems.

External potentials consisting of periodic arrays of minima or pinning locations were studied experimentally [41,42] and with Brownian dynamics simulations [43,44]. A special example of a periodic potential is the one with triangular symmetry that can be realized as interference pattern of three laser beams (see also section 3.3). In a triangular potential, interesting new phases were observed, especially for the cases where two or more colloids populate each potential minimum [42–44]. For a pair of particles, called dimer, or three colloids per pinning location, termed trimer, the phase diagram was also determined analytically [45, 46] by mapping the problem onto a 3-state Potts model or other Ising-like theories.

A simple one-dimensional periodic potential can already lead to a surprising phase behavior. It first induces triangular ordering in a colloidal suspension if the colloidal density is chosen appropriately. Then, for increasing potential strength and appropriate colloidal interactions, the triangular phase melts again. We discuss this so-called laser-induced freezing and reentrant melting in section 6.1.

Studies of the dynamics of particles in external potentials revealed interesting new phenomena: If, for example, an ordered colloidal structure is dragged with a constant force over a triangular periodic potential, prefered directions for the colloidal motion exist and above a threshold velocity the ordering of the floating particles is destroyed [47–50].

Furthermore, laser fields can also be used to geometrically confine a system. To study particles moving in channels, lines of high laser intensity or circles of a fast rotating beam are employed. Such systems were, e.g., applied to explore single-file diffusion [51–53] (see also section 6.4), colloidal drift velocities and diffusion constants in tilted one dimensional periodic potentials [54, 55], or hydrodynamic interactions between colloids [56].

Note, there are many other examples where colloidal systems are applied. They are, e.g., used to study melting and elastic properties in two dimensions (see section 5.3), ordering of binary mixtures (e.g. [57–63]), crystallization processes [64–69], glass phases and glassy dynamics [70–76], and micro-rheology [77–81, E]. Furthermore, collective phenomena such as the behavior in shear flows [82–89] and lane formation [90–94] are explored. Experimentally, colloidal suspension are an interesting system to study multiple scattering of light [95–100] or to measure very small interactions such as depletion forces [101–104]. Other particle interactions and their properties are also investigated, for example, three-particle interactions and derivations from central forces [105–110] or hydrodynamic interactions (e.g. [56, 111–113], even artificial swimmers can be constructed with colloids [114, 115]).

Chapter 3

Quasicrystals and decagonal laser fields

A well-known result of crystallography states that periodic lattices are only compatible with 1, 2, 3, 4 or 6-fold rotational symmetry. Quasicrystals possess a perfect long-range positional order but nevertheless they are not periodic, i.e., it is not possible to obtain the same structure after any translation of the system. As a consequence, other rotational symmetries with, e.g., five-, eight-, or ten-fold axes are allowed. In addition, quasicrystals have also other unique properties, such as the so-called phasons, which correspond to special atomic rearrangements that do not change free energy. This chapter gives an overview over the most important properties of quasicrystals and of modulated laser fields with quasicrystalline symmetry, which we use in this work.

Section 3.1 is a brief summary of the history of quasicrystals, their construction methods, and their classification. In section 3.2, we present some properties of the number of the golden ratio, because it is an important and interesting number often found in pentagonal and decagonal patterns. Quasicrystalline laser fields are described in detail in section 3.3. In section 3.4, the hydrodynamic modes of a quasicrystal are discussed, especially the so-called phasons, which do not exist in periodic crystals. Finally, in section 3.5, we discuss systems, where a quasicrystalline symmetry is induced by a substrate or another external potential. Examples are thin films on surfaces of quasicrystals or atomic clouds in optical traps with quasicrystalline symmetry.

3.1 A brief introduction to quasicrystals

3.1.1 History

Recently, it was reported that non-periodic, quasicrystalline tilings were used in Islamic architecture a long time before they were discovered in the west [116]: Starting around 1200 AD some complex, but still periodic patterns were created using non-trivial tiles leading to very large unit cells. Later, in the 15^{th} century, a nearly perfect quasicrystalline

tiling, corresponding to the one later constructed by Penrose, was used as decoration on the Darb-i Imam shrine in Isfahan, Iran. In the west, during the first half of the 19$^{\text{th}}$ century, a standard classification of crystals was developed. It seemed natural that every two-dimensional structure with long-range order has to be periodic. Then, only 1, 2, 3, 4, or 6-fold rotational symmetries are possible [117]. An aperiodic tiling was still considered to be impossible in the early 1960s [118]. However, in 1966 Berger published a proof that aperiodic 2D-tilings exist [119], i.e., tilings without a translational symmetry but a perfect long-range order. He explicitly invented a tiling that is constructed out of a set of 20426 elementary tiles. A few years later aperiodic tilings consisting of just six tiles were found [120]. The most famous aperiodic tiling of the plane was presented by Penrose in 1974 [121]. This so called Penrose tiling can be constructed by using two elementary tiles (see also section 3.1.2). It has a five-fold rotational symmetry but no translational symmetry. Other aperiodic tilings were discovered in the following years (see also section 3.1.2), however, they seemed to be only of interest as theoretical models in mathematics. This changed in 1984 when Shechtman *et. al.* [1] published the observation of sharp ten-fold symmetric Bragg peaks in small metallic grains, which form in fast cooled alloys of Al with 14 at.% Mn. Shortly later, Levine and Steinhardt proposed that this is due to a quasicrystalline ordering without any translational symmetry [122]. Today, many quasicrystals with different point symmetries are known. Some quasicrystals are aperiodic in all three directions of space, for example the icosahedral Al-Mn grains in [1], others are periodic stacks of 8-, 10- or 12-fold symmetric two-dimensional quasicrystalline structures. Quasicrystals are not only observed in metallic alloys but they can even be constructed, e.g., with macromolecules [123].

The interest in quasicrystals is not only due to their non-crystallographic rotational symmetry, they also have many new properties that can probably lead to new applications in material science (cf. [124]). Because of the aperiodicity it was not obvious, whether quasicrystals are closer to amorphous or to crystalline materials. The material properties of quasicrystals turned out to be unique. For example, quasicrystals have an electronic band structure which contains a special pseudo-gap [125–127] leading to characteristic conductance properties [128, 129]. The mechanical properties are also very interesting: At low temperatures they are often very brittle [130, 131], whereas they become ductile at higher temperatures [132]. In recent time, there has been much research activity in the field of photonics and photonic crystals. The idea is to build components similar to electronic semiconductor devices such as transistors working with photons instead of electrons. Similar to the electronic band structure, an optical band structure can be calculated for crystals [133]. Quasicrystals have a very special optical band structure [134–136] with properties that may be used to construct photonic devices.

One of the most fascinating new properties of a quasicrystal is the larger number of independent hydrodynamic modes. Aside from phonons, which also exist in normal crystals, there are additional modes in quasicrystals called phasons. These new modes are important for elastic properties, the brittleness at low temperatures, and the melting behavior of quasicrystals. Phonons and phasons will be introduced in more detail in section 3.4.

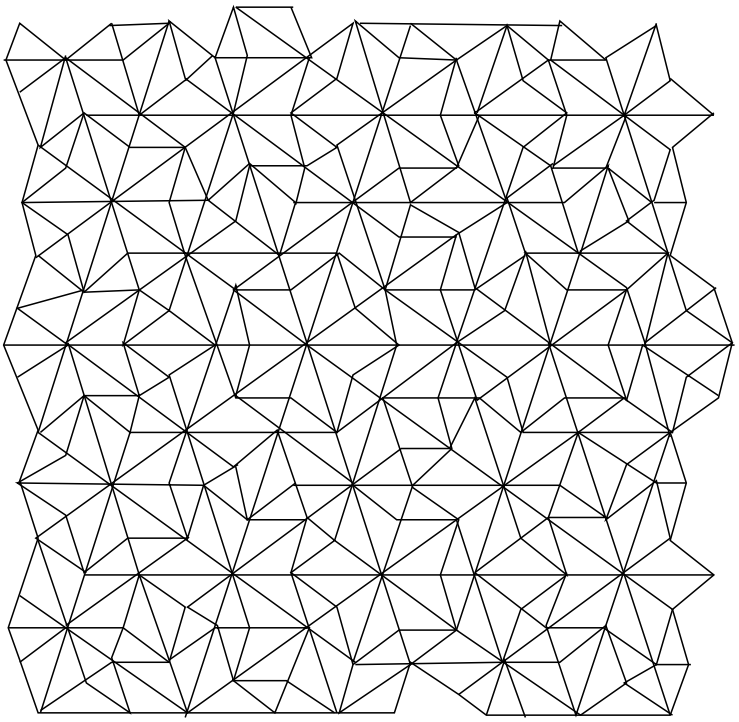

Figure 3.1: Penrose tiling.

3.1.2 Tilings

In this and the next subsection we discuss common methods to construct quasicrystalline patterns. Probably the most famous quasicrystalline pattern is the Penrose tiling [121] shown in figure 3.1. It has a 5-fold rotational symmetry and perfect long-range order. The Penrose pattern can be constructed by using four triangular elementary tiles [see figure 3.2(a)]. It is not allowed to combine the tiles in an arbitrary way. There are some matching rules which have to be obeyed. One possibility to implement such rules is to mark the edges of the triangles with arrows. Edges in contact must always have the same number of arrows pointing into the same direction [137, 138]. Other elementary tiles for building up Penrose pattern are shown in figures 3.2(b) and (c).

There are a lot of other quasicrystalline patterns that are usually assembled with tiles. Two examples are presented in figure 3.3. However, the matching rules usually are much more complicated than those for the Penrose tiling (see e.g. [139–141]).

Often tilings are also constructed by the so-called deflation method [121], which uses the self-similarity of the patterns. In each step of the deflation process every tile is replaced by a set of smaller tiles that cover the same area. This can be done in a way that the matching rules are obeyed. Therefore, after a few steps of deflation, a perfect quasicrystalline tiling covers the original starting tile.

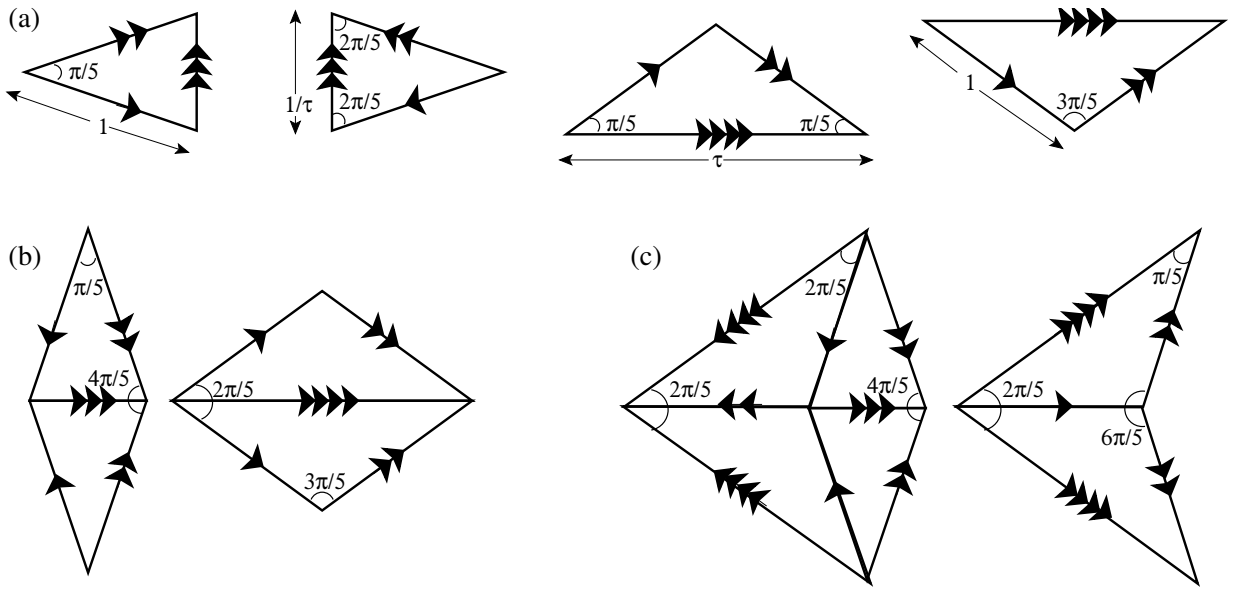

Figure 3.2: (a) Tiles of the Penrose pattern. The arrows on the edges symbolize matching rules. If two triangles are put together, the edges at contact must have the same number of arrows pointing into the same direction. The triangles can also be combined to (b) two rhombic tiles or (c) a kite and a dart tile, which serve as alternative elementary tiles for constructing a Penrose pattern.

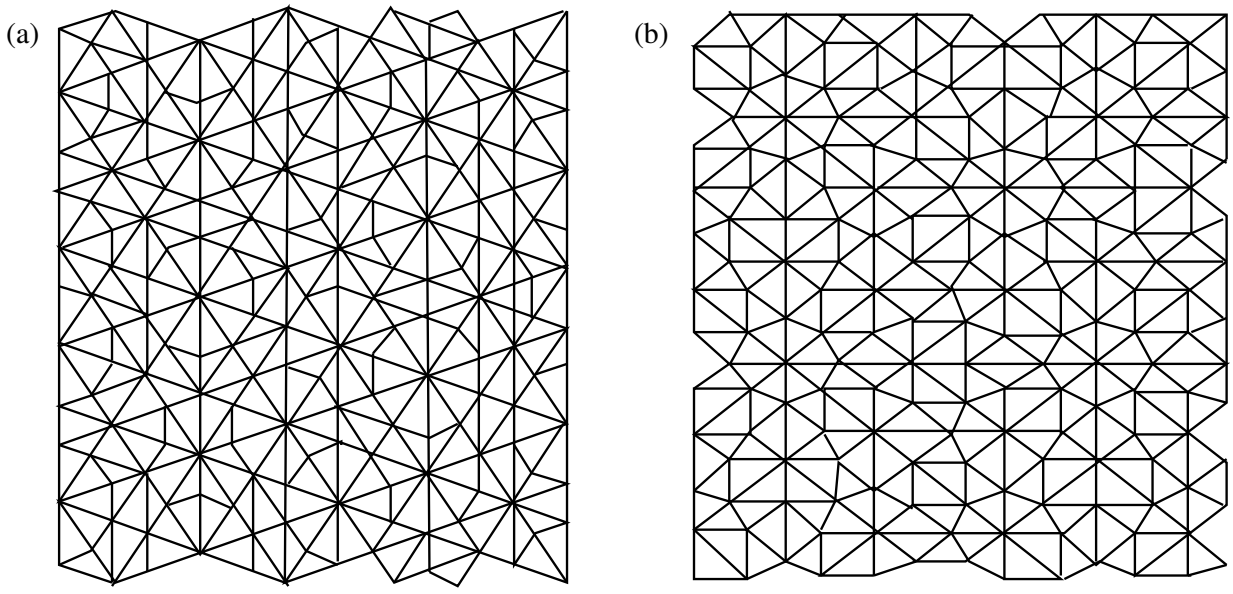

Figure 3.3: Other examples of quasicrystalline tilings: (a) decagonal Tübingen tiling, (b) octagonal Ammann tiling.

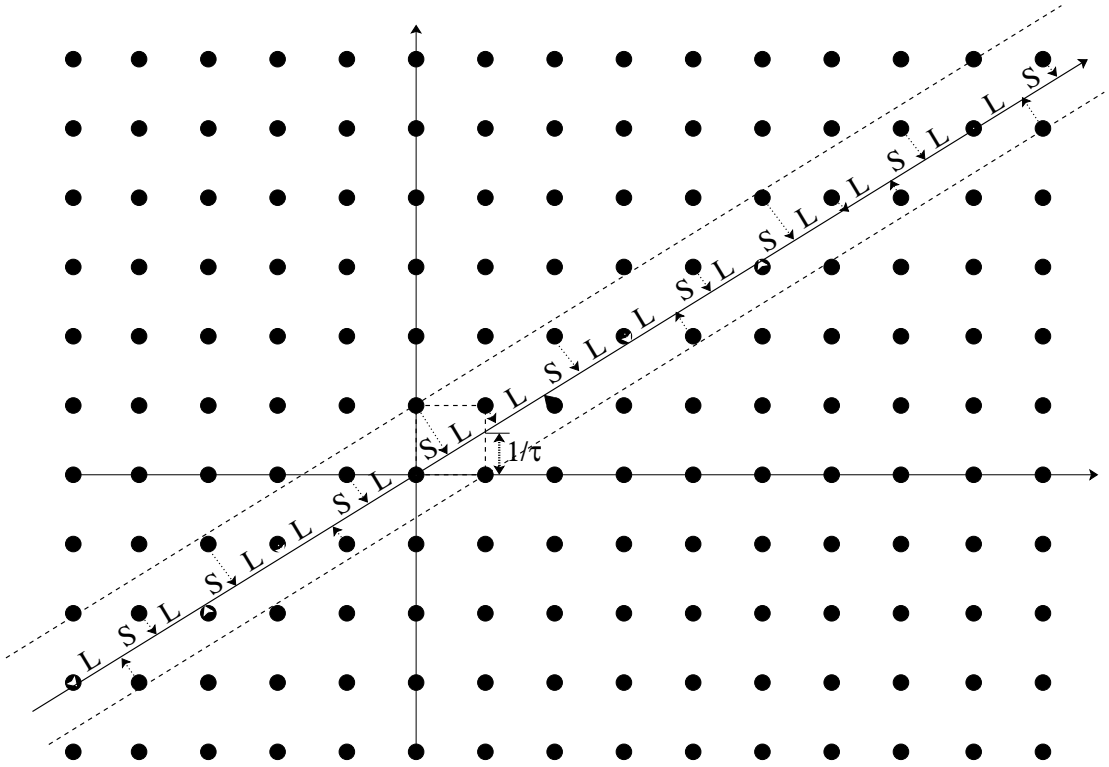

Figure 3.4: Projection of a two-dimensional square lattice on a line with slope $1/\tau$. The limiting, dashed lines of the acceptance region are defined by two vertices of the unit cell. The resulting one-dimensional sequence of small (S) and long (L) distances corresponds to the Fibonacci chain.

3.1.3 Projection methods

Two-dimensional quasicrystalline patterns can also be constructed by projecting a higher dimensional periodic lattice onto a plane. The Penrose tiling for example can be achieved by projecting a five-dimensional cubic structure onto a two-dimensional plane [137, 138, 142].

Here we shortly demonstrate the projection method for constructing a one-dimensional quasicrystal by starting with a two-dimensional square lattice and projecting the lattice points onto a line. The projection formalism works as follows: All points of the square lattice which are within some acceptance region are projected onto the line. If the slope of the line is an irrational number, the projected points form a non-periodic lattice, which nevertheless has a perfect long-range ordering and therefore is a quasicrystal. In the example shown in figure 3.4 we choose the slope $1/\tau$ where $\tau = (1 + \sqrt{5})/2$ is the number of the golden ratio (see section 3.2). The limiting lines of the acceptance region are defined by the unit cell of the square lattice in a way, that only one of the two outermost particles is accepted for the projection (see figure 3.4). The resulting quasicrystal corresponds to the so-called Fibonacci chain. A Fibonacci chain is a series of two elements L and S, here representing long and short distances between the points of the quasicrystal. The Fibonacci chain can also be constructed by starting a sequence with L and then re-

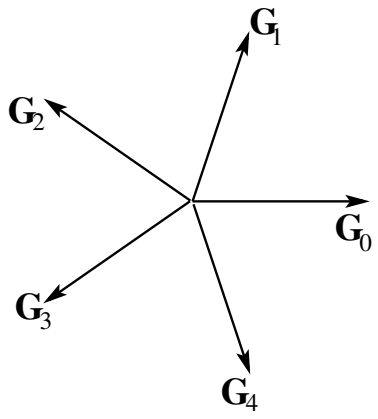

Figure 3.5: Reciprocal lattice vectors of a decagonal quasicrystal. Note that the negative vectors often are also considered as part of an elementary star of vectors describing the lattice. For the quasicrystalline laser field described in section 3.3, the vectors shown here correspond to the wave vectors of the laser beams projected into the sample plain.

peating the following replacements: $L \rightarrow LS$ and $S \rightarrow L$. The steps towards a longer Fibonacci chain therefore are: L, LS, LSL, $LSLLS$, $LSLLSLSL$, $LSLLSLSLLSLLS$, $LSLLSLSLLSLLSLSLLSLSL$ etc. The probability to find the element L at a certain position in such a chain is calculated in section 3.2.

In another construction method, patterns of parallel lines are drawn in each symmetry direction, e.g., five sets of parallel lines. The vortices of, e.g., a decagonal pattern then are located at positions close to certain line intersections [137, 138, 143].

3.1.4 Classification of quasicrystals

One way to group quasicrystals is to consider them as projection of a higher-dimensional lattice as introduced in the previous subsection. Using the classification for such regular crystals and describing the method of projection directly gives a method to characterize quasicrystals (see e.g. [139, 144]).

Another possibility is to look at the Fourier representation of a quasicrystal [145, 146]. The mass density $\rho(\mathbf{r})$ can be written in terms of the Fourier coefficients $\rho_{\mathbf{G}}$ according to

$$\rho(\mathbf{r}) = \sum_{\mathbf{G}} \rho_{\mathbf{G}} \exp\left(i\mathbf{G} \cdot \mathbf{r}\right), \tag{3.1}$$

where the sum is over all reciprocal lattice vectors $\mathbf{G}$. For an ordered structure, it is usually sufficient to consider a small set of vectors $\mathbf{G}$ such that their linear combinations generate the complete set of reciprocal lattice vectors. A set of vectors $\mathbf{G}$ that reflects the rotational symmetry of the reciprocal lattice forms a star (see e.g. figure 3.5). Note that with a vector $\mathbf{G}$ also its negative belongs to the reciprocal lattice. As a consequence, reciprocal lattices always display rotational symmetries with m-fold axes where m is even. However, the the corresponding quasicrystal in real space posses either a m- or $m/2$-fold symmetry axis.

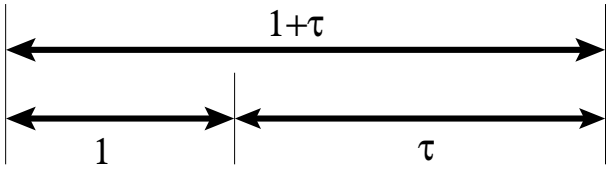

Figure 3.6: A division according to the golden ratio. The ratio of length of the complete line and the length of the longer segment equals the ratio of the lengths of the long and the short segment.

For a quasicrystal the points of the reciprocal lattice lie dense in the reciprocal space. For example, for any given point in the plane a linear combination of the five lattice vectors shown in figure 3.5 exists that describes a point at an arbitrary small distance. Bragg peaks in experiment correspond to reciprocal lattice points. The intensities of these peaks are given by $|\rho(\mathbf{G})|^2$. As a consequence, the diffraction patterns contains spots of different brightness and, therefore, displays the symmetry of the reciprocal lattice.

3.2 The number of the golden ratio

The number of the golden ratio τ is an important algebraic irrational number in mathematics that also appears in arts and even in some biological systems (see e.g. [147]). It is usually defined as the positive solution of the quadratic equation

$$\tau^2 - \tau - 1 = 0, \tag{3.2}$$

i.e., it is

$$\tau = \frac{1+\sqrt{5}}{2} \approx 1.618. \tag{3.3}$$

Dividing a line according to the golden ratio (see figure 3.6) means that the length of the total line $1+\tau$ divided by the length of the longer segment τ equals the length of the longer segment τ divided by the length 1 of the shorter one:

$$\frac{1+\tau}{\tau} = \frac{\tau}{1}, \tag{3.4}$$

which corresponds to equation (3.2). An interesting consequence of such a way of dividing a line is that the ratio of the shorter segment and the difference of the lengths of the segments is again τ, since

$$\frac{1}{\tau - 1} = \tau \text{ or } \frac{1}{\tau} = \tau - 1 \tag{3.5}$$

again corresponds to equation (3.2).

The number of the golden ratio can also be written as continued fraction

$$\tau = 1 + \frac{1}{1 + \frac{1}{1 + \frac{1}{1+\ldots}}}. \tag{3.6}$$

This implies

$$\tau = 1 + \frac{1}{\tau} \tag{3.7}$$

or again equation (3.2). Another interesting formula uses a continued square root:

$$\tau = \sqrt{1 + \sqrt{1 + \sqrt{1 + \sqrt{1 + ...}}}}, \tag{3.8}$$

equivalent to the relation

$$\tau = \sqrt{1 + \tau} \tag{3.9}$$

that also gives the positive solution of equation (3.2).

The golden ratio is related to the Fibonacci series, which is given by its first elements $F_0 = 0$ and $F_1 = 1$ and the recurrence relation

$$F_n = F_{n-2} + F_{n-1} \text{ for } n \geq 2. \tag{3.10}$$

Therefore, the first Fibonacci numbers are 0, 1, 1, 2, 3, 5, 8, 13, 21, 34, 55, 89, 144, 233, 377 etc. An explicit formula for the Fibonacci numbers exists [148]

$$F_n = \frac{\tau^n - (-\tau)^{-n}}{\sqrt{5}}. \tag{3.11}$$

It can be proven by induction: Equation (3.11) is valid for F_0 and F_1. Furthermore, if F_{n-2} and F_{n-1} are given by (3.11), one finds

$$\begin{aligned} F_n = F_{n-2} + F_{n-1} &= \frac{\tau^{n-2} - (-\tau)^{-n+2}}{\sqrt{5}} + \frac{\tau^{n-1} - (-\tau)^{-n+1}}{\sqrt{5}} \\ &= \frac{\tau^{n-2} + \tau^{n-1} - (-\tau)^{-n+2} - (-\tau)^{-n+1}}{\sqrt{5}} \\ &= \frac{\tau^{n-1}\left(\frac{1}{\tau} + 1\right) - (-\tau)^{-n+1}(-\tau + 1)}{\sqrt{5}} \\ &= \frac{\tau^n - (-\tau)^{-n}}{\sqrt{5}}, \end{aligned} \tag{3.12}$$

where $\tau = 1/\tau + 1$ or $1/\tau = 1 - \tau$ was used. Now, the golden ratio is the ratio of two successive Fibonacci numbers in the limit $n \to \infty$, i.e.,

$$\tau = \lim_{n\to\infty} \frac{F_n}{F_{n-1}}, \tag{3.13}$$

which follows from (3.11):

$$\lim_{n\to\infty} \frac{F_n}{F_{n-1}} = \lim_{n\to\infty} \frac{\tau^n - (-\tau)^{-n}}{\tau^{n-1} - (-\tau)^{-n+1}} = \lim_{n\to\infty} \frac{\tau^n}{\tau^{n-1}} = \tau, \tag{3.14}$$

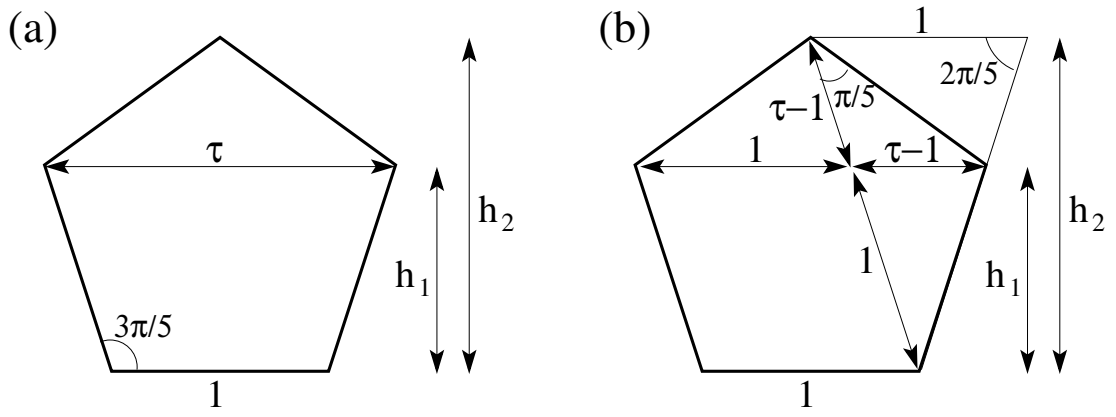

Figure 3.7: (a) In a regular pentagon with edges of length 1, the indicated line has length τ. In addition, $h_2/h_1 = \tau$. (b) Illustration of the proof as described in the text.

using $\lim_{n\to\infty} \tau^{-n} = 0$. We will employ the approximation of the golden ratio by the ratio of two successive Fibonacci numbers to implement the periodic boundary conditions in our simulations (see section 4.3).

The golden ratio is connected to the Fibonacci chain that consists of elements L and S and is constructed by repeating the replacement rules $L \to LS$ and $S \to L$ (see section 3.1.3). In an infinite Fibonacci chain, the probability $p_\infty(L)$ to find L at a certain position is connected to the probability $p_\infty(S)$ to find S via

$$\frac{p_\infty(L)}{p_\infty(S)} = \tau. \tag{3.15}$$

This can be shown as follows: The probability $p_n(L)$ to find L after n iterations of the replacement rules is given by the probabilities $p_{n-1}(L)$ and $p_{n-1}(S) = 1 - p_{n-1}(L)$ to find L or S after $n-1$ iterations by

$$p_n(L) = \frac{p_{n-1}(S) + p_{n-1}(L)}{p_{n-1}(S) + 2p_{n-1}(L)} = \frac{1}{1 + p_{n-1}(L)}. \tag{3.16}$$

Equation (3.16) follows directly from the replacement rules. In the limit $n \to \infty$,

$$p_\infty(L) = \frac{1}{1 + p_\infty(L)} \tag{3.17}$$

and therefore

$$p_\infty(L) = \frac{\sqrt{5} - 1}{2} = \tau - 1, \tag{3.18}$$

which with $p_\infty(S) = 1 - p_\infty(L)$ leads to (3.15).

The golden ratio is also important in pentagons: As illustrated in figure 3.7(a), in a regular pentagon, where the length of the edges is 1, the length of a line parallel to one

edge and connecting two vertices of the pentagon is τ. The ratio of the total height h_2 to the partial height h_1 is also given by the golden ratio [see figure 3.7(a) for the definition of h_1 and h_2]. To proof these properties, we use the geometric relations indicated in figure 3.7(b) and the intercept theorem and find

$$\frac{\tau - 1 + 1}{1} = \frac{1}{\tau - 1}. \tag{3.19}$$

This corresponds to equation (3.2), i.e., τ given in the pentagon is indeed the number of the golden ratio. Furthermore, the intercept theorem gives

$$\frac{h_2}{h_1} = \frac{1}{\tau - 1} = \tau, \tag{3.20}$$

where we used $\tau - 1 = 1/\tau$.

The relations for the lengths in a pentagon give us the opportunity to express τ in terms of trigonometric functions. We find [see figure 3.7(b)]

$$\tau = \frac{1}{2\cos(2\pi/5)} = 2\cos(\pi/5) \tag{3.21}$$

$$\text{and } \tau = \frac{h_1}{h_2 - h_1} = \frac{\sin(2\pi/5)}{\sin(\pi/5)}. \tag{3.22}$$

Equations (3.21) and (3.22) will often be used throughout this work.

3.3 Quasicrystalline laser fields

In this section we introduce methods to obtain laser fields with quasicrystalline symmetry. First, we present different types of patterns that can be produced by varying the number of laser beams or the polarization. In subsection 3.3.2 we introduce the potential we use in this work. For such a potential the distribution of the depths of the minima is shown in subsection 3.3.3 and finally in subsection 3.3.4 the number and distance of nearest neighbors for the positions of the minima are determined. The results of subsections 3.3.3 and 3.3.4 are needed for the random trap model that we develop in section 8.3 to describe the Brownian motion in a decagonal potential.

3.3.1 Zoo of possible interference patterns

To obtain a quasicrystalline laser field in an experiment, a laser beam is split up in n beams of equal strength. The beams are arranged along the n edges of a prism that is made of a perfect n-sided polygonal base. Finally, the beams are focused onto the sample containing the colloidal suspension (see figure 3.8 as an example for five beams). In the plane of the sample, which in the following will be termed the xy-plane, the beams interfere and form a crystalline or quasicrystalline interference pattern of m-fold rotational symmetry,

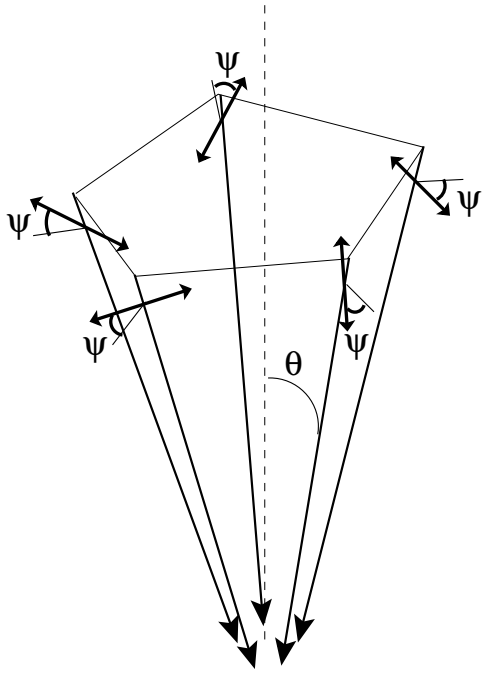

Figure 3.8: Five laser beams arranged symmetrically around the vertical axis are focused onto the sample. The polarization vectors are given by the angle ψ, which is measured between the direction of polarization and the vector pointing outward in radial direction. The opening angle θ is the angle between a beam and the symmetry axis.

where $m = n$ if the number of beams n is even and $m = 2n$ if n is odd. In theory, the intensity field in the xy-plane can be calculated by summing up the electric fields of all beams, taking the square of the total electric field to get the intensity, and averaging over one period of the pattern that oscillates with the circular frequency ω of the light. The corresponding potential then is (see also e.g. [149]):

$$\begin{aligned}
V(\mathbf{r}) &\propto -\int_0^T dt \left\{ \sum_{j=0}^{n-1} \mathbf{E}_j \cos\left[\mathbf{G}_j \cdot \mathbf{r} + \varphi_j + \omega t\right] \right\}^2 \\
&= -\int_0^T dt \sum_{j=0}^{n-1} \sum_{k=0}^{n-1} \mathbf{E}_j \cdot \mathbf{E}_k \cos\left[\mathbf{G}_j \cdot \mathbf{r} + \varphi_j + \omega t\right] \cos\left[\mathbf{G}_k \cdot \mathbf{r} + \varphi_k + \omega t\right] \\
&\propto -\int_0^T dt \sum_{j=0}^{n-1} \sum_{k=0}^{n-1} \mathbf{E}_j \cdot \mathbf{E}_k \left\{ \cos\left[(\mathbf{G}_k - \mathbf{G}_j) \cdot \mathbf{r} + \varphi_k - \varphi_j\right] \right. \\
&\qquad \left. + \cos\left[(\mathbf{G}_k + \mathbf{G}_j) \cdot \mathbf{r} + \varphi_k + \varphi_j + 2\omega t\right] \right\} \\
&\propto -\sum_{j=0}^{n-1} \sum_{k=0}^{n-1} \mathbf{E}_j \cdot \mathbf{E}_k \cos\left[(\mathbf{G}_k - \mathbf{G}_j) \cdot \mathbf{r} + \varphi_k - \varphi_j\right] + const, \qquad (3.23)
\end{aligned}$$

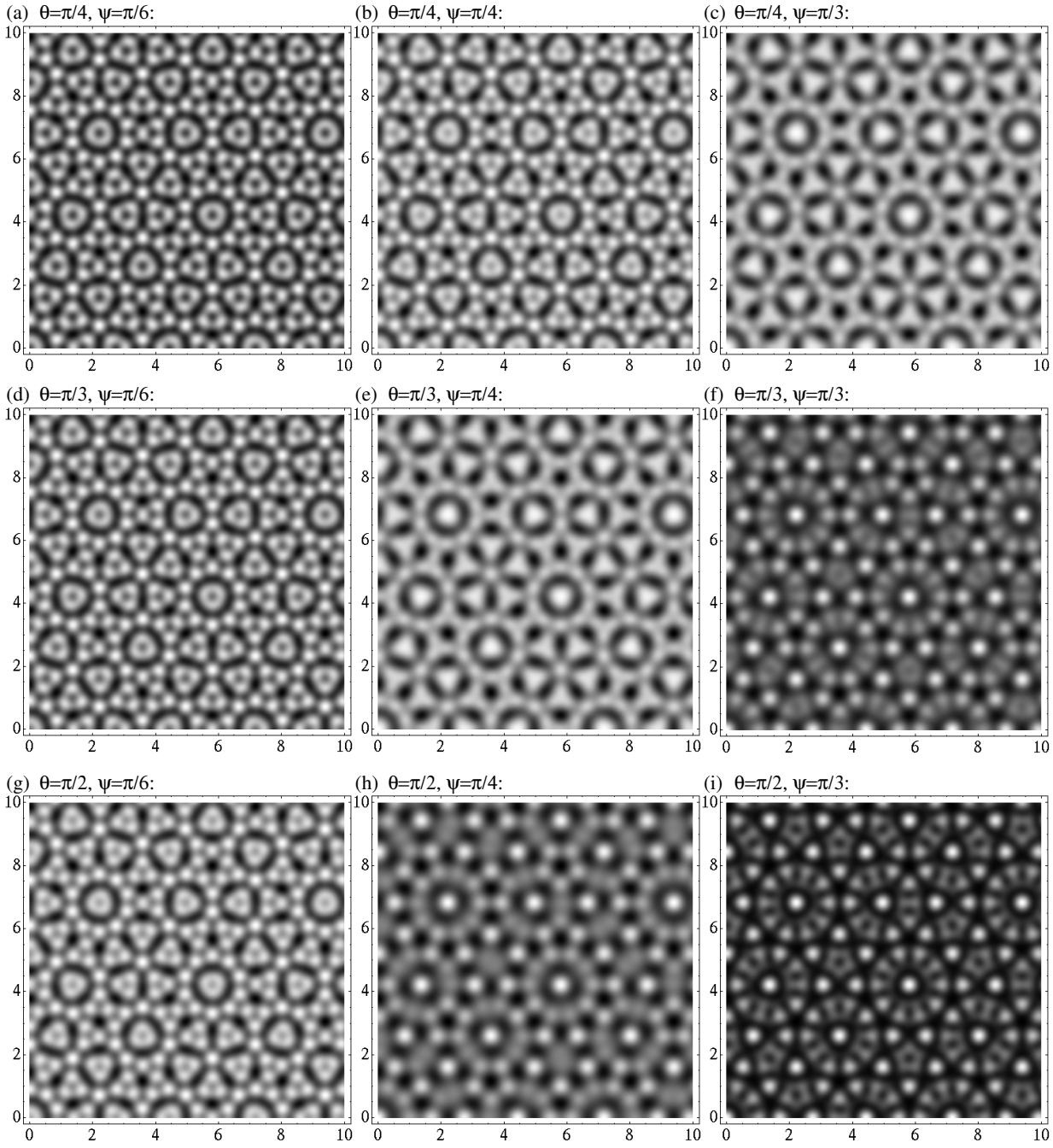

Figure 3.9: Intensity fields of five interfering laser beams calculated by equation (3.23) for different opening angles θ and polarizations characterized by the angle ψ. The angles θ and ψ are explained in figure 3.8. The phases φ_j are set to zero.The lengthscale is given by $a_V = 2\pi/|\mathbf{G}_j|$, where $\mathbf{G}_j$ is a wave vector projected onto the xy-plane.

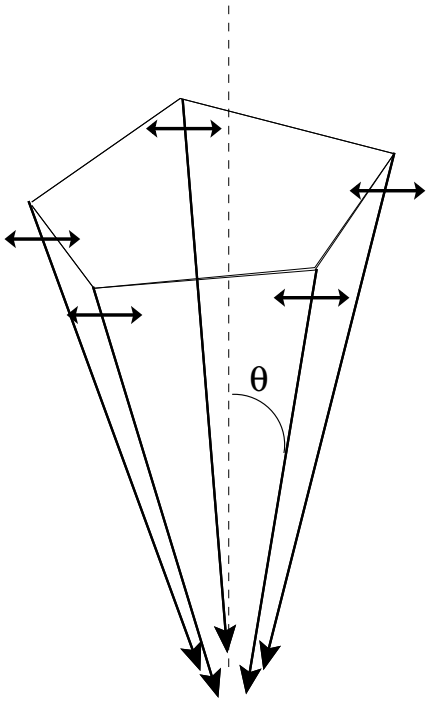

Figure 3.10: For the standard decagonal laser field, the five laser beams all have the same polarization. The opening angle θ between a beam and the symmetry axis is assumed to be small.

where $\mathbf{G}_j$ are the wave vectors projected onto the xy-plane (see figure 3.5) and $\mathbf{r} = (x, y)$ is the position in the xy-plane. A beam has the time period $T = 2\pi/\omega$, the phase φ_j, and the electric field vector $\mathbf{E}_j$. To really obtain a perfect rotational symmetry the polarizations vectors $\mathbf{E}_j$ of the beams have to be chosen in a symmetric way (see e.g. figure 3.8). In figure 3.9 examples of interference patterns that are obtained by five laser beams without phase differences are shown for different polarizations and opening angles.

In an experiment, it is easier to realize a configuration, where all beams are polarized in the same direction (see figure 3.10). For a finite opening angle $\theta > 0$, the resulting intensity pattern no longer has perfect rotational symmetry. However, in experiments, θ usually is very small. Therefore, in the following we assume the limit $\theta \to 0$ in equation (3.23) and find potentials with perfect rotational symmetry:

$$V(\mathbf{r}) \propto -\sum_{j=0}^{n-1}\sum_{k=0}^{n-1} \cos\left[(\mathbf{G}_k - \mathbf{G}_j)\cdot\mathbf{r} + \varphi_k - \varphi_j\right]. \tag{3.24}$$

In figure 3.11 such intensity patterns for different numbers of beams with identical phases are shown. Note, all patterns have a center of perfect rotational symmetry at $(x, y) = (0, 0)$.

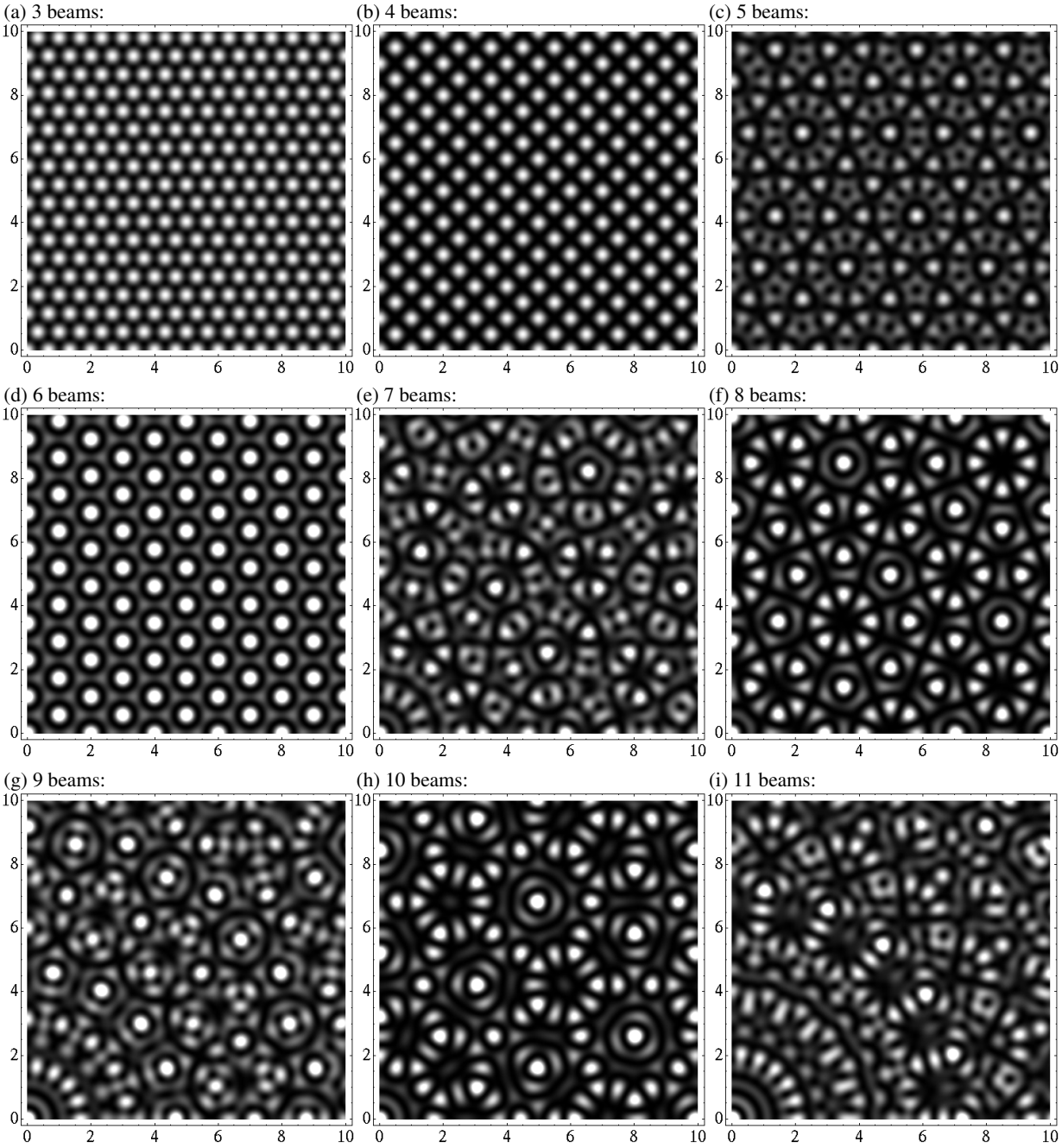

Figure 3.11: Interference patterns of different numbers of beams with identical polarization vectors and phases φ_j calculated according to equation (3.24). The length scale is given by $a_V = 2\pi/|\mathbf{G}_j|$, where $\mathbf{G}_j$ is the projection of the wave vector of a laser beam onto the xy-plane.

3.3.2 The standard decagonal potential

The decagonal standard potential is obtained by five laser beams with the same polarization vectors as shown in figure 3.10 in the limit $\theta \to 0$ for the opening angle. Using (3.24), we find

$$V(\mathbf{r}) = -\frac{V_0}{25} \sum_{j=0}^{4} \sum_{k=0}^{4} \cos\left[(\mathbf{G}_k - \mathbf{G}_j) \cdot \mathbf{r} + \varphi_k - \varphi_j\right], \tag{3.25}$$

where $\mathbf{G}_j$ are the five wave vectors projected onto the xy-plane as shown in figure 3.5 and φ_j are the phases of the beams. The prefactor is chosen such that $-V_0$ is the depth of the deepest potential minimum.

Grey-scale representations as well as a three-dimensional plot of the landscape of the potential energy are shown in figure 3.12. Some local structures repeatedly occur in the potential. Examples are a deep minimum surrounded by a broad ring with almost ten-fold rotational symmetry [see left-hand side of figure 3.12(a)] and weak minima forming a pentagon surrounded by another pentagon of deeper minima [right-hand side of figure 3.12(a)]. Another striking feature of the potential are perfect lines of low intensity [cf. black lines in figure 3.12(b)] that appear in five directions. If all phases φ_j are set to zero, the decagonal intensity pattern possesses a center of perfect rotational symmetry at $x = y = 0$. However, the potential contains a lot of points that are very similar to the perfect symmetry center. Therefore, the uniqueness of the perfect center will be neglected in the following. Furthermore, after certain translations of the intensity pattern, which will be explained in detail in section 4.3.2, the potential is very similar to the original one. As a consequence, the actual position where the simulation box of our numerical investigations is placed within the potential does not affect the results.

In the following, we define the length scale a_V of the potential with the help of the projected wave vectors $\mathbf{G}_j$ of the laser beams according to $a_V = 2\pi/|\mathbf{G}_j|$.

3.3.3 Distribution of depths of the minima

As can be seen in figure 3.12(c), the potential mainly consists of a pattern of wells. An important function characterizing the decagonal laser field is the probability to find a well of a certain depth. We therefore determine the probability density $\rho(V_m)$ for a minimum to have a potential value between $-V_m$ and $-V_m + dV_m$. The distribution is plotted in figure 3.13. In literature it is known that such distributions often are very complicated [150]. However, here we find a continuous distribution which, interestingly, for deep minima behaves like $V_m^{-3/4}$. Furthermore, minima with depths below $V_m/V_0 < 0.24$ do not exist indicating that the potential mainly consists of quiet deep wells.

The depths distribution $\rho(V_m)$ is obtained in a rectangular area of the potential by analyzing all local minima. Because the potential is not periodic, the area has to be chosen in a way, that it well represents the whole potential. We explain the method to find such an area in section 4.3. We just note that we analyzed 24094 minima in the area given by $0 \le x < 110 a_V$ and $0 \le y < 89 a_V / \sin(2\pi/5)$.

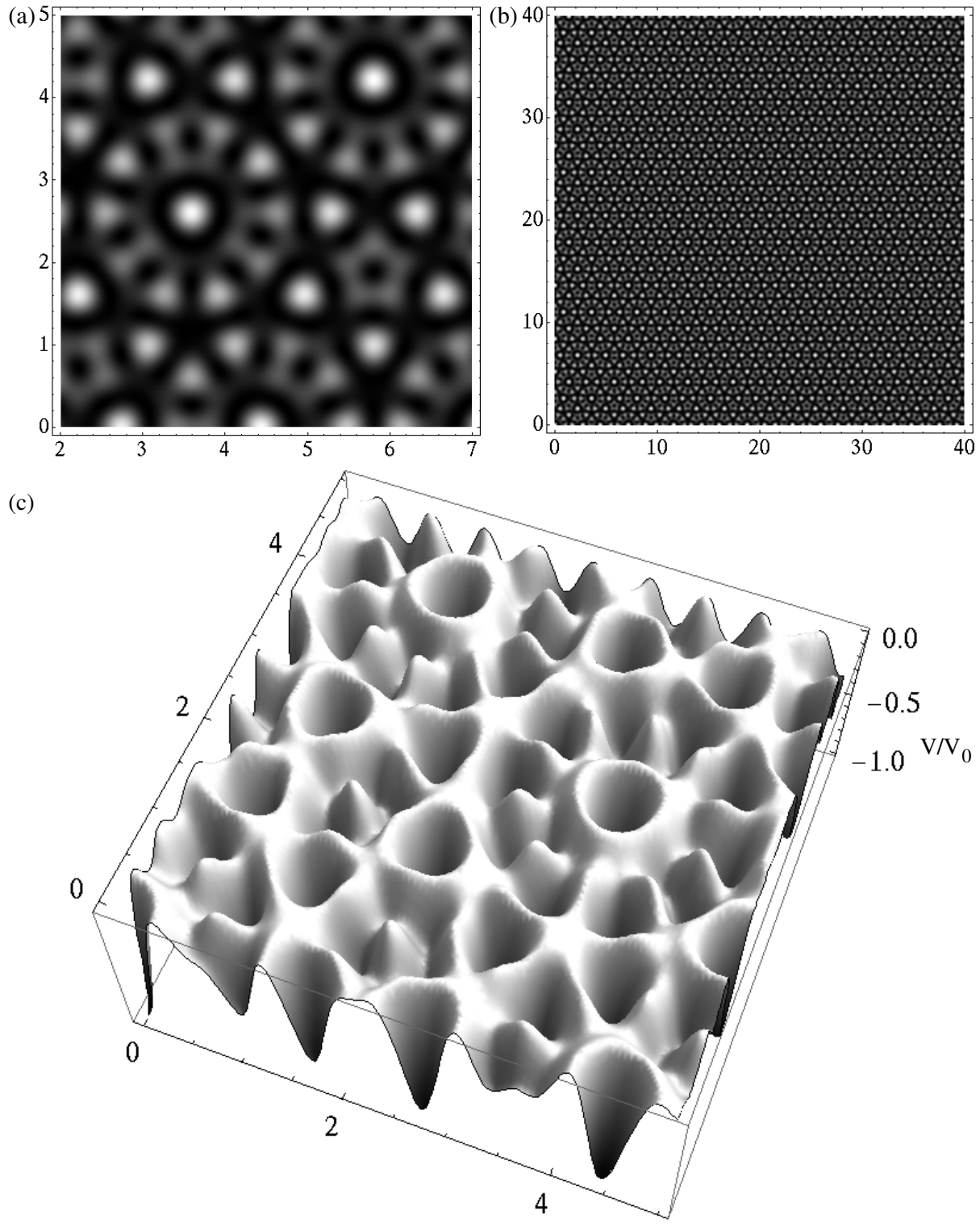

Figure 3.12: Standard decagonal potential. The length scale is given by $2\pi/|\mathbf{G}_j|$, where $\mathbf{G}_j$ is the projection of the wave vector of a laser beam onto the xy-plane (see figure 3.5). All phases φ_j are set to zero.

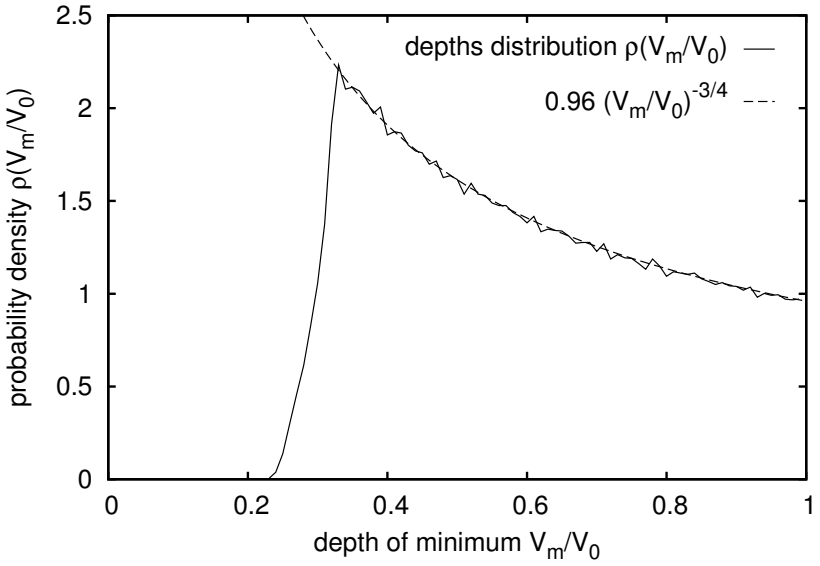

Figure 3.13: Probability density $\rho(V_m)$ of the depths of the minima in the standard decagonal potential. The dashed line behaves as $V_m^{-3/4}$.

3.3.4 Nearest neighbors in the decagonal potential

We define nearest neighbors as particles connected with a bond in a Delaunay triangulation. A Delaunay triangulation connects the vertices of a two-dimensional set of points such that a circumcircle constructed through the three vertices of any triangle does not contain any other point of the pattern. The Delaunay triangulation is unique if more than three points never lie on a circle. Therefore, for random point patterns it usually gives a unique description how to define nearest neighbors [151]. A Delaunay triangulation is the dual pattern of a Voronoi diagram (also called Dirichlet tessellation), which consists of the Wigner-Seitz cells around each of the points.

We construct the Delaunay triangulation using the program Triangle by J. R. Shewchuk [152]. Using the same area for the decagonal potential as in the previous subsection, we determine the mean values for the number of nearest neighbors z and their distance l and find $z = 5.85$ and $l = 0.73a_V$. Note that in a totally random point pattern the average value of the number of nearest neighbors is always six [153]. Therefore, the pattern of the positions of minima does not fully correspond to a random pattern but contains some degenerations.

3.4 Phonons and Phasons

Besides phonons that are also known from usual crystals, in quasicrystals there also exist so-called phasons, which we want to introduce in this section.

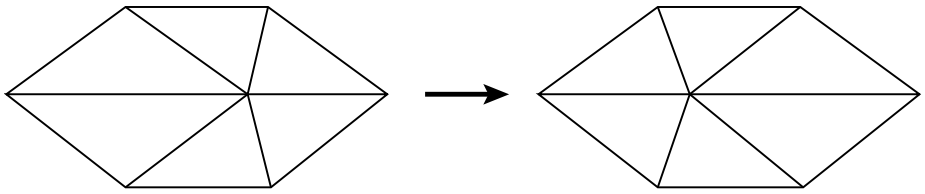

Figure 3.14: Phasonic flip in a Penrose or Penrose-like quasicrystalline pattern.

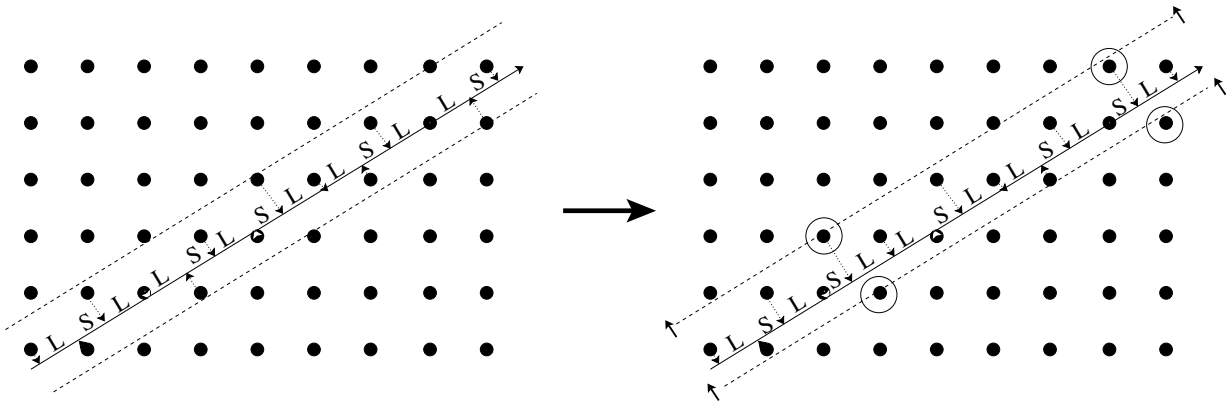

Figure 3.15: Phasonic rearrangement in a one-dimensional quasicrystal caused by a displacement of the acceptance region. The points which are no longer in the acceptance region or just entered it are marked by circles.

3.4.1 Phasons

Phasons are global rearrangements of atoms that do not change the free energy of the quasicrystal in the limit of long wavelengths. They are unique to quasicrystals and still a main topic in recent discussions [4]. Phasonic fluctuations were already observed in experiments, e.g., [154, 155].

There are different ways phasons can be defined. First, in a quasicrystalline pattern given by a tiling, a phasonic rearrangement corresponds to locally changing some tiles as, e.g., shown in figure 3.14. Such a rearrangement often is called phasonic flip. Note that the new configuration may violate some of the matching rules. Examples of works in literature using phasonic flips in tiling models are [131, 156–158].

Second, since quasicrystals can be constructed via the projection of a higher dimensional regular lattice (see section 3.1.3), a uniform phasonic shift corresponds to a displacement of the acceptance region. Figure 3.15 shows the Fibonacci chain as a projection of a two-dimensional square lattice. By displacing the whole acceptance region, some local phasonic flips of the form $LS \rightarrow SL$ occur. The consequences of such phasonic flips for physical properties such as elasticity were, e.g., studied in [159–161].

Finally, phasons can be defined as hydrodynamic modes in a continuum description of a quasicrystal. We introduce this approach in the next subsection.

3.4.2 Hydrodynamic modes

Hydrodynamic modes are excitations in a system that do not change the free energy in the limit of long wavelengths. Following the work of Socolar *et. al.* [3], we determine the hydrodynamic modes in a continuum picture where the crystal or quasicrystal is given by a density field $\rho(\mathbf{r})$. We consider an expansion of the free energy $\mathcal{F}$ in terms of $\rho(\mathbf{r})$:

$$\mathcal{F} = \int dA \sum_{k=1}^{\infty} B_k \rho(\mathbf{r})^k. \tag{3.26}$$

B_k are coefficients that depend on the details of the actual system and the integration is over the whole plane. With the Fourier series for the density,

$$\rho(\mathbf{r}) = \sum_j \rho_j \exp\left(-i\mathbf{G}_j \cdot \mathbf{r}\right), \tag{3.27}$$

where $\mathbf{G}_j$ are reciprocal lattice vectors and ρ_j the corresponding Fourier components, the free energy then is

$$\begin{aligned} \mathcal{F} &= \int dA \sum_{k=1}^{\infty} B_k \sum_{j_1,\ldots,j_k} \prod_{l=1}^{k} \rho_{j_l} \exp\left(-i \sum_{l=1}^{k} \mathbf{G}_{j_l} \cdot \mathbf{r}\right) \\ &= A \sum_{k=1}^{\infty} B_k \sum_{j_1,\ldots,j_k} \delta\left(\sum_{l=1}^{k} \mathbf{G}_{j_l}\right) \prod_{l=1}^{k} \rho_{j_l}. \end{aligned} \tag{3.28}$$

Here A is the area of the system and the Kronecker symbol $\delta\left(\sum_{l=1}^{k} \mathbf{G}_{j_l}\right)$ is 1 if $\sum_{l=1}^{k} \mathbf{G}_{j_l} = 0$ and zero in all other cases. Setting $\rho_j = |\rho_j| \exp\left(i\varphi_j\right)$, we find

$$\mathcal{F} = A \sum_{k=1}^{\infty} B_k \sum_{j_1,\ldots,j_k} \delta\left(\sum_{l=1}^{k} \mathbf{G}_{j_l}\right) \prod_{l=1}^{k} |\rho_{j_l}| \exp\left(i \sum_{l=1}^{k} \varphi_{j_l}\right) \tag{3.29}$$

and realize that the free energy only depends on the sum of all phases $\sum_{l=1}^{k} \varphi_{j_l}$. Therefore, collective changes in all phases that do not affect the sum of the phases will help to identify hydrodynamic modes. In the next paragraph, we determine the number of independent long wavelength excitations that are given by such collective phase changes.

In an ordered system usually only a small set of reciprocal lattice vectors $\mathbf{G}_j$ is considered for expansion (3.29) [cf. section 3.1.3]. To construct density fields with the right point symmetry, often stars of lattice vectors such as the ones shown in figures 3.5 or 3.16 and their negative vectors are used. The minimal number of vectors in a star is connected to the number of base vectors of the reciprocal lattice. For example, in periodic crystals the minimal number of base vectors to construct the reciprocal lattice is equal to the number of dimensions of the system. Therefore, a two-dimensional triangular lattice has two base vectors. The star describing triangular ordering contains an additional lattice

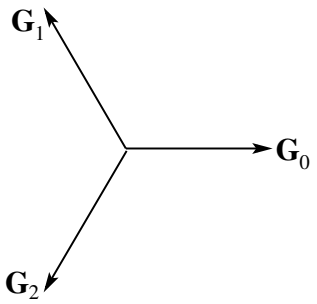

Figure 3.16: Lattice vectors of the triangular phase. For the free energy expansion, the inverse lattice vectors $-\mathbf{G}_0$, $-\mathbf{G}_1$, and $-\mathbf{G}_2$ have to be added.

vector obtained by applying simple point symmetry operations to the basis. Including the negative vectors, the total number of lattice vectors to be considered in the free energy expansion is, at least, six. Because the density $\rho(\mathbf{r})$ is real, one finds $|\rho_{\mathbf{G}}| = |\rho_{-\mathbf{G}}|$ and $\varphi_{\mathbf{G}} = -\varphi_{-\mathbf{G}}$. Therefore, the total number of independent phases in a triangular lattice is three. To identify hydrodynamic modes the sum of these phases has to stay constant, i.e., only two independent hydrodynamic modes exist. For infinite wavelength, they correspond to displacements of the whole lattice in x or y direction. Usually, these modes are called phonons.

In quasicrystals the number of base vectors needed to obtain all lattice vectors is higher than the number of dimensions of the system. The minimal set of base vectors is given as projection of the higher-dimensional lattice if the quasicrystal is obtained by the projection method (see section 3.1.3). Another possibility to find the minimal number $n_{\mathbf{G}}$ of reciprocal base vectors is to look on the number n_i of incommensurable length scales in each lattice direction. One finds $n_{\mathbf{G}} = n_i d$, where d is the number of dimensions [3]. In a decagonal quasicrystal, there are two length scales in the direction of each reciprocal vector (see figure 3.5). As a consequence, the minimal number of lattice vectors needed is four. The free energy expansion (3.29) uses the five vectors shown in figure 3.5 and their inverse ones, i.e., there are five independent phases φ_j with $j = 0..4$. To identify hydrodynamic modes, the sum of these phases has to stay constant. Therefore, we find four independent hydrodynamic modes in a decagonal quasicrystal.

Usually the hydrodynamic modes are defined by changes of the phases φ_j in the following way [2, 3]:

$$\varphi_j = \mathbf{u} \cdot \mathbf{G}_j + \mathbf{w} \cdot \mathbf{G}_{3j \bmod 5} + \gamma. \tag{3.30}$$

Here γ corresponds to a global phase change, which is not a hydrodynamic mode, because it affects the sum of all phases φ_j. The vector $\mathbf{u} = (u_x, u_y)$ leads to global displacements of the whole crystal along $\mathbf{u}$ as can be seen when $\rho_j = |\rho_j| \exp(i\mathbf{u} \cdot \mathbf{G}_j)$ is inserted in (3.27). Therefore, $\mathbf{u}$ describes the long wavelength limit of phonons. A uniform vector $\mathbf{w} = (w_x, w_y)$ does also not change the free energy and therefore describes the long wavelength limit of two additional hydrodynamic modes. They correspond to global rearrangements usually termed phasons. Examples will be shown in the next subsection.

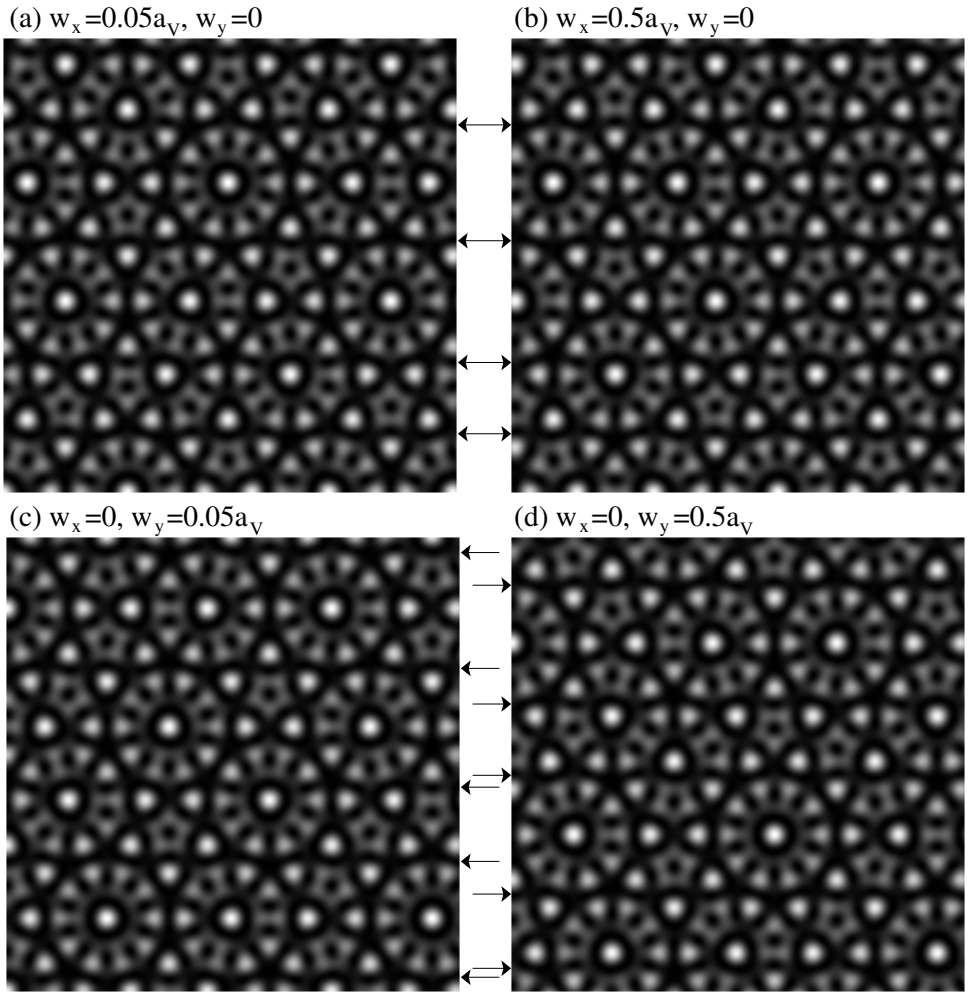

Figure 3.17: Decagonal potential for constant phasonic displacements. The arrows between the figures mark dark horizontal lines, that change their position if w_y is increased but not if w_x is changed.

3.4.3 Examples of phasonic displacements, drifts, and gradient fields

In this subsection we study phasonic displacements. First we consider only constant displacements, later the phasonic displacements depend on time or position. We also show that phasons can be assigned to some direction and determine how phasonic displacements are related to shifts of the quasicrystal in real space.

In general, hydrodynamic modes found in the previous subsection depend on the position $\mathbf{r}$ and the time t. Therefore, the phases are determined by phononic and phasonic displacement fields, $\mathbf{u}(\mathbf{r},t)$ and $\mathbf{w}(\mathbf{r},t)$, according to

$$\varphi_j(\mathbf{r},t) = \mathbf{u}(\mathbf{r},t)\cdot\mathbf{G}_j + \mathbf{w}(\mathbf{r},t)\cdot\mathbf{G}_{3j \bmod 5} + \gamma, \tag{3.31}$$

i.e., for any given displacement fields, we can calculate the phases and the standard decago-

nal potential by using (3.25). Phononic displacement fields are well known from crystals. Therefore, in this subsection we focus on variations of the phasonic displacement field and choose $\mathbf{u} = \mathbf{0}$. Note that only differences of the phases enter the decagonal potential (3.25). Therefore, it does not depend on the global phase γ at all.

In figure 3.17 examples of intensity patterns with constant phasonic displacements are shown. The potentials are similar to the one with zero phasonic displacement. However, the center of perfect symmetry no longer is in the point $(x, y) = (0, 0)$. A method to determine its new position, will be described later in this subsection. Since for our studies the position of the symmetry center is not important (cf. subsection 3.3.2), potentials with different constant phasonic displacements do not have to be considered separately.

Interestingly, the direction of a phasonic displacement vector $\mathbf{w}$ is connected to directions in real space: For phasonic changes in w_x-directions, i.e., for changes of w_x with constant w_y, the dark horizontal lines in figure 3.17 do not move or disappear [see arrows between figures 3.17(a) and (b)], whereas the lines in all other direction do so. The horizontal lines change if w_y is increased [see arrows between figures 3.17(c) and (d)]. In general, lines in the direction defined by the vector $(x, y) = (\cos(m\pi/5), \sin(m\pi/5))$ are not affected by a phasonic displacement along $(w_x, w_y) = (\cos[3m\pi/5], \sin[3m\pi/5])$ for $m = 0..9$.

Now we want to describe the connection between phasonic displacements and shifts of the quasicrystal in real space. In figures 3.18(a-f) three-dimensional snapshots of the potential landscape are shown for uniform phasonic displacements $w_y = j\tau\kappa/10$ with $j = 0..5$, where $\tau = (1 + \sqrt{5})/2$ is the number of the golden ratio (see subsection 3.2) and

$$\kappa = \frac{1}{10}\sqrt{10 - 2\sqrt{5}}a_V = \frac{4}{5}\sin(4\pi/5)\, a_V. \tag{3.32}$$

As usual, $a_V = 2\pi/G_j$ and G_j is the length of a wave vector of the laser beam projected onto the xy-plane. As we will show in the following, phasonic displacements chosen in such a way reveal interesting properties of their relation to uniform phononic shifts. The minima in the front, i.e., at $y = 0$, slowly vanish, however for $w_y = \tau\kappa/2$ new minima appear along a line $y = \kappa/2$ [dashed line in figure 3.18(f)]. Furthermore, as shown in figures 3.18(a), (g) and (i), for $w_y = \tau\kappa$ or $w_y = 2\tau\kappa$ the potential is identical to the one without phasonic displacement but shifted by κ or 2κ in y-direction, i.e., there is a connection between potentials with a phasonic displacement and shifted intensity pattern.

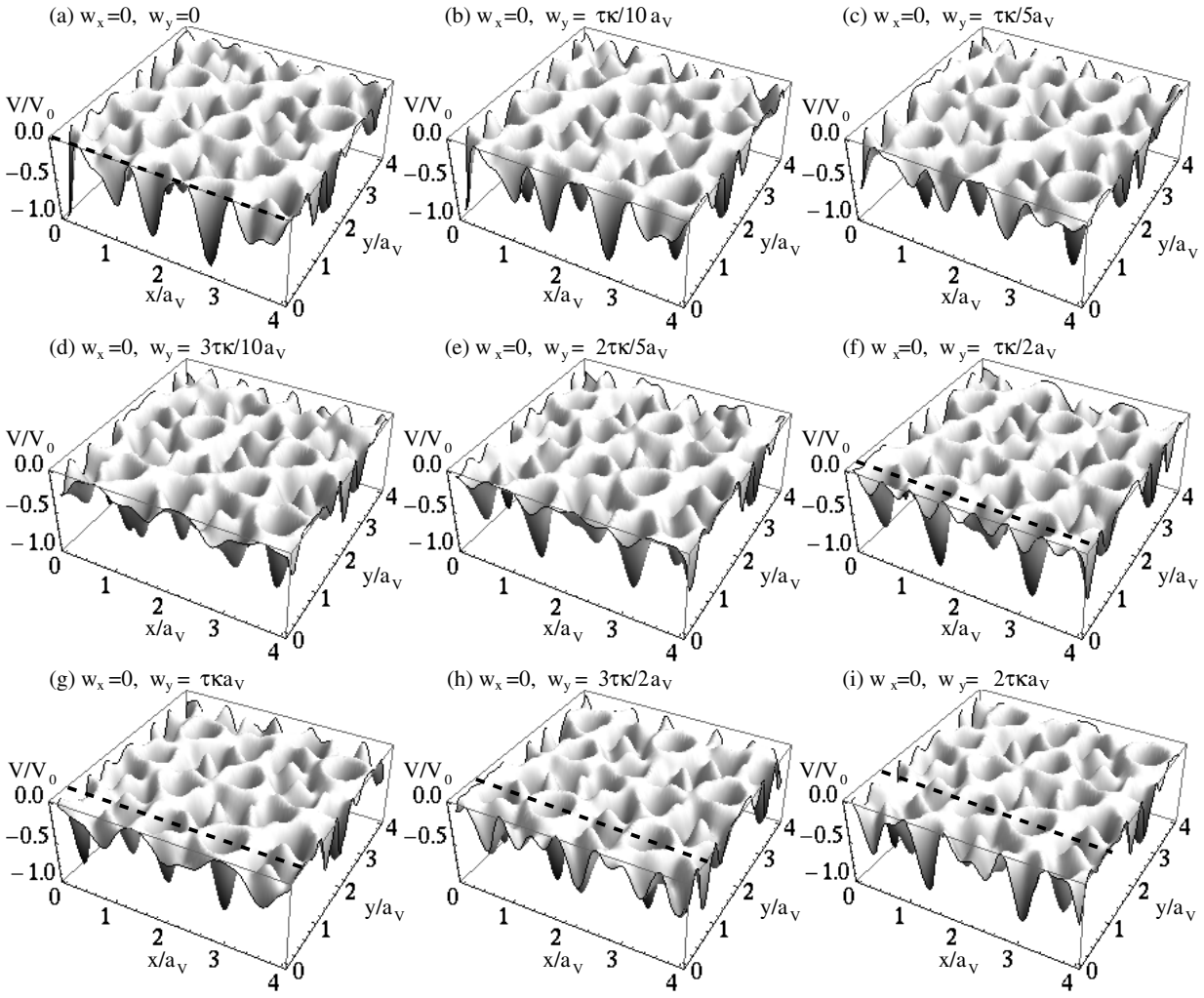

Figure 3.18: Potential landscape for different phasonic displacements w_y. It is $\tau = (1+\sqrt{5})/2$ and $\kappa = 4\sin(4\pi/5)a_V/5$. The dashed lines mark rows of minima described in the text.

In general, for the potential $V_{w_x,w_y}(x,y)$ with a phasonic displacement w_x and w_y, we find

$$\begin{aligned} V_{w_x+\Delta w_x, w_y+\Delta w_y}(x,y) &= V_{w_x,w_y}(x-\Delta x, y-\Delta y) \qquad (3.33)\\ \text{with } \Delta w_x &= -\sum_{m=0}^{9} j_m \tau\kappa \sin(3m\pi/5)\,,\\ \Delta w_y &= \sum_{m=0}^{9} j_m \tau\kappa \cos(3m\pi/5)\,,\\ \Delta x &= -\sum_{m=0}^{9} j_m \kappa \sin(m\pi/5)\,,\\ \text{and } \Delta y &= \sum_{m=0}^{9} j_m \kappa \cos(m\pi/5)\,, \end{aligned}$$

where j_m for $m = 0..9$ are integer numbers. If only one j_m is non-zero, the displacement is in a direction perpendicular to dark lines in the intensity pattern. By choosing appropriate numbers j_m, displacements in other direction can be realized. For example a displacement in x-direction is found for non-zero integer numbers $j = j_7 = j_8$ or $j' = j_6 = j_9$. Note the displacements that can be described by (3.33) lie dense in the plane, i.e., for every given phasonic or real space displacement, $(\Delta w_x, \Delta w_y)$ or $(\Delta x, \Delta y)$, integer numbers j_m can be chosen such that the displacement given by these numbers and (3.33) is arbitrarily close to $(\Delta w_x, \Delta w_y)$ or $(\Delta x, \Delta y)$. As a consequence, for every positive number ΔV and for every phasonic displacement, a displacement in real space can be found such that the difference of the shifted pattern and the potential with phasonic displacement in every point is smaller than ΔV. Furthermore, in all potentials with constant phasonic displacements, there always is a symmetry center which is arbitrarily close to the center of perfect symmetry. For a phasonic displacement $(\Delta w_x, \Delta w_y)$ given by integers j_m and (3.33), a perfect symmetry center is located in $(\Delta x, \Delta y)$.

In addition, changes of the intensity patterns caused by variations of the phasonic displacements can be studied for a simplified potential that one obtains by averaging the decagonal light field along a direction, where lines of low intensity exist, e.g., along the x-direction. The advantage of such an average is that it only depends on one space coordinate. Moreover, since an average along a direction defined by the vector $(x, y) = (\cos[m\pi/5], \sin[m\pi/5])$ (for $m = 0..9$) corresponds to an average over a phasonic displacement along $(w_x, w_y) = (\cos[3m\pi/5], \sin[3m\pi/5])$, the average one-dimensional potential only has one remaining phasonic degree of freedom. For example, $\langle V\rangle_x = \langle V\rangle_{w_x}$ only depend on y and w_y where $\langle V\rangle_x$ and $\langle V\rangle_{w_x}$ are obtained by averaging the full potential over x or w_x. Here we study the properties of $\langle V\rangle_x = \langle V\rangle_{w_x}$ in more detail. We find

$$\begin{aligned} \langle V\rangle_x &= \frac{V_0}{25}\left\{-5 - 2\cos\left(k_1\left[\tau w_y y\right]\right) - 2\cos\left(k_2\left[w_y/\tau - y\right]\right)\right\} \qquad (3.34)\\ \text{with } k_1 &= \frac{4\pi}{\sqrt{5}\tau\kappa} = \sqrt{10 - 2\sqrt{5}}\frac{\pi}{a_V}\\ \text{and } k_2 &= \frac{4\pi}{\sqrt{5}\kappa} = \sqrt{10 + 2\sqrt{5}}\frac{\pi}{a_V} = \tau k_1. \end{aligned}$$

A minimum of $\langle V\rangle_x$ corresponds to a row of minima in the two-dimensional potential. The relation corresponding to (3.33) is

$$\langle V_{w_y + j\Delta w_y/2}\left(y\right)\rangle_x = \langle V_{w_y}\left(y - j\Delta y/2\right)\rangle_x \qquad (3.35)$$

with $\Delta w_y = \tau\kappa$ and $\Delta y = \kappa$. Note that the allowed displacements here are half of those found for the decagonal potential. Figure 3.19 shows $\langle V\rangle_x$ for different phasonic displacements w_y. For increasing w_y, the minimum originally at $y = 0$ first becomes shallower, drifts right, and becomes deeper again [see figure 3.19(a)]. This will be important in section 8.5.1 where we study the Brownian motion of colloids in the decagonal potential under the influence of a phasonic displacement that increases at a constant rate in time. The property given by (3.35) is illustrated in figure 3.19(b). At phasonic displacements

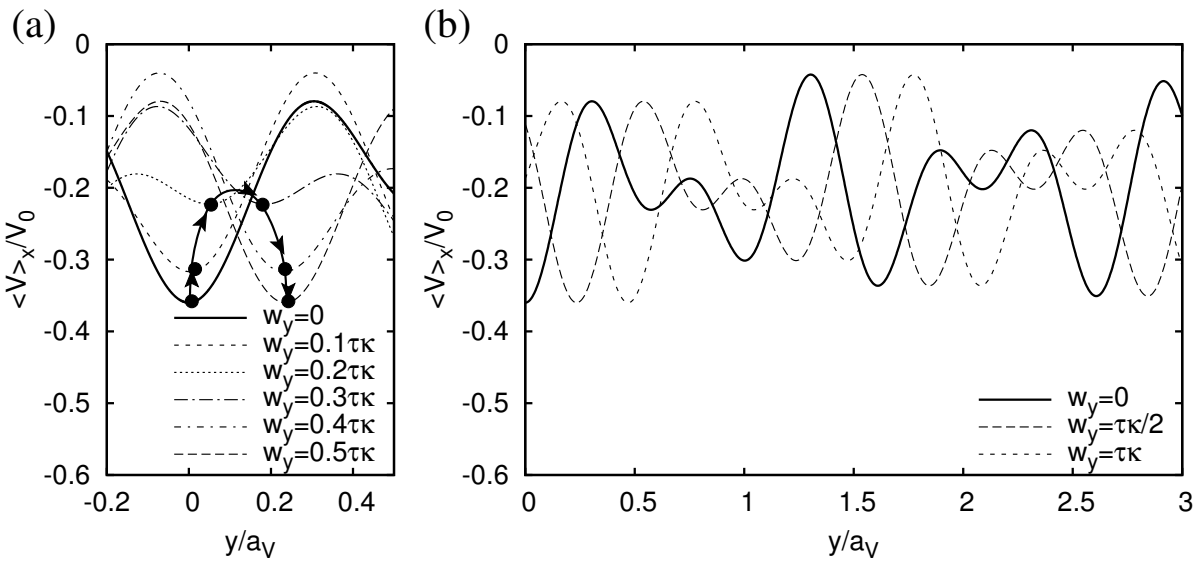

Figure 3.19: Average $\langle V\rangle_x = \langle V\rangle_{w_x}$ of the decagonal potential over x or w_x for different phasonic displacements w_y. (a) The minimum originally at $y = 0$ is moving in y-direction for increasing w_y. First it gets shallower, than deeper again (see points and arrows). (b) For $w_y = j\Delta w_y/2 = j\tau\kappa/2$ with $\tau = (1+\sqrt{5})/2$ and $\kappa = 4\sin(4\pi/5)a_V/5$ the averaged potential $\langle V\rangle_x$ corresponds to the one for $w_y = 0$ displaced by $j\Delta y/2 = j\kappa/2$.

$w_y = j\Delta w_y/2$ the averaged potential $\langle V\rangle_x$ corresponds to the one for $w_y = 0$ shifted by $j\Delta y/2$.

As we have shown for the decagonal laser field as well as for the averaged pattern, these potentials change in a very interesting way when the phasonic displacement is increased. To study the behavior of a colloidal suspension in such a varying potential, we will use phasonic displacements that increase at a constant rate in time, i.e., $(w_x, w_y) = (v_{w_x}t, v_{w_y}t)$. Because an increase of a phononic displacement u_x or u_y according to $(u_x, u_y) = (v_x t, v_y t)$ results in a drift of the system, we term the corresponding process for phasons a phasonic drift. The rate of increase (v_{w_x}, v_{w_y}) is named phasonic drift velocity.

Finally, we consider phasonic displacement fields $w_x(x, y)$ and $w_y(x, y)$. A special case is a field that linearly increases along one direction, i.e., a field with constant gradients $\nabla w_x(x, y)$ and $\nabla w_y(x, y)$, which we call phasonic gradients. Figure 3.20 shows examples of decagonal light patterns with phasonic gradients. The lines of low intensity are infinite along a direction of zero phasonic gradient or along a direction given by the phasonic displacement vector, the dark lines in other directions only have finite length as indicated by dashed lines. As we will show in section 7.2, the light field in the experiment usually contains phasonic gradients that lead to a prefered direction of the system.

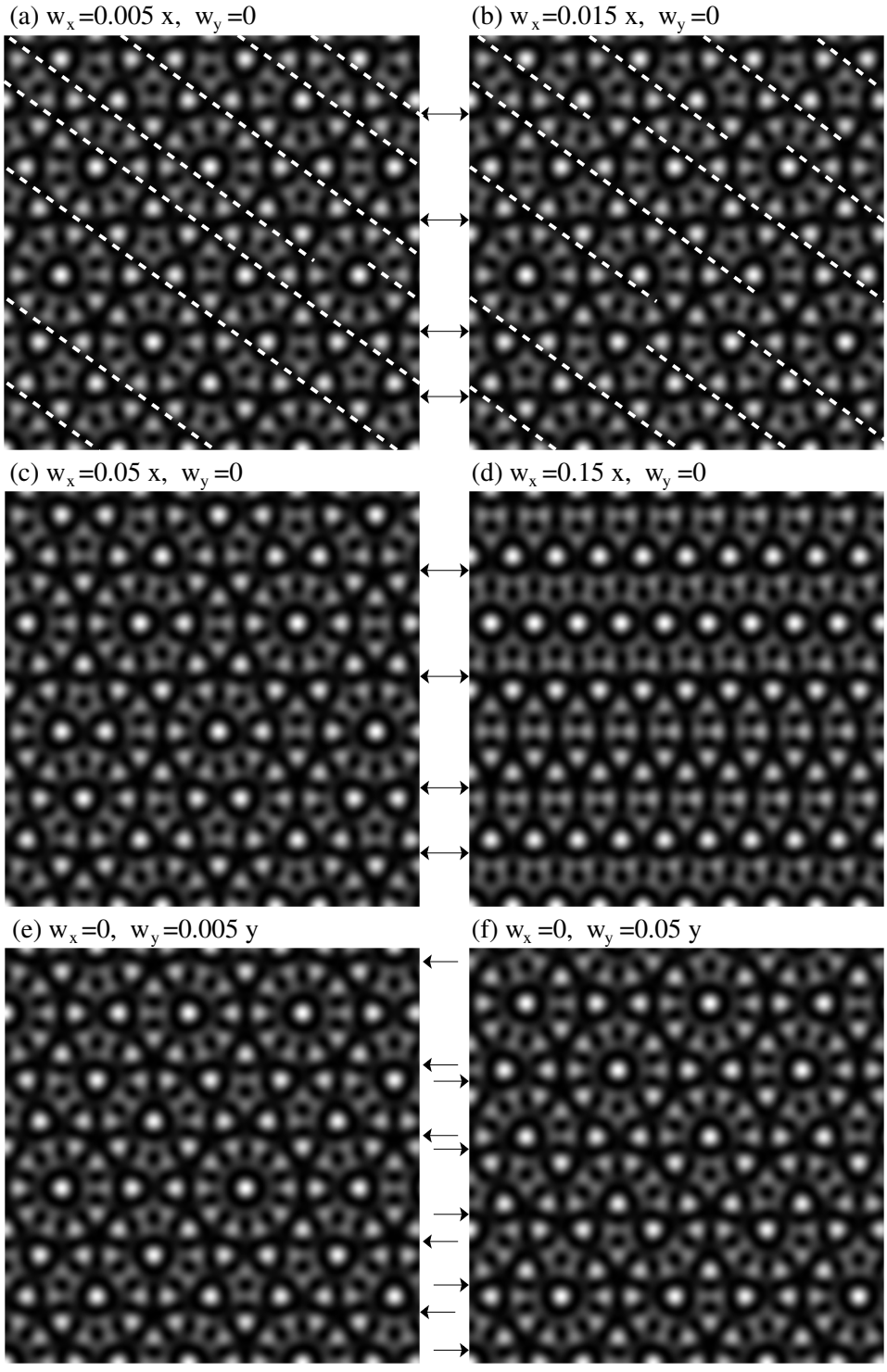

Figure 3.20: Decagonal potential with phasonic gradients. For $\nabla w_x \neq 0$ and $w_y = \text{const.}$ (a-d) or for phasonic displacements that only depend on y (e,f), the horizontal dark lines have infinite length as in the potential without phasonic displacements. The lines in other directions [see, e.g., white lines in (a) and (b)] only have finite length.

3.4.4 Indexing problem

The analysis of a quasicrystalline point pattern, for example given by the positions of colloids in a decagonal potential, is a very difficult task. Especially, the detection of phasonic displacements is highly non-trivial. In this subsection, we present a method how uniform phasonic displacements can be detected by analyzing a quasicrystalline point pattern. A widely used ansatz in crystallography considers quasicrystals as projections of regular crystals in a higher-dimensional space (see section 3.1.3). In principle, one tries to find the point in the high-dimensional space that corresponds to a certain point in the quasicrystalline pattern (see e.g. [162–165]). However, due to problems explained in detail in the following, we do not use the method in this work.

A two-dimensional decagonal quasicrystal can, e.g., be considered as projection of a four-dimensional lattice. A point (x, y) in the 2D pattern is connected to a point in the four-dimensional space (a_1, a_2, a_3, a_4) according to (see e.g. [159])

$$\begin{aligned} x &= a_1 v_1 + a_2 v_2 \\ y &= a_3 v_3 + a_4 v_4, \end{aligned} \tag{3.36}$$

where v_j are the typical length scales in the quasicrystal; v_1, v_2 belong to the x-direction and v_3, v_4 to the y-direction. If one assumes that the lattice in higher-dimensional space is a cubic lattice, the numbers a_j for $j = 1..4$ have to be integers. Typical length scales in the standard decagonal potential are

$$\begin{aligned} &\text{in } x\text{-direction: } v_1 = a_V \text{ and } v_2 = \tau a_V, \\ &\text{in } y\text{-direction: } v_3 = a_V \sin(4\pi/5) \text{ and } v_4 = a_V \sin(2\pi/5) = \tau v_3. \end{aligned} \tag{3.37}$$

As an example, we use the pattern consisting of the positions (x, y) of local minima in the decagonal potential (see also section 3.3.3). We search for integer numbers that best fulfill the equations in (3.36). Of course, only a certain range of numbers a_j can be scanned. We choose a range determined by Fibonacci numbers, because $v_2/v_1 = \tau$ and $v_4/v_3 = \tau$ can be approximated as ratio of large Fibonacci numbers (see section 3.2). In figure 3.21(a) two coordinates of the points in four-dimensional space are plotted. The points form elongated clusters, which correspond to the acceptance regions, i.e., only points in these regions were projected onto the two-dimensional plane to obtain the quasicrystalline pattern. Note that the acceptance regions themselves form a lattice. In the example we introduced in section 3.1.3 to construct a Fibonacci chain (see figure 3.4), the acceptance area was a connected region consisting of a stripe limited by two lines. To obtain a Fibonacci chain a two-dimensional square lattice was projected. In general, one can also considers other types of higher-dimensional lattices or even lattices with a non-trivial basis. It is possible, to map such non-cubic lattices on a cubic one, however a connected acceptance region in the non-cubic lattice then corresponds to disconnected acceptance areas for the cubic lattice (see e.g. [166–168]). Therefore the disconnected acceptance clusters we find here for a four-dimensional cubic lattice probably corresponds to a connected acceptance region for a non-cubic lattice, possibly also with a non-trivial basis.

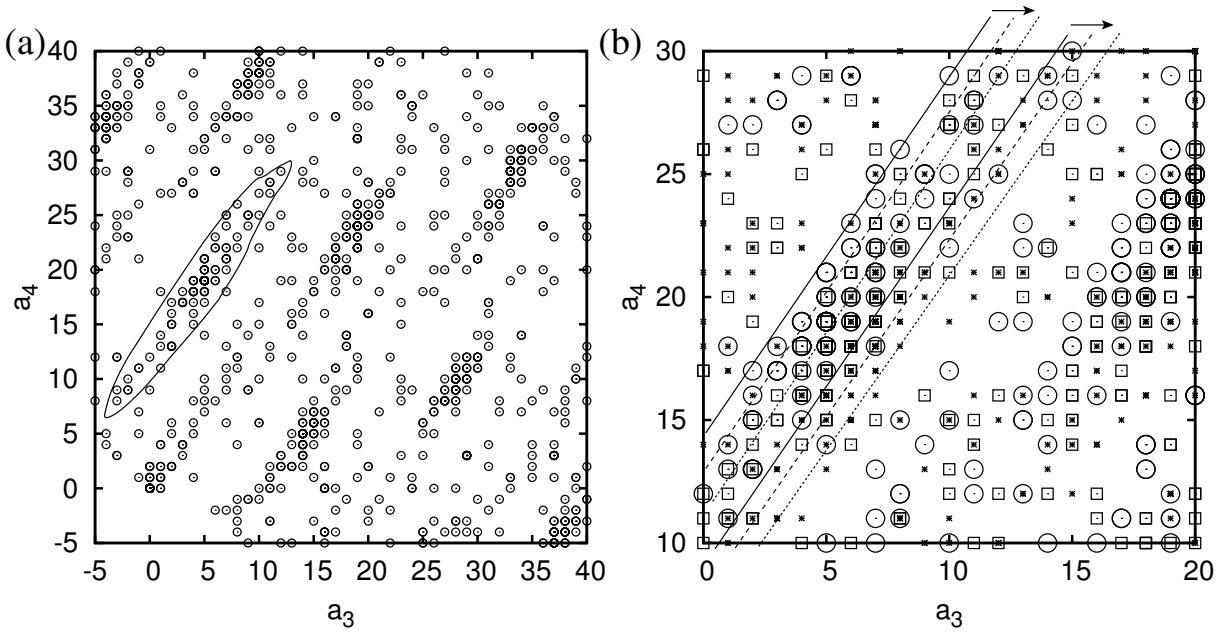

Figure 3.21: Coordinates a_3 and a_4 of points in four-dimensional space, whose projection gives the positions of local minima of the decagonal potential (a) without phasonic displacement an (b) for phasonic displacements $w_y = 0$ (circles), $w_y = 0.15a_V$ (squares), and $w_y = 0.3a_V$ (crosses). A cluster of the acceptance region is marked by lines as guide to the line. Solid lines are used for $w_y = 0$, dashed for $w_y = 0.15a_V$, and dotted ones for $w_y = 0.3a_V$.

In figure 3.21(b) the coordinates a_3 and a_4 are shown for different phasonic displacements w_y. As a guide to the eye a cluster is roughly marked by lines. The acceptance regions seem to be slightly shifted to the right for increasing phasonic displacement (cf. figure 3.15). In principle, the observed shift can be used to determine the phasonic displacement of the original quasicrystalline pattern.

The method presented in this subsection has some severe drawbacks. First, the limitation of range for the integers a_j is arbitrary and has some influence on the result. Second, the points found in four-dimensional space are scattered even for a perfect pattern given by the positions of local minima. An analysis of the positions of colloidal particles probably has even worse quality due to random fluctuations. Third, the form of the acceptance region is not clear, however, to use this method to determine phasonic displacements, the behavior of the acceptance region has to be known. In summary, the method of indexing presented here in principal is working, but the quality of the results is to low to be useful for the analysis of quasicrystalline colloidal patterns.

3.5 Induced Quasicrystals

In this work we consider colloidal suspensions exposed to decagonal laser fields in order to induce quasicrystalline ordering. Our system is a model system whose behavior can be compared to many other situations. Some examples are given in this section.

3.5.1 Quasicrystalline films

The most important examples for induced quasicrystals are patterns of atoms on the surface of quasicrystals [5, 7–13]. Usually the free surfaces of Al-Ni-Co, which has decagonal symmetry, or of the alloy Al-Pd-Mn with icosahedral symmetry are taken as substrates. Their surfaces act as a five- or ten-fold symmetric potential for the adatoms (see e.g. [5,6]). Often noble gases, such as Ar or Xe, or metallic atoms such as Ag, Au, or Cu were used as adatoms, i.e., atoms that do not form quasicrystals without substrate. It is very difficult to analyze the local ordering, because the positions of the atoms cannot be observed directly. Usually the structure factor is determined, revealing liquid or triangular phases and sometimes a quasicrystalline ordering with the same symmetry as the substrate, e.g., decagonal ordering was found on decagonal surfaces. Ledieu *et. al.* observed an ordering containing lines at distances given by a Fibonacci chain [11]. These lines can be part of a decagonal structure or a more complex ordering such as the Archimedean tiling phase that will be explained in detail in section 7.1.5. A phase with twenty bond directions, which we describe in section 7.1.3, has not been found yet.

There are also grand-canonical simulations of noble atoms on quasicrystalline surfaces [14–17] and recently, works using molecular dynamics simulations have been published [18,19]. As in the experimental works, the ordering is usually determining by the structure factor, leading to similar results as in the experiments. The local structure has not been analyzed yet and a phase with twenty bond directions or an Archimedean tiling phase has not been reported.

The behavior of atoms on the surfaces of quasicrystals is important for a large number of applications (see also [5,124] for an overview). Quasicrystals can be employed as catalysts, e.g., an AlCuFe quasicrystal efficiently catalyzes the steam reforming of methanol, i.e., the reaction $CH_3OH + H_2O \rightarrow 3H_2 + CO_2$ that is used to produce hydrogen from methanol and water [169]. The low friction and the good corrosion-resistance of quasicrystals also lead to possible applications, for instance, the development of new wear-resistant or non-sticky materials [170–172]. Furthermore, the dynamics of adatoms on surfaces probably influences the growth of quasicrystals (see also section 8.7).

3.5.2 Atomic clouds in quasicrystalline traps

Laser beams can also be employed to trap a gas of atoms and to cool it. Usually the beams are combined with magnetic fields in so-called optomagnetic traps. In such a trap, it is possible to achieve Bose-Einstein condensation, i.e., a cloud of bosonic atoms, which all occupy the same quantum mechanical ground state [173]. By using five laser beams, a

decagonal potential was applied to an atomic cloud [174] and the diffusion of atoms was studied in such a potential [175]. A brief intoduction to atoms in optical lattices in general is given in [176].

3.5.3 Light-induced quasicrystals in polymer-dispersed liquid-crystal materials

Different laser fields were also used to induce quasicrystalline structures in so-called holographic polymer-dispersed liquid crystal materials [149]. The polymers in such a material are photopolymers that in combination with a photoinitiator polymerize if exposed to light. If a laser field is applied to a homogeneous mixture of photopolymers, liquid crystal, and photoinitiator, the polymers polymerize in the brightest regions of the fields and therefore the liquid crystals diffuse into the dark regions. Finally, most of the liquid crystals are captured in the regions of low intensity of an interference pattern. The system was studied for different numbers of laser beams, achieving quasicrystals with five-, seven-, and nine-fold rotational symmetry [149].

3.5.4 Induced non-linear optical quasicrystal

In a photosensitive nonlinear material, e.g., $Sr_{0.6}Ba_{0.4}Nb_2O_6$, the refractive index of light is affected by the light intensity. Light passing through such a sample can be described by a nonlinear equation similar to a nonlinear Schrödinger equation where the time is replaced by the propagation distance. Therefore the evolution of the equation at different points of time can be studied by analyzing the intensity patterns of the light that passed through samples of different thicknesses.

By using the interference pattern of five laser beams, a decagonal quasicrystal can be induced in the material [177]. If a decagonal interference pattern with a phason-strain field is applied, the relaxation of such phasonic strains can be directly observed by looking on the decagonal pattern for different propagation distances, i.e., for different sample thicknesses [178].

Chapter 4

Simulation techniques

In this chapter we present the theoretical background of the simulation techniques and discuss the details and tricks used for their implementation. In sections 4.1 Brownian dynamics simulations and in section 4.2 Monte-Carlo algorithms are introduced. Because quasicrystals are not periodic, the choice of the simulation box is not obvious. In section 4.3 we present our solution for simulation boxes that fit well to quasicrystals.

4.1 Brownian dynamics simulations

4.1.1 The Langevin equation

Brownian dynamics simulations are used for overdamped systems in contact with a surrounding medium which is in thermal equilibrium and therefore has a well-defined temperature T. The surrounding medium effectively leads to random thermal forces. Internal particle-particle interactions or external forces can also be included. The Langevin equation describing such a system is derived from Newton's equation

$$m\frac{\partial}{\partial t}\mathbf{v} = \mathbf{F}_{frict} + \mathbf{F}_{int} + \mathbf{F}_{ext} + \mathbf{F}_{therm}, \tag{4.1}$$

where m is the mass and $\mathbf{v}$ the velocity of the particle, $\mathbf{F}_{frict}$ is the friction force, $\mathbf{F}_{int}$ the force due to internal interactions, $\mathbf{F}_{ext}$ denotes the external and $\mathbf{F}_{therm}$ the random thermal forces. Without turbulence, e.g., for small Brownian particles, the friction forces are proportional to the velocity, i.e., $\mathbf{F}_{frict} = -\gamma\mathbf{v}(t)$ with the friction constant γ. The friction constant depends on the size and geometry of the particle and on the viscosity η of the surrounding liquid, e.g., for small spheres the friction constant according to Stokes's law is $\gamma = 6\pi R\eta$, where R is the radius of the particle. The Langevin equation then is [179] (see also e.g. [180])

$$m\frac{\partial}{\partial t}\mathbf{v} + \gamma\mathbf{v} = \mathbf{F}_{int} + \mathbf{F}_{ext} + \mathbf{F}_{therm}. \tag{4.2}$$

The thermal forces have to fulfill the following relations:

$$\langle \mathbf{F}_{therm}(t) \rangle = 0, \tag{4.3}$$

$$\langle F_{therm,i}(t) F_{therm,j}(t') \rangle = 2B\delta_{ij}\delta(t-t'), \tag{4.4}$$

i.e., the average is zero and the thermal forces in different directions or at different times are totally uncorrelated corresponding to white noise. The strength B is connected to the diffusion constant D of a freely diffusing particle or to the thermal energy k_BT and the friction constant γ. To derive these dependencies, we first calculate the solution of the Langevin equation without interaction or external forces:

$$\mathbf{v}(t) = \mathbf{v}(0)e^{-\frac{\gamma}{m}t} + e^{-\frac{\gamma}{m}t} \int_0^t dt' \; \frac{1}{m} e^{\frac{\gamma}{m}t'} \mathbf{F}_{therm}(t'). \tag{4.5}$$

By using (4.3) and (4.4), we find the mean square velocity

$$\begin{aligned} \left\langle \mathbf{v}(t)^2 \right\rangle &= v(0)^2 e^{-2\frac{\gamma}{m}t} + e^{-2\frac{\gamma}{m}t} \int_0^t dt' \int_0^t dt'' \; \frac{1}{m^2} e^{\frac{\gamma}{m}(t'+t'')} \left\langle \mathbf{F}_{therm}(t') \cdot \mathbf{F}_{therm}(t'') \right\rangle \\ &= v(0)^2 e^{-2\frac{\gamma}{m}t} + \left(1 - e^{-2\frac{\gamma}{m}t}\right) \frac{nB}{m\gamma}, \end{aligned} \tag{4.6}$$

where n is the number of dimensions. For long times $t \gg m/\gamma$, one finds

$$\left\langle \mathbf{v}(t)^2 \right\rangle = \frac{nB}{m\gamma}. \tag{4.7}$$

Employing the equipartition theorem $m\langle \mathbf{v}(t)^2 \rangle / 2 = nk_BT/2$, a relation of the strength B to the thermal energy k_BT follows:

$$B = k_BT\gamma. \tag{4.8}$$

On the other hand, the mean square displacement in the long-time limit is

$$\begin{aligned} \left\langle [\mathbf{r}(t) - \mathbf{r}(0)]^2 \right\rangle &= \frac{1}{\gamma^2} \int_0^t \int_0^t dt' dt'' \; \left\langle \mathbf{F}_{therm}(t') \cdot \mathbf{F}_{therm}(t'') \right\rangle \\ &= \frac{1}{\gamma^2} \int_0^t \int_0^t 2nB\delta(t'-t'') dt' dt'' = \frac{2nB}{\gamma^2} t. \end{aligned} \tag{4.9}$$

The free diffusion constant D is defined by

$$\left\langle (\mathbf{r}(t) - \mathbf{r}(0))^2 \right\rangle = 2nDt, \tag{4.10}$$

which gives

$$B = D\gamma^2. \tag{4.11}$$

Now, combining (4.8) and (4.11), we find the famous Einstein relation (cf. [181])

$$D = \frac{k_BT}{\gamma}. \tag{4.12}$$

In the following, we are only interested in the dynamics of our system on time scales much larger than the very short momentum relaxation time m/γ, which for micron-sized particles in water is approximately 10^{-7}s. Then the inertial term $m\frac{\partial}{\partial t}\mathbf{v}(t)$ is much smaller than the other terms in (4.1) and can, therefore, be neglected. Such a system is also called overdamped.

4.1.2 Discretized equation and simulation details

The overdamped Langevin equation reads

$$\gamma\mathbf{v} = \mathbf{F}_{int} + \mathbf{F}_{ext} + \mathbf{F}_{therm}. \tag{4.13}$$

For the Brownian dynamics simulations, we discretize equation (4.13). The position at time $t + \Delta t$ is

$$\mathbf{r}(t + \Delta t) = \mathbf{r}(t) + \frac{\Delta t}{\gamma}\left(\mathbf{F}_{int}(t) + \mathbf{F}_{ext}(t) + \mathbf{F}_{therm}(t)\right). \tag{4.14}$$

The thermal force is realized by random kicks: At each simulation step a randomly generated number is used as thermal force. The probability distribution of these random numbers is not important, as long as (4.3) and (4.4) are satisfied, i.e., if the average of the random numbers is zero, if the probability distribution does not depend on time or previous random numbers, and if the second moment is chosen correctly. The last requirement is related to the free diffusion constant that follows from the random numbers: According to (4.14) and for $\mathbf{F}_{int} = \mathbf{F}_{ext} = 0$, the mean square displacement is

$$\begin{aligned}\left\langle(\mathbf{r}(t) - \mathbf{r}(0))^2\right\rangle &= \left\langle\left(\frac{\Delta t}{\gamma}\sum_{j=0}^{t/\Delta t}\mathbf{F}_{therm}(j\Delta t)\right)^2\right\rangle \\ &= \frac{\Delta t^2}{\gamma^2}\sum_{j=0}^{t/\Delta t}\left\langle\mathbf{F}_{therm}(j\Delta t)^2\right\rangle = \frac{\Delta t^2}{\gamma^2}\frac{t}{\Delta t}\left\langle\mathbf{F}_{therm}^2\right\rangle. \end{aligned} \tag{4.15}$$

Here we used the facts that the random forces at different times are uncorrelated, i.e., $\langle\mathbf{F}_{therm}(j\Delta t)\cdot\mathbf{F}_{therm}(k\Delta t)\rangle = 0$ for $j \neq k$ and that the probability distribution is time-independent $\langle\mathbf{F}_{therm}(j\Delta t)^2\rangle = \langle\mathbf{F}_{therm}^2\rangle$. From equations (4.15), (4.10), and the Einstein relation (4.12), we find that thermal kicks have to comply with

$$\left\langle\mathbf{F}_{therm}^2\right\rangle = \frac{2n\gamma k_B T}{\Delta t}. \tag{4.16}$$

Gaussian distributed random numbers centered around zero with a second moment of $2n\gamma k_B T/\Delta t$ are a possible choice for simulations. However, generating equally distributed random numbers is easier and faster. Therefore, we usually use random kicks in a random direction with lengths evenly distributed between 0 and $\sqrt{12\gamma k_B T/\Delta t}$, where the prefactor

of the upper limit follows from the requirement for the second moment (4.16). We tested our program with Gaussian as well as with evenly distributed random numbers and obtained the same results. Without interactions and external forces, we find the constant of free diffusion exactly as predicted by the Einstein relation (4.12).

To produce random numbers, we use a pseudo-random number generator called Mersenne Twister mt19937 [182, 183] that according to the documentation of the GNU Scientific Library is one of the fastest algorithm appropriate for scientific simulations [184].

The quality and the speed of the simulations depend on the choice of the time step duration Δt. The easiest way to accelerate the simulations is to increase Δt. However, the upper limits of Δt are:

- The time scale we are interested in when analyzing the results. This time must be much larger than a single-step duration so that the results are averaged over enough random kicks.

- If the step duration Δt is too long, a particle can be kicked over a deep potential well, which then is not recognized in the simulation. Therefore, the step length should be small compared to the length scale of the potential.

Usually, the second requirement leads to much smaller values of Δt. In our simulations we choose an upper limit of Δt at $0.005\beta\gamma a_V^2$ for single colloids (in chapter 8) and $0.001\beta\gamma a_V^2$ for many particle systems (chapters 6 and 7), where $\beta = 1/(k_B T)$ and a_V is the typical length in the potential, e.g., the modulation length in the one-dimensional potential or in the decagonal potential (see sections 6.1, 6.3 or 3.3) or the distance between minima in the square potentials (section 8.2.1). To prevent the occurrence of steps that are too long, we calculate the step length for the case of the maximum possible thermal kick perfectly aligned with the other forces before every step. If this length is larger than a threshold Δl, we reduce the size of Δt until the step length is always smaller than Δl. Therefore, on the one hand, no important features of the potential are missed. On the other hand, the time steps are not smaller than necessary. We usually choose $\Delta l = 0.02 a_V$ as threshold in the decagonal potential (in chapters 7 and 8) and $\Delta l = 0.1 a_V$ in the one-dimensional quasicrystalline potential (chapter 6). We tested our program with different values of Δt and Δl, with constant as well as with adaptive step duration. We found no differences between simulations with our standard procedure and runs with smaller steps in time or length.

4.2 Monte-Carlo simulations

We use the Monte-Carlo algorithm originally introduced by Metropolis *et. al.* [185], which today is a standard method in computational physics [186, 187]. The Metropolis algorithm allows to treat the system in a canonical ensemble, i.e., the single configurations occur with a probability given by the Boltzmann factor $\exp(-\beta E)$, where E is the total energy of the system and $\beta = 1/(k_B T)$ the inverse of the thermal energy. Therefore, the average of an

observable A, e.g., an order parameter, is determined by calculating A for each configuration obtained by the simulation and then by averaging over all these configurations. The result is the correctly weighted average $\langle A \rangle$ of a canonical ensemble:

$$\langle A \rangle = \frac{1}{N} \sum_{\substack{j \text{ result of} \\ \text{MC-simulation}}} A_j = \frac{\sum_j A_j \exp(-\beta E_j)}{\sum_j \exp(-\beta E_j)}, \tag{4.17}$$

where N is the number of simulated configurations, E_j the energy and A_j the value of the observable in configuration j.

According to the Metropolis algorithm, in a Monte-Carlo step, first the configuration of the system is changed randomly. Then the energy E_{new} of the new configuration is calculated and compared to the energy E_{old} of the old one. The simulation is continued with the new configuration if $E_{new} < E_{old}$. In case of $E_{new} > E_{old}$, the new configuration is accepted with a probability proportional to $\exp(-\beta[E_{new} - E_{old}])$. If the new configuration is not accepted, the simulation is continued with the old one. The acceptance probabilities are chosen this way, because then the transitions between the configurations explored during the simulations satisfy detailed balance, i.e., the ratio of the transition probability $p_{j\to k}$ to get from state j to state k and the probability of the reverse transition $p_{k\to j}$ is

$$\frac{p_{j\to k}}{p_{k\to j}} = \frac{\exp(-\beta E_k)}{\exp(-\beta E_j)}. \tag{4.18}$$

If the system is ergodic and all possible configurations are explored, relation (4.18) guarantees that the probability to be in configuration j is proportional to $\exp(-\beta E_j)$, i.e., we obtain a canonical ensemble of configurations. In a real simulation it is of course impossible to explore all possible configurations. For a good implementation of the Metropolis algorithm it is important to find the configurations with the highest probability, which are the ones with the lowest energies. Such configurations are usually quiet similar and, therefore, it is not necessary to consider a completely new configuration at each Monte-Carlo step. It is more convenient to just slightly vary the old one. However, the variation must be big enough, at least with some probability, to explore a sufficiently large area of the configuration space. The quality of an implementation is mainly given, on the one hand, by the speed of finding the configurations close to the ground state and, on the other hand, by the explored area of the configuration space.

To obtain a new configuration in our implementation of the Metropolis algorithm, we take a colloid out of the system and place it at a random position. The energy is calculated and, according to the Metropolis algorithm, it is decided, whether the new position is accepted or not. To get a sufficient number of accepted new configurations, the colloid usually is placed in an area close to its original position. The size of the area is chosen such that the acceptance rate is approximately 50%: If it is smaller, the placement area is reduced and therefore the new configurations have a higher probability to be accepted. If the acceptance rate is too large, the area is increased. This procedure guarantees that a large number of configurations close to the lowest energy state is explored very fast.

However, with such a local displacement procedure one can get stuck to a region of the configuration space with a local minimum in energy. In order to find the global minimum, one also has to allow global replacements. For example, it has to be possible to cross high energy barriers. Therefore, in our simulations with a probability of 20% a colloid is not placed locally but is put on some random position anywhere in the sample. To implement the Metropolis algorithm, we use the same pseudo-random number generator as for the Brownian dynamics simulations, i.e., the so-called Mersenne Twister mt19937 algorithm [182, 183].

In one simulation step, the procedure described above is applied to each colloid of the sample, i.e., after one step about one half of the colloids have been replaced. Usually a simulation is started in a triangular configuration and one million steps are performed to guarantee that the equilibrium of the canonical ensemble is reached. Of course, we also tested our program with other starting configurations and other step numbers. We found that usually after about 100000 steps the system is already close to equilibrium and after about 500000 steps it is equilibrated no matter what starting configuration was used. Mean values as in (4.17), e.g., order parameters, are calculated as average over 1000 configurations: The first configuration is taken after one million equilibration steps and then always 100 steps are performed before the next configuration is used. To test that such a result is indeed the one of the canonical ensemble, we ran simulations up to 10 million steps before calculating the mean values. However, we never found any substantial deviations.

Recently, a so-called genetic algorithm was introdued to condensed matter physics [188, 189] based on general genetic algorithms originally developed by Holland [190]. As in a Monte-Carlo simulation, a new configuration is created and then it is decided whether to accept the new configuration (this was termed the selection process for genetic algorithms). A so-called fitness function, which usually depends on the free energy or free enthalpy, leads to an acceptance probability similar to the one in Monte-Carlo simulations. The main difference between genetic algorithms and usual Monte-Carlo simulations is the process of finding new configurations. In a genetic algorithm, a new configuration (also called individual of a new generation) is usally not obtained by random displacements of the particles as in a Monte-Carlo simulation, but by random changes in an abstract representation (termed genom) of the individual. Furthermore, a new generation can also be created by combining different parts of old configurations (called recombination process). Genetic algorithms were also applied to colloidal systems [63, 94]. In this work, we only use conventional Monte-Carlo simulations.

4.3 Size of the simulation box

In our simulations, we use periodic boundary conditions. However, the quasicrystalline potentials as well as any induced quasicrystal are not periodic. Therefore, these structures can never fit into any simulation box with periodic boundary conditions. However, we

show in this section that special box sizes exist for which there are only minor distortions or discontinuities at the boundaries.

4.3.1 Approximations for the 1D quasicrystalline potential

In section 6.3 we apply a one-dimensional quasi-periodic potential to the colloidal suspension. The potential is given as sum of two periodic modulations whose wavelengths differ by a factor of τ^2, where $\tau = (1+\sqrt{5})/2$ is the number of the golden ratio (see section 3.2). However, such a potential is not periodic and therefore does not fit into a simulation box with periodic boundary conditions. Therefore, we use approximations for τ to obtain a periodic potential. To be concrete, in our simulations we use the potential

$$V(\mathbf{r}) = -\frac{V_0}{2}\left[\cos\left(\mathbf{G}_\alpha \cdot \mathbf{r}\right) + \cos\left(\mathbf{G}_\beta \cdot \mathbf{r}\right)\right], \tag{4.19}$$

where $\mathbf{G}_\alpha = \tau_\alpha G_0 \mathbf{e}_x$, $\mathbf{G}_\beta = (-1/\tau_\beta) G_0 \mathbf{e}_x$; $\mathbf{e}_x$ is the unit vector in x-direction, and $G_0 = \pi/(\sqrt{3}a_S)$ is the lattice vector connected to the nearest neighbor particle distance a_S in the triangular starting configuration. The number of the golden mean can be approximated by the ratio of consecutive Fibonacci numbers (see section 3.2). We choose the approximations $\tau_\alpha = 55/34$ and $\tau_\beta = 34/21$. The box size is given by $x_{max} = 34 \cdot 2\pi/G_0 = 34\sqrt{3}a_S/2$ in x-direction and $y_{max} = 34/\sin(\pi/5) \cdot \sqrt{3}a_S/2$ in y-direction. The number of particles in the box then is 1054. In x-direction the approximated potential (4.19) is perfectly periodic and fits into the simulation box. The box size in y-direction is selected such that a possible pentagonal colloidal ordering fits as good as possible into the simulation box. This is fulfilled for our choice of y_{max} since y_{max} is an integer multiple of both characteristic length scales of a pentagonal quasicrystal in y-direction approximated as $2\pi/G_{1,y} = y_{max}/34$ and $2\pi/G_{2,y} = \tau \cdot 2\pi/G_{1,y} \approx y_{max}/21$ (see figure 3.5).

4.3.2 Approximations for the decagonal potential

In case of the decagonal potential (see section 3.3), we leave the potential undistorted. Therefore, a particle crossing the box boundary experiences a discontinuity. However, we choose the box size in a way that the discontinuity is very small. To obtain an appropriate rectangular box, we have to find translations which leave the potential almost unchanged, i.e., a vector $(\Delta x, \Delta y)$ such, that $V(x,y) \approx V(x+\Delta x, y)$ and $V(x,y) \approx V(x, y+\Delta y)$. This can be realized by choosing Δx and Δy to be integer multiples of the length scales, which are given by $2\pi/G_{j,x}$ and $2\pi/G_{j,y}$, where $G_{j,x}$ and $G_{j,y}$ are the components of the projected wave vectors (see figure 3.5). Then $\cos(G_{j,x}\Delta x) \approx 1$ and $\cos(G_{j,y}\Delta y) \approx 1$ for $j = 0, .., 4$. The length scales in x-direction are: $a_V = 2\pi/G_0$, $2\pi/G_{1,x} = 2a_V/\tau$, $-2\pi/G_{2,x} = \tau a_V/2$, where again $\tau = 2\cos(\pi/5)$ is the number of the golden mean, which can be approximated as ratio of successive Fibonacci numbers (see section 3.2). In y-direction we find the length scales $2\pi/G_{1,y} = a_V/\sin(\pi/5)$ and $2\pi/G_{a,y} = \tau a_V/\sin(\pi/5)$. Therefore, appropriate box sizes are $\Delta x = 2na_V$ and $\Delta y = ma_V/\sin(\pi/5)$, where n and m are Fibonacci numbers (1, 2, 3, 5, 8, 13, 21, 34, 55, 89, ...). We usually use m to be the Fibonacci number following

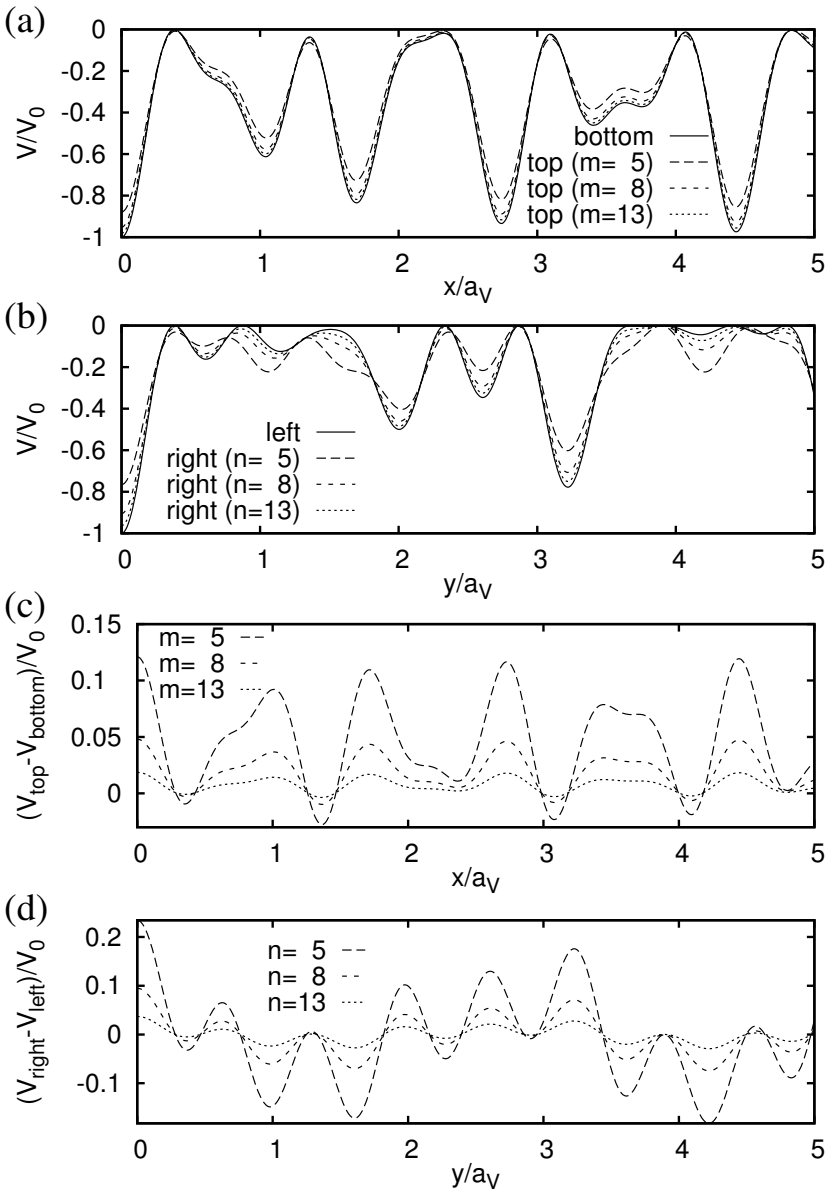

Figure 4.1: Value of the decagonal potential (a) at the lower ($y = 0$) and upper ($y = \Delta y$) boundary of the simulation box and (b) at the left ($x = 0$) and right ($x = \Delta x$) side of the box. In (c) the differences of the upper and lower, in (d) of the left and right sides of the box are plotted in units of the depth V_0 of the deepest minimum. The box sizes are chosen according to $\Delta x = 2na_V$ and $\Delta y = ma_V/\sin(\pi/5)$ with Fibbonacci numbers m and n.

on n so that the width and height of the simulation box do not differ to much. Figure 4.1 shows the potential values at the boundaries. Obviously even for quiet small Fibonacci numbers the discontinuities are negligible.

For a fixed particle density, thenumber of colloids depends on the chosen box size. We try to select one of the allowed box sizes as determined above such that a simulation box contains between 400 and 900 colloids. Therefore, finite-size effects are small and, on the other hand, the simulations are not becoming to slow.

4.4 Parameter values

The colloidal particles are not allowed to overlap and their interaction is given by the Derjaguin-Landau-Verwey-Overbeek-theory [see equation (2.1)] with a large-distance cutoff of the potential at $5a_S$, where a_S is the spacing between the colloids if they form an ideal triangular lattice. The interaction parameters together with the properties of the external potential determine the parameter set of our system, i.e., the free parameters usually are: the radius R of a colloid, its effective surface charge Z^*, its friction coefficient in water γ, the dielectric constant of water ϵ_r, the inverse Debye screening length κ, the potential strength V_0, its typical length scale a_V, the absolute temperature T, and the colloidal density given by the particle spacing a_S.

To study the colloidal behaviour in a one-dimensional potential (see chapter 6), we vary the potential strength V_0 and the inverse screening length κ. We employ the same values for the parameters as used by Strepp, Sengupta, and Nielaba in their study of a colloidal suspension in a commensurate periodic potential [32]: $R = 0.535$ μm, $Z^* = 7800$, $\epsilon_r = 78$, and the temperature $T = 293.15$ K. The density is chosen such that the spacing in an ideal triangular lattice would be $a_S = 2.53$ μm. These parameters are also taken for the case of a low-density suspension in a two-dimensional potential, where there are less colloids than minima in the potential (see chapter 7). However, there we vary the potential strength V_0 and the density (given by a_S) but choose a constant value for the characteristic length $a_V = 2\pi/\left|\mathbf{G}_j\right| = 2.53$ μm and the screening length $\kappa^{-1} = 0.506$ μm $= a_V/5$. For the case of high densities, i.e., where more colloids than minima occupy the simulation box, we use $R = 1.2$ μm, $Z^* = 1000$, $\epsilon_r = 78$, $T = 300$ K, $a_V = 5.0$ μm, and $\kappa^{-1} = 0.25$ μm $= a_V/20$, which leads to a behavior close to the one observed in experiments by Mikhael *et al.* [20,191].

Chapter 5

Theory of Melting in 2D

In this chapter we shortly introduce different widely used theories that describe melting in two dimensions. The Landau-Alexander-McTague theory presented in section 5.1 is based on an expansion of the free energy with respect to the order parameter. In section 5.2 a brief introduction to density functional theory is given. The probably most sucessful theory for melting in two dimensions is the so called KTNHY-theory, named after Kosterlitz, Thouless, Nelson, Halperlin, and Young. It is based on the dissociation of disclination and dislocation pairs and predicts an interesting new phase between the solid triangular and the liquid phase, termed hexatic. Section 5.3 gives a short overview over the main ideas of the KTNHY-theory also with respect to quasicrystals. The theories presented in this chapter were also employed to explain the phase behavior in a one-dimensional commensurate periodic potential (see section 6.1). Furthermore, we use the Landau-Alexander-McTague theory to study the phase behavior in a laser field with one-dimensional quasicrystalline symmetry (section 6.3.2).

5.1 Landau-Alexander-McTague theory

The Landau-theory of phase transitions [192, 193] is based on the expansion of the free energy with respect to an order parameter. The order parameter is usually zero in the high-symmetry phase, e.g., in a liquid, and non-zero in the low-symmetry phase, which for a two-dimensional colloidal system without external potential is the solid triangular phase. By minimizing the free energy, the value of the order parameter in thermal equilibrium is determined and therefore the phase of the system.

The Landau-Alexander-McTague theory was first used in 1978 by Alexander and McTague to compare the free energy of bcc and fcc crystals [194]. Here we shortly introduce the theory for the triangular to liquid transition in a two-dimensional system. The basic idea is to consider a liquid with a homogeneous density $\overline{\rho}$ and then expand the free energy $\mathcal{F}$ with respect to small variations of the density $\delta\rho(\mathbf{r}) = \rho(\mathbf{r}) - \overline{\rho}$, where $\rho(\mathbf{r})$ is the

density field, e.g., the mass density field, in real space (cf. expansion in section 3.4.2):

$$\mathcal{F} = \int dA \left\{ \frac{b'}{2} \left[\delta\rho(\mathbf{r})\right]^2 - \frac{d}{6} \left[\delta\rho(\mathbf{r})\right]^3 + \frac{e}{24} \left[\delta\rho(\mathbf{r})\right]^4 \right\}. \tag{5.1}$$

The integration is over the whole plane. The signs are chosen such that the parameters b', d, and e are positive: e has to be positive to have a stable global minimum of the free energy and for other signs of d and b' no phase transition would occur as will be illustrated below. To transform the free energy into reciprocal space we use a Fourier series for the density variations:

$$\delta\rho(\mathbf{r}) = \sum_j \rho_j e^{-i\mathbf{G}_j \cdot \mathbf{r}}, \tag{5.2}$$

where $\mathbf{G}_j$ are the relevant reciprocal lattice vectors and ρ_j the corresponding Fourier components. The free energy density in reciprocal space then is

$$\begin{aligned} \frac{\mathcal{F}}{A} &= \frac{1}{2} b' \sum_j |\rho_j|^2 - \frac{1}{6} d \sum_{j,k,l} \rho_j \rho_k \rho_l \delta\left(\mathbf{G}_j + \mathbf{G}_k + \mathbf{G}_l\right) \\ &\quad + \frac{1}{24} e \sum_{j,k,l,m} \rho_j \rho_k \rho_l \rho_m \delta\left(\mathbf{G}_j + \mathbf{G}_k + \mathbf{G}_l + \mathbf{G}_m\right), \end{aligned} \tag{5.3}$$

where $\delta(\cdot)$ denotes the Kronecker symbol, which is 1 if the argument vanishes and zero in all other cases. There are three parameters in the free energy expansion: b', d and e. Because it is possible to rescale the free energy density $\mathcal{F}/A$ and the Fourier components ρ_j, two parameters can be set to unity. We name the rescaled quantities $\tilde{\mathcal{F}}/A$ and $\tilde{\rho}_j$, introduce the remaining rescaled parameter b, and then write the rescaled free energy as

$$\begin{aligned} \frac{\tilde{\mathcal{F}}}{A} &= \frac{1}{2} b \sum_j |\tilde{\rho}_j|^2 - \frac{1}{6} \sum_{j,k,l} \tilde{\rho}_j \tilde{\rho}_k \tilde{\rho}_l \delta\left(\mathbf{G}_j + \mathbf{G}_k + \mathbf{G}_l\right) \\ &\quad + \frac{1}{24} \sum_{j,k,l,m} \tilde{\rho}_j \tilde{\rho}_k \tilde{\rho}_l \tilde{\rho}_m \delta\left(\mathbf{G}_j + \mathbf{G}_k + \mathbf{G}_l + \mathbf{G}_m\right). \end{aligned} \tag{5.4}$$

Since we want to illustrate the triangular to liquid phase transition, $\mathbf{G}_j$ are the three lattice vectors $\mathbf{G}_0$, $\mathbf{G}_1$, and $\mathbf{G}_2$ of the triangular phase as shown in figure 3.16 and the inverse vectors $-\mathbf{G}_0$, $-\mathbf{G}_1$, and $-\mathbf{G}_2$. The third-order term contains contributions where the three lattice vectors form triangles. The fourth-order term consists of pairs of antiparallel vectors (e.g. $\mathbf{G}_k = -\mathbf{G}_j$ and $\mathbf{G}_m = -\mathbf{G}_l$). No other non-trivial sum of $\mathbf{G}_j + \mathbf{G}_k + \mathbf{G}_l + \mathbf{G}_m$ vanishes. Due to the six-fold rotational symmetry of the triangular phase, all Fourier components are the same, i.e., $\tilde{\rho}_0 = \tilde{\rho}_1 = \tilde{\rho}_2 = \tilde{\rho}$. Counting all the contributions, we finally find

$$\frac{\tilde{\mathcal{F}}}{A} = 3b\tilde{\rho}^2 - 2\tilde{\rho}^3 + 4\tilde{\rho}^4. \tag{5.5}$$

For $b > 3/32$ the free energy only has one minimum at $\tilde{\rho} = 0$. For $b < 3/32$ there are two minima, for $b > 1/12$ the minimum for $\tilde{\rho} = 0$ is the global minimum, but for $b < 1/12$

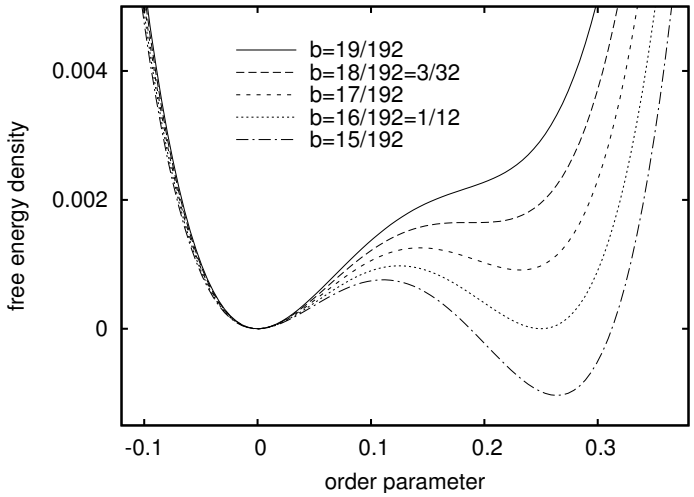

Figure 5.1: Free energy density $\tilde{\mathcal{F}}/A$ for the triangular to liquid phase transition [see equation (5.5)] as a function of the order parameter $\tilde{\rho}$. The curves are for different values of the control parameter b.

the second minimum with $\tilde{\rho} > 0$ is deeper (see figure 5.1). The amplitude $\tilde{\rho}$ is the order parameter of the system. Since it jumps discontinuously from $\tilde{\rho} > 0$ to $\tilde{\rho} = 0$ at $b = 1/12$, there is a first-order phase transition from a triangular ordering at $b < 1/12$ into a liquid phase at $b > 1/12$. The control parameter b is usually identified with the temperature but as we will see below, the inverse screening length of the DLVO potential can also control the phase transition.

In section 6.1.2 we shortly present the Landau-Alexander-McTague theory for a two-dimensional system under the influence of an one-dimensional periodic potential as introduced by Chowdhury, Ackerson, and Clark [28]. We also use this theory to calculate the phase diagram for colloids in a one-dimensional quasicrystalline potential (see section 6.3.2).

5.2 Density functional theory

The density functional theory in condensed matter physics is a widely used method to describe phase transitions. For a system consisting of simple spherical particles with pure pair interactions it was pioneered by Ramakrishnan and Yussouff in the late 70s [195, 196] (for reviews see e.g. [197–199]). It is, e.g., used to study freezing in three dimensions [200–203] and in two dimensions [204], and to investigate the liquid-solid interface or the crystallization behavior [205, 206].

The basic idea is to calculate the grand canonical potential or the free energy as a functional depending on the density field $\rho(\mathbf{r})$. The difference of the grand canonical

potential in the solid compared to the liquid phase is [197]

$$\Delta\Omega\left[\rho(\mathbf{r})\right] = k_B T \int dA \left\{\rho(\mathbf{r})\left[\rho(\mathbf{r})/\overline{\rho}\right] - \rho(\mathbf{r}) + \overline{\rho}\right\} + \mathcal{F}^{int}\left[\rho(\mathbf{r})\right] - \mathcal{F}^{int}\left[\overline{\rho}\right], \tag{5.6}$$

where $\overline{\rho}$ is the average density and $\mathcal{F}^{int}$ is the interaction free energy. The first term in (5.6) corresponds to the grand canonical potential of an ideal gas.

Using a mean-field approach to approximate the interaction free energy $\mathcal{F}^{int}$ and solving a self-consistency condition for the density (for details see e.g. [196]), one finds:

$$\Delta\Omega\left[\rho(\mathbf{r})\right] = -k_B T \ln \Phi\left[\rho(\mathbf{r})\right] + \sum_j \frac{\rho_j}{2c_1(\mathbf{G}_j)}. \tag{5.7}$$

Here the functional $\Phi\left[\rho(\mathbf{r})\right]$ is

$$\Phi\left[\rho(\mathbf{r})\right] = \frac{1}{A}\int_A dA \exp\left[\sum_j \rho_j \exp\left(i\mathbf{G}_j \cdot \mathbf{r}\right)\right], \tag{5.8}$$

A is the area of the unit cell of the lattice, j is the index of the reciprocal lattice vectors $\mathbf{G}_j$, and ρ_j are the corresponding Fourier components (see previous section). The constants $c_1(\mathbf{G}_j) = \overline{\rho}\,\overline{g}(G_j)$ denote the peak values of the structure factor $\overline{g}(G)$, which corresponds to the pair correlation function $g(|\mathbf{r}-\mathbf{r}'|)$ in Fourier space where $g(|\mathbf{r}-\mathbf{r}'|)$ is given by the probability to find two colloids at distance $|\mathbf{r}-\mathbf{r}'|$. To determine the phase behavior, $\Delta\Omega$ (or the free energy) has to be minimized. Interestingly, the only free parameters are $c_1(\mathbf{G}_j)$, which is given by the pair correlation function (or the structure factor).

Finally we note that freezing in two dimensions according to the density functional theory is a first-order phase transition [204] as it is for the Landau-Alexander-McTague theory.

5.3 KTHNY theory

The KTHNY theory of melting in two dimensions was developed and named after Kosterlitz and Thouless [21], Halperin and Nelson [22–25], and Young [26, 27]. The basic idea is that starting from a perfect lattice an increasing number of defects appear if the temperature is raised. The defects destroy the order of the crystal and lead to a two-stage transition into the liquid phase. Melting in three dimensions usually starts at the surface of the crystal, whereas in two dimensions the defects can be easily created in bulk and therefore the surface is not as important. Defect mediated melting for two-dimensional quasicrystals corresponding to the KTHNY theory was developed by De and Pelcovits [207–210]. In the following, we shortly give an overview of the main ideas of this melting theory for triangular and for decagonal lattices.

In figure 5.2 defects in a triangular lattice are shown. A dislocation characterizes defects in the translational order of a lattice whereas a disclination describes defects in the

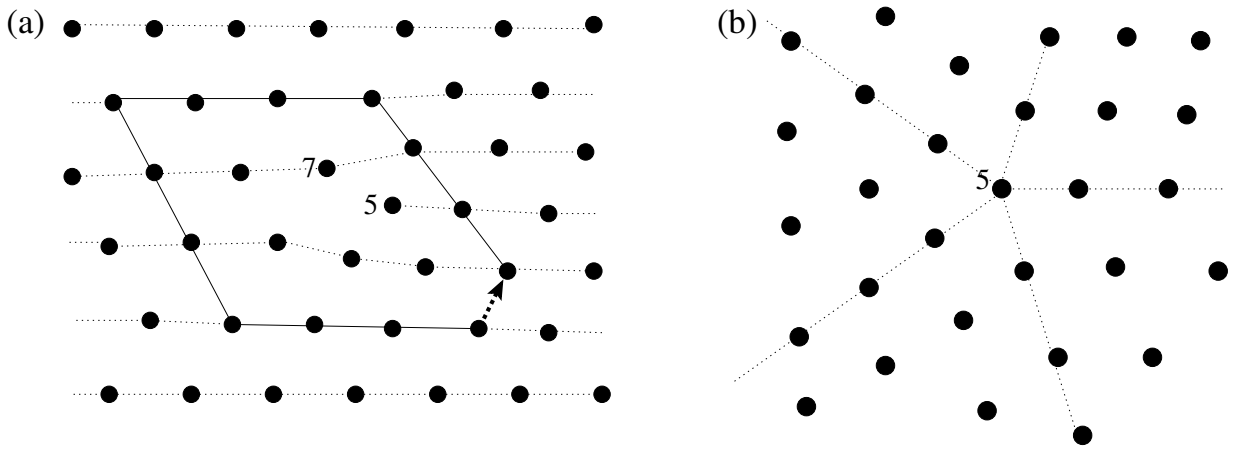

Figure 5.2: Defects in a triangular lattice: (a) dislocation with corresponding Burgers vector and (b) disclination. The numbers give the number of nearest neighbors if it differs from 6.

orientational order. As figure 5.2(a) illustrates, a dislocation is always accompanied by a pair of disclinations. A dislocation is characterized by a Burgers vector as shown in figure 5.2(a): In a perfect lattice without any dislocations, a path that consist of the same number of steps along each of the basis vectors and their inverse vectors is closed. However, if one goes around a dislocation, the path is not closed and the open part defines the Burgers vector. Note that such a characterization of dislocations is also possible for quasicrystals, where a Burgers vector has four components: The first two give the phononic and the last two the phasonic displacements (see [3]).

Now the defect-mediated melting works as follows (see also figure 5.3). For high enough temperatures, a pair of dislocations can be easily produced by thermal fluctuations in the positions of the atoms. Increasing the temperature, dislocations are able to dissociate which corresponds to a phase transition from the solid into an intermediate phase where long-range translational order is completely lost. For triangular systems the intermediate phase is called hexatic, since the bonds between the atoms still display long-range orientational order. For quasicrystals, the intermediate phase was termed pentahedratic phase (the decagonal ordering sometimes is also called pentagonal phase). In a second phase transition the dislocations, i.e., pairs of disclinations, dissolve into single free disclinations. The resulting phase is a liquid where any long-range order is destroyed completely.

The phases are usually characterized by correlation functions. The positional correlation function $C_{\mathbf{G}}(\mathbf{r})$ describes the correlation of the translational order parameter at point 0 and $\mathbf{r}$:

$$C_{\mathbf{G}}(\mathbf{r}) = \langle \rho_{\mathbf{G}}(\mathbf{0}) \rho^*_{\mathbf{G}}(\mathbf{r}) \rangle \,. \tag{5.9}$$

The average is over configurations, the star denotes the complex conjugate, and the translational order parameter $\rho_{\mathbf{G}}(\mathbf{r})$ in a certain point $\mathbf{r}$ is given by

$$\rho_{\mathbf{G}}(\mathbf{r}) = \exp\left[i\mathbf{G}_j \cdot \mathbf{r} + i\mathbf{G}_j \cdot \mathbf{u}(\mathbf{r}) + i\mathbf{G}_{(3j \bmod 3)} \cdot \mathbf{w}(\mathbf{r}) \right], \tag{5.10}$$

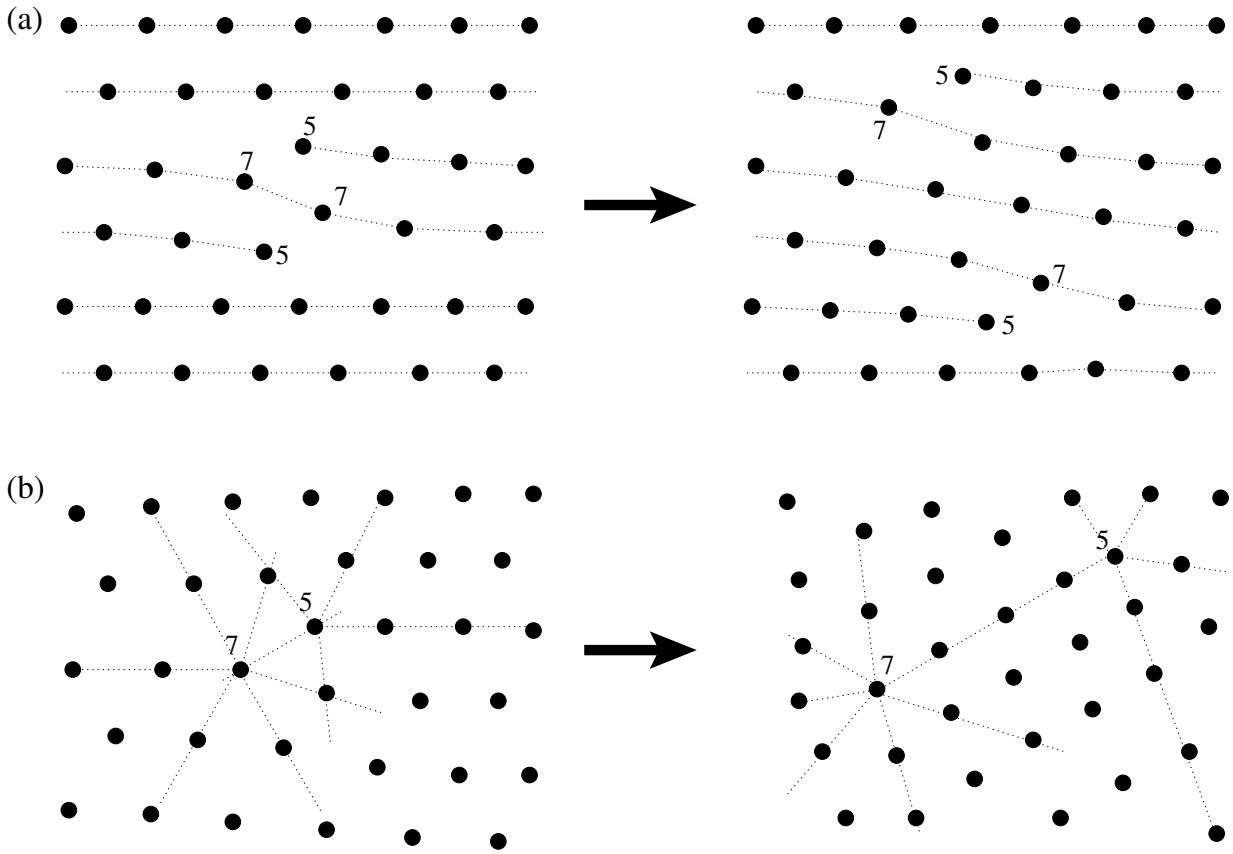

Figure 5.3: Dissociation of (a) a dislocation pair and of (b) a dislocation into two disclinations. In both cases a phase transition takes place.

where $\mathbf{u}(\mathbf{r})$ and $\mathbf{w}(\mathbf{r})$ are the phononic and phasonic displacement fields at position $\mathbf{r}$, and $\mathbf{G}_j$ is a lattice vector. Note in a triangular crystal phasons do not occur and $\mathbf{w}(\mathbf{r}) = \mathbf{0}$. In a two-dimensional lattice perfect long-range positional order does not exist, i.e., even in the solid phase $C_{\mathbf{G}}(\mathbf{r})$ decays algebraically according to

$$C_{\mathbf{G}}(\mathbf{r}) \propto r^{-\eta_{\mathbf{G}}} \tag{5.11}$$

with an exponent $\eta_{\mathbf{G}}$ that depends on the elastic constants of the lattice (see e.g. [210]). However, perfect long-range orientational correlations can exist in two dimensions. The orientational correlation function is given by

$$C_{\theta,m}(\mathbf{r}) = \langle \psi_m(\mathbf{0}) \psi_m^*(\mathbf{r}) \rangle \,, \tag{5.12}$$

where the bond orientational order parameter $\psi_m(\mathbf{r})$ in point $\mathbf{r}$ is

$$\psi_m(\mathbf{r}) = \exp\left[im\theta(\mathbf{r})\right] \tag{5.13}$$

with $m = 6$ for the triangular and $m = 10$ in the decagonal lattice; $\theta(\mathbf{r})$ is called bond angle field $\theta(\mathbf{r})$ and is defined as the angle of a bond between a particle at position $\mathbf{r}$ and a nearest neighbor with respect to an arbitrary reference direction (cf. section 7.1.1).

Since free dislocations destroy the long-range positional order and free disclinations also the long-range orientational order, the correlation functions behave as follows: as already mentioned, in the solid phase $C_{\mathbf{G}}(\mathbf{r})$ decays algebraically whereas $C_\theta(\mathbf{r})$ approaches a nonzero constant for $r \to \infty$. In the hexatic or pentahedratic phase free dislocations exist and $C_{\mathbf{G}}(\mathbf{r})$ decays exponentially but $C_\theta(\mathbf{r})$ only algebraically. Finally, in the liquid, the free disclinations lead to an exponential decay of $C_\theta(\mathbf{r})$.

By using symmetry arguments, the elastic free energy density up to second order in the strain variables is given by [2,3]

$$\begin{aligned} f_{el} &= \frac{1}{2}\lambda u_{ii}u_{ii} + \mu u_{ij}u_{ij} + \frac{1}{2}K_1 w_{ij}w_{ij} + K_2\left(w_{xx}w_{yy} - w_{yx}w_{xy}\right) \\ &\quad + K_3\left[\left(u_{xx} - u_{yy}\right)\left(w_{xx} + w_{yy}\right) + 2u_{xy}\left(w_{xy} - w_{yx}\right)\right], \end{aligned} \tag{5.14}$$

where $u_{ij} = (\partial u_i/\partial r_j + \partial u_j/\partial r_i)/2$ and $w_{ij} = \partial w_i/\partial r_j$. The elastic constants are λ, μ, K_1, K_2 and K_3. In a triangular crystal $K_1 = K_2 = K_3 = 0$. The elastic free energy allows to calculate the interaction energy between two disclinations or between two dislocations. Therefore, the phase transition temperatures can be determined as unbinding transitions of the corresponding defects (see e.g. [25] for triangular crystals and [210] for quasicrystals): The temperature $T_{(m)}$ of the solid to hexatic or pentahedratic transition is given by the relation

$$c_{(m),R}\left(\lambda_R, \mu_R, K_{1,R}, K_{2,R}, K_{3,R}\right) = \frac{16\pi k_B T_{(m)}}{a_S^2}, \tag{5.15}$$

where a_S is the particle spacing. The transition to the liquid takes place at temperature $T_{(i)}$ with

$$c_{(i),R}\left(\lambda_R, \mu_R, K_{1,R}, K_{2,R}, K_{3,R}\right) = M\frac{k_B T_{(i)}}{\pi}, \tag{5.16}$$

where $M = 72$ for the hexatic-liquid and $M = 100$ for the pentahedratic-liquid transition. Since the interaction between two defects is usually screened by other defects the elastic constants have to be renormalized. All constants marked with an index R are the renormalized quantities of the constants introduced in (5.14). The quantities $c_{(m),R}\left(\lambda_R, \mu_R, K_{1,R}, K_{2,R}, K_{3,R}\right)$ and $c_{(i),R}\left(\lambda_R, \mu_R, K_{1,R}, K_{2,R}, K_{3,R}\right)$ depend on the elastic constants; $c_{(i),R}\left(\lambda_R, \mu_R, K_{1,R}, K_{2,R}, K_{3,R}\right)$ is the Frank constant defined in the free energy density f_θ depending on the variations of the bond angle field $\theta(\mathbf{r})$:

$$f_\theta = \frac{1}{2}c_{(i),R}\left(\lambda_R, \mu_R, K_{1,R}, K_{2,R}, K_{3,R}\right)\left[\left(\frac{\partial\theta}{\partial x}\right)^2 + \left(\frac{\partial\theta}{\partial y}\right)^2\right]. \tag{5.17}$$

In certain limits, $c_{(i),R}\left(\lambda_R, \mu_R, K_{1,R}, K_{2,R}, K_{3,R}\right)$ can be expressed explicitly in terms of λ_R, μ_R, $K_{1,R}$, $K_{2,R}$, and $K_{3,R}$ depending on the system; $c_{(m),R}\left(\lambda_R, \mu_R, K_{1,R}, K_{2,R}, K_{3,R}\right)$ is given

by

$$\begin{aligned} c_{(m),R}\left(\lambda_R, \mu_R, K_{1,R}, K_{2,R}, K_{3,R}\right) &= 2K_{1,R} \\ &+ \frac{4K_{3,R}^2\left(-K_{2,R}+\lambda_R+\mu_R\right) + 2K_{1,R}\left[K_{3,R}^2 - 2\mu_R\left(\lambda_R+\mu_R\right)\right]}{K_{3,R}^2 - K_{1,R}\left(\lambda_R+2\mu_R\right)} \\ &+ \frac{K_{1,R}K_{3,R}^2\left(-K_{1,R}+2K_{2,R}\right)\left(\lambda_R+\mu_R\right)}{\left(-K_{3,R}^2+K_{1,R}\mu_R\right)\left[-K_{3,R}^2+K_{1,R}\left(\lambda_R+2\mu_R\right)\right]} \end{aligned} \tag{5.18}$$

for quasicrystals and

$$c_{(m),R}\left(\lambda_R, \mu_R\right) = \frac{4\mu_R\left(\mu_R+\lambda_R\right)}{2\mu_R+\lambda_R} \tag{5.19}$$

for triangular ordering.

Nelson and Halperin also predict the phase behavior in commensurate and incommensurate potentials as well as on totally disordered substrates [24, 25]. In commensurate periodic potentials, i.e., triangular substrates with a lattice constant given by the particle spacing, there is a phase transition from a floating solid phase for weak to a pinned solid phase for strong potentials. The floating phase has triangular ordering that is almost not affected by the substrate and therefore has, like the solid phase without potential, no perfect long-range positional order. However, in a strong potential the particles are pinned to the minima and the resulting pinned solid phase displays perfect positional order. In a disordered potential also two different solid phases exist: A floating phase corresponding to the triangular one existing without potential and a pinned disordered phase, where the particles are just sitting in the minima of the potential. On incommensurable substrates, Nelson and Halperin predict a floating solid phase not affected by the potential, an intermediate phase where the orientations of some clusters are locked to the potential, and a pinned phase, where the ordering is completely given by the substrate. The intermediate phase exhibits an orientational order given by the smallest common multiplier of the rotational order of the substrate and the orientational order that the adsorbed particles would have without potential. Therefore, a colloidal suspension that displays triangular ordering without potential would in a square potential posses an intermediate phase with 12-fold orientational order [24,25]. Correspondingly, colloids on a decagonal potential should have a 30-fold bond-orientational symmetry for intermediate potential strengths. However, in our simulations we are not able to identify such a phase (see section 7.1.4).

The KTHNY theory along with its predictions for the elastic properties were also tested experimentally using, e.g., charged particles [211–214] or supermagnetic colloids, whose interaction can be tuned by an external magnetic field [215–220].

In this work we consider quasicrystals induced by an external potential. Therefore the melting properties differ from the ones predicted by the defect mediated melting theory for systems that display intrinsic quasicrystalline order.

Chapter 6

Colloids in a 1D quasicrystalline potential

In this chapter we study colloidal ordering and dynamics in a potential that is constant in one direction and quasi-periodically modulated in the other. In literature, the case of one-dimensional periodic potentials is well known. Therefore, in section 6.1, we give a brief overview of the phase behavior in a periodic laser field. In section 6.2, we introduce the quasicrystalline potential and explain why it is of special interest. By using Monte-Carlo simulations and the Landau-Alexander-McTague theory, we determine the phase diagram in section 6.3. As we will show, it is possible to destroy any periodic ordering by applying a quasicrystalline laser field with sufficiently large intensity. Therefore, in section 6.4, we study colloidal dynamics in the case of very large potential strength and discover an interesting aperiodic locked phase. We shortly comment on experimental results and on alternative quasicrystalline potentials in sections 6.5 and 6.6, respectively. Finally, we summarize our results in section 6.7. Some parts of this chapter are published in our letter [A].

6.1 Colloids in a 1D periodic potential

We consider a one-dimensional periodic potential, i.e.,

$$V(\mathbf{r}) = V_0 \cos\left(\mathbf{G}_0 \cdot \mathbf{r}\right), \tag{6.1}$$

where $\mathbf{G}_0 = G_0 \mathbf{e}_x$ is a vector of length G_0 in x-direction. Usually, we choose a commensurate potential, i.e., a potential with a wave number G_0 that fit the height of a triangle in a perfect triangular lattice. Therefore, in a commensurate laser field $G_0 = 4\pi/(\sqrt{3}a_S)$, where a_S is the particle spacing in the triangular phase. With such a potential triangular ordering can be induced in the system. However, by further increasing the potential strength the ordering can be destroyed again depending on the two-particle interaction. We discuss these observations in the next subsection and then present the corresponding theories to treat them in the subsections 6.1.2 to 6.1.4.

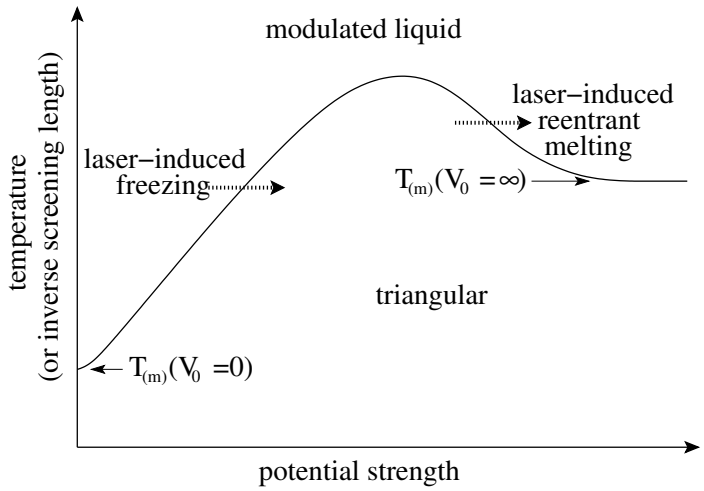

Figure 6.1: Schematic phase diagram displaying the laser-induced freezing and laser-induced reentrant melting transitions in a one-dimensional commensurate periodic potential. The transition temperatures $T_{(m)}(V_0 = 0)$ without potential and $T_{(m)}(V_0 = \infty)$ in the limit of very large intensities can be determined using a defect-mediated melting theory (see section 6.1.4).

6.1.1 Laser-induced freezing and melting

Chowdhury, Ackerson, and Clark discovered that a one-dimensional commensurate periodic potential induces two-dimensional triangular ordering [28]. They considered a system which is liquid without external potential but sufficiently close to the freezing point. If the potential is applied, it first induces a one-dimensional modulation. Accordingly, the new phase is often called modulated liquid. However, at a certain potential strength the system becomes ordered in both directions, i.e., it freezes into a triangular phase. Chowdhury, Ackerson, and Clark explained this behavior with the help of the Landau-Alexander-McTague theory (see next subsection). The laser induced freezing phenomena was also studied in more detail experimentally [221], with Monte-Carlo simulations [222], and with a density functional theory [223] (cf. section 6.1.3).

By using more detailed Monte-Carlo simulations, Chakrabarti, Krishnamurthy, Sood, and Sengupta found out that it is also possible to destroy an induced triangular ordering by further increasing the potential strength [224]. This phenomena was termed light induced reentrant melting. Experimentally, it was first observed in a colloidal system by Wei, Bechinger, Rudhardt, and Leiderer [225]. Later, the whole phase behavior was explored in experiments [29, 30] and with Monte-Carlo simulations [31, 32, 226, 227]. Figure 6.1 schematically shows a typical phase diagram. The reentrant melting cannot be explained by the conventional density functional theory and the predictions of the Landau-Alexander-McTague theory for high laser intensities are probably not correct [223] (see also section 6.1.3). Chakrabarti and Sinha added fluctuations to the density functional theory and found out that these are important for light-induced melting [228]. A full theoretical description of the reentrant melting, based on the KTNHY theory, was developed by Frey,

Nelson, and Radzihovsky [229, 230] and will be reviewed in subsection 6.1.4. The theory predicts that crystalline order in the colloidal system can only be destroyed if the system is liquid without potential, i.e., if the ordering to be destroyed is induced by the external potential. A crystal that is stable without potential cannot be melted by applying a commensurate periodic laser field.

6.1.2 Landau-Alexander-McTague theory

The Landau-Alexander-McTague theory was first applied to a colloidal system in a one-dimensional commensurate periodic potential by Chowdhury, Ackerson, and Clark [28]. The modulation wave vector of the potential equals one of the lattice vectors of the induced triangular phase (shown in figure 3.16). In section 5.1, the expansion of the free energy with respect to variations of the density was derived. Since a density variation with this wave vector lowers the total free energy of the system, the coupling of the system to the potential can be described by adding a term proportional to $-V_L\rho_0$ to the free energy expansion of equation (5.4). As introduced in section 5.1, ρ_j are the Fourier components of the density modulation with wave vector $\mathbf{G}_j$. Note that due to the symmetry of the system we still assume $\rho_1 = \rho_2$, however these coefficients can differ from ρ_0. From equation (5.4) in combination with the new potential term, we find the (rescaled) free energy expansion:

$$\frac{\tilde{\mathcal{F}}}{A} = -2V_L\tilde{\rho}_0 + 2b\left(\tilde{\rho}_0^2 + 2\tilde{\rho}_1^2\right) - 2\tilde{\rho}_0\tilde{\rho}_1^2 + \frac{1}{3}\tilde{\rho}_0^4 + \frac{5}{3}\tilde{\rho}_1^4 + 2\tilde{\rho}_0^2\tilde{\rho}_1^2, \tag{6.2}$$

where V_L is a rescaled parameter characterizing the strength of the potential and $\tilde{\rho}_j$ are the rescaled Fourier components. Minimizing the free energy with respect to $\tilde{\rho}_0$ and $\tilde{\rho}_1$ for given values of the parameters b and V_L, determines the phase: If both order parameters $\tilde{\rho}_0$ and $\tilde{\rho}_1$ are non-zero, triangular ordering occurs; if both order parameters are zero, the system is liquid. The case $\tilde{\rho}_0 > 0$ but $\tilde{\rho}_1 = 0$ refers to the so-called modulated liquid. Due to the coupling of $\tilde{\rho}_0$ to the external potential, $\tilde{\rho}_0 > 0$ as soon as the potential is applied. Therefore, only a modulated liquid and a triangular ordering exist for non-zero potential and the phases can be distinguished by the order parameter $\tilde{\rho}_1$. Because of the second and fourth-order term in (6.2), the free energy increases for non-zero $\tilde{\rho}_1$. However, $\tilde{\rho}_1$ also couples to $\tilde{\rho}_0$ by the third-order term, which lowers the total free energy by a transition into the triangular phase. The Landau-Alexander-McTague theory therefore helps to understand the effect of laser-induced freezing: By applying a laser field with a wave vector $\mathbf{G}_0$, a modulation along $\mathbf{G}_0$ is induced resulting in $\tilde{\rho}_0 > 0$. Due to the coupling of the density variations in different direction, this can also lead to modulations along other directions, e.g., along $\mathbf{G}_1$ and $\mathbf{G}_2$ (corresponding to $\tilde{\rho}_1 > 0$), hence a transition into the triangular phase occurs.

In figure 6.2 the phase diagram calculated with the help of the Landau-Alexander-McTague theory is shown. To determine the phases from the order parameter ρ_1, we employ a small threshold value. If ρ_1 is larger than the threshold, we mark the point in parameter space to be triangular otherwise as modulated liquid. We choose a threshold value of 10^{-8} but even values up to 10^{-1} do not change the phase behavior significantly.

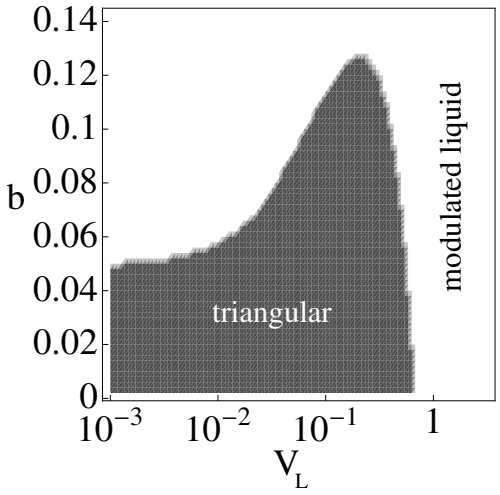

Figure 6.2: Phase diagram for a two-dimensional system in a one-dimensional commensurate periodic potential determied with the Landau-Alexander-McTague theory. The parameters V_L and b can be identified by the potential strength and the inverse screening length, respectively.

For a small potential strength V_L there is a phase transition from triangular ordering for small values of b into a modulated liquid phase for large b corresponding to the triangular to liquid transition for vanishing potentials. The parameter b can be identified with the temperature, the inverse screening length of the DLVO potential acting between colloids, or the inverse density. With increasing potential strength, it is possible to induce a triangular phase even for parameter values of b, where the system was liquid without external field. This corresponds to the light-induced freezing effect. Note that the phase diagram in figure 6.2 also shows light-induced melting. According to the Landau-Alexander-McTague theory it is possible the system melts if a very strong laser field is applied, even if the colloids were in a stable triangular phase without potential. This unphysical effect is probably due to the truncation of the free energy expansion [223] (see also the remarks at the end of the next subsection).

According to the Landau-Alexander-McTague theory, a phase is more likely to be stable if for that phase many triangles of lattice and wave vectors occur. Every set consisting of three vectors $\mathbf{G}_j$, $\mathbf{G}_l$, and $\mathbf{G}_l$ with $\delta\left(\mathbf{G}_j + \mathbf{G}_k + \mathbf{G}_l\right) = 1$ lowers the free energy (5.4). Based on such reasoning, Das and Krishnamurthy introduced a special one-dimensional quasicrystalline potential and claimed that it should induce pentagonal ordering in the system [231] (see also section 6.2). However, as we will show in section 6.3.2, a carefully applied Landau-Alexander-McTague theory for colloids in this potential only allows stable triangular and rhombic phases.

6.1.3 Density functional theory

Chakrabarti *et. al.* applied density functional theory (see section 5.2) to study colloidal ordering in the periodic laser field [223]. As in the previous subsection, the external

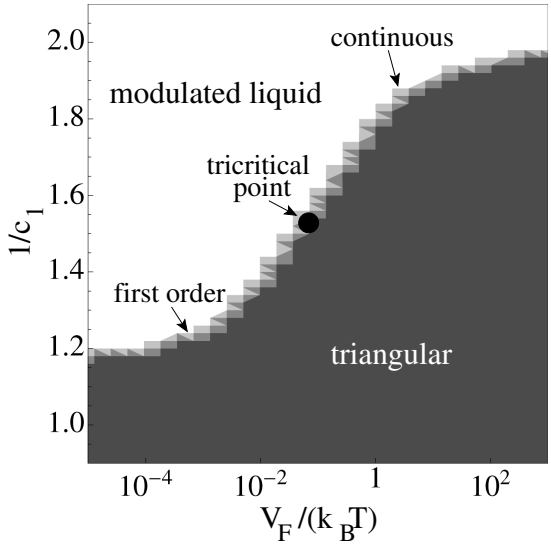

Figure 6.3: Phase diagram according to the density functional theory (cf. [223]).

potential is introduced by an additional contribution to the grand canonical potential (or free energy)

$$\mathcal{F}^{ext} = -\frac{\rho_0}{c_1} V_F, \tag{6.3}$$

that has to be added to equation (5.7). The strength of the potential is given by V_F and ρ_0 is again the Fourier component for the lattice vector $\mathbf{G}_0$, which here also corresponds to the wave vector of the external modulation. The constant $c_1 = \overline{\rho}\,\overline{g}(G_0)$ denote the peak values of the structure factor $\overline{g}(G)$, i.e., the pair correlation function in Fourier space. Note, in (6.3) c_1 is only used to rescale ρ_0. The importance of c_1 as a control parameter is based on its occurrence in the part of the free energy (5.7) that does not depend on the potential. By minimizing the total free energy, the phase diagram is determined (see figure 6.3). For small laser intensities, the phase transition is a first order transition while for large potential strength it is continuous. Accordingly, a critical point can be found at intermediate intensities.

Laser-induced reentrant melting does not occur according to density functional theory, i.e., it is not possible to destroy triangular order by increasing the laser intensity, even if the order has been induced by the external potential. Furthermore, Chakrabarti *et. al.* expanded the free energy calculated according to the density functional theory into a power series. They showed that phase diagrams determined with truncated power series allow light-induced melting [223]. Therefore, the fact that light-induced melting is possible according to the Landau-Alexander-McTague theory (see previous section) is probably due to the truncation of the free energy expansion. For large potential strengths such a truncation obviously leads to wrong results.

Chakrabarti and Sinha found out that laser-induced melting can be explained by incorporating the effects of fluctuations in the density functional analysis [228]. With a pure

mean-field treatment obviously it is not possible to predict laser-induced melting while a theory that includes fluctuations can account for this phenomenon.

Density functional theory can also be applied to a colloidal system in a quasicrystalline potential. However, the integral in (5.8) is over a unit cell which does not exist for quasicrystals. Therefore one has to integrate over large areas similar to the simulation boxes introduced in section equation 4.3. Because the integration is usually performed numerically and is repeated many times during the minimization process, it is not possible to determine a phase diagram within a reasonable amount of time.

6.1.4 Laser-induced melting due to fluctuations

Frey, Nelson, and Radzihovsky developed a theory of defect-mediated melting in one-dimensional periodic potentials [229, 230], which is in good agreement with the results of experiments and simulations (see e.g. [30] for a review). Without potential the melting temperature $T_{(m)}$ is given by equations (5.15) and (5.19) obtained from the KTHNY theory, i.e.,

$$T_{(m)}\left(V_0 = 0\right) = \frac{a_S^2}{4\pi} \frac{\mu_R\left(\mu_R + \lambda_R\right)}{2\mu_R + \lambda_R}, \tag{6.4}$$

where μ_R and λ_R are the renormalized elastic constants of those given by [cf. equation (5.14) with $K_1 = K_2 = K_3 = 0$]:

$$f_{el} = \frac{1}{2}\lambda u_{ii} u_{ii} + \mu u_{ij} u_{ij}. \tag{6.5}$$

For a system in a potential, Frey, Nelson, and Radzihovsky consider a free energy density $f_{el,V}$ that takes into account that displacements u_x perpendicular to the potential wells are suppressed by the potential. Therefore, the modes in x-direction are integrated out and one finds

$$f_{el,V} = \frac{1}{2}\left[B_{xy}\left(\partial_x u_y\right)^2 + B_{yy}\left(\partial_y u_y\right)^2\right], \tag{6.6}$$

where B_{xy} and B_{yy} are effective elastic constants. A calculation similar to the ones employed in the KTHNY theory leads to a relation for the melting temperature:

$$\sqrt{B_{xy} B_{yy}} = \frac{8\pi k_B T_{(m)}}{a_S^2} \tag{6.7}$$

For infinite potential strength, i.e., without any displacements perpendicular to the wells at all, one finds by comparing (6.6) and (6.5)

$$B_{xy} = \mu_R \text{ and } B_{yy} = 2\mu_R + \lambda_R. \tag{6.8}$$

Therefore, the melting temperature for infinite potential strength is

$$T_{(m)}\left(V_0 = \infty\right) = \frac{a_s^2}{8\pi}\sqrt{\mu_R\left(2\mu_R + \lambda_R\right)}. \tag{6.9}$$

As a consequence, there is a limiting melting temperature for $V_0 \to \infty$, i.e., not all lattices can be melted by increasing the potential. Furthermore, because of $T_{(m)}(V_0 = \infty) > T_{(m)}(V_0 = 0)$, a crystal stable without laser field cannot be destroyed by applying a periodic commensurate potential. Note in experiments or simulations often the inverse screening length κ is varied. However, qualitatively the results can be compared to the theoretical results for varying temperature T.

If one starts at infinite potential strength V_0 and then lowers V_0, fluctuations perpendicular to the wells become important. Therefore, the relations (6.8) that determine the effective elastic constants in the limit $V_0 \to \infty$ are no longer fulfilled. Frey, Nelson, and Radzihovsky found out that due to the fluctuations a range of finite V_0 exists, where the melting temperature $T_{(m)}(V_0)$ exceeds $T_{(m)}(V_0 = \infty)$ [229, 230]. Therefore, at a temperature $T > T_{(m)}(V_0 = \infty)$ a triangular ordering may be stable for intermediate potential strength, however it becomes unstable for $V_0 \to \infty$. This corresponds to laser-induced reentrant melting.

For incommensurate periodic potentials, Frey, Nelson, and Radzihovsky in [229, 230] also predict phases with smectic ordering and floating phases similar to those predicted by Nelson and Halperin for commensurate and incommensurate 2D potentials (see section 5.3).

6.2 Motivation for the quasicrystalline potential

In this section we introduce the one-dimensional quasicrystalline potential. It was first proposed by Das and Krishnamurthy, who claimed that it is possible to induce a phase with pentagonal symmetry with such a laser field [231]. The quasicrystalline potential consists of two modulations whose wavelengths differ by a factor of τ^2 (see figure 6.4), where $\tau = (1 + \sqrt{5})/2$ is the number of the golden ratio (see section 3.2):

$$V(\mathbf{r}) = -\frac{V_0}{2}\left[\cos\left(\mathbf{G}_\alpha \cdot \mathbf{r}\right) + \cos\left(\mathbf{G}_\beta \cdot \mathbf{r}\right)\right] \tag{6.10}$$

with $\mathbf{G}_\alpha = \tau G_0 \mathbf{e}_x$, $\mathbf{G}_\beta = (-1/\tau) G_0 \mathbf{e}_x$. The vector $\mathbf{e}_x$ denotes the unit vector in x-direction and G_0 is the length of a reciprocal lattice vector that belongs to the ideal triangular configuration of the colloids without any external potential. If a_S is the particle spacing in this configuration, $G_0 = 4\pi/(\sqrt{3} a_S)$. Within the set of the wave vectors G_α and $\mathbf{G}_\beta$ combined with the lattice vectors of the pentagonal phase [see figure 6.5(a)] one can find many triangles. To be concrete, the following relations hold:

$$\begin{aligned} \mathbf{G}_0 - \mathbf{G}_\alpha - \mathbf{G}_\beta &= 0, \\ \mathbf{G}_1 + \mathbf{G}_4 + \mathbf{G}_\beta &= 0, \\ \text{and } \mathbf{G}_2 + \mathbf{G}_3 + \mathbf{G}_\alpha &= 0. \end{aligned} \tag{6.11}$$

These relations can be proven using the special properties of the number of the golden mean τ, e.g., $-2G_{2,x} = 1/(2G_{1,x}) = \tau G_0$(see also section 3.2). They lead to additional third-order terms in the expansion of the free energy and therefore decrease it (cf. section 6.1.2).

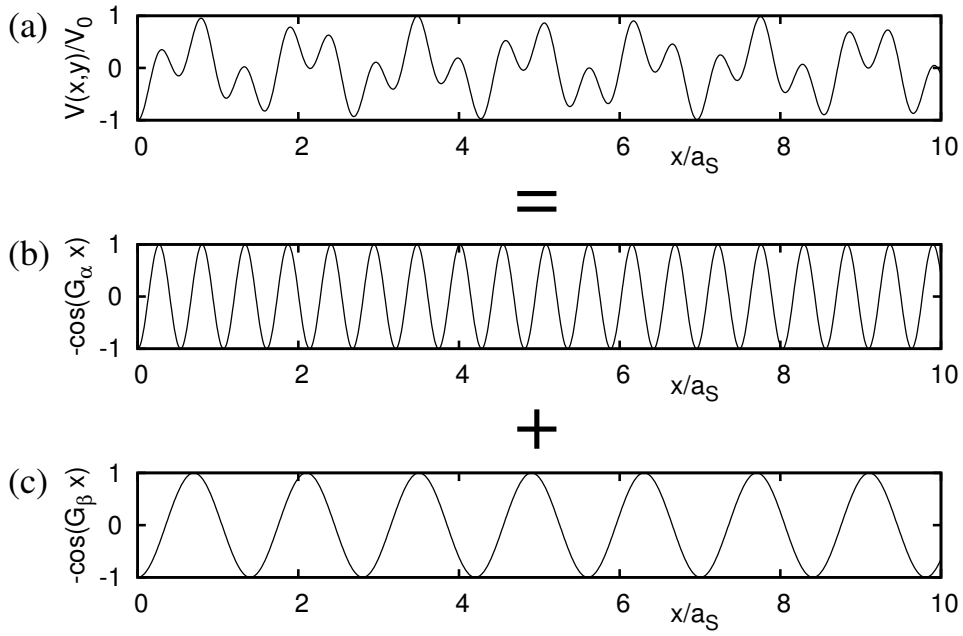

Figure 6.4: (a) One-dimensional quasicrystalline potential consisting of two modulations shown in part (b) and (c). The wavelengths of the modulations differ by a factor of τ^2.

Hence, Das and Krishnamurthy claimed that for certain parameters the quasicrystalline potential (6.10) induces a stable pentagonal (or decagonal) phase [231], i.e., a phase defined by five lattice vectors as shown in figure 6.5(a) and, therefore, exhibiting five- or ten-fold rotational symmetry. However, as we show in the following section, the free energy of the pentagonal phase has to be compared to the free energy of other possible orderings such as those pictured in figure 6.5(b)-(d). Especially the rhombic-α phase has a lower free energy than the pentagonal ordering. The lattice vector G_0 of the rhombic-α or rhombic-β phase is equal to the wave vector G_α or G_β, respectively. In both cases, the other wave vector of the potential is ignored completely. The length and direction of the lattice vectors $\mathbf{G}_1$ and $\mathbf{G}_2$ are determined by the following requirements: The sum of the three lattice vectors has to be zero, i.e., $\mathbf{G}_0 + \mathbf{G}_1 + \mathbf{G}_2 = 0$ and the density has to equal the density of a triangular lattice, i.e., the corresponding unit cells must have the same area. In the next section, we present complete phase diagrams determined by Monte-Carlo simulations and a refined Landau-Alexander-McTague theory. We find no pentagonal but only rhombic ordering.

6.3 Phase behavior

In this section we determine the phase behavior in the one-dimensional quasicrystalline potential. First, we use Monte-Carlo simulations to calculate a complete phase diagram.

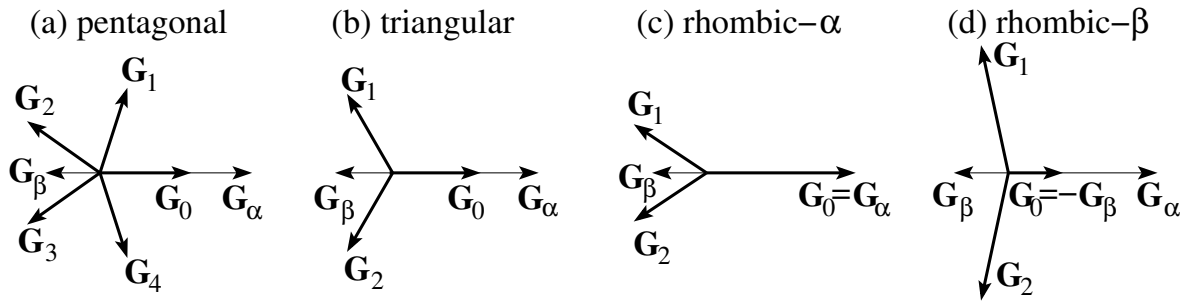

Figure 6.5: Modulation vectors G_α and G_β of the one-dimensional quasicrystalline potential together with the lattice vectors of (a) a pentagonal, (b) a triangular, (c) a rhombic-α, or (d) a rhombic-β ordered phase.

Then we develop a modified Landau-Alexander-McTague theory, which confirms the results of the simulations.

6.3.1 Results of Monte-Carlo simulations

The method of Monte-Carlo simulations was shortly introduced in section 4.2. We employ the same parameter values as Strepp, Sengupta, and Nielaba in [32] (see also section 4.4) and use a rational approximation of the potential as explained in section 4.3.1.

In figure 6.6 typical snapshots of the equilibrated system for different values of the potential strength V_0 and the inverse screening length κ of the DLVO potential are shown. We find triangular or rhombic-α ordering as well as the modulated liquid phase. No pentagonal or decagonal quasicrystal is stable for any set of parameters. On a first glance the triangular and the rhombic-α phase look quite similar. However, there are easy ways to distinguish the two lattices. The angle between nearest-neighbor bonds is $\pi/3$ in the triangular phase, whereas in the rhombic-α phase it is $\arctan\left(\sqrt{3}\tau^2/3\right) \approx 0.31\pi$ as can be calculated from the lattice vectors (see figure 6.5 and last paragraph of the previous subsection). Of course, it is also possible to measure the distances between rows of particles and compare them to the values expected by the lattice vectors. A very easy way to distinguish the structures, is to look on the orientation of a hexagon that consists of the nearest neighbors of a colloid. A hexagon in the rhombic-α phase is rotated by $\pi/2$ compared to the hexagon in the triangular phase.

We calculated the following order parameter $\phi(\mathbf{G}_1)$ for each of the possible phases illustrated in figure 6.5:

$$\phi(\mathbf{G}_1) = \frac{1}{N}\langle \sum_{i,j} \exp[i\mathbf{G}_1 \cdot (\mathbf{r}_j - \mathbf{r}_i)] \rangle, \tag{6.12}$$

where the sum is over all colloidal pairs of nearest neighbors and N is the number of such pairs; $\mathbf{G}_1$ is one of the lattice vectors shown in figure 6.5, it depends on the structure whose order parameter one wants to determine. The order parameter looks similar to a Fourier component of a density modulation with wave vector $\mathbf{G}_1$, however it only considers nearest

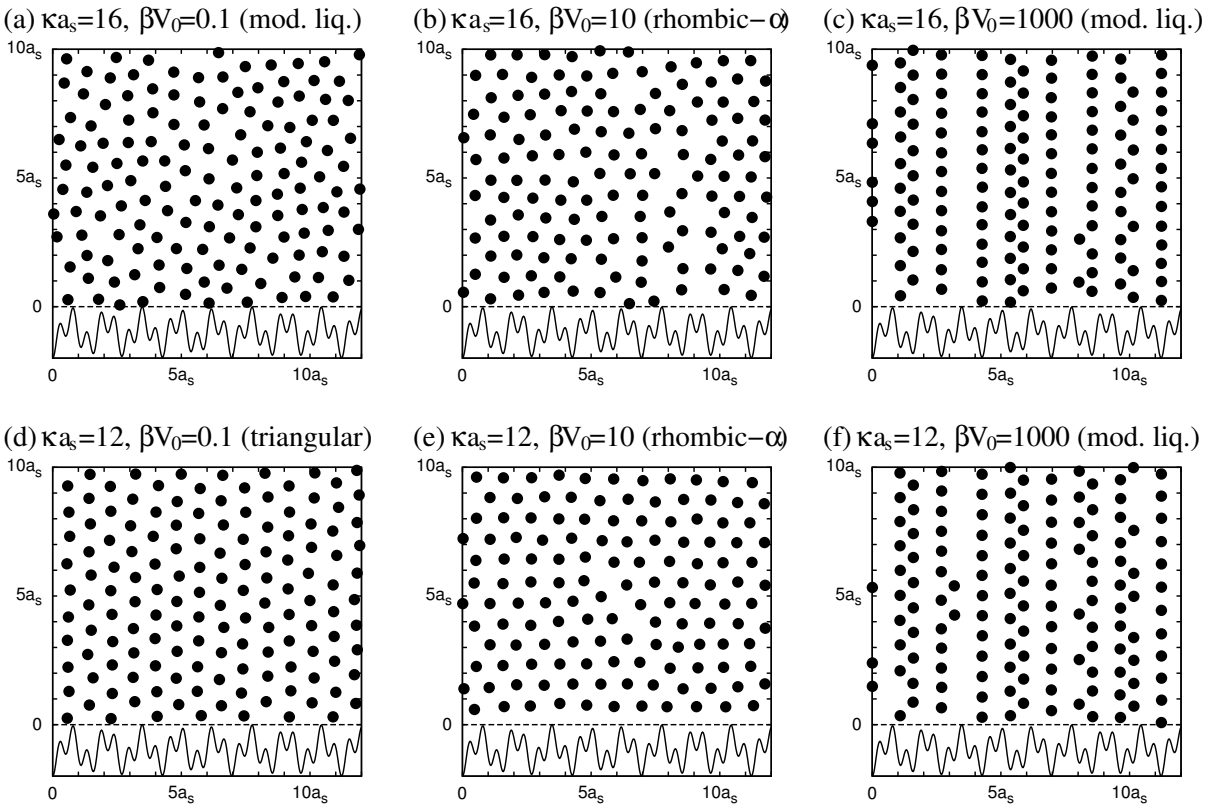

Figure 6.6: Snapshots of Monte-Carlo simulations for different values of the potential strength βV_0 and the inverse screening length κa_S. The potential is plotted in the lower part of the figures. The snapshots show just a small region of the simulation box.

neighbors. The simulation box fits best the pentagonal phase (see section 4.3.1), whereas the triangular and rhombic phases are weakly distorted on a global scale to fit into the box. Therefore, summing over all colloidal pairs in equation (6.12) would not lead to correct results and the local order parameter defined in (6.12) is more appropriate. It is similar to the one used in [232]. For a triangular and pentagonal lattice a bond orientational parameter can also be calculated (see section 7.1). However such a parameter is difficult to determine for a rhombic phase, which only has a two fold rotational symmetry.

Figure 6.7 shows the complete phase diagram and the order parameters for the triangular and the rhombic-α phase as a function of V_0 and κ. For the decagonal and the rhombic-β phase, the order parameters always vanish. As one expects, for weak potentials we find a transition from triangular ordering for small inverse screening lengths κ into a liquid for high values of κ. When the laser strength increases, a transition of the triangular phase into the rhombic-α phase occurs. We also find light induced freezing: Within a certain range of the inverse screening length, the system shows rhombic-α ordering in the laser field although it is liquid without external potential. Interestingly at very large laser intensities, we do not find any periodic or decagonal ordering at all. In principle, one can

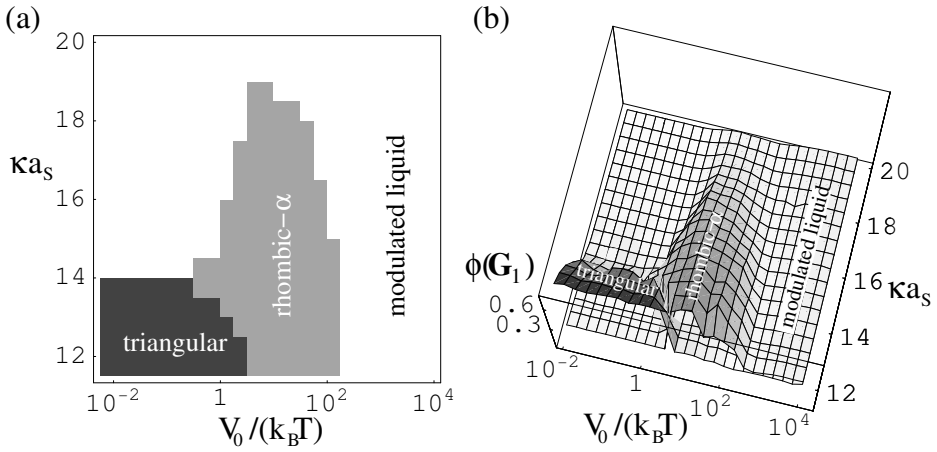

Figure 6.7: (a) Phase diagram and (b) order parameters as defined in (6.12) depending on the potential strength V_0 and the inverse screening length κ. The potential strength is given in terms of the thermal energy k_BT and the screening length is normalized by the nearest neighbor distance a_S of the triangular starting configuration. To get the phase diagram in (a), we checked for each possible ordering, if the corresponding order parameter is larger than 0.1. If none of the order parameters is large enough, we marked the phase as modulated liquid.

melt the system by applying a strong enough quasicrystalline potential no matter whether the colloids form a stable triangular phase without laser field or not. This is different from the case of a periodic commensurate potential, where light-induced reentrant melting needs a liquid phase at zero potential strength (see sections 6.1.1 and 6.1.4). A snapshot of a system melted by a quasicrystalline laser field of high intensity is shown in figure 6.6(f). All particles are located in local minima of the potential, i.e., on lines parallel to the y-axis. The potential wells have an approximate distance of $a_S\tau$ and their depths are modulated on the wave length τa_S. Therefore, the line density is different in every well. Some wells are almost empty or at least the probabilities to find a colloid in such wells are very small. Obviously, the potential induces quasicrystalline ordering in x-direction. The ratio of the line densities of neighboring wells is usually irrational. As a consequence, it is impossible to have any periodic ordering along the wells. This explains why there is no periodic phase for sufficiently large potential strengths and why every periodic ordering is destroyed by the quasicrystalline laser field. This is a type of light-induced melting different from the fluctuation-driven melting in a periodic commensurate potential. We will study the modulated liquid phase at high laser intensities in more detail in section 6.4.

6.3.2 Refined Landau-Alexander-McTague theory

The usual Landau-Alexander-McTague free energy expansion as in (5.4) [see also section 5.1] with some coupling to the potential (cf. section 6.1.2) does not distinguish between the rhombic-α and of the rhombic-β phase. This is due to the fact that the same number of triangles occur for the lattice vectors of these phases. In the following we therefore derive

an extended expansion of the free energy that also includes the elastic energy needed to deform a lattice, i.e., to change the length of lattice vectors.

The free energy $\mathcal{F}$ is expanded with respect to small density variations $\delta\rho(\mathbf{r}) = \rho(\mathbf{r}) - \overline{\rho}$, where $\rho(\mathbf{r})$ is the density field in real space, e.g., of the mass density, and $\overline{\rho}$ is the average density:.

$$\begin{aligned}\mathcal{F} &= \int dA \Big\{ -V(\mathbf{r})\delta\rho(\mathbf{r}) + \frac{b'}{2}\left[\delta\rho(\mathbf{r})\right]^2 - \frac{c_1}{2}\left[\nabla\delta\rho(\mathbf{r})\right]^2 + \frac{c_2}{2}\left[\nabla^2\delta\rho(\mathbf{r})\right]^2 \\ &\quad -\frac{d}{6}\left[\delta\rho(\mathbf{r})\right]^3 + \frac{e}{24}\left[\delta\rho(\mathbf{r})\right]^4 \Big\}, \end{aligned} \tag{6.13}$$

As in section 5.1 the integration is over the whole plane and the signs are chosen such that with positive parameters b', c_1, c_2, d and e a phase transition into some stable ordered phase occurs if b' is sufficiently small. However, extending the free energy used in section 5.1, we now include a coupling $-V(\mathbf{r})\delta\rho(\mathbf{r})$ to the external potential $V(\mathbf{r})$ and in the second-order term we also take into account the first and second derivative of the density field. Using (6.10) for the external potential and the Fourier expansion for the density variation $\delta\rho(\mathbf{r}) = \sum_j \rho_j e^{-i\mathbf{G}_j\cdot\mathbf{r}}]$ where $\mathbf{G}_j$ denotes the relevant reciprocal lattice vectors, including $\mathbf{G}_\alpha$ and $\mathbf{G}_\beta$, the free energy (6.13) is transformed into its representation in reciprocal space:

$$\begin{aligned}\frac{\mathcal{F}}{A} &= -V_0\left(\rho_\alpha + \rho_\beta\right) + \sum_j \left(b' - c_1 G_j^2 + c_2 G_j^4\right)\left|\rho_j\right|^2 \\ &\quad -\frac{d}{6}\sum_{j,k,l}\rho_j\rho_k\rho_l\delta\left(\mathbf{G}_j + \mathbf{G}_k + \mathbf{G}_l\right) + \frac{e}{24}\sum_{j,k,l,m}\rho_j\rho_k\rho_l\rho_m\delta\left(\mathbf{G}_j + \mathbf{G}_k + \mathbf{G}_l + \mathbf{G}_m\right). \end{aligned} \tag{6.14}$$

In the second-order term, the prefactor of $|\rho_j|^2$ has a minimum for a certain wave number which we choose to be $G_j = G_0$ so that without external potential we find a phase transition into the triangular phase. Therefore, the second-order term is rewritten as

$$\sum_j \left(b' - c_1 G_j^2 + c_2 G_j^4\right)\left|\rho_j\right|^2 = \sum_j \left(b'' - c'\left[G_j^2 - G_0^2\right]^2\right)\left|\rho_j\right|^2, \tag{6.15}$$

with new positive parameters b'' and c'. Now, the free energy depends on six free parameters V_0, b'', c', d, e, and G_0. We rescale the free energy density $\mathcal{F}/A$, the order parameters ρ_j, and the lengths of the lattice vectors G_j such that only three free parameters V_L, b, and c remain

$$\begin{aligned}\frac{\tilde{\mathcal{F}}}{\tilde{A}} &= -V_L\left(\tilde{\rho}_\alpha + \tilde{\rho}_\beta\right) + \sum_j \left(b - c\left[\tilde{G}_j^2 - 1\right]^2\right)\left|\tilde{\rho}_j\right|^2 \\ &\quad -\frac{1}{6}\sum_{j,k,l}\tilde{\rho}_j\tilde{\rho}_k\tilde{\rho}_l\delta\left(\mathbf{G}_j + \mathbf{G}_k + \mathbf{G}_l\right) + \frac{1}{24}\sum_{j,k,l,m}\tilde{\rho}_j\tilde{\rho}_k\tilde{\rho}_l\tilde{\rho}_m\delta\left(\mathbf{G}_j + \mathbf{G}_k + \mathbf{G}_l + \mathbf{G}_m\right), \end{aligned} \tag{6.16}$$

where we termed the rescaled quantities $\tilde{\mathcal{F}}/\tilde{A}$, $\tilde{\rho}_j$, and $\tilde{G}_j$.

The parameter space is formed by the three parameters V_L, b, and c. Their meaning is explained in the following:

- V_L describes the strength of the potential.
- b is the main control parameter, responsible for the transition into an ordered phase for small values of b. It can be identified with the temperature, the inverse screening length κ, or the inverse density.
- c is a typical elastic constant that distinguishes soft systems with small c from rigid ones with large c. This can be seen in the second-order term in (6.16), where any deviation from the length G_0 of the ideal lattice vector of the triangular phase (rescaled to 1) is penalized by an increase of the free energy weighted with the factor c.

To calculate the free energy (6.16) for each of the lattices given by the lattice vectors in figure 6.5, we need to determine the combinations, where three or four lattice vectors add up to zero. In the following, trivial combinations such as $\mathbf{G}_0 - \mathbf{G}_0 + \mathbf{G}_1 - \mathbf{G}_1$ are not stated explicitly. For the pentagonal phase shown in figure 6.5(a) we find the following non-trivial relations:

$$\begin{aligned} \mathbf{G}_0 - \mathbf{G}_\alpha - \mathbf{G}_\beta &= 0, \\ \mathbf{G}_1 + \mathbf{G}_4 + \mathbf{G}_\beta &= 0, \\ \mathbf{G}_2 + \mathbf{G}_3 + \mathbf{G}_\alpha &= 0. \\ \mathbf{G}_0 - \mathbf{G}_\alpha + \mathbf{G}_1 + \mathbf{G}_4 &= 0. \\ \text{and } \mathbf{G}_0 - \mathbf{G}_\beta + \mathbf{G}_2 + \mathbf{G}_3 &= 0. \end{aligned} \tag{6.17}$$

For the triangular phase [see figure 6.5(b)], one finds

$$\begin{aligned} \mathbf{G}_0 + \mathbf{G}_1 + \mathbf{G}_2 &= 0, \\ \mathbf{G}_0 - \mathbf{G}_\alpha - \mathbf{G}_\beta &= 0, \\ \text{and } \mathbf{G}_1 + \mathbf{G}_2 + \mathbf{G}_\alpha + \mathbf{G}_\beta &= 0. \end{aligned} \tag{6.18}$$

For the rhombic-α phase shown in figure 6.5(c) we have only four reciprocal vectors ($\mathbf{G}_\alpha = \mathbf{G}_0$, $\mathbf{G}_1$, $\mathbf{G}_2$, and $\mathbf{G}_\beta$) and there is only the non-trivial relation

$$\mathbf{G}_\alpha + \mathbf{G}_1 + \mathbf{G}_2 = 0. \tag{6.19}$$

Correspondingly, in the rhombic-β phase [see figure 6.5(d)]

$$-\mathbf{G}_\beta + \mathbf{G}_1 + \mathbf{G}_2 = 0. \tag{6.20}$$

For the pentagonal ordering Das and Krishnamurthyn did not consider the non-trivial combinations of four lattice vectors that appear in the fourth and fifth line of (6.17). They also did not consider any rhombic phases. Therefore, they could predict a stable pentagonal phase [231], which we do not find.

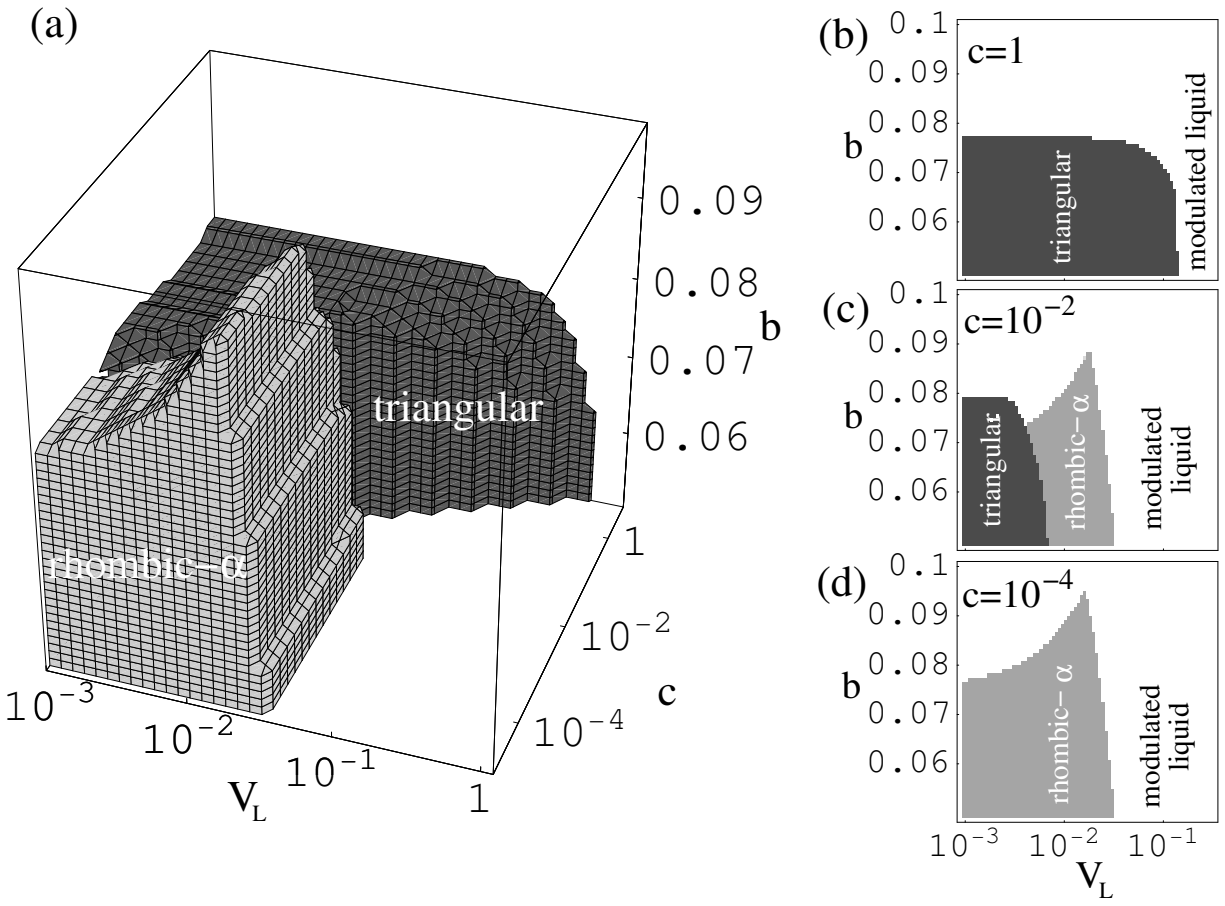

Figure 6.8: (a) Phase diagram showing the regions of stable triangular (dark gray) and rhombic-α (light gray) phase. In all other regions of the parameter space, a modulated liquid is found. (b)-(d) Phase diagrams for (b) rigid systems with $c = 1$, (c) intermediate crystals with $c = 10^{-2}$, and (d) soft systems with $c = 10^{-4}$.

By using (6.16) together with the relations (6.18) to (6.20), we can formulate the free energies for each of the four possible structures. At a given point V_L, b, c of the parameter space, we minimize the free energies with respect to the order parameters $\tilde{\rho}_j$. We assume that the system has the ordering of the structure with the smallest free energy, if all order parameters are non-zero. If at least one order parameter vanishes, we term the phase modulated liquid. Figure 6.8(a) shows the full phase diagram for the whole parameter space. Figures 6.8(b) to (d) present phase diagrams for constant values of the elastic constant c. For very rigid crystals (large c), we only find a triangular phase that can be melted by increasing b or the potential strength V_L. In contrast, in very soft systems triangular order only exists for very small strength $V_L < 10^{-5}$. For intermediate laser strength a rhombic-α phase is induced. This is even possible if the system is liquid without any external potential. The situation of intermediate elastic constants c, as shown in figure 6.8(c), is very close to the simulations (see figure 6.7). Though the predictions of

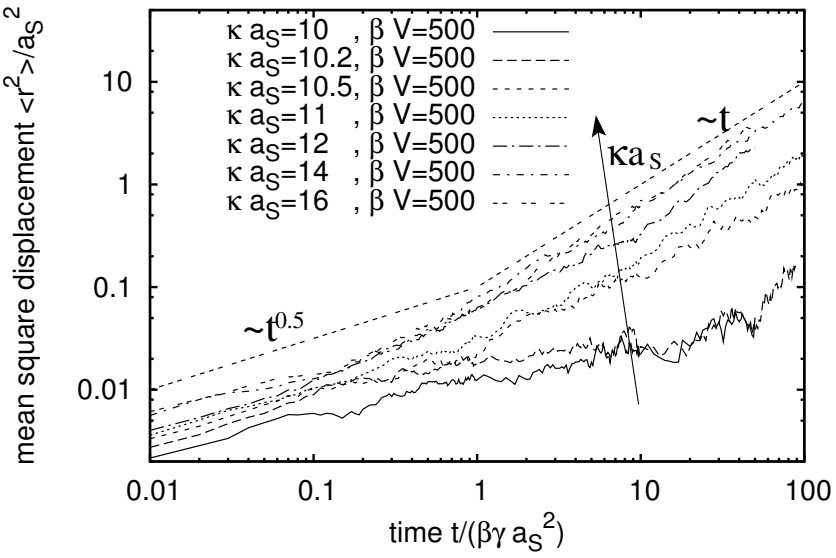

Figure 6.9: Time dependence of the mean square displacement.

a Landau-Alexander-McTague theory for large V_L are sometimes not reliable (see section 6.1.2), here even the phase behavior for large laser intensities is in good agreement with the simulations. Only the small region in figure 6.8(c) where the triangular phase first melts before it crystallizes into the rhombic-α phase by increasing V_L is not found in the simulations. In the next section we study the dynamics of the modulated liquid at large potential strength.

6.4 Dynamics: Non-periodic locked phase for large laser intensities

In systems with a commensurate potential $V_{ext}(x) = \cos(G_0 x)$, only crystals produced by light-induced freezing can melt at large laser intensities [229, 230] (see also section 6.1.4). In the one-dimensional quasicrystalline potential, light-induced melting is due to the quasiperiodicity of the potential, which enforces that for very high potential strengths the number of colloids is different in every potential well. Therefore, periodic ordering is not possible, i.e., by increasing the laser intensity all periodic crystalline structures can be destroyed in a quasicrystalline potential. In this section, we study the properties of the resulting non-periodic phase(s) at high potential strengths.

We perform Brownian dynamics simulations (see section 4.1 for details) of the colloids in strong laser fields ($\beta V_0 = 500$) and determine the mean square displacement. We consider systems with only 195 particle but averaged over 20 independent runs, i.e., for each run we first use one million Monte-Carlo steps to find an equilibrium configuration and then

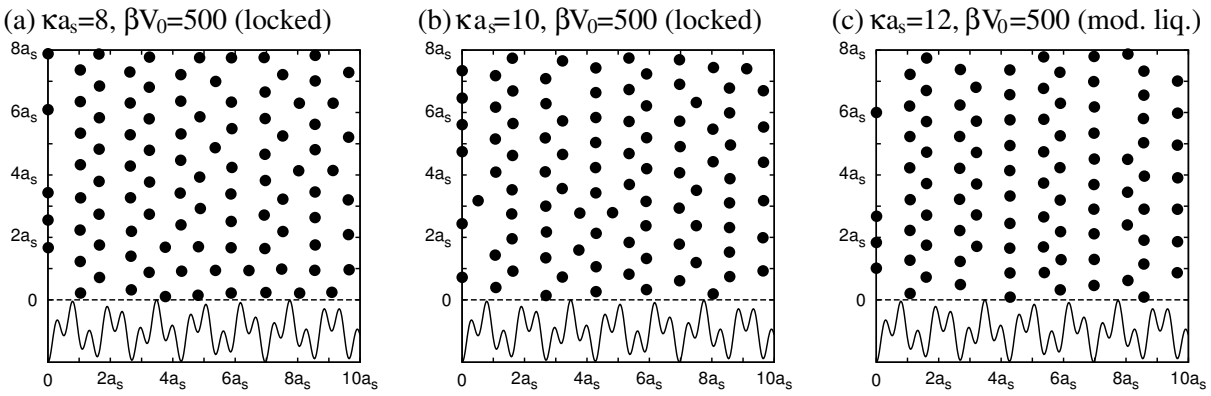

Figure 6.10: Snapshots of simulations with the 1D quasicrystalline laser field for large potential strengths. The potential is shown in the lower parts of the figures.

started the Brownian dynamics simulations. The mean square displacement is determined according to

$$\left\langle r^2(t)\right\rangle = \left\langle |\mathbf{r}(t) - \mathbf{r}(0) - \langle \mathbf{r}(t) - \mathbf{r}(0)\rangle|^2 \right\rangle , \tag{6.21}$$

i.e., $\langle r^2(t)\rangle$ is corrected by movements of the center of mass and therefore the random motion of the whole system does not affect the results. In figure 6.9 the time dependence of the mean square displacement is shown. There is a crossover from subdiffusion $\langle r^2\rangle \propto t^{0.5}$ on short time scales (reminiscent to single-file diffusion) to normal diffusion $\langle r^2\rangle \propto t$ in the asymptotic long time limit. Single-file diffusion usually occurs for particles, which are confined in a one-dimensional channel and cannot pass each other (see e.g. [51–53,233,234]). In our system we observe a similar diffusion process on time scales, where colloids in neighboring walls do not pass each other. For very small inverse screening lengths κa_S, a crossover into the regime of normal diffusion is not observed, i.e., for small κa_S the colloids do not pass particles in neighboring wells even on long time scales. Hence, there is a transition into a dynamically locked state. The transition takes place between $\kappa a_S = 10.2$ and $\kappa a_S = 10.3$. However, there are no differences visible in snapshots of the modulated liquid and the locked phase (see figure 6.10). In the locked phase the number of colloids within a certain potential well is the same as in the modulated liquid phase. No periodic ordering along the wells is possible and the locked phase cannot be crystalline. Perhaps there is some quasicrystalline order along the wells. However, all differences we have found so far between the modulated liquid and the locked phase concern their dynamics.

To further study the transition from the modulated liquid into the non-periodic locked phase, we considered the mean square distance of colloids that were nearest neighbors at time $t = 0$, i.e.,

$$\left\langle r^2_{\mathrm{NN}}(t)\right\rangle = \left\langle \frac{1}{N}\sum_j \frac{1}{n_{\mathrm{NN}}} \sum_{k\in \mathrm{NN}_j(t=0)} |\mathbf{r_j}(t) - \mathbf{r_k}(t)|^2 \right\rangle . \tag{6.22}$$

Note that $\langle r^2_{\mathrm{NN}}(t)\rangle$ is similar to the modified Lindemann parameter [215, 235, 236]: In the

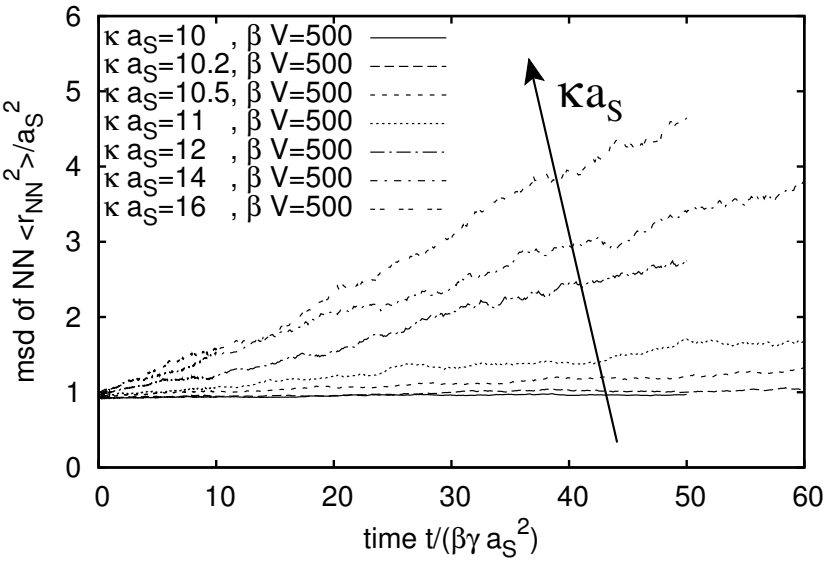

Figure 6.11: Time dependence of the mean square distance of colloids that were nearest neighbors at time $t = 0$.

modified Lindemann parameter usually the mean distance between nearest neighbors is subtracted before the distance is squared. Such a substraction does not make sense in our system because the nearest neighbor distance is not even close to the mean distance.

In figure 6.11 the time dependence of the mean square distance is shown. In the modulated liquid it grows linearly in time, whereas in the locked phase it stays almost constant, i.e., nearest neighbors remain nearest neighbors. By linear fits we determined the effective diffusion constant D_{NN} as defined in $\langle r_{\mathrm{NN}}^2 \rangle = 4 D_{\mathrm{NN}} t$. We plot D_{NN} as a function of the inverse screening length κa_s in figure 6.12. Obviously, the effective diffusion constant is useful as an order parameter to indicate the transition from the modulated liquid to the locked phase. It is zero in the locked phase and non-zero in the modulated liquid. This is different from usual order parameters, which are zero in the disordered phase and non-zero in the low-symmetry phase. Therefore, D_{NN} can also be seen as a disorder parameter. At the transition, D_{NN} is continuous in κa_S.

Since the phase transition in our system is described by its dynamical properties, it might resemble the glass transition. However, in our case the locked phase is a real equilibrium phase, whereas in a non-ergodic glass the glassy phase is approached dynamically by fast cooling to prevent crystallization. Most glasses are characterized as non-ergodic systems, i.e., not all possible micro states are approached by the temporal evolution of the system. A Monte-Carlo simulation would relax such a glassy system to the equilibrium state, which usually corresponds to a crystalline state and not to a glassy state. In our system it is possible to find the locked state by Monte Carlo simulations. Therefore, the colloids in a quasicrystalline potential are closer to a geometrical frustrated system, i.e., a

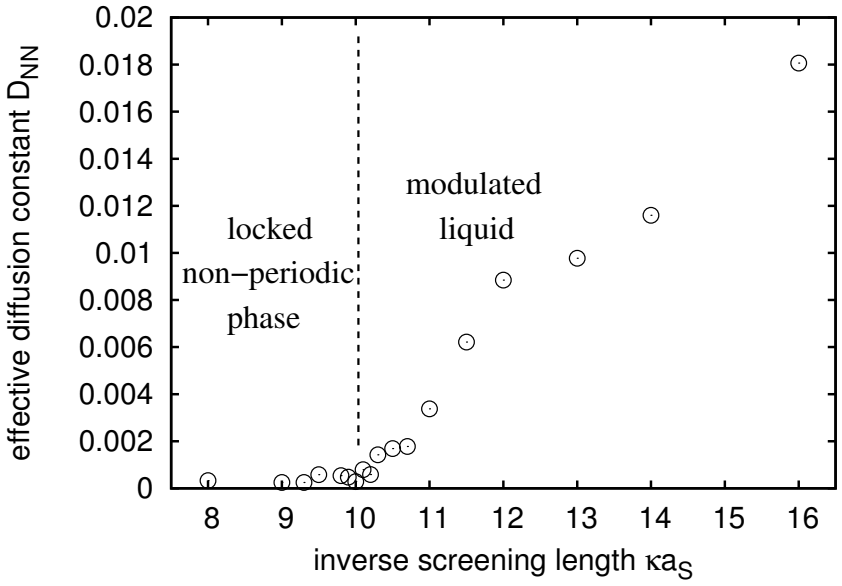

Figure 6.12: Effective diffusion constant D_{NN} as a function of the inverse screening length κa_s; D_{NN} is defined by $\langle r^2_{\mathrm{NN}} \rangle = 4 D_{\mathrm{NN}} t$ where $\langle r^2_{\mathrm{NN}} \rangle$ is the mean square distance of nearest neighbors [cf. equation (6.22)].

system that cannot crystallize for pure geometric reasons. A classical example of a frustrated system is a two-dimensional spin model of an antiferromagnet, where the spins sit on a two-dimensional triangular lattice and energetically prefer to be antiparallel to neighboring spins [237]. Since this is impossible, the system is prevented from crystallisation and stays in a disordered state known as quenched disorder. Such a system is also called spin glass, though it is ergodic. Another example of frustration is a fluid of hard disks that is prevented from crystallization by curvature of the plane [238]. In systems with quenched disorder the ground state is usually degenerated, i.e., there are many disordered states with the same energy. In our case crystallization is prevented by the irrational ratio of the occupation numbers of neighboring potential wells with colloids and therefore a frustrated state is reached. So far we cannot exclude that some quasicrystalline order exists in y-direction. If there is such a quasicrystalline ground state, its realizations for different phasonic displacements possibly correspond to the degenerated ground states of a system with quenched disorder. We may not have found any quasicrystalline ground state so far because the free energy of some disordered states is only slightly higher than the ground-state energy. A way to improve the simulations in order to identify possible quasicrystalline order is proposed in section 6.7.

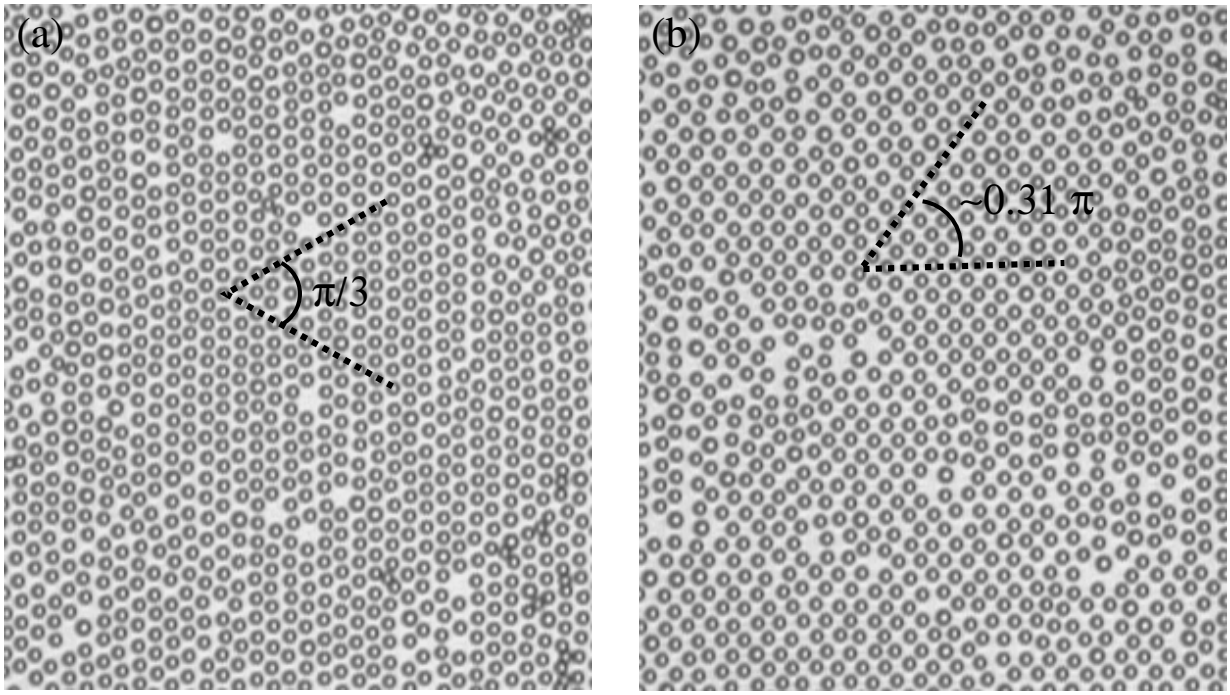

Figure 6.13: Micrographs of an aqueous colloidal suspension of charged polystyrene spheres (with diameter 2.4 μm on a 1D quasicrystalline substrate created with interfering laser beams. The colloids form (a) a triangular lattice for small laser intensities and (b) a rhombic-α-phase for higher potential strength. The two phases can be distinguished by measuring the angles as shown in the figures (see also section 6.3.1). Experiment and micrographs by J. Baumgartl [239].

6.5 Experimental results

Some results of the simulations and the theory were verified experimentally by J. Baumgartl [239], e.g., a transition from a triangular phase for small potential strength [see figure 6.13(a)] towards a rhombic-α-phase for higher laser intensities [see figure 6.13(b)] was found. However, the non-periodic locked phase for very large potential strengths described in the last subsection has not been observed yet in experiments since the rhombic-α phase is kinetically stabilized against the modulated liquid by large potential barriers.

6.6 Other quasicrystalline potentials

We also used other quasicrystalline potentials for the simulations. For example, a potential with wells of equal depth and distances corresponding to the Fibonacci chain (see section 3.2). In another potential, the wave vectors of the modulation fit to the y-projection of the decagonal lattice vectors shown in figure 3.5. For all potentials we tried, we did not find any stable two-dimensional quasicrystalline ordering. Usually for intermediate strengths of the potential, the colloids order in a rhombic way and only one possible length

scale of the potential is represented in the ordering, all other length scales are ignored. For large potential strengths, the periodic phases melt into a modulated liquid. From the results of subsection 6.4 we expect that the phase for large laser intensities is also a locked, frustrated phase without any periodicity. This is different for periodic potentials, where rhombic phases are also observed (see section 6.1 or [240] as an example for a non-commensurate potential). However, these are even stable for very large potential strengths since there frustration does not occur.

6.7 Summary and Outlook

We studied a two-dimensional colloidal system in a one-dimensional quasicrystalline potential obtained by the superposition of two modulations characterized by the wave vectors $\tau G_0 \mathbf{e}_x$ and $(-1/\tau G_0)\mathbf{e}_x$, where τ is the number of the golden ratio (see section 3.2) and G_0 is related to the nearest neighbor distance a_S in a triangular crystal via $a_S = 2\pi/G_0$. We determined the phase diagram by using Monte-Carlo simulations and by applying the Landau-Alexander-McTague theory. We found a triangular to liquid phase transition for weak potentials. For intermediate laser intensities the system is in a rhombic phase, i.e., the colloids lock to the modulation given by $\tau G_0 \mathbf{e}_x$ and ignore the other one. For large potential strengths the colloids can only move in the potential wells. Due to the varying depths of the wells, the numbers of colloids occupying the wells are different. Usually the ratio of these numbers for neighboring wells is irrational and therefore periodic ordering along the well direction is not possible. Using Brownian dynamics simulations, we found a transition from a modulated liquid at large inverse screening lengths κ into a locked phase at small κ. In the locked phase the colloids of neighboring wells no longer pass by each other and system is frustrated since periodic order is impossible.

The Brownian dynamics simulations of the modulated liquid and the locked phase are performed for a two-dimensional system. Because fluctuations out of the well minimum can be neglected for large strengths of the potential, a simpler model using particles that can only move on lines is sufficient to describe the properties at large laser intensities. Such a simplified model should be used in future works. It has the advantage that simulations are much faster and therefore the system size can be increased to prevent possible finite-size effects. In addition the statistics is easily improved, which allows to study the behavior close to the phase transition in more detail. Furthermore, very long simulation runs may help to reveal any possible quasicrystalline ordering along the wells.

The potential strengths needed to obtain the locked non-periodic phase are usually to large for experiments. However, a frustrated locked state can also be achieved in any line potential (even a periodic one) if the line potential is strong enough to prevent colloids to jump from one line to the other. A non-periodic phase is realized by placing colloids into the wells in a way that the ratio of the numbers of colloids in neighboring wells is irrational. Note the resulting locked non-periodic phase is not an equilibrium phase then, however it is close to the theoretical equilibrium phase obtained in very strong quasicrystalline laser fields.

Chapter 7

Colloidal ordering in a decagonal potential

In this chapter we study the ordering of colloidal particles in the decagonal potential. In section 7.1 we present phase diagrams determined by Monte Carlo simulations and discuss the observed phases with ten-fold, twenty-fold, and without bond orientational order and a phase reminiscent to an Archimedean tiling. We compare our findings to experimental results in section 7.2 and study the effect of phasonic displacements, drifts, and distortions in section 7.3. Finally we conclude in section 7.4. Reference [D] is based on some parts of this chapter.

7.1 Phase behavior

We usually characterize the phases with the bond orientational order parameter which we introduce in subsection 7.1.1. In the following, the density is qualified by the particle spacing a_S of the ideal triangular lattice. At a density corresponding to a particle spacing of $a_S = 0.7a_V$, the colloids exactly occupy all local minima of the decagonal potential. We use this density to distinguish between the low-density case ($a_S > 0.7a_V$), which we study in subsections 7.1.2 and 7.1.3, and the high-density case ($a_S < 0.7a_V$) investigated in subsections 7.1.4 and 7.1.5. The parameters for the simulations were given in section 4.4. They are chosen such that for zero potential the phase transition from the solid triangular to the liquid phase is observed in both the low and the high density cases. Finally, in subsection 7.1.6 we determine pair correlation functions to get a deeper insight to the phase behavior.

7.1.1 Bond orientational order parameter

A translational order parameter (like the one used in section 6.3) is not as suitable as an order parameter that measures the orientational symmetry. Here we use the bond

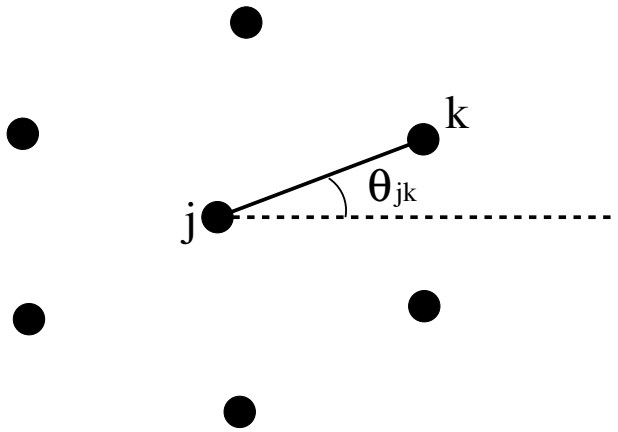

Figure 7.1: The bond orientational order parameter uses the directions of bonds between nearest neighbors. A detailed explanation is given in the text.

orientational order parameter

$$\psi_m = \left\langle \left| \frac{1}{N} \sum_{j=1}^{N} \frac{1}{n_j} \sum_{k=1}^{n_j} e^{im\theta_{jk}} \right| \right\rangle , \tag{7.1}$$

where the inner sum is over all n_j nearest neighbors of colloid j, N is the total number of particles, and θ_{jk} is the angle of the bond connecting colloids j and k given with respect to some arbitrary reference direction (see figure 7.1). The ensemble average in equation (7.1) is calculated over 1000 configurations taken every 100 steps as described in detail in section 4.2. We are particularly interested in bond orientational order with $m = 6$, 10, or 20, which characterizes phases with nearest neighbor bonds that point, respectively, along 6, 10, or 20 equally distributed directions around the central colloid. In the phase diagrams a m-fold bond order is assigned to the phases if $\psi_m > 0.1$. In particular, we call phases with $\psi_6 > 0.1$ triangular including structures where only domains of triangles occur with the same orientation. The order parameter ψ_m in equation (7.1) is defined such that ψ_m becomes non-zero if within one configuration the number of bonds in m equally distributed directions exceeds the number of bonds in other directions. In another direction these m directions may be different meaning that the configuration is rotated as a whole. However, if within one configuration two or more domains exist with different preferred directions, then ψ_m vanishes. Therefore, a phase possesses a m-fold bond orientational order only if a long-range orientational order exists throughout the colloidal configuration. We also checked that the choice of the threshold value 0.1 hardly affects the phase boundaries.

Before we analyze the Monte-Carlo simulations, we calculate the order parameters ψ_{10} and ψ_{20} for ideal colloidal patterns created by placing particles directly at the positions of local potential minima: First we determine all local minima in a certain region (cf. section 3.3.3) and then fill them by first placing a particle in the deepest one. We proceed by placing further colloids in the deepest unoccupied minima until the requested density is

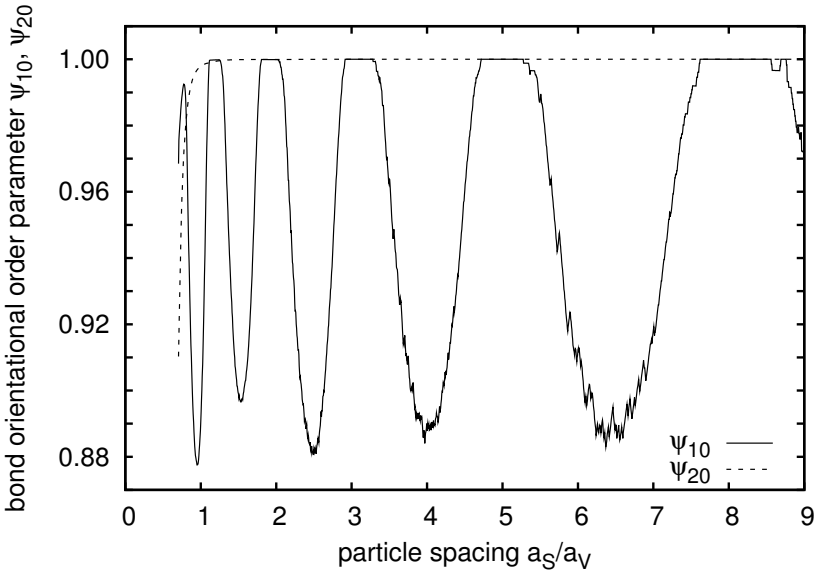

Figure 7.2: Order parameters ψ_{10} and ψ_{20} for a pattern of colloids constructed by placing them at the positions of the deepest minima up to a density corresponding to a triangular lattice with particle spacing a_S.

reached. Figure 7.2 shows the order parameters ψ_{10} and ψ_{20} as a function of the colloidal density given by the particle spacing a_S of an ideal triangular lattice. The curve starts at $a_S \approx 0.7a_V$, where all local minima are occupied. Obviously, the value of ψ_{10} strongly depends on the density whereas ψ_{20} is almost constant. For most densities $\psi_{20} > \psi_{10}$, i.e., the potential allows 20 bond directions however 10 of them are preferred. The positions of neighboring maxima in ψ_{10} are related to each other by a factor equal to the number of the golden ratio $\tau = (1 + \sqrt{5})/2$, which reveals some self-similar properties.

7.1.2 Low-density case

Figure 7.3 shows the phase diagram for the low-density case in the parameter space given by the particle spacing a_S versus potential strength V_0. For weak potential strengths, i.e., when the colloidal interactions dominate the phase behavior, a phase transition from the triangular ($\psi_6 > 0.1$) to the liquid ($\psi_m \approx 0$ for all m) phase is observed. On the other hand, at sufficiently large V_0 a decagonal quasicrystalline phase with ten preferred bond directions ($\psi_{10} > 0.1$) is favored by the decagonal potential. The interesting phases occur for intermediate potential strengths, where a quasicrystalline phase with twenty bond directions is found, i.e., where $\psi_{20} > 0.1$ but $\psi_{10} \approx 0$. It is bounded by the solid and dashed lines. We will study it in more detail in the next subsection. The dotted line indicates the border of a triangular-quasicrystalline coexistence region, where we find that both the triangular and the quasicrystalline order parameters are non-zero.

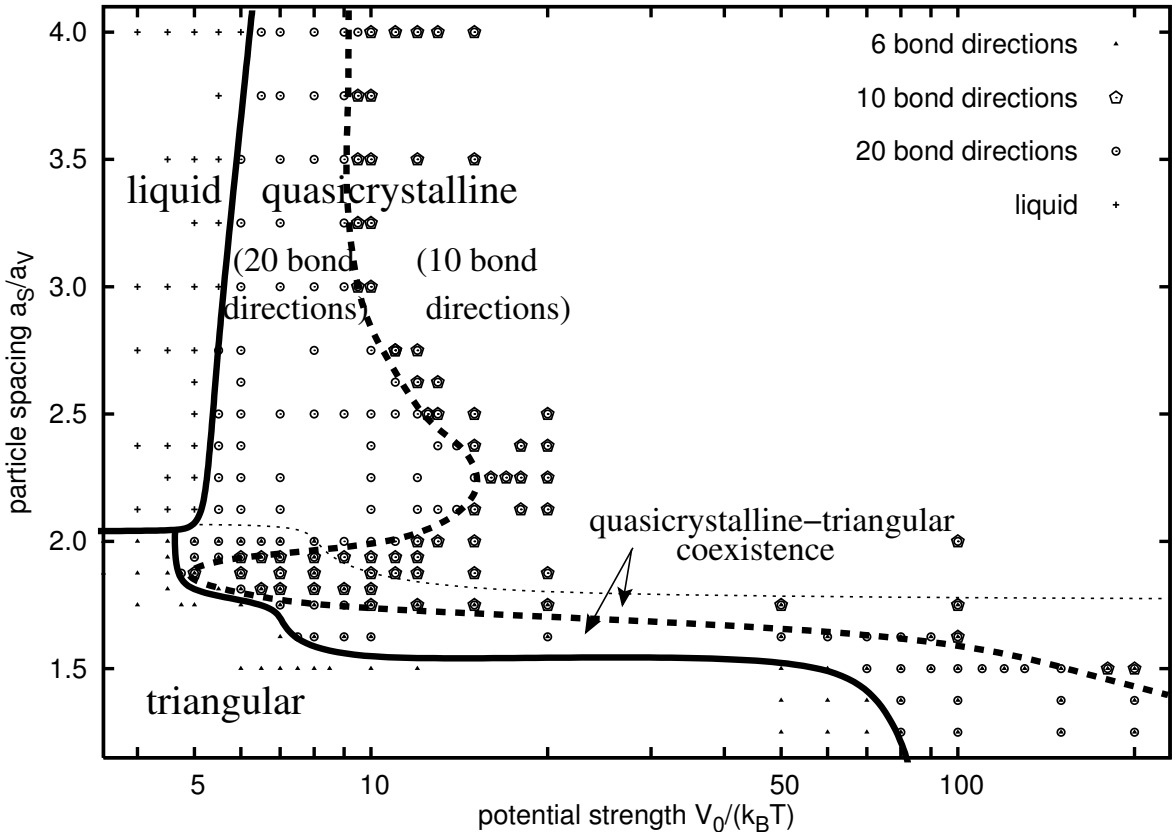

Figure 7.3: Phase diagram for low colloidal densities as a function of the potential strength V_0 (in units of the thermal energy k_BT) and the particle spacing a_S (in units of $a_V = 2\pi/|\mathbf{G}_j|$) in the ideal triangular lattice. The symbols denote the order parameters that are larger than 0.1. If all order parameters are close to zero a small cross is plotted. The phase boundaries are drawn as guide to the eye. Note there is a coexistence region, where ψ_6 and ψ_{20} or ψ_{10} are larger than 0.1. A detailed description is given in the text.

7.1.3 Phases with ten or twenty bond directions

To understand the occurrence of the intermediate phase with 20 bond directions in figure 7.3, we draw possible bond directions in the representation of the decagonal potential (see figure 7.4). The full lines indicate 10 directions where predominantly deep minima are found. They are occupied for large potential strengths and, therefore, the phase with 10 bond directions is stable. If the potential strength is decreased, the colloidal interactions become more important and some particles are pushed to more shallow minima situated along the dashed lines in figure 7.4 in order to increase the interparticle distance. When the colloids occupy all 20 bond directions uniformly, ψ_{10} vanishes and $\psi_{20} > 0.1$ indicates the 20-fold bond orientational order.

Figure 7.5 shows snapshots of the two quasicrystalline phases. In (b), where 10-fold bond order exists, one can identify lines formed by the particles and oriented along the 10

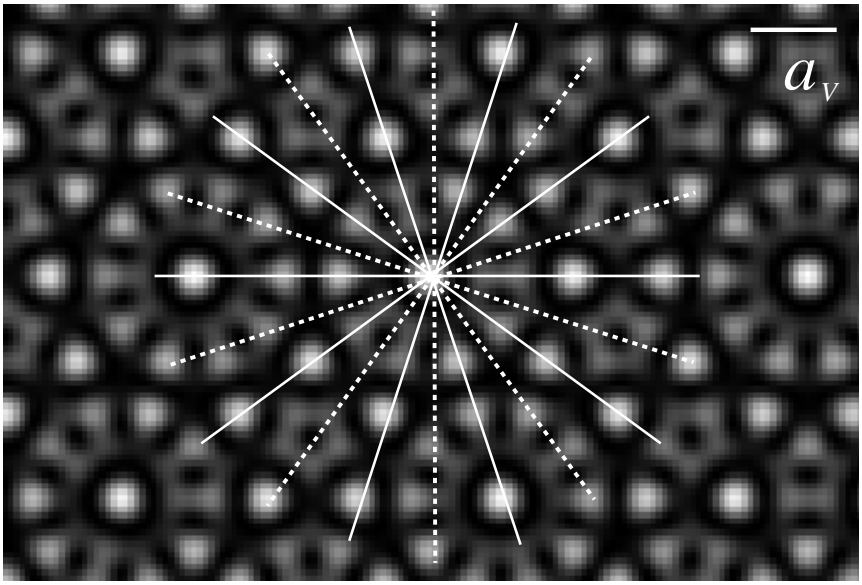

Figure 7.4: Bond directions in the decagonal potential. If only the deepest minima are considered, 10 bond directions exist (solid lines). If also more shallow minima are included, 20 bond directions are possible (solid and dotted lines).

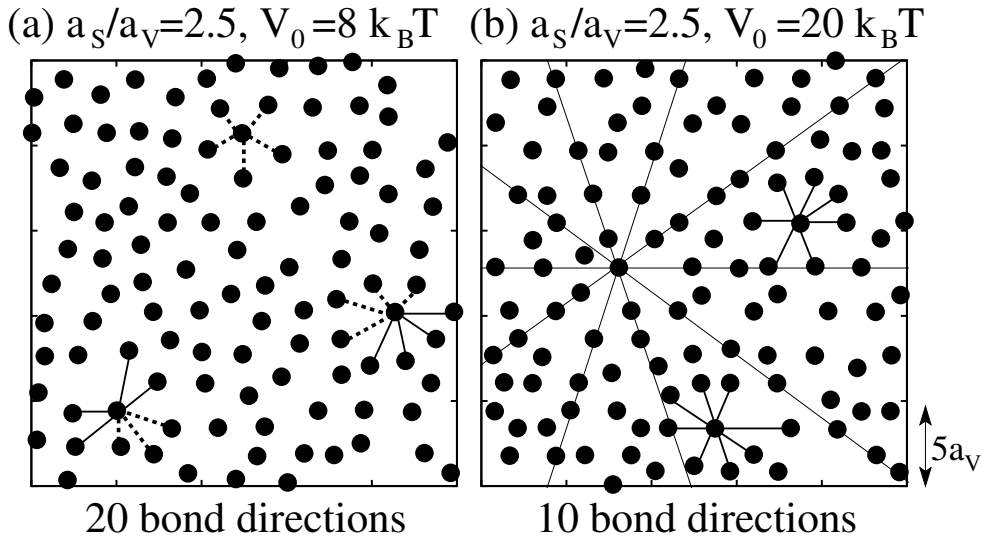

Figure 7.5: Snapshots for particle positions for the two quasicrystalline phases with (a) 20 and (b) 10 bond directions. Examples for the bonds are given. In (a) the dashed lines indicate the additional bond directions of ψ_{20}. In (b) lines formed by particles are visible.

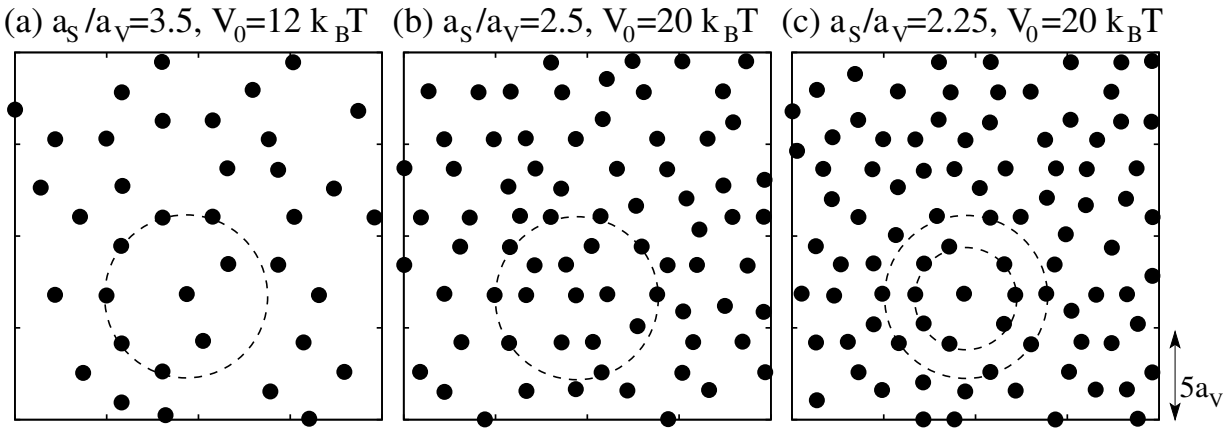

Figure 7.6: Snapshots of particle positions of the phase with ten bond directions for different densities.

bond directions. Examples of these directions are given. In (a) additional bond directions for the 20-fold bond order are indicated. However, clear lines occupied by the particles are hard to recognize. Note that even the snapshots of the phase with 10 bond directions look different depending on its density. At certain densities [see e.g. figure 7.6(a) and (c)], circles of particles can be drawn around a center colloid. These are the densities, where the ψ_{10} order parameter plotted in figure 7.2 is close to one. For other densities [see, e.g., figure 7.6(b)], several colloids besides the center particle are located inside the circle. However, there are not enough colloids to form a new, smaller circle.

7.1.4 High-density case

Figure 7.7 shows the phase diagram for large colloidal densities. The phase behavior for small and high potential strength is similar to the low-density case described in subsection 7.1.2, i.e., there is a triangular to liquid transition for small and a decagonal phase for large laser intensities.

However, the intermediate phase does not display any bond orientational order. We checked that $\psi_m \approx 0$ for $m = 6$, 10, 12, 15, 20, and 30. The occurrence of such a phase without any apparent bond orientational order can be understood as follows: All the minima of the decagonal potential are occupied by particles and an excess of colloids has to fill the space between the minima. This precludes any 20-fold bond orientational order. From the theory of melting on incommensurate substrates [24, 25] (see also section 5.3), one would at least expect an intermediate phase with thirty bond directions where the six triangular directions lock into the ten preferred directions of the potential. However, from the simulations we find that ψ_{30} is close to zero in all points of the intermediate phase, probably because very small displacements, caused by interactions with other particles and with the substrate, can easily destroy any detectable 30-fold bond order. We also performed Monte-Carlo simulations where within one million Monte Carlo steps we slowly decreased the temperature to zero. In the intermediate regime, the resulting patterns usually did not

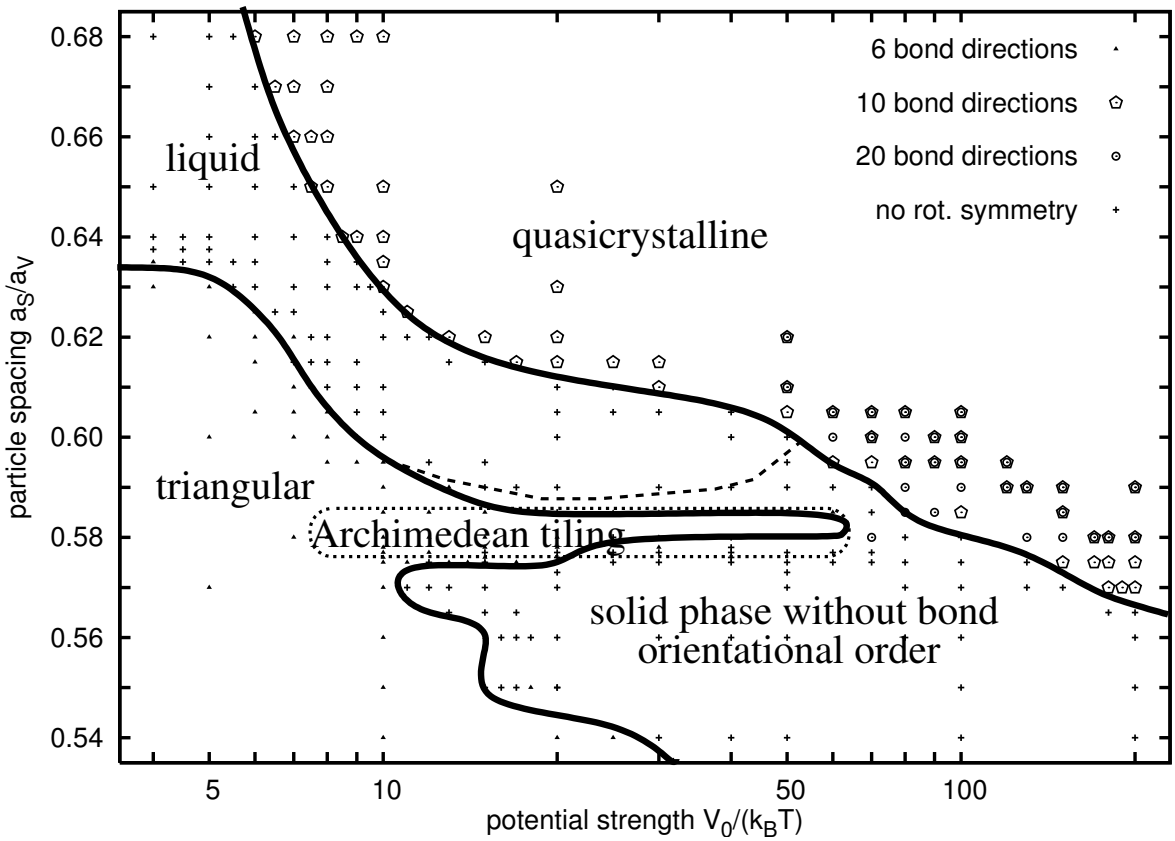

Figure 7.7: Phase diagram for large colloidal densities as a function of the potential strength V_0 (in units of the thermal energy k_BT) and the particle spacing a_S (in units of $a_V = 2\pi/|\mathbf{G}_j|$) in the ideal triangular lattice. The symbols denote the order parameters that are larger than 0.1. If all order parameters are close to zero a small cross is plotted. The phase boundaries are drawn as guide to the eye. The dotted elliptical line marks the region where Archimedean-like tilings are found (see subsection 7.1.5). The dashed transition line was determined by Brownian dynamics simulations. A detailed description is given in the text.

reveal any bond orientational order. Therefore, it is not just due to thermal fluctuations that prevent any bond orientational symmetry. The potential itself does not seem to allow any orientational order.

In addition, the disordered phase seems to change from a liquid to a solid with increasing density. We tried to determine this phase transition by calculating the mean square displacement of the colloids using Brownian dynamics simulations (see figure 7.8). The differences in the time dependence of the mean square displacement are not as pronounced as for the phase transition from the modulated liquid into the locked non-periodic phase described in section 6.4. The asymptotic regime was not yet reached within our Brownian dynamics simulations and we have not found any obvious phase transition so far. Only within the phase with Archimedean-like tiling (see also section 7.1.5) for $a_S/a_V \approx 0.8$, the mean square displacement stays very small, indicating that the colloids are firmly bound to

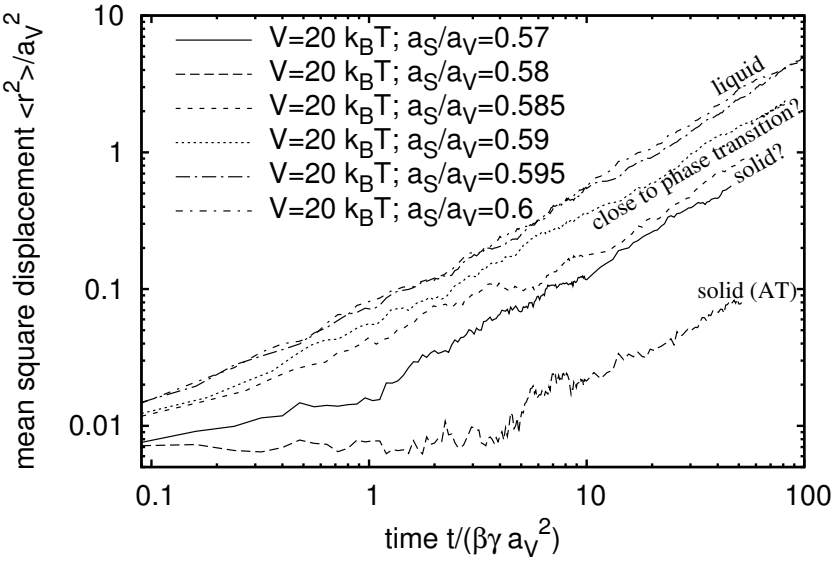

Figure 7.8: Mean square displacement calculated by Brownian dynamics simulations (as described in section 4.1) for systems in the phase with no bond orientational order. There seems to be a phase transition, perhaps between a solid and a liquid state. The Archimedean-like tiling (see also section 7.1.5) for $a_S/a_V = 0.8$ is an extraordinary stable phase.

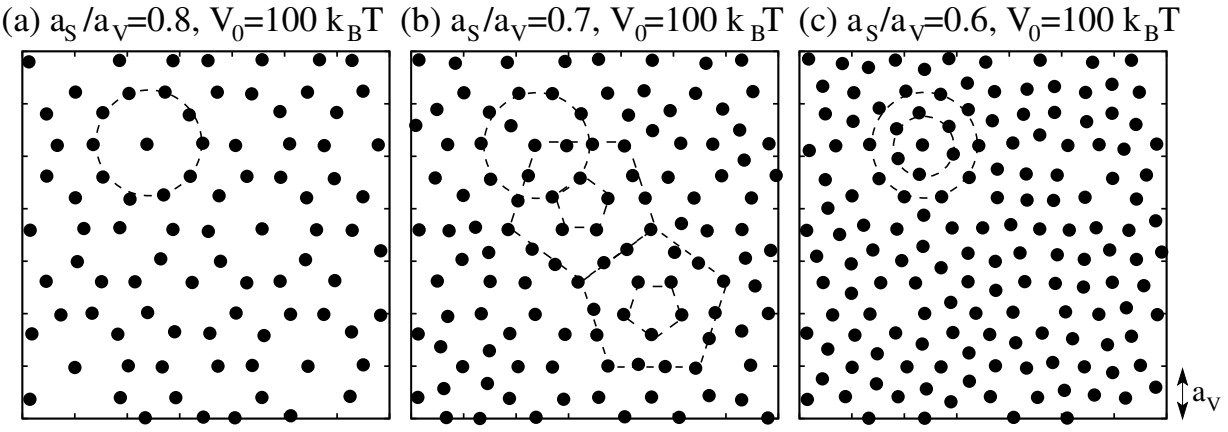

Figure 7.9: Snapshots for particle positions of the phase with ten bond directions for different densities. Note, the density in figure (b) corresponds to one particle per minimum. In (a) there are less colloids than minima, in (c) there are more.

the lattice positions of the Archimedean-like structure. For other densities, the curves for $\beta V_0 = 20$ shown in figure 7.8 as well as corresponding curves for other potential strengths seem to group: For low densities, the colloidal motion is diffusive corresponding to the dynamics of a liquid. For larger densities (below the dashed line in figure 7.7), the mean square displacement increases much slower. Perhaps this is due to a solid phase where the particles can diffuse within a region that is large compared to the area around a minimum. For example, colloids can move on circular trajectories in the regions of the shallow wells that form rings around the very deep minima. Another possibility is, that some particles are pinned to the potential while others can float around them. Therefore, the transition that we mark as liquid to solid transition can also be a transition between different solid or liquid phases. Studying the dynamics in more detail and extending the Brownian dynamics simulations to much longer times will be important for future works.

Finally, we want to comment on our observation, that snapshots of the phase with ten bond direction sometimes appear very different depending on the density (see also figure 7.6 in subsection 7.1.3). For the density of the colloidal patterns shown in figure 7.9(a) and (c) almost complete circles formed by particles exist whereas in figure 7.9(b) the most striking structures are pentagons. The circles correspond to circles [figure 7.9(a)] or double circles [figure 7.9(c)] of potential wells around a very deep minimum (cf. section 3.3.2). Colloids of a partially filled inner circle [as in figure 7.9(b)] are usually placed in a way that they are located on the edge of large pentagons. Therefore the pentagons are extraordinary conspicuous for densities with partially filled circles.

7.1.5 Archimedean tiling

At densities with particle spacing a_S/a_V around 0.58 the triangular ordering reaches deep into the region where bond-orientational order is not expected (see figure 7.7). As we demonstrate in this section, the extraordinary stability is due to a very special structure.

In figure 7.10 we show the Delaunay triangulation of the colloidal patterns for some of the simulation results. For better visibility, all bonds that are longer than $1.1a_S$ are not shown. Interestingly, in figures 7.10(c) to (f) domains of a highly ordered structure are visible. This structure corresponds to an Archimedean tiling of type $(3^3.2^2)$ [see figure 7.11(a)] and consists of rows of squares and triangles. Sometimes there are also two rows of triangles enclosed by the rows of squares [see figure 7.11(b)]. Archimedean tilings are interesting complex structures which can also be found on periodic substrates [241, 242, C]. They are composed of regular polygons and characterized by the number and type of polygons that are grouped around one node [143]. For example, in an Archimedean tiling of type $(3^3.2^2)$ one finds three triangles and two squares when going around a vertex [see arrow in figure 7.11(a)]. On the decagonal substrate the square rows of the Archimedean tiling of type $(3^3.2^2)$ or its modified version with double triangular rows can appear with five different orientations corresponding to the directions of the lines of low intensities in the laser fields. Usually a domain with one specific orientation is quiet small and within one colloidal configuration domains of two or three different orientations coexist.

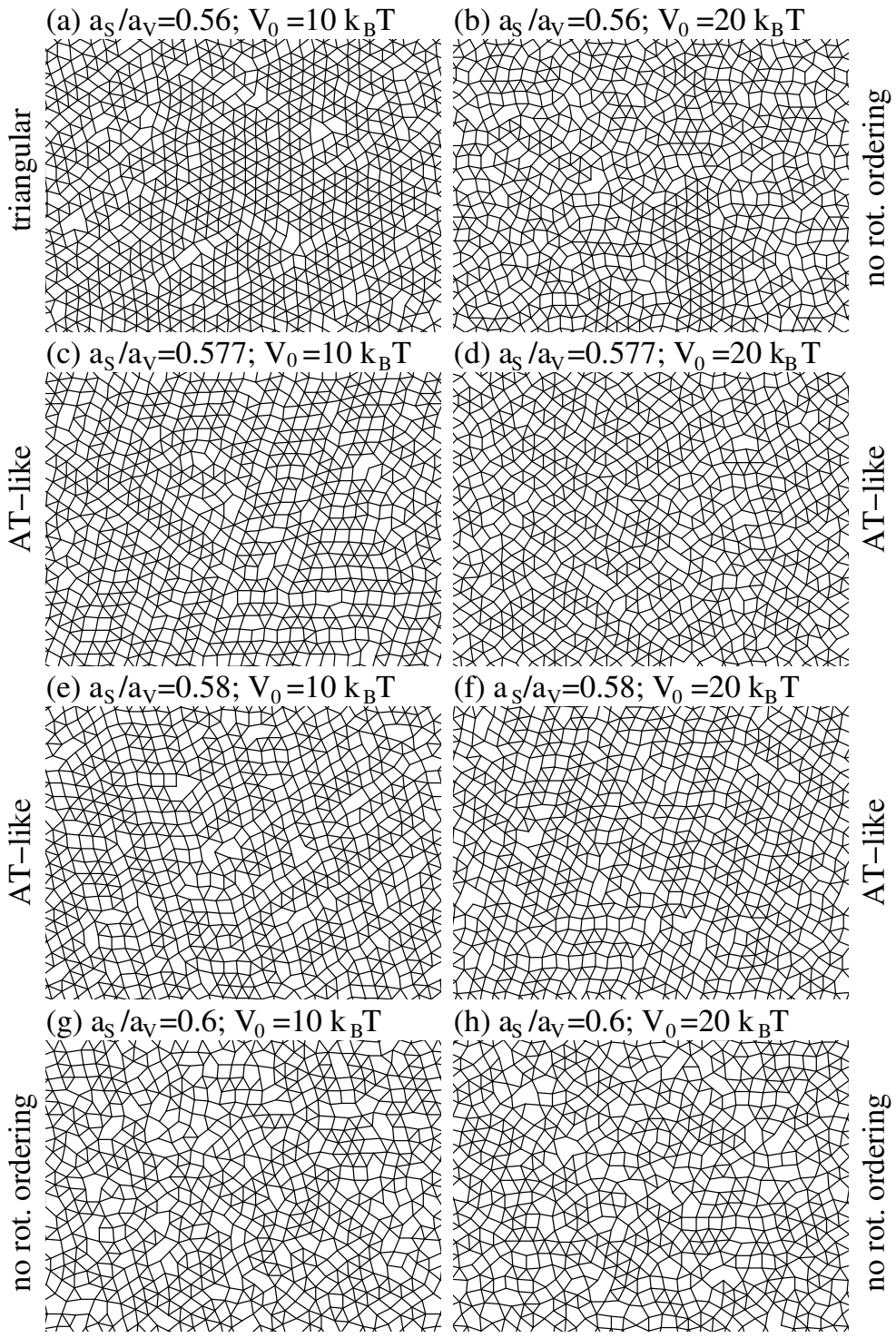

Figure 7.10: Delaunay triangulation of colloidal patterns obtained by Monte-Carlo simulations. Bonds that are longer than $1.1a_S$ are not shown. A detailed description of the observed phases is given in the text.

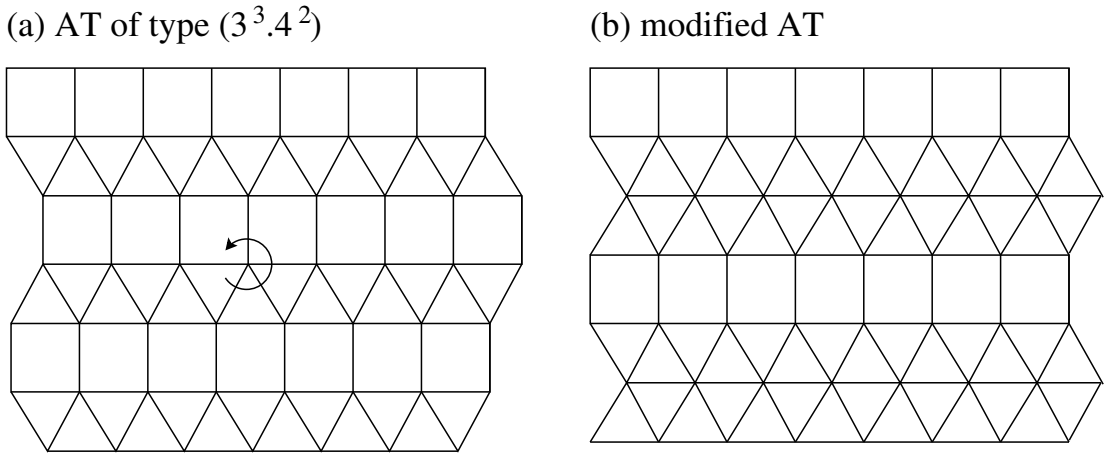

Figure 7.11: (a) Archimedean tiling (AT) of type $(3^3.2^2)$ and (b) modified AT with double rows of triangles. The Archimedean-like tiling observed in our simulations is a combination of these structures (see figure 7.12).

For the Archimedean-like tiling the distances between the square rows behave as in a Fibonacci chain, i.e., short distances corresponding to a single row of triangles and long distances due to a double row of triangles are ordered in the same way as the short and long distances in a Fibonacci chain (see figure 7.12).

Archimedean-like tilings for colloids in decagonal laser fields were first observed in experiments by Mikhael *et. al.* [191] (see also section 7.2). Structures found by Ledieu *et. al.* [11] for Cu atoms on the surface of the icosahedral quasicrystal $Al_{70}Pd_{21}Mn_9$ may correspond to such tilings.

By analyzing the Delaunay triangulations of colloidal snapshots, we find the Archimedean-like tiling in a very small density range with $0.577 \leq a_S/a_V \leq 0.585$ which is framed by a dotted line in figure 7.7. Triangles dominate these structures and therefore usually $\psi_6 > 0.1$.

In the following, we calculate the density (or a_S/a_V) where an Archimedean-like tiling is expected to fit best in the decagonal potential. The orientations of the rows of the Archimedean-like tiling correspond to the directions of the lines of low intensities in the decagonal laser fields. As described in section 3.4.3, an average of the decagonal potential over these directions leads to an one-dimensional potential that is the sum of two modulations [cf. equation (3.34)]. The wavelengths of these modulations are

$$\begin{aligned} \lambda_1 = \frac{2\pi}{k_1} &= \sqrt{\frac{5+\sqrt{5}}{10}} a_V \approx 0.851 a_V \\ \text{and } \lambda_2 = \frac{2\pi}{k_2} &= \sqrt{\frac{5-\sqrt{5}}{10}} a_V = \frac{\lambda_1}{\tau} \approx 0.526 a_V, \end{aligned} \tag{7.2}$$

where τ is the number of the golden ratio. The positions of the minima of the averaged

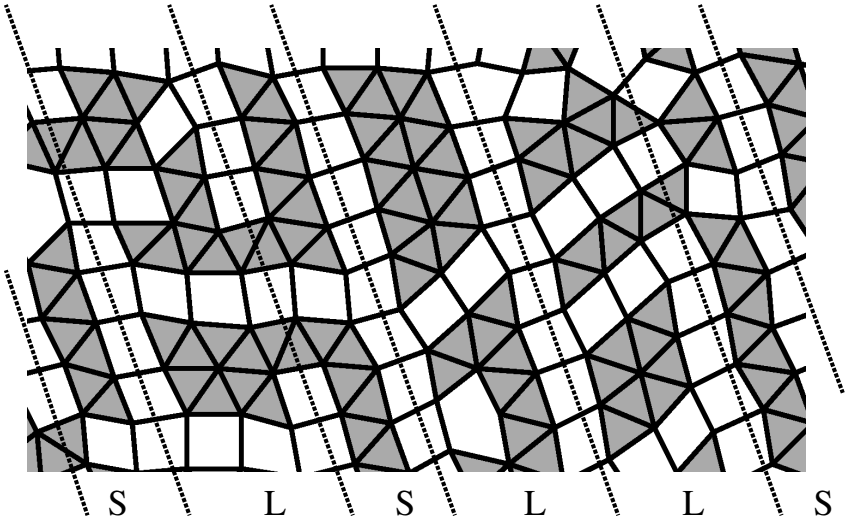

Figure 7.12: Archimedean-like tiling pattern for $a_S/a_V = 0.577$ and $V_0/(k_BT) = 20$. The sequence of short and long distances between the rows of squares corresponds to the sequence of S and L in a Fibonacci chain (cf. section 3.1.3).

potential are roughly given as multiples of λ_2, however their exact positions and their depths are modulated with λ_1. The Archimedean tiling of type $(3^3.2^2)$ [see figure 7.11] best fits the potential, if the sum of the heights of one row of triangles and and the height of one row of squares equals two wavelengths λ_2. For the modified Archimedean tiling [see figure 7.11(b)] the height of two rows of triangles and one row of squares has to be $3\lambda_2$. Therefore, the length a_{AT} of the edges of the squares and triangles in the Archimedean tiling are

$$\begin{aligned} a_{AT} &= \frac{2}{1+\frac{\sqrt{3}}{2}}\lambda_2 \approx 0.563 a_V \text{ for an Archimedean tiling of type } (3^3.2^2) \\ \text{and } a_{mod-AT} &= \frac{3}{1+2\frac{\sqrt{3}}{2}}\lambda_2 \approx 0.577 a_V \text{ for a modified Archimedean tiling.} \end{aligned} \tag{7.3}$$

This corresponds to a density given by the particle spacing a_S of the ideal triangular lattice with

$$\begin{aligned} a_{S,AT} &= \frac{4\sqrt{3}}{3}\sqrt{\sqrt{3}-\frac{3}{2}}\lambda_2 \approx 0.585 a_V \text{ for an Archimedean tiling of type } (3^3.2^2) \\ \text{and } a_{S,mod-AT} &= \sqrt{3-\sqrt{3}}\lambda_2 \approx 0.592 a_V \text{ for the modified Archimedean tiling.} \end{aligned} \tag{7.4}$$

Since the averaged potential is quasiperiodic, none of the periodic structures described above fits the potential very well. In the simulations, we found that the sequence of the distances between the square rows are given by a Fibonacci chain and therefore Archimedean-like tiling that appears in the decagonal potential is a combination of the Archimedean

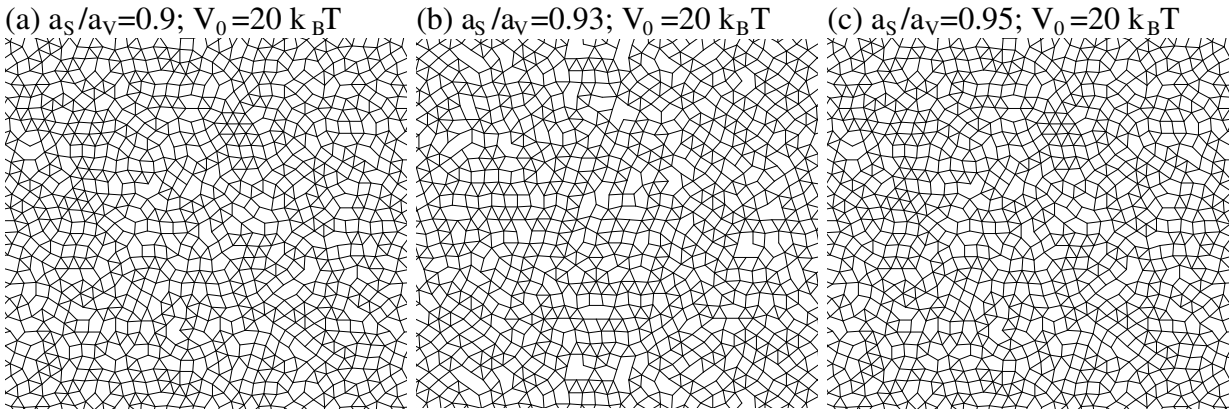

Figure 7.13: Delaunay triangulation of point patterns without bonds longer than $1.1a_S$. Archimedean-like tiling can be observed. The particle spacing a_S is roughly by a factor of τ larger than for the Archimedean-like tilings in figure 7.10. The parameters of the low density case are used (see section 4.4), only the charge of the colloids is set to $Z^* = 20000$.

tiling of type $(3^3.2^2)$ and the modified one. In the observed Archimedean-like tiling, the probability to find double rows of triangles is τ-times the probability to find single rows of triangles (see section 3.2). Therefore, one finds

$$\begin{aligned} a_{fib-AT} &= \frac{3\tau+2}{\left(\sqrt{3}+1\right)\tau+\sqrt{3}/2+1}\lambda_2 \approx 0.573 a_V \\ \text{and } a_{S,fib-AT} &= \sqrt{\frac{2\sqrt{3}}{3}\frac{3\tau+2}{\left(\sqrt{3}+1\right)\tau+\sqrt{3}/2+1}}\lambda_2 \approx 0.590 a_V. \end{aligned} \tag{7.5}$$

The particle spacing $a_{S,fib-AT}$ for the theoretically predicted Archimedean-like tiling therefore is just slightly larger than the one found in the simulation, which ranges from approximately 0.577 to 0.585. The difference probably is due to the imperfections of the patterns in simulations, which lead to higher densities compared to perfect structures.

Note that the Archimedean-like tiling can also lock to the distance $\lambda_1 = \tau\lambda_2$. The ideal density for such a structure with the characteristics of the Fibonacci chain then is

$$a_{S,\lambda_1-fib-AT} = \tau a_{S,fib-AT} \approx 0.954 a_V. \tag{7.6}$$

This structure can be observed in simulations (see figure 7.13) and in experiments [20]. No Archimedean-like tilings were found for even more dilute systems corresponding to distances $\tau\lambda_1$, i.e., they seem to be restricted to densities determined by the wavelengths λ_1 and λ_2.

7.1.6 Pair correlation function and structure factor

In figure 7.14 we plot the pair correlation functions $g(d)$ for several colloidal patterns, which is given by the probability to find two colloids with a distance d. In figure 7.14(a) $g(d)$ is plotted when the colloids are only allowed to occupy the potential minima; namely all of them (full line) or just the deepest one (dotted line). Clearly, in the second case a few distances are preferred. The arrows indicate peak positions that follow from their left-hand neighbors by multiplication with the number of the golden ratio τ, which again reveals a self-similar property of the decagonal potential. The pair correlation function [figure 7.14(b)] determined from Monte-Carlo simulations indicates for small V_0 a clear peak close to $d = a_S = 2a_V$, as expected for the ideal triangular phase. For increasing potential strength V_0, new peaks start to develop in the quasicrystalline region at positions of the deepest minima but they are still quite broad so that only ψ_{20} is non-zero (dashed line). Just crossing the phase boundary to the 10-bond-direction phase, the peaks become more pronounced (dotted line) meaning that the colloids settle more and more into the deepest minima. Furthermore, for densities with a_S around 1.85, the quasicrystalline phase with 20 bond directions only exists in a very small range of V_0 (cf. figure 7.3). This is understandable from the pair correlation functions in figure 7.14(c). They show that the main peak in the triangular phase is already close to one pronounced peak of the ideal $g(d)$ in figure 7.14(a). As a result, the colloids can settle into the deepest minima of the decagonal potential without the need of strong rearrangements and, therefore, the 20-bond-direction phase hardly occurs.

In figure 7.14(e), we plot the pair correlation function for $a_S = 0.56$ for increasing potential strengths V_0. The most pronounced peak is just determined by the colloidal density. During the transition from the triangular ($\psi_6 > 0.1$) to the disordered ($\psi_m < 0.1$) phase, $g(d)$ changes so that the other peaks better fit to the ideal pair correlation function in figure 7.14(a). The pair correlation functions of the Archimedean-like tiling shown in figure 7.7(d), the peaks (besides the highest one) fit very well to the ideal $g(d)$ in figure 7.14(a). Therefore, this ordering is extraordinary stable and the transition into the disordered phase is delayed to larger V_0. The observation that the Archimedean like tiling fits to the decagonal potential very well is also discussed in [191].

Finally, in figure 7.15, we plot the two-dimensional direct correlation functions for the liquid and the phases with 10 or 20 bond directions. We also calculated the corresponding structure factors, which are the Fourier transformed of the direct correlation functions. The structure factors confirm the long-range order of the quasicrystalline phases. Since sometimes it is hard to determine the actual symmetry by just calculating the correlation functions or the structure factors, the quantitative method that employs the bond orientational order parameter is more appropriate to quantitatively analyze colloidal ordering.

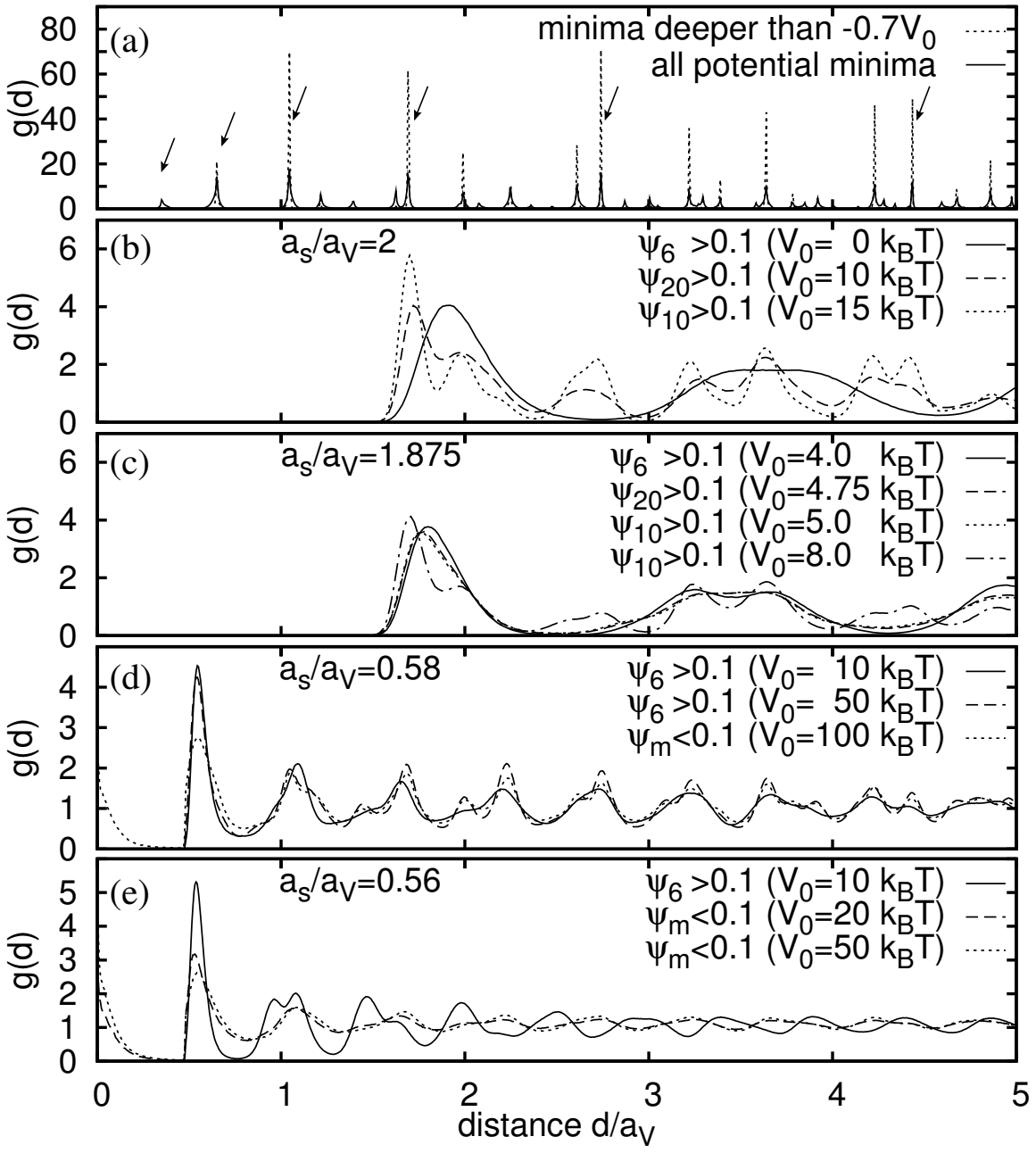

Figure 7.14: Pair correlation function $g(d)$ as a function of the particle distance d: (a) for colloids placed at the positions of all minima (solid line) or of all minima deeper than $-0.7V_0$ (dotted line) in the decagonal potential, (b-d) determined by Monte-Carlo simulations in the low (b,c) and high (d,e) density case. In each graph, $g(d)$ is drawn for constant a_S/a_V and several strengths V_0.

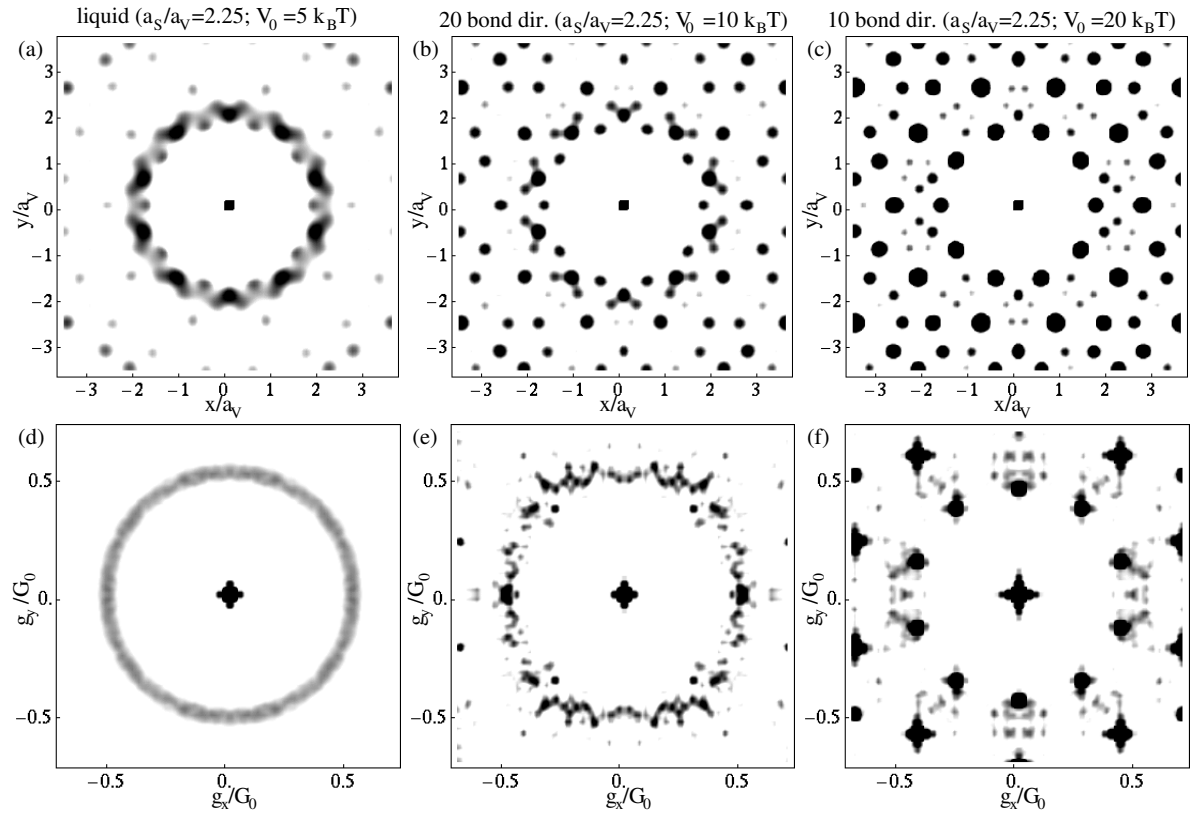

Figure 7.15: (a-c) Two-dimensional direct correlation functions and (d-f) structure factors for (a,d) the liquid for $\beta V_0 = 5$, (b,e) the phase with 20 bond directions for $\beta V_0 = 10$, and (c,f) the phase with 10-fold bond orientational order for $\beta V_0 = 20$. In all cases, the density is given by $a_S/a_V = 2.25$. One quadrant for each of the plots was calculated, the other quadrants are mirror images.

7.2 Comparison to experimental results

In the experiments performed at the University of Stuttgart by J. Mikhael, L. Helden, and C. Bechinger the decagonal laser field (see figure 7.16) is realized by five linearly polarized laser beams that are arranged along the edges of a prism with pentagonal basis and then interfere to create the potential (cf. section 3.3). The colloidal suspension is confined between two class plates. By pushing the colloids against the lower glass surface with an additional laser beam with a broad focus, they can only move in two dimensions. A boundary is created with the help of a laser beam that rotates along a circle around the region that contains the colloidal system to be studied. By changing the radius of the circle, the density can be adjusted. The interaction strength is regulated via the concentration of counter ions in the suspension. Highly charged polystyrene spheres with radius $R = 1.45$ μm and a polydispersity of about 4% dispersed in deionized water are used. The mean particle spacing is about $a_S = 4.6$ μm. Usually the laser power is gradually increased up to 10 Watts. The positions of the colloids are determined via video microscopy.

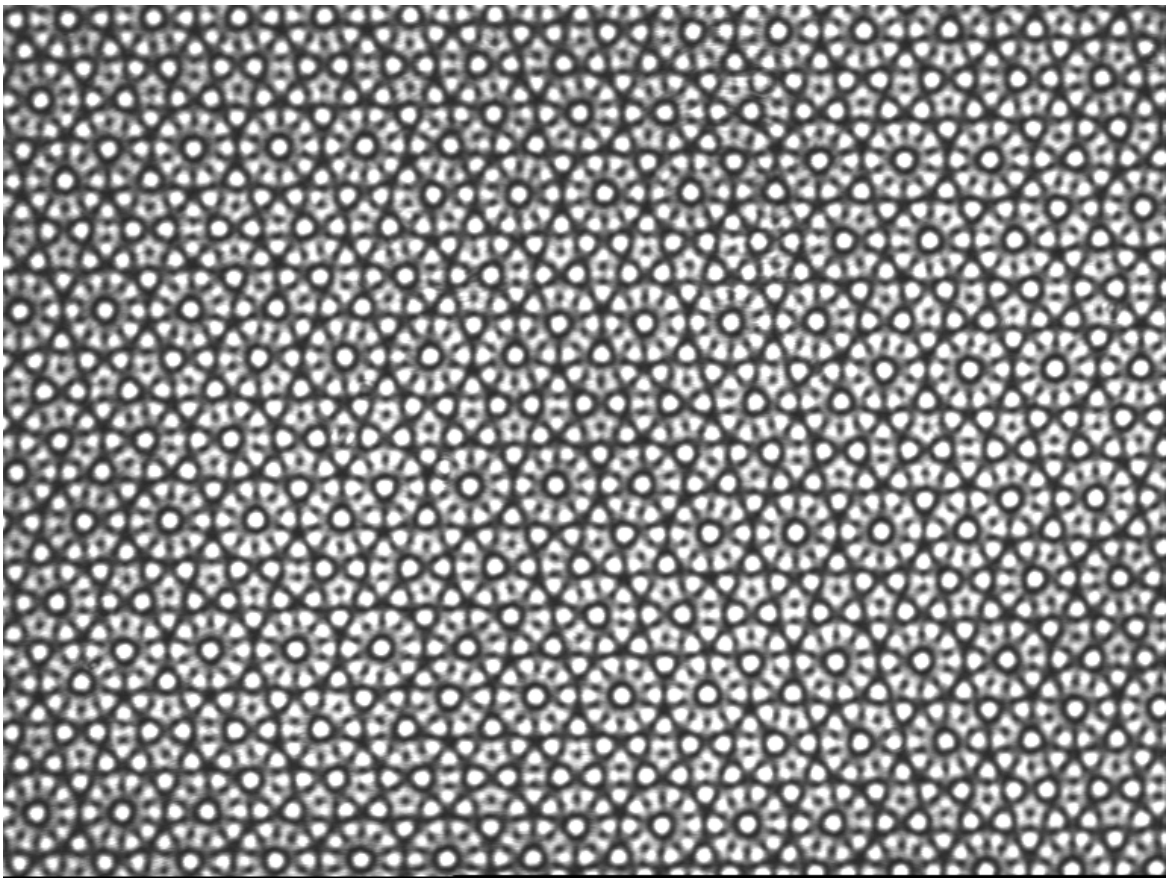

Figure 7.16: Decagonal laser field in experiment. Experiment and photograph by J. Mikhael [20].

In figure 7.17 a micrograph of the decagonal phase at high laser intensities is shown. Archimedean-like tilings were first observed in the experiments (see figure 7.18 and [191]) and can be found at different densities probably because the systems locks into the two length scales λ_1 and λ_2 introduced in section 7.1.5.

As in the simulations, domains of an Archimedean-like tiling with different orientations are found in experiments. However, one direction usually seems to be preferred and therefore large domains of an almost perfect Archimedean-like tiling with just one orientation can be observed. Very likely, this is caused by a small imperfection in the experimentally created potential. If for example not all angles of the laser beams with respect to the sample plane are equal, the lengths of the projected wave vectors G_j may vary. If one of the vectors G_j is slightly different from the others, this corresponds to a gradient in the phase, which is equivalent to a combination of a constant phononic and phasonic strain along a certain direction in the decagonal potential [178]. Because in a potential with such a phase gradient the lines of low intensities are all finite except those in the gradient direction (see figure 7.19), the orientation along this direction is preferred by the Archimedean-like tiling (see also section7.3.4).

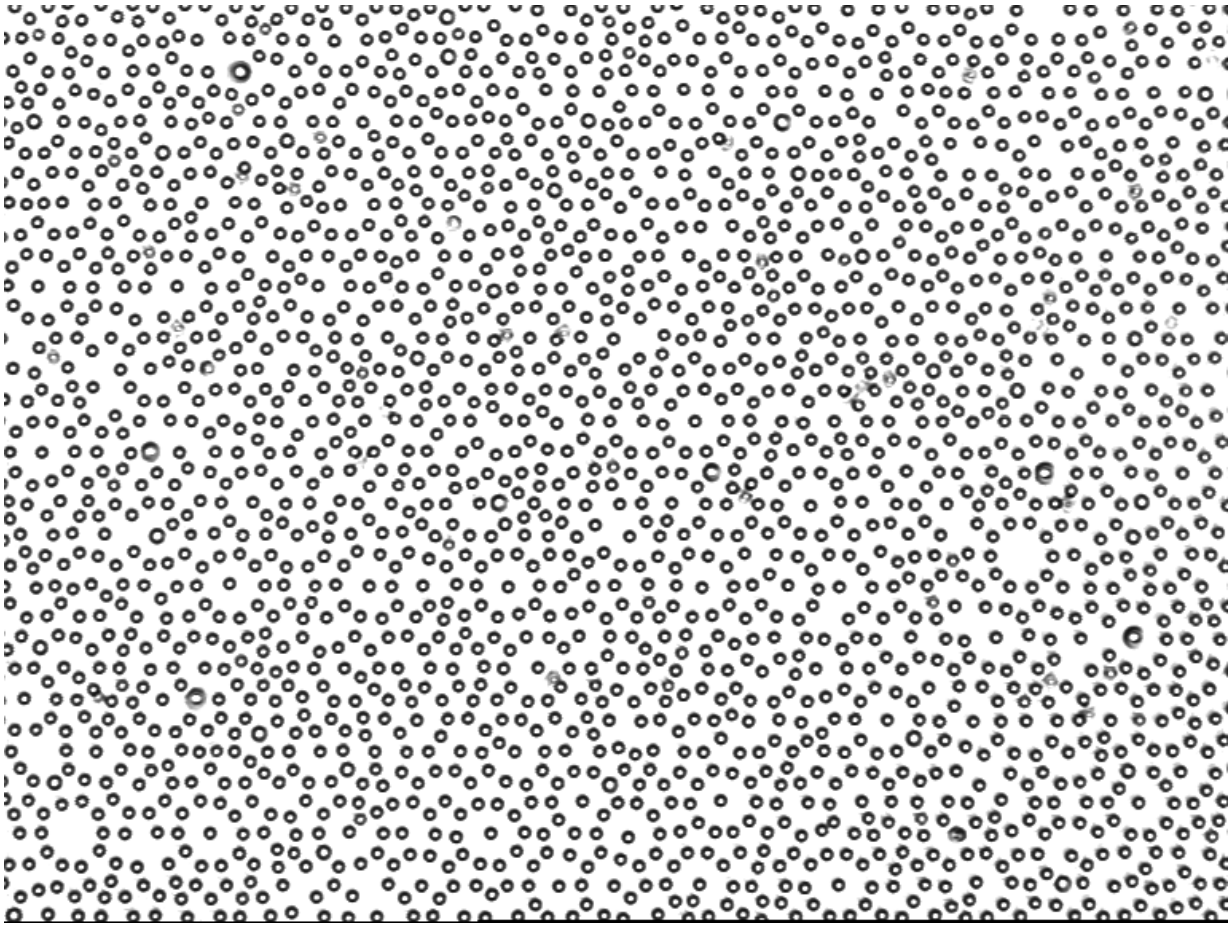

Figure 7.17: Decagonal ordering in experiment. Experiment and micrograph by J. Mikhael [20].

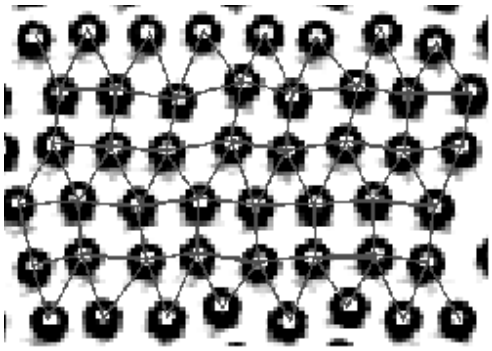

Figure 7.18: Archimedean-like tiling in experiment. Experiment and micrograph by J. Mikhael [20].

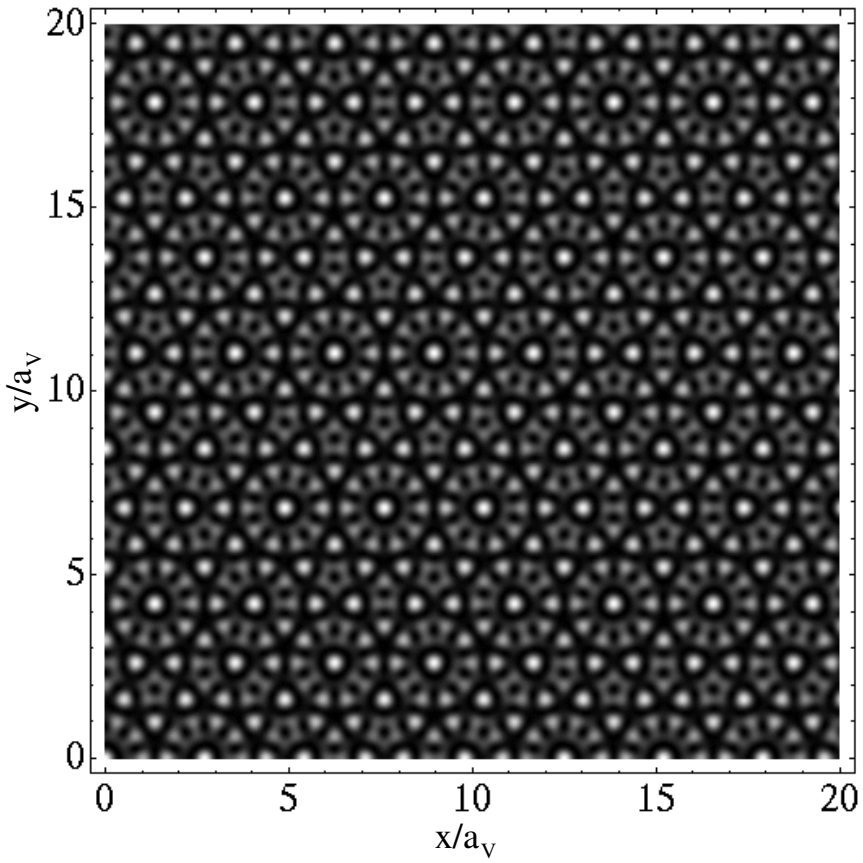

Figure 7.19: Theoretically calculated decagonal potential with a gradient in the phase φ_0 attached to wave with wave vector $\mathbf{G}_0$: $\varphi_0 = 0.2x/a_V$. It creates a gradient in the phononic and phasonic displacements along the x-direction. The lines of low intensity are infinite in x-direction, but finite in all other directions.

7.3 Phasonic displacements and drifts

In this section, we shortly demonstrate how the colloidal system can be used to study the properties and consequences of phasonic displacements, gradients, and drifts.

7.3.1 Rearrangements in a decagonal quasicrystal

First we demonstrate how a phasonic flip in a decagonal pattern can be induced by a change of the phasonic displacement of the potential.

Figure 7.20 shows patterns within the decagonal phase before and after a phasonic displacement, i.e., the phasonic displacement is $w_x = 0$ on the left-hand side and $w_x = 0.1a_V$ on the right; w_y is 0 in both cases. The pattern is decagonal independent of the displacement, however the orientation of some of the sketched pentagons has changed. It seems that always two neighboring pentagons flip their orientation at the same time. Furthermore, the row of pentagon does not change its y-position, which is probably due to

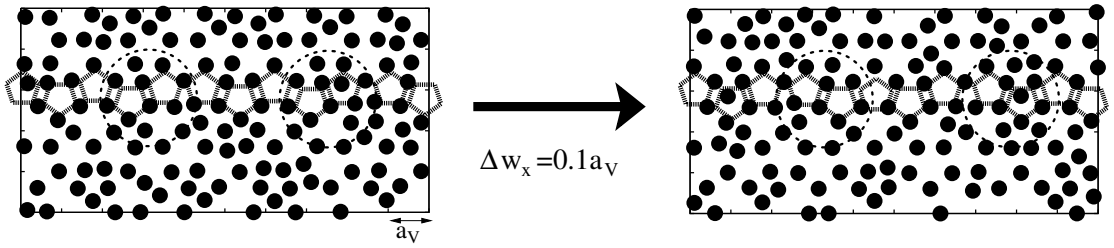

Figure 7.20: Inducing a phasonic flip: Colloidal point patterns within the decagonal phase ($a_S/a_V = 0.65$, $V_0/(k_BT) = 1000$) for $w_x = 0$ (left) and $w_x = 0.1a_V$ (right). The flipping pentagons are marked by dotted circles.

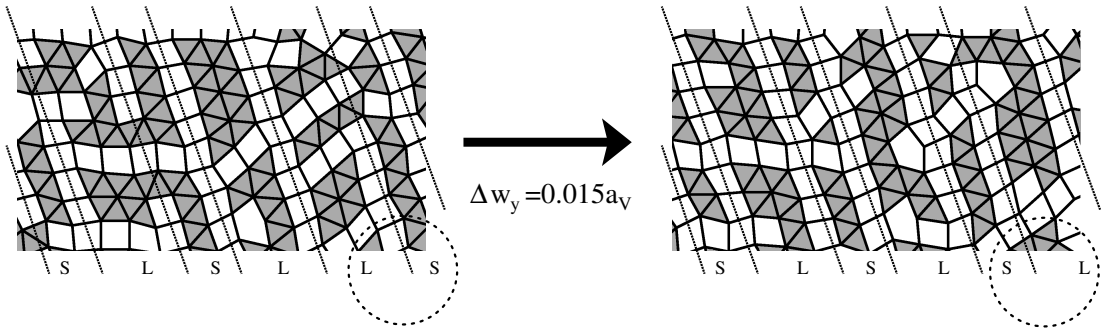

Figure 7.21: Inducing a phasonic flip: Delaunay triangulation of colloidal point patterns (without bonds longer than $1.1a_S$) for the Archimedean-like tiling ($a_S/a_V = 0.577$, $V_0/(k_BT) = 20$) for $w_y = 0$ (left) and $w_y = 0.015a_V$ (right). The flip in the Fibonacci chain is marked by dotted circles.

the fact that the horizontal lines of low laser intensity are not affected by a change of w_x (see section 3.4.3).

7.3.2 Rearrangements in an Archimedean-like tiling

Here we want to demonstrate the consequences of a phasonic displacement on the Archimedean-like tiling. Figure 7.21 shows patterns of the Archimedean-like tiling for different phasonic phases w_y. Note a whole row of triangles and a row of squares have interchanged their position on the right-hand side of figures 7.21. Therefore, phasonic flips occur in the sequence of the distances between the square rows that corresponds to a Fibonacci chain (cf. sections 3.1.3 and 3.4.1).

If the phasonic displacement is changed such that the lines of low intensity in the direction of the square or triangular rows are not shifted, the whole Archimedean-like tiling is not affected by the phasonic displacement.

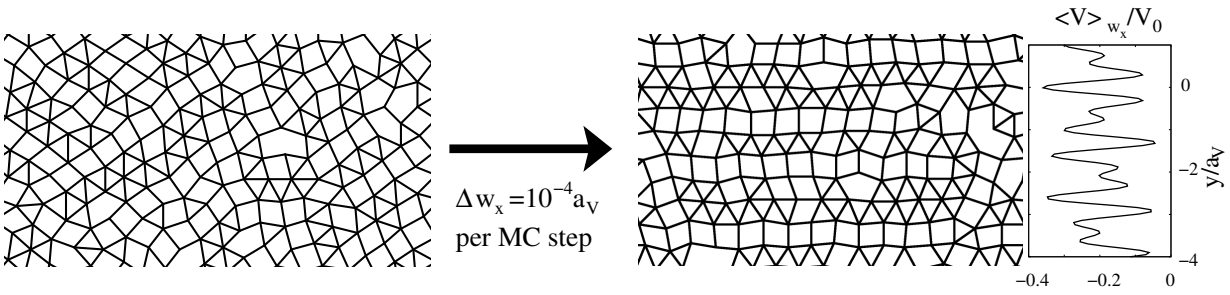

Figure 7.22: Stabilization by a phasonic drift: Delaunay triangulation of colloidal point patterns (without bonds longer than $1.1a_S$) for the Archimedean-like tiling ($a_S/a_V = 0.577$, $V_0/(k_BT) = 20$) without phasonic displacement (left) and in a potential with a phasonic drift of $\Delta w_x = 10^4 a_V$ per Monte-Carlo step (right). The small graph on the right-hand side shows the potential averaged over w_x depending on y [see also equation (3.34)].

7.3.3 Stabilizing the Archimedean-like tiling by a phasonic drift

Fluctuations in w_x or a steadily growing w_x orients the Archimedean-like tiling along the x-direction. This is demonstrated in figure 7.22) for a phasonic drift $\Delta w_x = 10^4 a_V$ per Monte-Carlo step. Domains that are not oriented along the x-direction are reduced because a change in w_x would always displace the rows of squares and triangles in the Archimedean-like tiling except when they are oriented along the x-direction. A colloid in a decagonal laser field with a fast phasonic drift in w_x-direction can be considered as a particle in an effective potential that is the decagonal potential averaged over w_x (see right-hand side of figure 7.22). As introduced in section 3.4.3, the average of the decagonal laser field over w_x corresponds to the average over x and does not depend on y. Such an averaged potential only supports domains of Archimedean-like tiling oriented in x-direction. In summary, phasonic fluctuations or drifts help to create large domains of Archimedean-like tilings.

7.3.4 Stabilizing the Archimedean-like tiling by a phasonic gradient

Another possibility to reduce the domains of Archimedean-like tiling that are not oriented along the x-direction is to induce a phasonic gradient in x-direction. Such a gradient destroys all continuous lines of low intensity in the potential landscape, except those in x-direction (see also section 3.4.3). Therefore, in a potential with a phasonic gradient, the Archimedean-like tiling is mainly oriented along the phasonic gradient (see figure 7.23). This very likely is the reason for the very large domains of Archimedean-like tiling found in experiments that preferentially orientate along the same direction. A phasonic gradient field is caused when the laser beams are not perfectly adjusted (see also section 7.2).

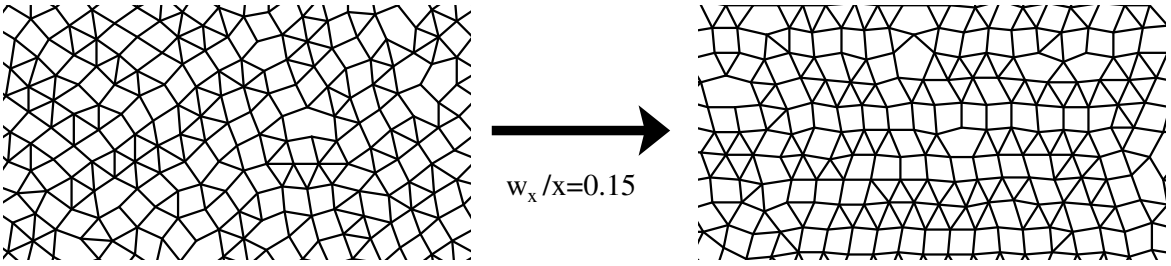

Figure 7.23: Stabilization by a phasonic gradient: Delaunay triangulation of point patterns (without bonds longer than $1.1a_S$) for the Archimedean tiling like phase ($a_s/a_l = 0.577$, $V_0/(k_BT) = 20$) without phasonic displacement (left) and in a potential with a phasonic gradient with $w_x/x = 0.15$ (right).

7.4 Summary and Outlook

In this chapter, we determined the phase behavior of colloids on a 2D decagonal substrate. We found a triangular to liquid phase transition for small laser intensities and decagonal ordering in strong potentials. For intermediate intensities, however, where the colloidal ordering is influenced by both the colloidal interaction and the substrate potential, we identify a series of interesting phases: For systems with low densities, where the number of colloidal particles is less than the number of potential minima, there is a quasicrystalline phase which exhibits bond orientations in 20 different directions. When the number of colloids exceeds the number of potential minima, we usually find a solid phase without any apparent bond orientational order. However, for certain densities the system locks into a highly ordered phase that is close to an Archimedean tiling.

We also demonstrated how the system can be used to study the effects of phasonic displacements, drifts, or gradients. We showed how phasonic colloidal flips in the Archimedean-like tiling and in the decagonal phase are induced by phasonic displacements in the substrate potential. Furthermore, the Archimedean-like tiling orientated along one direction is stabilized with the help of a phasonic drift or gradient.

Interestingly, in experiments the Archimedean-like tilings seem to be extraordinary stable [20]. The density in experiments usually cannot be controlled as easy as in simulations: In Monte-Carlo simulations the density is extremely homogeneous due to possible global steps. In experiments, the density often seem to self-adjust right inside the small stability region of the Archimedean-like tiling. Therefore, Brownian dynamics simulations with open boundary conditions would give a deeper inside into the stability of Archimedean tilings.

In triangular phases induced by triangular substrates the phonon spectrum was determined from simulations, experiments, and analytical calculations [243, 244] (cf. also [245–248]). Such an analysis for the phonon and phason spectra of induced quasicrystals would be very interesting, however, also extremely difficult due to the problems of splitting up the observed displacements into phononic and phasonic contributions (cf. section 3.4.4).

Finally, as a very general outlook, we discuss the following question: What is really needed to induce quasicrystalline order in a mono-atomic system? Usually, two appro-

priately chosen characteristic lengths are needed to achieve quasicrystalline order, e.g., quasicrystals are observed for systems with two length scales in the interaction potential [249, 250]. In binary systems studied so far the free energy of periodic and quasicrystalline states are close [57, 61, 251, 252]. In the most recent work the ground state seems to be periodic [252]. Patrykiejew and Sokołowski claimed to have found decagonal ordering in a mono-atomic system, where one length scale is given by the particle interactions and another by a periodic potential [241]. However, the observed phase turned out to be a periodic Archimedean tiling [242, C]. Probably a promising candidate for mono-atomic quasicrystalline ordering on a periodic potential is a system, where the mean particle spacing differs by an irrational factor (e.g. by a factor of τ) from the lattice constant of the substrate. A pinned phase for high potential strength therefore usually cannot order periodically (cf. the frustrated non-periodic phase in section 6.4). To study such a phase is very interesting, especially to find out, whether it exhibits quasicrystalline ordering, perhaps even with some non-crystallographic rotational symmetry. Such a system, i.e., with a mismatch in the lattice structure of the substrate and the colloidal adsorbate, was already studied in [253], however mainly for selected mismatch ratios that lead to periodic structures.

Chapter 8

Brownian particles in a decagonal potential

In this chapter we consider a single colloidal particle moving in decagonal or square potentials. In the long-time limit we find conventional diffusion as it is known in literature for systems whose depth of the potentials is limited. However, for large potential strengths the particle needs a very long time to approach its asymptotic diffusive limit. For an intermediate time regime, which can span over several decades, we find subdiffusive motion. To explore this regime, we especially study in this chapter how the diffusive limit in thermal equilibrium is approached. First, in section 8.1 we shortly introduce anomalous diffusion. We then concentrate on the Brownian motion of a particle in potential landscapes of different symmetry. In section 8.2 results of Brownian dynamics simulations are presented, where the colloid is started at an arbitrary position in the potential, i.e., in non-equilibrium. In section 8.3 an analytic theory for this situation is developed, based on a model where the particle jumps between random trapping sites, and the theory is compared to the results of the simulations. The motion of a colloid in thermal equilibrium is discussed in section 8.4 and compared to experimental results. In section 8.5 the Brownian dynamics of particles that are driven out of equilibrium by a phasonic drift is studied. Relation known in non-equilibrium statistics can be applied to such a system and are, therefore, shortly introduced in section 8.6. Finally we conclude in section 8.7. Parts of this chapter are based on publication [B].

8.1 A short introduction to anomalous diffusion

Free Brownian motion leads to diffusion at time scales where inertia can be neglected and is well understood since Einstein's seminal paper [181] (see also section 4.1.1). Conventional diffusion of a particle is characterized by its mean square displacement that is proportional to time: $\langle r^2 \rangle \propto t$. However, in systems with anomalous diffusion, one finds

$$\langle r^2 \rangle \propto t^{\nu} \tag{8.1}$$

with an exponent $\nu \neq 1$. For $\nu < 1$ the system is called subdiffusive and for $\nu > 1$ superdiffusive. For superdiffusive motion, one also uses the notions subballistic for $\nu < 2$, ballistic for $\nu = 2$, and superballistic for $\nu > 2$. In this section we present some approaches to theoretically address anomalous diffusion as well as important examples of systems where it occurs.

Asymptotic anomalous diffusion, i.e., sub- or superdiffusive motion in the long time-limit $t \to \infty$, is often explained by using so-called Lévy walks (see e.g. [254–258]). These are modified random walks with special distributions for step length or step duration. Sometimes waiting times in between the steps are included. Asymptotic anomalous diffusion occurs, if the first or second moment of the step length distribution or of the waiting time distribution is not finite. Note that even if the first and second moment are convergent and therefore the motion is diffusive in the long time limit, there still can be anomalous diffusion at intermediate times. In modifications of the standard Lévy walk model, e.g., in random walk models with nontrivial coupling between step length and duration (see e.g. [257]) or in models with a random distribution of velocities [259, H], asymptotic anomalous diffusion is also found.

Diffusion is often characterized by the parabolic differential equation

$$\frac{\partial}{\partial t} p(\mathbf{r}, t) = D \nabla^2_{\mathbf{r}} p(\mathbf{r}, t), \tag{8.2}$$

where $p(\mathbf{r}, t)$ is the probability for the diffusing particle to be at position $\mathbf{r}$ at time t and D is the diffusion constant. To construct a generalized equation that describes anomalous diffusion, we apply a Laplace transformation in time and a Fourier transformation in space:

$$\tilde{p}(\mathbf{k}, s) = \int_0^\infty dt \int d\mathbf{r} \exp(-st) \exp(i\mathbf{k} \cdot \mathbf{r}) p(\mathbf{r}, t). \tag{8.3}$$

The integration in $\mathbf{r}$ is over the whole space. In Fourier-Laplace space equation (8.2) reads

$$\left(s + Dk^2\right) \tilde{p}(\mathbf{k}, s) = 0. \tag{8.4}$$

This equation can be generalized by introducing exponents α and β:

$$\left(s^\alpha + D \left|\mathbf{k}\right|^\beta\right) \tilde{p}(\mathbf{k}, s) = 0. \tag{8.5}$$

In real space and time, equations such as (8.5) are often written with fractional derivatives (i.e. $\partial^\alpha / \partial t^\alpha$) and the corresponding equations for anomalous diffusion are called fractional diffusion equations (see e.g. [260, 261]). The mean square displacement for a solution of equation (8.5) behaves as $\langle r^2 \rangle \propto t^{2\alpha/\beta}$ if it is convergent. Obviously, equation (8.5) describes subdiffusive as well as superdiffusive motion if the exponents α and β are chosen appropriately. Sometimes, the mean square displacement is divergent and therefore the scaling in time is studied by considering other moments [260]:

$$\langle |\mathbf{r}|^\delta \rangle \propto t^{\delta\alpha/\beta}. \tag{8.6}$$

However, the is a difference between the scaling of the moments and the (approximate) scaling of $p(\mathbf{r}, t)$. furthermore, if $p(\mathbf{r}, t)$ does not scale perfectly, the scaling of the moments depends on the exponent δ in a non-trivial way [I].

Superdiffusion is not only found in systems with a Lévy walker. There are also billiard models, i.e., systems where a particle is reflected when hitting the boundary of an obstacle, which exhibit superdiffusion for an ensemble of particles started with random conditions. The path of a particle in such a billiard system is not random but totally determined by the starting position and direction. A famous example of such a system is the Lorentz gas also called Sinai billiard, which in two dimensions consists of circular obstacles from which the particles are reflected. If there is no straight path of infinite length (finite horizon system), the particles behave diffusive [262]. However, if straight paths of infinite length exist, the mean square displacement asymptotically is proportional to $t \ln t$, i.e., the system is superdiffusive [263, 264]. There are also other billiard systems like zigzag channels [265] or hexagonal channel systems [F,G,J] that are superdiffusive due to some special paths on which the particles travel in one direction for very long times.

Also many subdiffusive systems have been studied in recent years. Examples are many-particle systems such as dense colloidal suspensions close to freezing [266] or other glassy systems (see e.g. [267–269]), where subdiffusion is due to caging from surrounding particles as demonstrated explicitly in experiments [270–272]. Permanent confinement leads to subdiffusion as well: many particles that move in narrow channels exhibit anomalous diffusion [233], which recently was also studied for single-file diffusion in colloidal systems [51, 52, 234]. Furthermore, particles confined to the space between obstacles forming a Lorentz gas behave subdiffusively on intermediate time scales [273].

Anomalous diffusion also plays an important role in many biological systems. Examples are the dynamics of molecular motors moving along heterogeneous substrates [274], superdiffusion of migrating cells [275], the subdiffusion of macromolecules in the cell due to crowding [276], the motion of beats in the cytoskeleton or artificial actin networks [277,278], or the dynamics of fluorescently labeled molecules in cells [279–281] and in membranes [282].

Even the simple Brownian motion of a single particle in a random potential exhibits subdiffusion. Honkonen and Pis'mak [283] showed that such a motion is subdiffusive on all time scales if the depth of the potential is not limited from below. This was extensively studied in many Brownian dynamics simulations, where for overdamped systems indeed asymptotic subdiffusion is observed [284], whereas for low damping also superdiffusion at intermediate times can be found [285–289]. However, if each potential well possesses a finite depth, the motion always becomes diffusive in the long-time limit. Modelling it by jumps between traps with random but finite strengths, the asymptotic diffusion constant can be calculated (see, e.g., Haus *et al.* in [290,291]). The random trap model we introduce in section 8.3 also leads to diffusive behavior at very long times.

8.2 Brownian motion in static potentials started in non-equilibrium

Here, the colloidal particles are started at random positions within the potentials. We perform Brownian dynamics simulations in two dimensions (see section 4.1 for the details of the simulations) under the influence of external potentials. We compare the motion of a colloidal particle in a potential with decagonal symmetry (see section 3.3) to its diffusive behaviour in regular or random square potentials, which we introduce in the next subsection.

8.2.1 Regular and random square potential

We consider regular or random square potentials that consist of wells located on a square grid with lattice constant a_V. Each well is modeled according to a product of cosines, i.e., within the area given by $|x - x_m| \leq a_V/2$ and $|y - y_m| \leq a_V/2$, the minimum of the potential at position $\mathbf{r}_m = (x_m, y_m)$ is described by

$$V(\mathbf{r}) = -\frac{V_m(\mathbf{r}_m)}{2}\left\{1 + \cos\left[\frac{2\pi(x - x_m)}{a_V}\right]\cos\left[\frac{2\pi(y - y_m)}{a_V}\right]\right\}, \tag{8.7}$$

where $V_m(\mathbf{r}_m)$ ist the depth of the minimum. In the regular square potential all minima have the same depth, i.e., $V_m(\mathbf{r}_m) = V_0 = \text{const}$. For the random square potential, the depths of the wells are randomly taken from the interval $[0, V_0]$ with the same probability. Therefore the distribution of the potential depths for the random square potential is much simpler than the one of the decagonal potential (see 3.3.3). As we demonstrate at the end of the next subsection, this leads to differences in the simulation results. Figure 8.1 shows the potential landscapes of the square and the decagonal potentials, and their grey-scale representations, which correspond to the intensity field of the respective light patterns in experiments.

8.2.2 Results of the simulations

Here, we calculate the mean square displacement with respect to the starting position $\mathbf{r}(0)$ of the random walker according to

$$\langle r^2 \rangle = \langle [\mathbf{r}(t) - \mathbf{r}(0)]^2 \rangle, \tag{8.8}$$

where the ensemble average is realized with 5000 different runs in the simulations.

The particles start at random positions. The left-hand side of figure 8.2 shows the simulation results for the time dependence of the mean square displacement for all potentials. The different curves correspond to different values of the strength V_0 of the potentials normalized by the thermal energy $\beta^{-1} = k_B T$. The characteristic length scale a_V is used to rescale length, the time is plotted in units of $\beta\gamma a_V^2$, where γ is the friction coefficient of the colloid. For zero potential $\beta V_0 = 0$ the system is diffusive with $\langle r^2 \rangle = 4Dt$, where

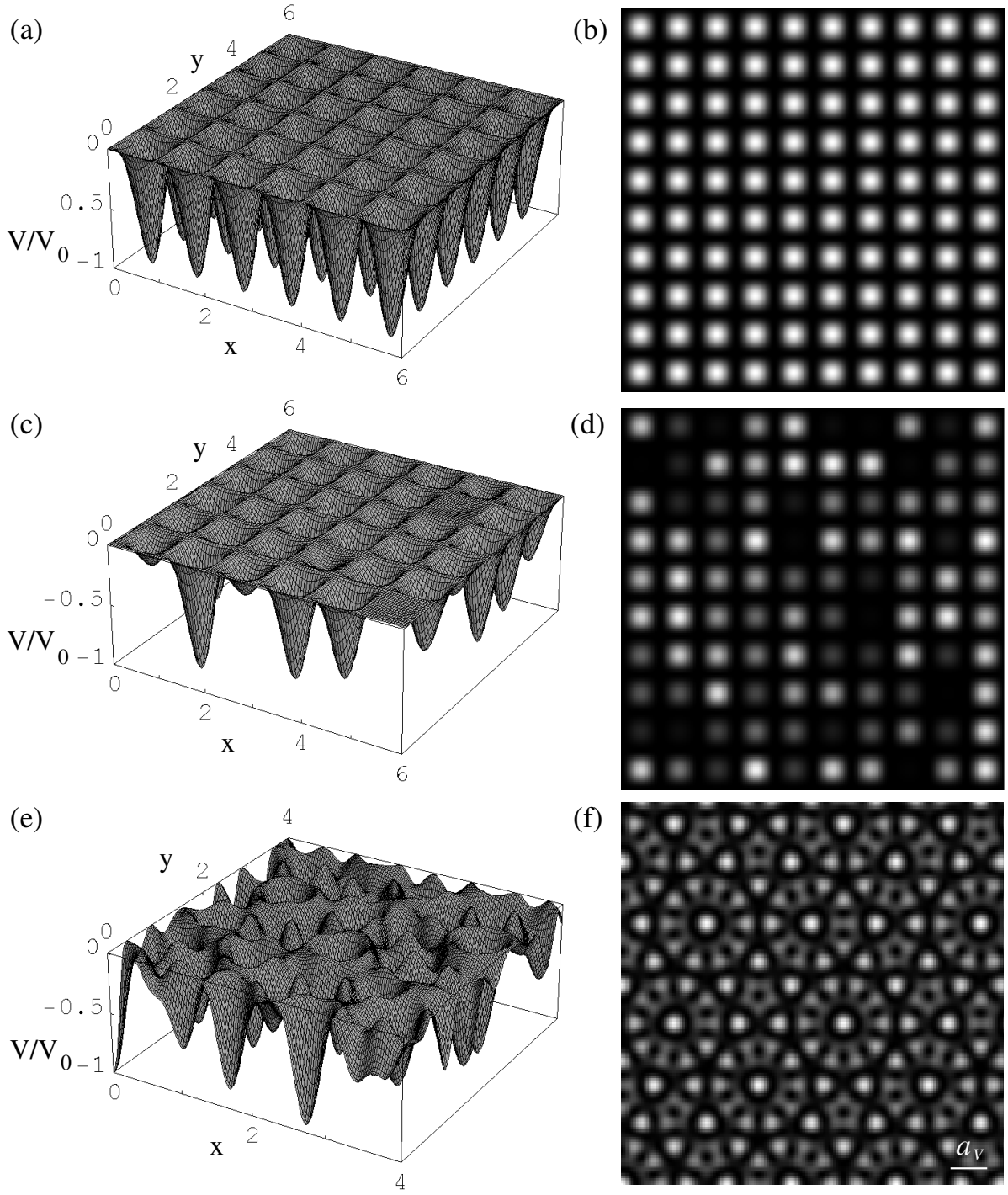

Figure 8.1: (a,c,e) Potential landscapes and (b,d,f) their grey-scale representations for (a,b) a regular square, (c,d) a random square, and (e,f) a decagonal potential. The exact definitions of the potentials are given in sections 8.2.1 for the square and 3.3 for the decagonal potential. The bar in the lower right corner of figure (f) indicates the characteristic length $a_V = 2\pi/|\mathbf{G}_j|$.

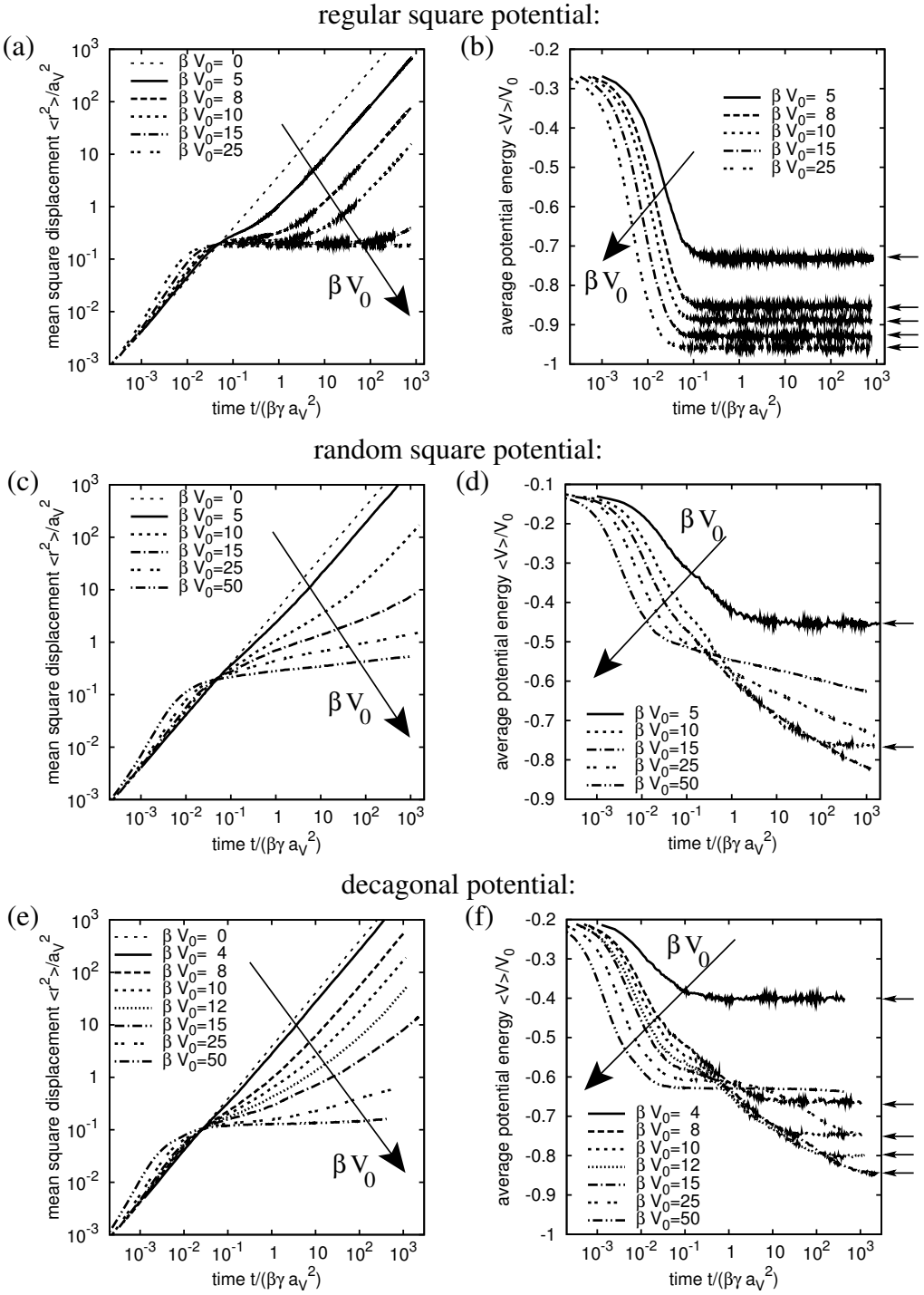

Figure 8.2: Mean square displacement (left hand side) and average value of the potential energy at the position of the particle (right hand side) obtained by Brownian dynamics simulations as function of time for different types of potentials: (a,b) regular square potential, (c,d) random square potential, (e,f) decagonal potential.

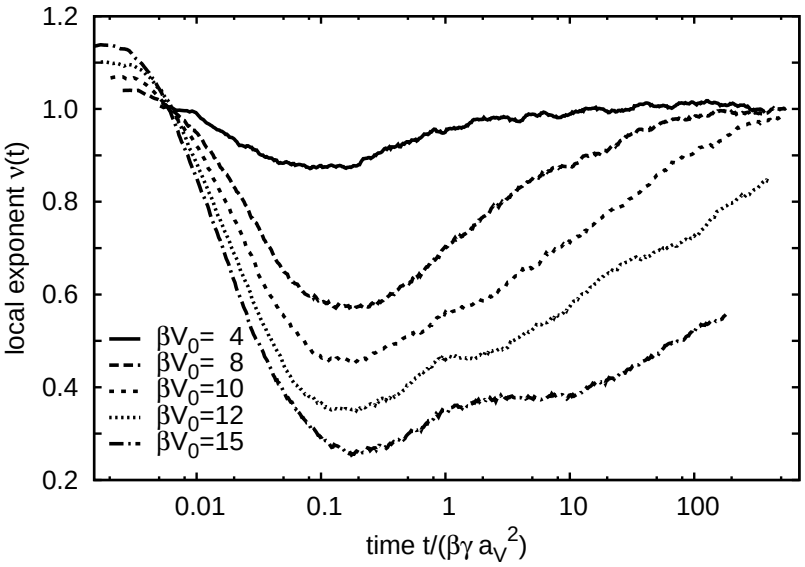

Figure 8.3: Time dependence of the local exponent $\nu(t)$ as defined in equation (8.9) for the decagonal potential.

the diffusion constant D obeys the Einstein relation $D = (\beta\gamma)^{-1}$ [see equation (4.12)]. For a non-zero potential and at short times, the particles first relax into the nearest minima. For stronger potentials, the relaxation process is faster. Nevertheless, after the short-time relaxation interestingly all curves for the mean square displacement seem to intersect in a common point, a behaviour we were not able to explain. In the long-time limit, we find normal diffusion. The asymptotic diffusion constant decreases with increasing potential strength. The behaviour at intermediate times strongly depends on the type of the potential. For the regular square potential [see figure 8.2(a)], the mean square displacement does almost not increase and the crossover to diffusion happens already before the mean square displacement has reached a_V^2, i.e., as soon as the particle leaves a potential well making a step of length a_V, diffusion sets in. By contrast, in a random or decagonal potential the colloid has to explore an area larger than a_V^2 and therefore several potential minima, before the motion becomes diffusive. The temporal range of the intermediate regime increases with increasing potential strength βV_0. For very high large V_0, the diffusive limit has not even been reached within the simulated time range. The motion in the intermediate regime is subdiffusive, i.e., if the mean square displacement is fitted locally by a power law $\langle r^2 \rangle \propto t^\nu$, the exponent ν is smaller than 1. In figure 8.3 we plot the local exponent ν for the decagonal potential calculated according to

$$\nu(t) = \frac{d \log \left[\langle r^2(t) \rangle / a_V^2 \right]}{d \log \left[t / \left(\beta\gamma a_V^2 \right) \right]}. \tag{8.9}$$

As expected, for small times the exponent is larger than 1 indicating the superdiffusive motion while the particle relaxes into the nearest minimum. For intermediate times, the

exponent is smaller than 1 and slowly relaxes towards $\nu = 1$ with increasing time, which means subdiffusive motion that slowly crosses over to conventional diffusion in the long time limit.

On the right-hand side of figure 8.2 we plot the time dependence of the average potential energy at the position of the particle, i.e., if $\mathbf{r}(t)$ is the colloidal position the average potential energy is

$$\langle V(t) \rangle = \langle V\left(\mathbf{r}(t)\right) \rangle, \tag{8.10}$$

where the average is taken over an ensemble of particle runs. Since the colloids are started at random positions the curves start at $t = 0$ from the mean value of the potential. It can be calculated analytically by integrating over the whole potential,

$$\langle V(0) \rangle = \lim_{A \to \infty} \frac{1}{A} \int_A dA \; V\left(\mathbf{r}\right), \tag{8.11}$$

where A is the area of the integration region. We find $\langle V(0) \rangle = -0.25 V_0$ for the regular, $\langle V(0) \rangle = -0.125 V_0$ for the random square, and $\langle V(0) \rangle = -0.2 V_0$ for the decagonal potential. At small times the particle relaxes into the minima closest to its starting position. In the regular potential, the colloid then has already reached its asymptotic average potential energy. However, in the random square and the decagonal potential it takes up to several decades in time before the long-time value is approached (marked by arrows in figure 8.2). The asymptotic average energies correspond to the canonical ensemble average of the potential energy of a particle. Interestingly, the long-time limit is reached, when the motion of the particle crosses over into the diffusive regime. Therefore, as long as the colloid has not explored the full variety of possible minima so that it is possible to find a potential well much deeper than the ones the colloid has visited before, the system behaves subdiffusively. As soon as the potential energy of the particle is thermally equilibrated, its motion is diffusive. The relaxation process reveals similarities and differences between the random and the decagonal potential. The curves for both potentials display a kink at times where the particles have relaxed into nearby minima. Their depth correspond to the mean potential depth $\langle V_m \rangle = -0.5 V_0$ in the random and $\langle V_m \rangle = -0.603 V_0$ in the decagonal potential (see also section 8.3.2). However, beyond the kink and for large laser intensities βV_0, the average potential energy stays on an almost constant plateau in case of the decagonal potential, but clearly decreases in the random potential. The different behavior is due to the different distributions $\rho(V_m)$ of the depths of the minima (see sections 3.3.3 and 8.2.1). In the decagonal potential minima with depths smaller than $0.24 V_0$ do not exist and the number of wells decreases with its depth. In contrast, in the random square potential all depths between 0 and V_0 occur with the same probability. Therefore, in the decagonal potential it takes longer to find minima much deeper than the average well and the potential energy decreases much slower.

8.3 Random trap model

In the following we develop a theory to calculate the time dependence of the mean square displacement. The theory is applicable to all potentials that display clear minima. In subsection 8.3.2 we compare the theoretical results to the simulations.

8.3.1 Theory

We consider the local minima of the potential as trapping sites for the colloid. The particle sits in a well and after a certain waiting time jumps into a neighboring minimum. Therefore, we consider a theory with a random walker jumping between trapping sites. The probability to leave a site is given by a transition rate Γ. Its inverse Γ^{-1} denotes a typical waiting time. The mean square displacement is calculated by

$$\left\langle r^2(t) \right\rangle = \sum_j p(x_j, y_j, t)(x_j^2 + y_j^2), \tag{8.12}$$

where the sum is over all trapping sites, i.e., all local minima of the potential, and $p(x, y, t)$ is the probability for the walker to be at position (x, y) at time t. In the square and also in triangular or hexagonal lattices, both the distance between nearest neighbors and the number of nearest neighbors is constant. In the decagonal potential this is not the case. Nevertheless, we will develop the theory for regular lattices and will then show that the results well approximate the random walk in the decagonal potential when mean values for the numbers of nearest neighbors and their distances are chosen.

The dynamics of the probability $p(x, y, t)$ is governed by the rate equation:

$$\frac{d}{dt} p(x_j, y_j, t) = -z\Gamma(x_j, y_j)p(x_j, y_j, t) + \sum_{i \in \mathrm{NN}_j} \Gamma(x_i, y_i)p(x_i, y_i, t), \tag{8.13}$$

where the sum is over all nearest neighbors of the minimum j located at x_j, y_j and z is the number of its nearest neighbors. Equation (8.13) describes the temporal change of the probability to be at the trapping site j. The first term on the right-hand side corresponds to particles leaving the trap and the second term to colloids reaching site j from neighboring traps. In the following we define a time-dependent diffusion constant $D(t)$ by

$$D(t) = \frac{d}{dt} \left\langle r^2(t) \right\rangle . \tag{8.14}$$

For normal diffusion this gives the conventional diffusion constant in $\langle r^2(t) \rangle = 4Dt$. Inserting equation (8.13) into the time derivative of equation (8.12), the diffusion constant is connected to the transition rates and $p(x_j, y_j, t)$:

$$D(t) = \frac{1}{4} \sum_j \left[-z\Gamma(x_j, y_j)p(x_j, y_j, t) + \sum_{i \in \mathrm{NN}_j} \Gamma(x_i, y_i)p(x_i, y_i, t) \right] (x_j^2 + y_j^2). \tag{8.15}$$

After interchanging the summation

$$\sum_j \sum_{i \in \mathrm{NN}_j} \Gamma(x_i, y_i) p(x_i, y_i, t)(x_j^2 + y_j^2) = \sum_i \sum_{j \in \mathrm{NN}_i} \Gamma(x_i, y_i) p(x_i, y_i, t)(x_j^2 + y_j^2), \tag{8.16}$$

the second term in (8.15) can be calculated for a square, triangular, and hexagonal lattice:

$$\sum_{j \in \mathrm{NN}_i} (x_j^2 + y_j^2) = z x_i^2 + z y_i^2 + z l^2, \tag{8.17}$$

where l is the jump length (e.g., the lattice constant a_V in the square lattice). Therefore with equations (8.17) and (8.16), equation (8.15) becomes

$$D(t) = \frac{z l^2}{4} \sum_j \Gamma(x_j, y_j) p(x_j, y_j, t). \tag{8.18}$$

In the long-time limit, this gives

$$D_\infty = \frac{z l^2}{4} \langle\langle \Gamma \rangle\rangle . \tag{8.19}$$

Equation (8.19) is a well known result for the time-independent asymptotic diffusion constant given, e.g., in reference [291]. The average $\langle\langle \cdot \rangle\rangle$ is weighted according to the occupation probabilities of the trapping sites. Note that equation (8.18) is a more general relation since it is not only valid in the asymptotic long-time regime but for all times, where the diffusion constants generally depend on time.

We now introduce the probability $P(V_m, t)dV_m$ for a colloid to be at time t in a minimum with the depth within the interval $[V_m, V_m + dV_m]$. In the following, we will study diffusion based on the rate equation for $P(V_m, t)$ instead of using $p(x, y, t)$. However, this is only possible if the transition rates Γ do not depend on the location of the trapping sites and, especially, if there are no positional correlations of the transition rates. Therefore we now assume that the transition rate Γ only depends on the depth of the well $V_m = |V(x, y)|$ at the trapping site. Later we will show that this assumption is reasonable, if one considers Kramer's rate theory to calculate the transition rate for leaving a minimum.

We replace the average in space in equation (8.18) by an average over all possible depths V_m. Therefore the diffusion constant becomes

$$D(t) = \frac{z l^2}{4} \int_0^{V_0} dV_m \Gamma(V_m) P(V_m, t), \tag{8.20}$$

where the depth V_m is limited to the range between 0 and V_0. The rate equation for $P(V_m, t)$ then reads

$$\frac{d}{dt} P(V_m, t) = -z\Gamma(V_m) P(V_m, t) + z\rho(V_m) \int_0^{V_0} dV_m' \Gamma(V_m') P(V_m', t). \tag{8.21}$$

The first term on the right-hand side is the probability of a colloid to leave a trapping site of depth V_m; the second term gives the averaged probability that the colloid jumps into the potential minimum of this site. The probability density $\rho(V_m)$ introduced in section 3.3.3 for the decagonal potential takes into account the distribution of potential depths. Note that the rate equation (8.21) does not depend on the history of the colloidal path. Therefore, it corresponds to a theory with annealed disorder. The simulations, however, correspond to a system with quenched disorder, i.e., the depth of a potential minimum has not changed when it is occupied by the colloid for a second time. It is known that theories with annealed disorder lead to the same results as theories with quenched disorder if the average mean waiting time is finite [292]. This is fulfilled in our system because the depth of our potentials is limited.

We now use the Laplace transform with respect to time:

$$\overline{P}(V_m, s) = \int_0^\infty dt \exp(-st) P(V_m, t). \tag{8.22}$$

The Laplace transform of equation (8.21) reads

$$s\overline{P}(V_m, s) - P_0(V_m) = -z\Gamma(V_m)\overline{P}(V_m, s) + z\rho(V_m) \int_0^{V_0} dV_m' \Gamma(V_m')\overline{P}(V_m', s), \tag{8.23}$$

where $P_0(V_m) = P(V_m, t = 0)$ is the distribution at $t = 0$. To solve equation (8.23) we define

$$c(s) = \int_0^{V_0} dV_m' \Gamma(V_m')\overline{P}(V_m', s), \tag{8.24}$$

and calculate $\overline{P}(V_m, s)$ from equation (8.23):

$$\overline{P}(V_m, s) = \frac{P_0(V_m)}{z\Gamma(V_m) + s} + \frac{z\rho(V_m)}{z\Gamma(V_m) + s} c(s). \tag{8.25}$$

Inserting Eq. (8.25) into (8.24) and solving for $c(s)$ gives

$$c(s) = \frac{\int_0^{V_0} dV_m' \frac{\Gamma(V_m')P_0(V_m')}{z\Gamma(V_m')+s}}{s\int_0^{V_0} dV_m' \frac{\rho(V_m')}{z\Gamma(V_m')+s}}. \tag{8.26}$$

Equation (8.26) together with (8.25) represents the Laplace transform of the solution to the rate equation (8.21). Since the inverse Laplace transform is too complicated, we calculate approximate solutions for the limit $t \to \infty$.

To determine the long-time behavior of the diffusion constant (8.20), we choose an ansatz, where the system relaxes exponentially to the asymptotic diffusion constant D_∞ on a time scale given by τ:

$$D(t) = D_\infty \left(1 + e^{-t/\tau}\right). \tag{8.27}$$

The limit of large times t corresponds to the limit $s \to 0$. We determine the long-time behavior of $D(t)$ by comparing the expansion for small s of the Laplace transform of ansatz (8.27)

$$s\overline{D}(s) \approx D_\infty (1 + s\tau) \tag{8.28}$$

to the Laplace transform of $D(t)$ in equation (8.20):

$$\overline{D}(s) = \frac{zl^2}{4} \int_0^{V_0} dV_m \Gamma(V_m) \overline{P}(V_m, s). \tag{8.29}$$

Calculating the expansion of $s\overline{D}(s)$ for $s \to 0$ by using equations (8.25), (8.26), and (8.29), we are able to identify the asymptotic diffusion constant

$$D_\infty = \lim_{t\to\infty} D(t) = \lim_{s\to 0} s\overline{D}(s) = \frac{zl^2}{4\int_0^{V_0} dV_m \frac{\rho(V_m)}{\Gamma(V_m)}} \tag{8.30}$$

and the time scale

$$\tau = \frac{1}{z} \frac{\int_0^{V_0} dV_m \frac{\rho(V_m)}{\Gamma(V_m)^2}}{\int_0^{V_0} dV_m \frac{\rho(V_m)}{\Gamma(V_m)}} + \frac{1}{z} \int_0^{V_0} dV_m \frac{\rho(V_m) - P_0(V_m)}{\Gamma(V_m)}. \tag{8.31}$$

Equation (8.30) corresponds to the well-known result

$$D_\infty = \frac{zl^2}{4\left\langle \frac{1}{\Gamma(V_m)} \right\rangle}, \tag{8.32}$$

where the average is taken over all trapping sites (see e.g. [290,291]). However, in addition we have also determined the time scale τ on which the system relaxes into the diffusive regime.

to calculate the transition rate $\Gamma(V_m)$ necessary in equations (8.30) and (8.31), we use Kramer's formula [293]

$$\Gamma(V_m) = \frac{\omega_m \omega_b}{2\pi\gamma} e^{-\beta V_m}. \tag{8.33}$$

Here, ω_m and ω_b are the square roots of the absolute values of the curvatures taken, respectively, at the potential minimum and the maximum of the potential barrier, the particle tries to overcome. Using equation (8.7), we find for the regular square potential:

$$\Gamma(V_m) = \frac{\pi V_m}{\gamma l^2} e^{-\beta V_m}. \tag{8.34}$$

In the random square lattice, the curvature or second derivative of the potential ist not continuous at the maximum situated between two minima. However, it is reasonable to take the one-sided value coming from the minimum the particle is trying to leave. Then $\omega_b = \omega_m$ and equation (8.34) still holds.

The regular square potential has only one possible minimum value, i.e., $\rho(V_m) = V_0\delta(V_m - V_0)$. So evaluating equations (8.30) and (8.31), we arrive at

$$D_\infty^{(reg)} = \frac{\pi z V_0}{4\gamma} e^{-\beta V_0} \tag{8.35}$$

and

$$\tau^{(reg)} = \frac{\gamma l^2}{\pi z V_0} e^{\beta V_0}. \tag{8.36}$$

Next we calculate D_∞ and τ for the random square potential. We will also use these results as an estimate for the decagonal potential. For $\beta V_0 \gg 1$, the integrals in equations (8.30) and (8.31) are determined by the behavior close to V_0 due to the exponential dependence of $\Gamma(V_m)$ on βV_m. We therefore expand $\log[\rho(V_m)/\Gamma(V_m)]$ and similar expressions for the other integrands around V_0 to linear order in $V - V_0$. Using these expansions in the various integrals of equations (8.30) and (8.31), we arrive at the approximate values

$$D_\infty^{(rand/deca)} \approx \frac{\pi z \beta V_0}{4\gamma\rho(V_0)} e^{-\beta V_0} \tag{8.37}$$

and

$$\tau^{(rand/deca)} \approx \frac{\gamma l^2}{2\pi z V_0} e^{\beta V_0}. \tag{8.38}$$

In the decagonal potential the numbers and distances of the nearest neighbors are not constant. To apply equations (8.37) and (8.38) to the decagonal potential, we use the average number $z = 5.85$ for the nearest neighbors and the average step length $l = 0.73a_V$ as introduced in section 3.3.4. Note that the approximate value of the time scale $\tau^{(rand/deca)}$ is independent of the initial distribution $P_0(V_m)$.

In the regular square lattice only one characteristic time scale exists and, therefore, a sharp crossover to conventional diffusion occurs when the particle escapes the potential minimum in which it has relaxed in the beginning. In contrast, a broad distribution of time scales seems to be important in the random and the decagonal potential. The time scale $\tau^{(rand/deca)}$ is the largest possible time scale of the system since it is associated with the deepest potential minimum at V_0 and therefore with the smallest of all possible Kramer's escape rates. In a potential, where the minimum value is not limited from below, there is no limiting time scale and the colloidal particle will always exhibit subdiffusion [283–286].

8.3.2 Results and comparison to simulations

We use the random trap model developed in the last subsection to calculate the full time dependence of the mean square displacement. The probability density $P(V_m, t)$ is determined from a discretized version of the rate equation (8.21). We choose $P(V_m, 0) = \rho(V_m)$ as starting condition corresponding to Brownian particles randomly placed into the minima. The mean square displacement is calculated from the diffusion constant by integrating equation (8.14), the resulting time dependence is plotted in figures 8.4(a) and (c). The

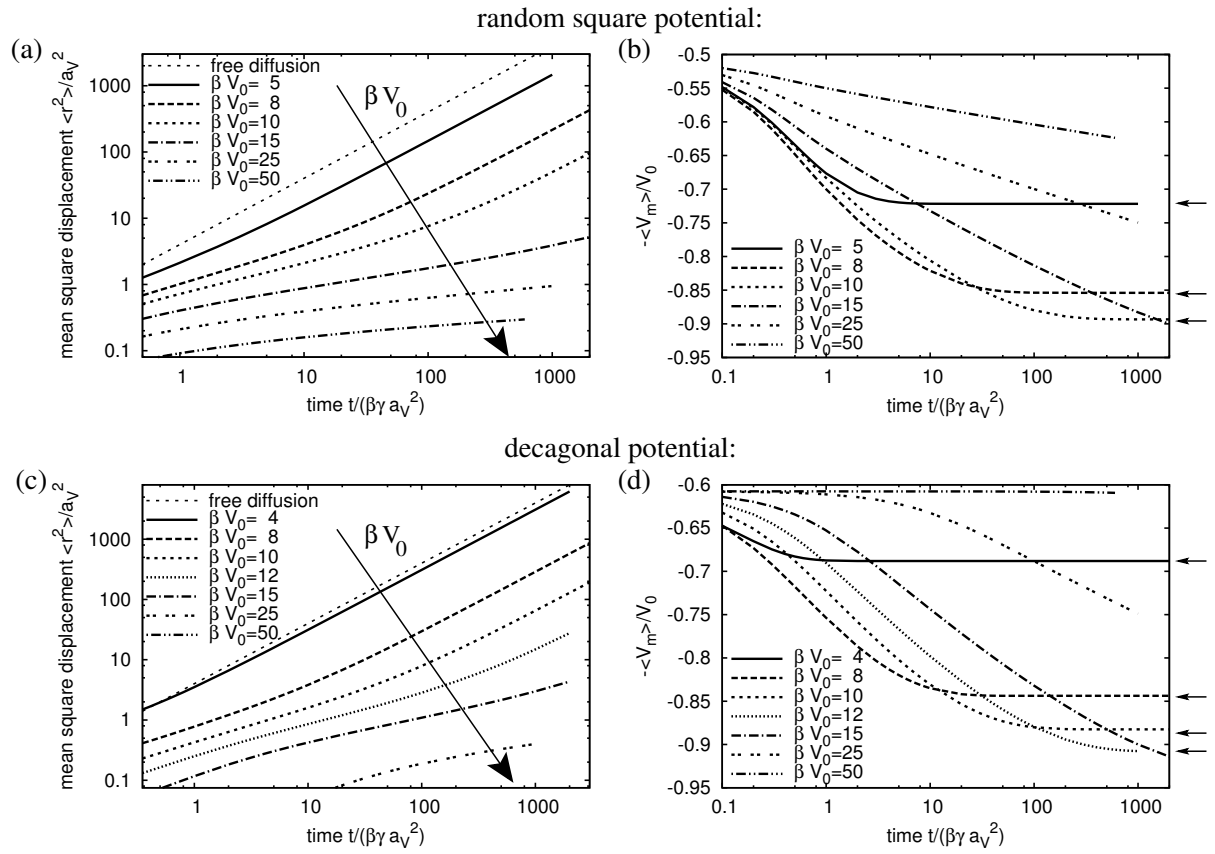

Figure 8.4: Mean square displacement (left-hand side) and average depth of the occupied minimum (right-hand side) calculated from the random trap model as function of time for the random square (a,b) and the decagonal (c,d) potential.

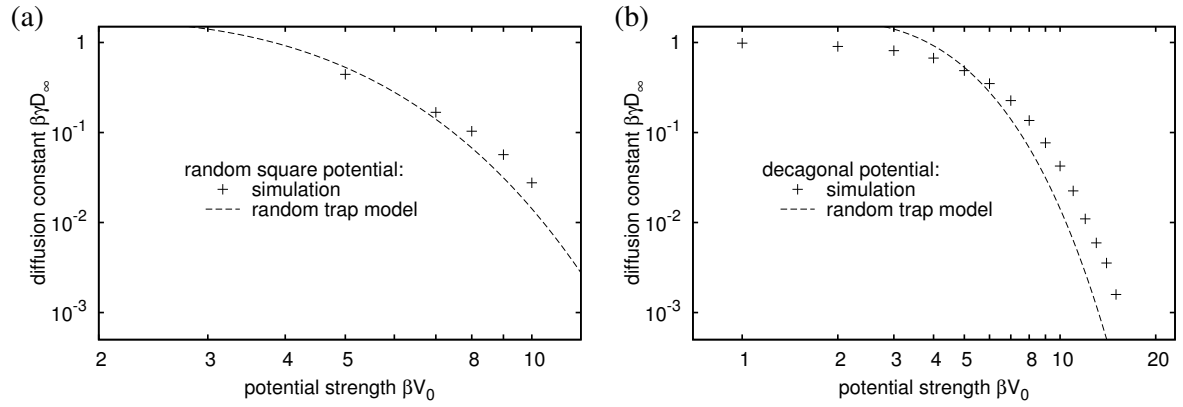

Figure 8.5: Diffusion constant in the long-time limit as a function of the potential strength βV_0 in (a) the random square potential and (b) the decagonal potential. The lines are calculated with the random trap model, the points are simulation results obtained by fits to the asymptotic regime of the mean square displacement.

right-hand side of figure 8.4 shows the average depth $\langle V_m \rangle$ of the minimum the particle occupies at time t. The results agree qualitatively with the simulation results (see figure 8.2). The crossover from subdiffusion to the asymptotic diffusive regime is clearly visible for the mean square displacement. Only the short-time behavior is different in the random trap model, because the particles already start in a minimum of the potential and therefore the short-time relaxation visible in the simulations is not included. Note that the average depth $\langle V_m \rangle$ of the occupied minimum shown in 8.4(b) and (d) is not the same quantity as the average potential energy plotted on the right-hand side of figure 8.2. Nevertheless, the behavior of the curves is very similar: In the random trap model the particles start in randomly chosen minima, i.e., for $t = 0$ one has $\langle V_m(0) \rangle = -0.5 V_0$ in the random and $\langle V_m(0) \rangle = -0.603 V_0$ in the decagonal potential. This corresponds to the positions of the kinks in the simulated curves (see end of section 8.2.2). For intermediate and long times the curves are very similar. Especially the plateau for $\beta V_0 = 50$ is found in theory and in the simulations for the decagonal potential, whereas in both cases there is no plateau but a decrease for the random potential.

Using equation (8.37), the asymptotic diffusion constant can be calculated for $\beta V_0 \gg 1$. In figure 8.5 we compare the theoretical results to the diffusion constants obtained by asymptotic fits to the simulated curves. There are differences especially for larger potential strengths βV_0 and our random trap model is only approximately valid. This probably is due to shallow minima in the potential landscape where the particle is not bound to the minimum and during a "jump" between two wells finite-time excursions outside the minimum occur. Furthermore, jumps exist that do not take place between nearest neighbors. Finally, we also neglected spatial correlations in the depths of the potential wells in our model.

It is difficult to determine the crossover time τ by fits to the curves of the simulations because the resulting values strongly depend on the range of the fit. Therefore, to quantitatively test our theory, we plot the time dependence of the mean square displacement where time is rescaled τ and the mean square displacement by $D_\infty \tau$. The rescaled curves are shown in figures 8.6(a) to (c). For the regular square potential the curves perfectly collapse on a single curve for $\beta V_0 \gg 1$, as can be seen in figure 8.6(a). However, for the random square and the decagonal potential shown in 8.6(b) and (c), respectively, the collapse is not as good. In figure 8.6(d) we plot the curves of the decagonal potential with the mean square displacement rescaled by $D_\infty^{(fit)} \tau$, where $D_\infty^{(fit)}$ is taken from asymptotic fits to the simulation results. The collapse in figure 8.6(d) is much better, therefore the main discrepancies between simulations and theory are the differences between the calculated asymptotic diffusion constants and the ones obtained by fits to the simulations. These differences can be seen in figure 8.5 and were already discussed.

Another test for our theory is to compare the distribution $P(V, t)$ in the limit $t \to \infty$. Comparing equations (8.20) and (8.30), one finds

$$P^{(stat)}(V_m) = \frac{\frac{\rho(V_m)}{\Gamma(V_m)}}{\int_0^{V_0} dV'_m \frac{\rho(V'_m)}{\Gamma(V'_m)}}. \tag{8.39}$$

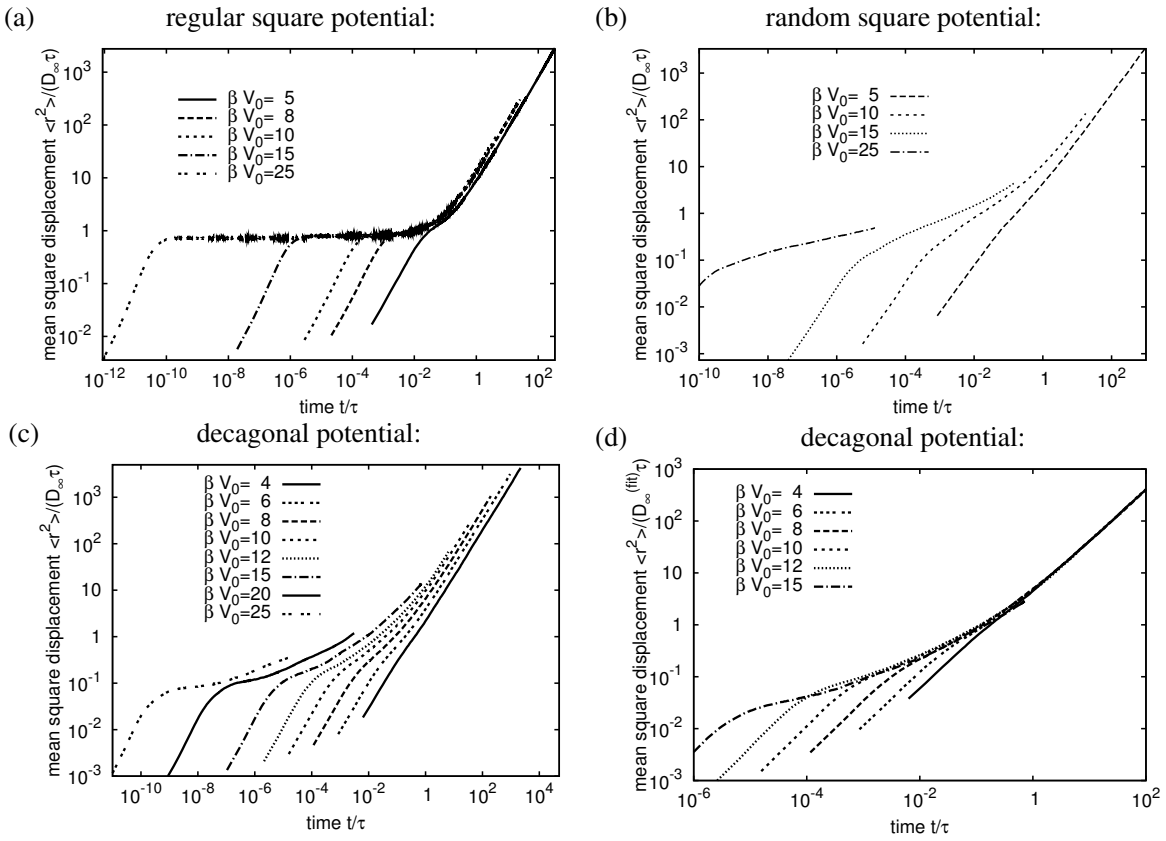

Figure 8.6: Rescaled mean square displacement of the Brownian dynamics simulations in (a) a regular square, (b) a random square, and (c,d) in a decagonal potential. The time is rescaled by an factor of $1/\tau$ and the mean square displacement by (a-c) $1/(D_\infty \tau)$ or (d) by $1/(D_\infty^{(fit)}\tau)$, where $D_\infty^{(fit)}$ is the fitted asymptotic diffusion constant.

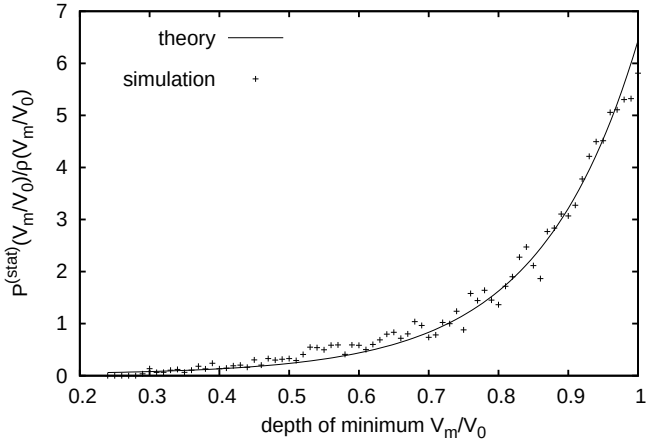

Figure 8.7: Stationary distribution $P^{(stat)}(V_m)$ in the long-time limit for the decagonal potential with $\beta V_0 = 8$.

Note that this distribution is stationary since it does not change with time anymore, $\frac{d}{dt}P^{(stat)}(V_m) = 0$. On the other hand, the distribution in real space $p(x, y, t)$ is not stationary for infinite systems. It is a big advantage of our approach, which is based on the distribution $P(V_m, t)$ for finding a particle in a minimum of depth V_m, rather than on the positional distribution $p(x, y, t)$, that $P(V_m, t)$ relaxes into a stationary long-time limit when the transition into the diffusive regime takes place. Figure 8.7 presents $P^{(stat)}(V_m)$ for the decagonal potential with $\beta V_0 = 8$ as given by the analytic formula (8.39) and compares it to the stationary distribution determined in the Brownian dynamics simulations in the long-time limit. Theory and simulation agree very well.

8.4 Brownian motion started in equilibrium

In section 8.2 the colloidal particles were started at random positions in the potential. In this section we consider the Brownian motion in equilibrium that was also studied experimentally. We will discuss the experiment and its results in the next subsection and compare it to simulations in subsection 8.4.2.

8.4.1 Experimental results

In experiments, the ensemble average is replaced by an average over time, i.e., the mean square displacement is determined according to

$$\langle r^2_{(exp)}(t)\rangle = \langle\langle[\mathbf{r}(t'+t) - \mathbf{r}(t')]^2\rangle_{t'}\rangle, \tag{8.40}$$

where $\langle\cdot\rangle$ denotes the usual average over different runs and $\langle\cdot\rangle_{t'}$ is the average over time t'. The results of experiments by J. Baumgartl [244] are shown in figure 8.8. Using video microscopy, the trajectories of up to 72 polystyrene spheres with a diameter of 1.8 μm immersed in water were recorded by taking 30.000 to 100.000 images at a frame rate of 10 Hz. The colloidal suspension was highly diluted so that neighboring particles did not interact during the diffusion process. At a first glance, the experimental results look similar to the simulation results of figure 8.2. However, only dynamics in thermal equilibrium was measured in the experiment. As we will show in the next subsection, the extended non-equilibrium relaxation process we found in theory, is not included in the experimental results. Note that as long as the mean square displacement is calculated according to (8.40) such a relaxation process cannot be observed, because most of the time the system is in equilibrium and possible non-equilibrium dynamics at the beginning of a measurement can be neglected.

8.4.2 Simulation results

In the simulation we calculate the mean square displacement as an ensemble average for trajectories started in equilibrium, i.e., with starting positions given by the stationary distribution of the asymptotic diffusive regime [see equation (8.39)]. In figure 8.9, results

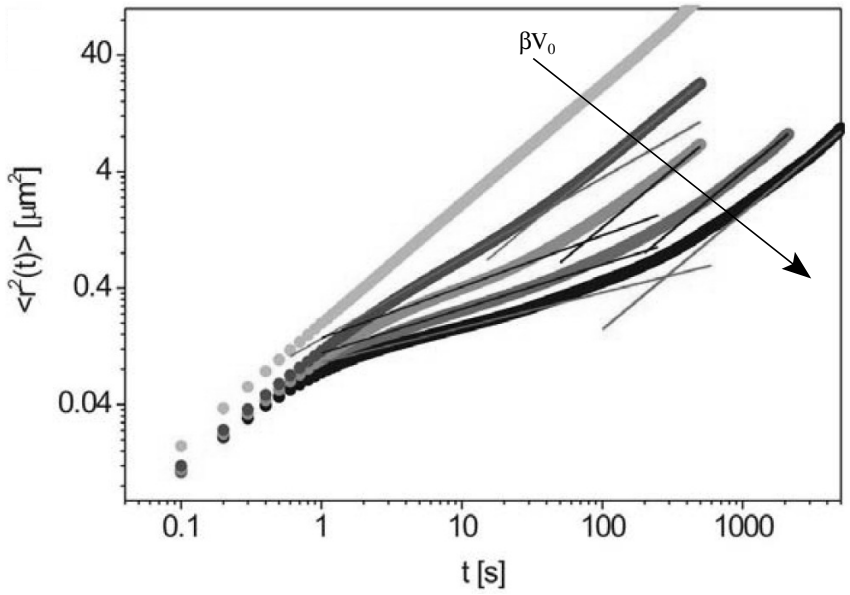

Figure 8.8: Experimental measurement of the time dependence of the mean square displacement in a decagonal potential measured in thermal equilibrium. The curves are the results for potential strengths βV_0 of 0, 5.5, 7.7, 14.4, and 20. Experiment and figure by J. Baumgartl [244].

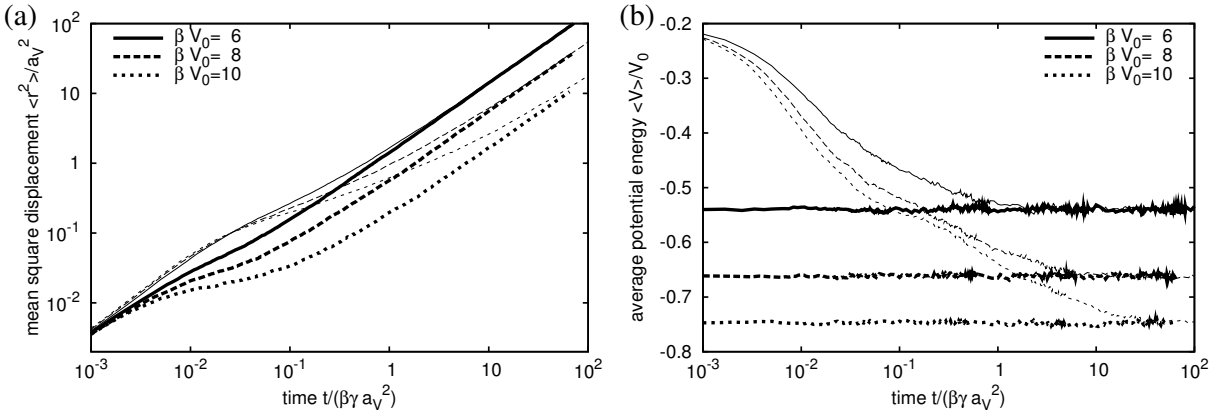

Figure 8.9: (a) Mean square displacement and (b) average potential energy obtained by Brownian dynamics simulations started with the stationary equilibrium distribution (thick lines) or at random positions in the potential (thin lines).

of Brownian dynamics simulation of the dynamics in thermal equilibrium are plotted with thick lines and compared to the ones obtained by particles started in non-equilibrium shown with thin lines. Obviously, the crossover into the asymptotic diffusive regime occurs at much shorter times and on much smaller length scales if the colloids are already in thermal equilibrium. The short-time dynamics is due to the motion within the initial well. As soon as the first jump into another minimum takes place, the diffusive limit is reached. Unlike in the non-equilibrium case, it is not necessary to explore different potential minima to relax towards the stationary distribution in thermal equilibrium. Therefore, the experiments presented in the last subsection do not show the very slow relaxation process of colloids starting in non-equilibrium. The observed small-time dynamics is the crossover from almost free diffusion within a potential well to the asymptotic diffusive regime, where the colloid jumps between minima.

8.5 Colloidal motion in potentials with phasonic drift

In this section we study the motion of a particle in a potential subject to a constant phasonic drift, i.e., the phasonic displacement is changed at a constant rate in time (cf. section 3.4.3). First, we determine the mean drift of the colloids induced by the phasonic drift. Second, we show that the phasonic drift leads to a crossover into a diffusive non-equilibrium state. Finally, we modify the random trap model such that the phasonic drift is included.

8.5.1 Ballistic motion

Colloidal particles in a potential with an imposed phasonic drift perform a drift motion on average, i.e., they move ballistically. To study this motion without including thermal fluctuation, we set the temperature to zero and perform Brownian dynamics simulations. Then the simulations are completely deterministic and the averages are taken over different starting conditions. In figure 8.10 the directions of the drift velocity $\mathbf{v}$ of the particles as a function of the directions of the phasonic drift velocity $\mathbf{v}_w$ are shown. The absolute value of the phasonic drift velocity is chosen sufficiently small so that the particles are able to follow the positions of the local minima they occupy. Viscous forces are not yet important. The directional dependence roughly follows a line, where the polar angle α_v of the drift velocity $\mathbf{v}$ with respect to the y-direction is related to the angle α_w of the phasonic drift velocity $\mathbf{v}_w$ via

$$\alpha_v = -3\alpha_w. \tag{8.41}$$

For angles α_w that are integer multiplies of $\pi/10$, this relation seems to be exact. The results of the simulation show a superimposed periodicity with period $\pi/5$, which is due to the symmetry of the potential. The factor 3 in relation (8.41) is probably connected to the index $3j$ mod 5 in the definition of the phasonic displacements [cf. equation 3.31].

In figure 8.11 the absolute value of the drift velocity as a function of the phasonic drift velocity is shown. For small phasonic drift velocities the dependence is linear, indicating

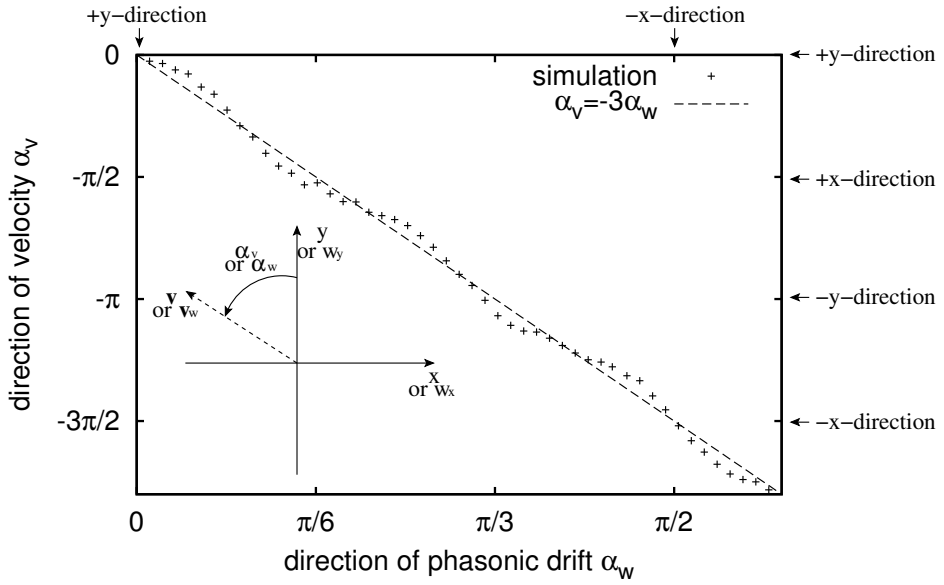

Figure 8.10: Direction α_v of the mean drift velocity $\mathbf{v}$ of the particles as a function of the direction α_w of the phasonic drift velocity $\mathbf{v_w}$, that causes the colloidal drift. The angles α_v and α_w are measured with respect to the y direction, as shown in the inset. The dashed line corresponds to $\alpha_v = -3\alpha_w$. The temperature was set to 0 in the Brownian dynamics simulations, and the absolute value of the phasonic drift velocity was $|\mathbf{v}_w| / (V_0/\gamma a_V) = 5 \cdot 10^{-4}$.

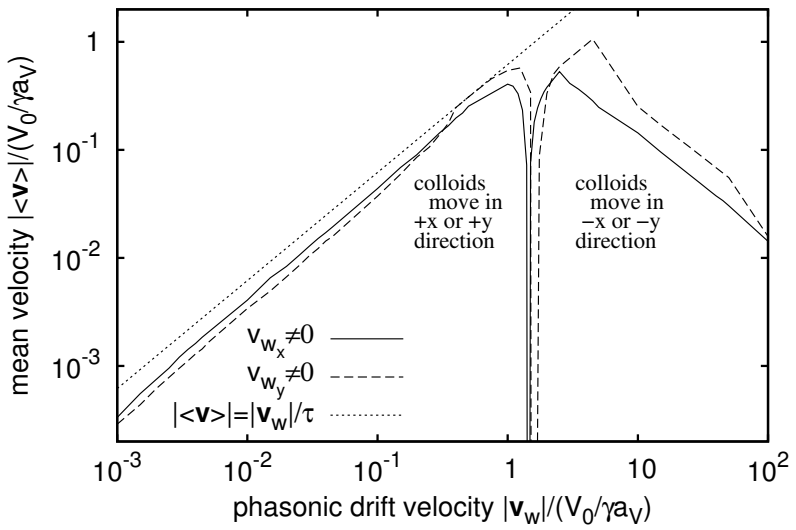

Figure 8.11: Absolute drift velocity of the colloids as a function of the phasonic drift velocity. The solid and dashed lines are for phasonic drifts in w_x- and w_y-direction, respectively. On the left-hand side, the motion of the colloids is in x- or y-direction, on the right hand side, it is in $-x$- or $-y$-direction. The dotted line shows a linear dependence explained in the text. The temperature was set to 0.

that the particles follow the position of the minimum they occupy. If the motion of the wells corresponds to the motion of the minimum of the averaged potential shown in figure 3.19, the drift velocity of the colloids should be [cf. equation 3.33 or 3.35]

$$|\langle \mathbf{v} \rangle| = |\mathbf{v}_w| / \tau, \tag{8.42}$$

where τ is the number of the golden ratio. Relation (8.42) is plotted in figure 8.11 as dotted line. Even for very small phasonic drift velocities, the values predicted by (8.42) are larger than the colloidal drift found in the simulations. Therefore, not all local minima move according to the minima in the averaged potential. In fact, most single particle trajectories display a zigzag-like shape (cf. minima in figure 3.18), which would lead exactly to relation (8.42). However, a few colloids (or positions of local minima) move in opposite direction and therefore the average velocity is decreased.

For a phasonic drift velocity $|\mathbf{v}_w| / (V_0/\gamma a_V)$ slightly larger than 1 the drift of the particles is suddenly reversed. This is caused by the fact that due to viscous forces the colloid can no longer follow the position of a minimum for such a large phasonic drift: The relaxation time, i.e., the time a colloid needs to relax into a local minimum, is roughly given by $\gamma a_V^2/V_0$. Therefore, for $|\mathbf{v}_w| / (V_0/\gamma a_V) \gg 1$, the time scale of the relaxation process is larger than the time scale $a_V / |\mathbf{v}_w|$ on which the minima of the potential change. For large phasonic drift velocities, the colloidal motion is no longer connected to the motion of the positions of local minima.

8.5.2 Mean square displacement and non-equilibrium steady state

In figure 8.12 the mean square displacement and the average potential energy obtained from Brownian dynamics simulation is shown for different phasonic drift velocities. The mean square displacement is calculated after subtracting the ballistic motion due to the phason-induced drift [cf. equation (6.21)].

Figure 8.12(a) shows that the crossover into an asymptotic diffusive regime occurs at earlier times if the phasonic drift velocity is increased. The average potential energy weakly oscillates around an asymptotic energy level. The oscillations are probably due to the almost periodic decrease and increase of the depths of the potential wells (cf. section 3.4.3). By increasing the phasonic drift velocity, the asymptotic energy level is also increased. Obviously, the phasonic drift acts as a constant influx of energy and therefore keeps the colloids in a non-equilibrium steady state in the long-time limit. In section 8.6.3 we show that this system can be used as a model system for studying the properties of the non-equilibrium.

8.5.3 Modification of the random trap model

If a phasonic drift is applied to the potential landscape, the depths of its minima are continuously changing. Therefore, the potential energy of a colloid changes either due to jumps into neighboring minima or due to the imposed phasonic drift. The probability

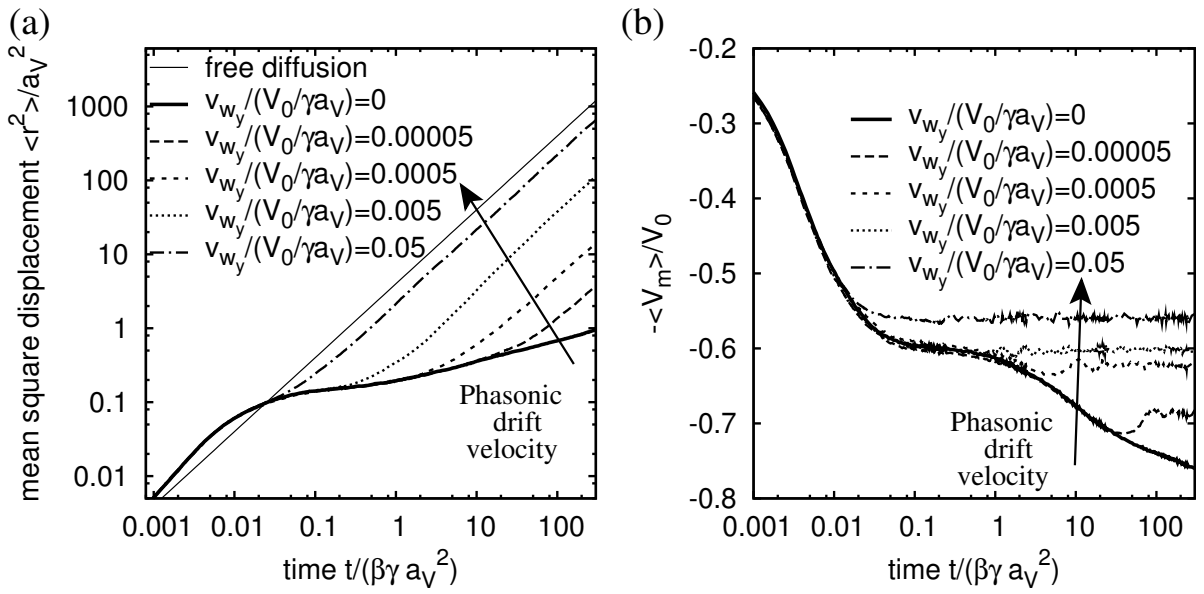

Figure 8.12: (a) Mean square displacement and (b) average potential energy obtained from Brownian dynamics simulation in a decagonal potential with $\beta V_0 = 20$ for different phasonic drift velocities v_{w_y}, given in units of $V_0/(\gamma a_V)$.

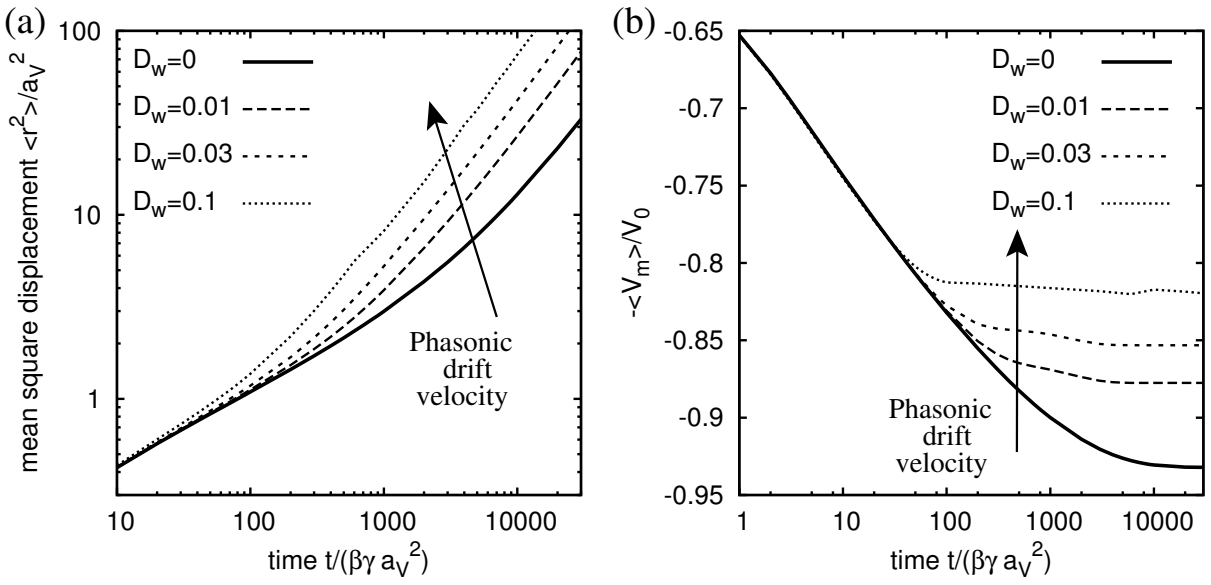

Figure 8.13: (a) Mean square displacement and (b) average potential energy obtained by the modified random trap model for different values of the parameter D_w, which in the simulations is controlled by the phasonic drift velocity. The potential strength is kept constant at $\beta V_0 = 15$.

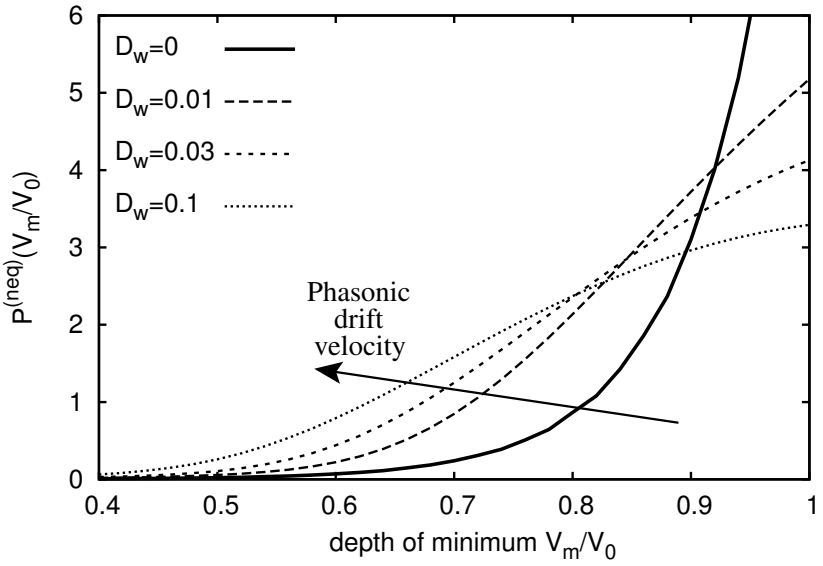

Figure 8.14: Probability distribution $P^{(neq)}(V_m)$ to find a particle in a minimum with a depth in $[V_m, V_m + dV_m]$ in the asymptotic long time limit for different phasonic drift velocities. The distributions were determined by the modified random trap model.

density $P(V_m, t)$ that a colloid occupies a minimum with a depth within $[V_m, V_m + dV_m]$ decreases at a rate proportional to $P(V_m, t)$ due to the changing depth of the minimum. However, at the same time it increases by a term proportional to $P(V_m - dV_m, t) + P(V_m + dV_m, t)$ because some minima of depth $V_m - dV_m$ or $V_m + dV_m$ will have the depth V_m at $t + dt$. In total, the additional temporal change of $P(V_m, t)$ due to the phasonic drift is proportional to

$$P(V_m - dV_m, t) + P(V_m + dV_m, t) - 2P(V_m, t) \propto \frac{d^2}{dV_m^2} P(V_m, t). \tag{8.43}$$

Since the depth of a minimum can be either decrease from V_m to $V_m - dV_m$ or increase to $V_m + dV_m$ we included a factor of 2 in the last term of the left-hand side of (8.43). Hence, the rate equation of the random trap model (8.21) is modified by adding a diffusion term, i.e.,

$$\frac{d}{dt} P(V_m, t) = -z\Gamma(V_m) P(V_m, t) + z\rho(V_m) \int_0^{V_0} dV_m' \Gamma(V_m') P(V_m', t) + D_w \frac{d^2}{dV_m^2} P(V_m, t), \tag{8.44}$$

where D_w describes the rate of changes in the depths of the minima. In the simulations these changes of the minima are controlled by the phasonic drift velocity $\mathbf{v}_w$. We solve equation (8.44) numerically and by using equation (8.20) to determine the diffusion constant of the colloids, we then calculate the mean square displacement. In figure 8.13 the time dependence of the mean square displacement and the average potential energy is shown. There is a good qualitative agreement with the simulation results (cf. figure 8.12).

Figure 8.14 shows the probability distribution $P^{(neq)}(V_m) = \lim_{t\to\infty} P(V_m, t)$ in the asymptotic long time limit. The phasonic drift decreases the occupation of deep minima and increases $P^{(neq)}(V_m)$ for intermediate V_m.

8.6 Non-equilibrium statistics

In this section, we shortly introduce some central ideas of non-equilibrium statistical theories and motivate how they may be applied to our system.

8.6.1 Derivation of path-ensemble averages

Mainly following the work of Crooks [294], we first present a derivation of path-ensemble averages, i.e., averages of observables over an ensemble of different paths, which a system performs with time. Usually the path ensemble is defined by an initial distribution in thermal equilibrium and a time-dependent external perturbation that drives the system out of equilibrium. We also derive some more general new relations where we do not assume that the equilibrium distribution is given in form of the Boltzmann distribution. The basic idea to derive path-ensemble averages is to split the dynamics of the system into a part caused by the coupling to the heat bath and a part due to external perturbations such as the temporal variation of the external potential, e.g., caused by a phasonic drift. The dynamics due to the coupling to the heat bath is characterized by the fact that it does not change an equilibrium distribution, i.e., a system is never driven out of equilibrium. On the other hand, external perturbations change the energies associated with the states of the system and therefore drive the system out of equilibrium.

We consider a system with discretized states at discretized times and assume that the dynamics is Markovian, i.e., it only depends on the current state but not on its history. The probability to be in state x at time t is $\rho_x(t)$. The external perturbations are characterized by the time-dependence of the state energy (or a similar quantity) $E_x(t)$. We assume that $E_x(t)$ never is infinite. We now split the dynamics of the system in two parts. First, the temporal evolution of the system due to the coupling to a heat bath is written as

$$\rho_{x'}(t+1) = \sum_x M(t)_{x'x}\rho_x(t), \tag{8.45}$$

where $M(t)$ is the transition matrix whose element $M(t)_{x'x}$ is the probability to get from state x to x'. In the following, we leave away the sum symbol and perform a summation over indices that appear twice. In the second part of the temporal evolution of the system, the new state x' assumes the energy $E_{x'}(t+1)$.

In equilibrium, there is a stationary distribution $\pi_{x(t)}(E(t)) = \rho^{(stat)}_{x(t)}(t)$ that usually is given by the equilibrium distribution of a canonical ensemble. It does not explicitly depend on time. However, it relies on the states $x(t)$ and the energy $E(t) = E_x(t)$, which both may be time-dependent due to the external perturbations (see below). We require

the dynamics described by M to fulfill the following relation:

$$\pi_{x'}(E) = M(t)_{x'x}\pi_x(E), \tag{8.46}$$

i.e., $\pi_x(E)$ has to be invariant under a transition $M(t)$ so that without external perturbations a system in equilibrium stays in equilibrium. Equation (8.46) is the central assumption to derive path-ensemble averages. It is valid in all systems with detailed balance

$$M(t)_{xx'}\pi_{x'}(E) = M(t)_{x'x}\pi_x(E), \tag{8.47}$$

however, detailed balance is not required here.

We assume a path $[x]$ that starts in state $x(t_0) = x_0$ and ends in $x(t_f) = x_f$. In the following we will always use square brackets $[\cdot]$ to denote such a path. The time-reversed path $[\hat{x}]$ starts at time t_f in state $\hat{x}(t_0) = x(t_f) = x_f$ and ends in $\hat{x}(t_f) = x(t_0) = x_0$. Correspondingly, $\hat{E}_{\hat{x}}(t)$ describes the time-dependence of the energy along the reversed path. In general, $\hat{x}(t) = x(t_f - t)$. The dynamics of the reverse path is governed by $\hat{M}(t)$ with

$$\hat{\rho}_{\hat{x}'}(t) = \hat{M}(t)_{\hat{x}'\hat{x}}\hat{\rho}_{\hat{x}}(t-1), \tag{8.48}$$

where $\hat{\rho}_{\hat{x}}(t)$ is the probability for the reversed path to be in state $\hat{x}(t)$ at time t.

Let $P([x]|x(t_0) = x_0)$ be the probability for a path $[x]$ that starts in state x_0 and $P([\hat{x}]|\hat{x}(t_0) = x_f)$ the probability for the reversed path $[\hat{x}]$ with $\hat{x}(t_0) = x(t_f) = x_f$. The ratio of these probabilities is

$$\frac{P\left([x]|x(t_0) = x_0\right)}{P\left([\hat{x}]|\hat{x}(t_0) = x_f\right)} = \prod_{t=t_0}^{t_f-1} \frac{M(t)_{x(t+1)x(t)}}{\hat{M}(t+1)_{\hat{x}(t+1)\hat{x}(t)}}. \tag{8.49}$$

Because $\prod_{t=t_0}^{t_f-1} \pi_{x(t)}(E(t)) = \prod_{t=t_0}^{t_f-1} \pi_{\hat{x}(t+1)}(\hat{E}(t+1))$, one finds

$$\begin{aligned}
\frac{P\left([x]|x(t_0) = x_0\right)}{P\left([\hat{x}]|\hat{x}(t_0) = x_f\right)} &= \prod_{t=t_0}^{t_f-1} \frac{M(t)_{x(t+1)x(t)}\pi_{x(t)}(E(t))}{\hat{M}(t+1)_{\hat{x}(t+1)\hat{x}(t)}\pi_{\hat{x}(t+1)}(\hat{E}(t+1))} \\
&= \frac{\pi_{\hat{x}(t_0)}(E(t_0))}{\pi_{\hat{x}(t_f)}(E(t_f))} \cdot \prod_{t=t_0}^{t_f-1} \frac{M(t)_{x(t+1)x(t)}\pi_{x(t)}(E(t))}{\hat{M}(t+1)_{\hat{x}(t+1)\hat{x}(t)}\pi_{\hat{x}(t)}(\hat{E}(t))} \\
&= \frac{\pi_{\hat{x}(t_0)}(E(t_0))}{\pi_{\hat{x}(t_f)}(E(t_f))} \cdot \prod_{t=t_0}^{t_f-1} \frac{\pi_{x(t+1)}(E(t))}{\pi_{\hat{x}(t)}(\hat{E}(t))} \\
&= \prod_{t=t_0}^{t_f-1} \frac{\pi_{x(t+1)}(E(t))}{\pi_{\hat{x}(t+1)}(\hat{E}(t+1))} \\
&= \prod_{t=t_0}^{t_f-1} \frac{\pi_{x(t+1)}(E(t))}{\pi_{x(t)}(E(t))}.
\end{aligned} \tag{8.50}$$

To arrive at the third line, we used relation (8.46). Equation (8.50) will be the starting point to derive different types of path-ensemble averages and fluctuation theorems in the next subsection.

Usually the stationary distribution $\pi_x(E(t))$ is given by the equilibrium distribution of the canonical ensemble,

$$\pi_x(E(t)) = \frac{\exp\left(-\beta E_x(t)\right)}{\sum_{x'} \exp\left(-\beta E_{x'}(t)\right)} = \exp\left(\beta F(t) - \beta E_x(t)\right), \tag{8.51}$$

where $\beta = 1/(k_B T)$, $E_x(t)$ is the energy of state x at time t, and $F(t)$ is the free energy

$$F(t) = -k_B T \ln \sum_{x'} \exp\left(-\beta E_{x'}(t)\right). \tag{8.52}$$

Equation (8.50) then becomes

$$\begin{aligned} \frac{P\left([x]|x(t_0)=x_0\right)}{P\left([\hat{x}]|\hat{x}(0)=x_f\right)} &= \prod_{t=t_0}^{t_f-1} \frac{\exp\left(\beta F(t) - \beta E_{x(t+1)}(t)\right)}{\exp\left(\beta F(t) - \beta E_{x(t)}(t)\right)} \\ &= \exp\left(-\beta \sum_{t=t_0}^{t_f-1} \left[E_{x(t+1)}(t) - E_{x(t)}(t)\right]\right) \\ &= \exp\left(-\beta Q\left([x]\right)\right), \end{aligned} \tag{8.53}$$

where $Q\left([x]\right) = \sum_{t=t_0}^{t_f-1} \left[E_{x(t+1)}(t) - E_{x(t)}(t)\right]$ is the total heat exchange with the reservoir, when the system changes its state from $x(t)$ to $x(t+1)$.

8.6.2 Examples of path-ensemble averages and fluctuation theorems

We consider a function $f([x])$ that depends on a path $[x]$ of the system. The average of $f([x])$ over the ensemble of paths is

$$\langle f \rangle_{[x]} = \sum_{[x]} \rho_{x_0}\left(t_0\right) P\left([x]|x(t_0)=x_0\right) f([x]). \tag{8.54}$$

Using equation (8.50), we find

$$\begin{aligned} \langle f \rangle_{[x]} &= \sum_{[x]} \rho_{x_0}\left(t_0\right) \prod_{t=t_0}^{t_f-1} \frac{\pi_{x(t+1)}(E(t))}{\pi_{x(t)}(E(t))} P\left([\hat{x}]|\hat{x}(t_0)=x_f\right) f([x]) \\ &= \sum_{[x]} \frac{\rho_{x_0}\left(t_0\right)}{\hat{\rho}_{x_f}\left(t_0\right)} \prod_{t=t_0}^{t_f-1} \frac{\pi_{x(t+1)}(E(t))}{\pi_{x(t)}(E(t))} \hat{\rho}_{x_f}\left(t_0\right) P\left([\hat{x}]|\hat{x}(t_0)=x_f\right) f([x]) \\ &= \left\langle f \frac{\rho_{x_0}\left(t_0\right)}{\hat{\rho}_{x_f}\left(t_0\right)} \prod_{t=t_0}^{t_f-1} \frac{\pi_{x(t+1)}(E(t))}{\pi_{x(t)}(E(t))} \right\rangle_{[\hat{x}]}. \end{aligned} \tag{8.55}$$

This is one of the most general forms of a path-ensemble average. If the path x and the inverse path $\hat{x}$ are started in equilibrium, $\rho_{x_0}(t_0) = \pi_{x_0}(E(t_0))$ and $\hat{\rho}_{x_f}(t_0) = \pi_{x_f}(E(t_f))$ and therefore

$$\langle f \rangle_{[x]} = \left\langle f \prod_{t=0}^{t_f-1} \frac{\pi_{x(t+1)}(E(t))}{\pi_{x(t+1)}(E(t+1))} \right\rangle_{[\hat{x}]} . \tag{8.56}$$

If $\pi_x(E(t))$ is given by (8.51), we find

$$\begin{aligned} \langle f \rangle_{[x]} &= \left\langle f \prod_{t=0}^{t_f-1} \frac{\exp\left(\beta F(t) - \beta E_{x(t+1)}(t)\right)}{\exp\left(\beta F(t+1) - \beta E_{x(t+1)}(t+1)\right)} \right\rangle_{[\hat{x}]} \\ &= \left\langle f \exp\left(\beta \left\{ F(t_0) - F(t_f) + \sum_{t=0}^{t_f-1} \left[E_{x(t+1)}(t+1) - E_{x(t+1)}(t)\right] \right\}\right) \right\rangle_{[\hat{x}]} \\ &= \langle f \exp\left(\beta \left\{F(t_0) - F(t_f) + W([x])\right\}\right) \rangle_{[\hat{x}]} , \end{aligned} \tag{8.57}$$

where $W([x])$ is the work performed on the system by the external perturbation $W([x]) = \sum_{t=t_0}^{t_f-1} \left[E_{x(t+1)}(t+1) - E_{x(t+1)}(t)\right]$. Usually f is replaced by $f \exp(-\beta W([x]))$ leading to

$$\langle f \exp(-\beta W([x])) \rangle_{[x]} = \langle f \exp(-\beta \Delta F) \rangle_{[\hat{x}]} , \tag{8.58}$$

with $\Delta F = F(t_f) - F(t_0)$. Equation (8.58) is a convenient and useful relation [294] that connects averages over the forward and the backward paths.

For $f = 1$, equation (8.58) becomes

$$\langle \exp(-\beta W([x])) \rangle_{[x]} = \exp(-\beta \Delta F) . \tag{8.59}$$

This is the well known Jarzynski non-equilibrium work relation [295], which is closely connected to relations known as integral fluctuation theorems in literature [296]. Usually the Jarzynski relation is derived from elementary statistical physics. It connects the free energy difference of two equilibrium states to the total work performed on the system while the system evolves along the paths. It can be used to determine free energy differences in experiments (see e.g. [297–299]). The Jarzynski theorem is also valid if the final state is a non-equilibrium steady state even though the free energy $F(t_f)$ is no longer well defined in non-equilibrium: If one considers $F(t_f)$ to be defined by the configuration sum in equation (8.52), the Jarzynski relation can still be used [300, 301].

Another important relation is derived from (8.58) with $f = \delta(\beta W - \beta W([x]))$, where $\delta(\cdot)$ is the Dirac-δ-function that is non-zero if the work along a paths $W([x])$ equals a given value W. One finds

$$\langle \delta(\beta W - \beta W([x])) \exp(-\beta W([x])) \rangle_{[x]} = \langle \delta(\beta W - \beta W([x])) \exp(-\beta \Delta F) \rangle_{[\hat{x}]} . \tag{8.60}$$

Using $W([x]) = -W([\hat{x}])$ this is

$$p_{[x]}(\beta W) \exp(-\beta W) = p_{[\hat{x}]}(-\beta W) \exp(-\beta \Delta F) , \tag{8.61}$$

where $p_{[x]}(\beta W) = \langle \delta(\beta W - \beta W([x])) \rangle_{[x]}$ is the probability to perform the work W on the forward path, and $p_{[\hat{x}]}(-\beta W)$ is the corresponding distribution for the backward path. For $p_{[\hat{x}]}(-\beta W) \neq 0$, one finds

$$\frac{p_{[x]}(\beta W)}{p_{[\hat{x}]}(-\beta W)} = \exp(\beta W - \beta \Delta F). \tag{8.62}$$

Relation (8.62) connects the work distribution of the forward path to the backward path. Often (8.62) is also rewritten in terms of the dissipated work or the change in entropy [296, 302–307]. Because it allows a decrease in entropy with a small probability, it was incorrectly referred to as a relation that allows the violation of the second law of thermodynamics with a certain probability [302,303]. Equation (8.62) or similar ones have also been tested experimentally [308–310].

Finally, we want to derive a relation which connects a non-equilibrium distribution $\rho_x^{(neq)}(t)$ to the distribution $\pi_x(E)$ in equilibrium. We assume an ensemble of paths $[x]$ that start in states x_0 with probabilities given by $\pi_{x_0}(E(t_0))$ and end in non-equilibrium states $x(t_f)$. Using (8.50), we find

$$\begin{aligned}
\rho_{x_f}^{(neq)}(t_f) &= \sum_{[x] \text{ with } x(t_f)=x_f} \pi_{x_0}(E(t_0)) P([x]|x(t_0)=x_0) \\
&= \sum_{[\hat{x}] \text{ with } \hat{x}(t_0)=x_f} \pi_{x_0}(E(t_0)) P([\hat{x}]|\hat{x}(t_0)=x_f) \prod_{t=t_0}^{t_f-1} \frac{\pi_{x(t+1)}(E(t))}{\pi_{x(t)}(E(t))} \\
&= \sum_{[\hat{x}] \text{ with } \hat{x}(t_0)=x_f} \pi_{x_f}(E(t_f)) P([\hat{x}]|\hat{x}(t_0)=x_f) \prod_{t=t_0}^{t_f-1} \frac{\pi_{x(t+1)}(E(t))}{\pi_{x(t+1)}(E(t+1))} \\
&= \pi_{x_f}(E(t_f)) \left\langle \prod_{t=t_0}^{t_f-1} \frac{\pi_{x(t+1)}(E(t))}{\pi_{x(t+1)}(E(t+1))} \right\rangle_{[\hat{x}],\, \hat{x}(t_0)=x_f} .
\end{aligned} \tag{8.63}$$

The non-equilibrium distribution is therefore related to the distribution that an equilibrium system would have at the same time. If $\pi_x(E)$ is given by (8.51), one finds

$$\begin{aligned}
\rho_{x_f}^{(neq)}(t_f) &= \pi_{x_f}(E(t_f)) \left\langle \prod_{t=t_0}^{t_f-1} \frac{\exp\left(\beta F(t) - \beta E_{x(t+1)}(t)\right)}{\exp\left(\beta F(t+1) - \beta E_{x(t+1)}(t+1)\right)} \right\rangle_{[\hat{x}],\, \hat{x}(t_0)=x_f} \\
&= \pi_{x_f}(E(t_f)) \left\langle \exp\left(\beta \left\{-\Delta F + W([x])\right\}\right) \right\rangle_{[\hat{x}],\, \hat{x}(t_0)=x_f} \\
&= \pi_{x_f}(E(t_f)) \exp(-\beta \Delta F) \left\langle \exp(\beta W([x])) \right\rangle_{[\hat{x}],\, \hat{x}(t_0)=x_f} ,
\end{aligned} \tag{8.64}$$

i.e., the non-equilibrium distribution is connected to the equilibrium distribution via the work performed on the paths into the non-equilibrium (see also [294]).

8.6.3 Colloidal motion in potentials with phasonic drift: a non-equilibrium system

In sections 8.3 and 8.5.3, where we introduced the random trap model, we showed that the natural distribution to determine the dynamics of a single colloid in quasicrystalline or random potentials is the probability density $P(V_m, t)$ to find the colloid at time t in a minimum with a depth within $[V_m, V_m + dV_m]$. To calculate path-ensemble averages for such a system, we therefore consider the states x to be the positions of the minima, whose actual depths $V_m(x,t)$ correspond to the energies $E_x(t)$ that change in time due to a phasonic drift. The probability $\rho_x(t)$ is replaced by $P(V_m(x,t),t)$ and the thermal equilibrium distribution $\pi_x(E(t))$ is the asymptotic stationary distribution $P^{(stat)}(V_m(x,t))$ as determined in equation (8.39). Note, $P^{(stat)}(V_m(x,t))$ is given for a canonical ensemble in thermal equilibrium, however, it does not have the form of a conventional Boltzmann distribution, because $V_m(x,t)$ is the depths of a minimum and not the actual potential energy of the colloid. The external perturbation that drives the system out of equilibrium is realized by a phasonic drift or other time-dependent phasonic displacements.

We find the following path-ensemble averages: First, the probabilities for a forward path compared to a backward path have to fulfill the relation [cf. equation (8.50)]

$$\begin{aligned}\frac{P\left([x]|x(t_0)=x_0\right)}{P\left([\hat{x}]|\hat{x}(t_0)=x_f\right)} &= \prod_{t=t_0}^{t_f-1}\frac{P^{(stat)}(V_m(x(t+1),t))}{P^{(stat)}(V_m(x(t),t))} \\ &= \prod_{t=t_0}^{t_f-1}\frac{V_m(x(t),t)}{V_m(x(t+1),t)}\frac{\rho(V_m(x(t+1),t))}{\rho(V_m(x(t),t))}e^{\beta[V_m(x(t+1),t)-V_m(x(t),t)]},\end{aligned} \tag{8.65}$$

where for the stationary distribution equations (8.39) and (8.34) were used and $\rho(V_m)$ is the distribution of the depths of the local minima in the potential (see section 3.3.3).

Second, a path-ensemble average over some function $f([x])$ is given by [cf. equation (8.56)]

$$\begin{aligned}\langle f\rangle_{[x]} &= \left\langle f\prod_{t=t_0}^{t_f-1}\frac{P^{(stat)}(V_m(x(t+1),t))}{P^{(stat)}(V_m(x(t+1),t+1))}\right\rangle_{[\hat{x}]} \\ &= \left\langle f\prod_{t=t_0}^{t_f-1}\frac{V_m(x(t+1),t+1)}{V_m(x(t+1),t)}\frac{\rho(V_m(x(t+1),t))}{\rho(V_m(x(t+1),t+1))}e^{\beta[V_m(x(t+1),t)-V_m(x(t+1),t+1)]}\right\rangle_{[\hat{x}]}.\end{aligned} \tag{8.66}$$

Finally, we find a relation for a non-equilibrium distribution [cf. equation (8.63)]:

$$\begin{aligned} P^{(neq)}(V_m(x_f,t_f),t_f) &= P^{(stat)}(V_m(x_f,t_f)) \left\langle \prod_{t=t_0}^{t_f-1} \frac{P^{(stat)}(V_m(x(t+1),t))}{P^{(stat)}(V_m(x(t+1),t+1))} \right\rangle_{[\hat{x}],\,\hat{x}(t_0)=x_f} \\ &= \left\langle \prod_{t=t_0}^{t_f-1} K_{V_m(x(t+1),t),V_m(x(t+1),t+1)} \right\rangle_{[\hat{x}],\,\hat{x}(t_0)=x_f} P^{(stat)}(V_m(x_f,t_f)) \\ \text{with } K_{V_0,V_1} &= \frac{V_1}{V_0}\frac{\rho(V_0)}{\rho(V_1)} e^{\beta[V_0-V_1]}. \end{aligned} \tag{8.67}$$

In figure 8.14 we already plotted examples for $P^{(neq)}(V_m(x_f,t_f))$ in a system with a constant phasonic drift. According to equation (8.67), these distributions are connected to the (known) equilibrium distribution $P^{(stat)}(V_m)$ by a factor that can be calculated if a large number of paths towards the non-equilibrium steady state is known.

The path-ensemble averages presented here are still quite complicated. In principle, it is possible to check these relations with simulations. However, since some paths that have to be included in the path-ensemble average occur with a very small probability, it is almost impossible to simulate a sufficient large number of paths for such a test. For the future, it would be interesting to determine the path-ensemble for explicit quantities such as the diffusion constant as defined in (8.20). This should also give useful relations for predicting such quantities even in the non-equilibrium.

8.7 Summary and Outlook

We studied the Brownian motion of an ensemble of single colloidal particles in the decagonal potential and compared it to the motion in a regular square and a random square potential. While Brownian motion is naturally treated in equilibrium, we started the ensemble of single Brownian particles from a non-equilibrium distribution and monitor how they reach thermal equilibrium. Brownian dynamics simulations clearly show that after a fast relaxation into local potential minima, the particles in the random square and decagonal potential pass a wide-stretched subdiffusive regime and then enter thermal equilibrium when they start to exhibit normal diffusive motion. While the mean-square displacement as a function of time looks qualitatively the same for both potentials, the temporal evolution of the mean potential energy reveals some differences which we explained by the different distributions for the depths of the potential minima.

Furthermore, we developed a random trap model based on the probability distribution $P(V_m,t)$ of finding a particle in a trap with depth V_m. It agrees with the results from the Brownian dynamics simulations, especially the temporal evolution of the average potential energy with its characteristic features is reproduced. While an analytic formula derived within the random trap model only approximates the long-time diffusion constant found in the Brownian dynamics simulations, the analytically given time scale on which the

particle relaxes into the diffusive state fits very well to the simulations. Finally, our model clearly identifies that normal diffusion is reached when $P(V_m, t)$ approaches its stationary distribution which corresponds to thermal equilibrium. While conventional treatments of Brownian motion use a positional distribution $p(x, y, t)$, we here introduced an alternative approach that is easier to treat and that might be applicable to other systems where Brownian motion in an external potential is studied.

If a phasonic drift is applied to the decagonal potential, the colloids no longer reach the thermal equilibrium. However, in the long-time limit, a non-equilibrium steady state of enhanced diffusion is found. The phasonic drift also induces a colloidal drift that for small temperatures and slow phasonic drifts is determined by the motion of the local minima. However, for large phasonic drift the direction of this colloidal motion is reversed.

Finally, Brownian particles in decagonal potential with phasonic drift can be used as a model system to study general properties of systems far from equilibrium. We derived some path integral relations that are applicable to our concrete system.

Since single colloids already show a surprising dynamics, we expect the collective motion of many particles in a decagonal potential without or even with a phasonic drift to exhibit a lot of interesting features, concerning, e.g., the dynamics of induced phasonic flips or the collective drift behavior. One can also think of studying the dynamics and ordering of colloids driven over a decagonal potential (cf. works for driven particles in periodic systems, e.g. [48, 49, 311]).

A central question for atomic quasicrystals is: How does the dynamics of the constituent particles on the surface of a quasicrystal affect its growth and how is the growth process influenced by phasonic fluctuations? Certainly, the diffusion constant is an important quantity that determines the speed with which new particles find optimal positions on the surface. We demonstrated here that phasonic drifts enhance diffusion. We expect a similar behavior for phasonic fluctuations. To elucidate the role of phasonic fluctuations, it is also important to clarify the microscopic details of how quasicrystals grow. recent literature reports evidences that single particles first form clusters and then stick to the surface [312, 313].

Chapter 9

Conclusions

Colloidal particles in light fields created by interfering laser beams are a very useful model system to study the ordering and dynamics of particles on quasicrystalline substrates such as atoms on the surface of a quasicrystal. With the help of Monte-Carlo and Brownian dynamics simulations, we studied a two-dimensional charge-stabilized colloidal suspension in external potentials with quasicrystalline symmetries in one- and two-dimensions. We also developed theoretical models and compared their results to the simulations.

The one-dimensional potential consists of two modulations, whose wavelengths differ by a factor of τ, where $\tau = \left(1+\sqrt{5}\right)/2 \approx 1.618$ is the number of the golden ratio. The two-dimensional potential possesses decagonal symmetry and can be realized in experiment by five interfering laser beams.

In both cases, for weak potentials, a triangular or liquid phase occurs depending on the strength of the particle interactions and their density. An interesting and unexpected phase behavior was found when the strength of the substrate potential increases and the triangular phase has compete with the destabilizing symmetry of the substrate. In the one-dimensional quasicrystalline potential the colloidal density modulations lock to one of the potential modulations while ignoring the other and therefore rhombic ordering can be observed. We explained the occurrence of such a phase with a refined Landau-Alexander-McTague theory. In the decagonal potential and for low particle densities, a quasicrystalline phase is stable with a surprising twenty-fold bond orientational order. On the other hand, at large particle densities, i.e., when the number of colloids exceeds the number of available minima in the substrate potential, no apparent bond orientational order was found. Furthermore, in two narrow ranges of densities, we identified structures that are reminiscent to Archimedian tilings. Finally, for very large potential strengths a quasicrystalline phase with ten bond directions was observed in decagonal laser fields, whereas colloids in the one-dimensional potential assemble in lines given by the potential wells. Since the ratio of number densities in neighboring wells usually is irrational due to their different depths, periodic ordering along the lines is not possible. Therefore, the one-dimensional quasicrystalline potential destroys any periodic ordering. However, the resulting phase is not necessarily liquid. By using Brownian dynamic simulations, we found a transition

into a solid-like frustrated state at large particle interactions, where neighboring rows of particles cannot pass each other.

Furthermore, we studied the Brownian motion of single colloids on a decagonal substrate. From Brownian dynamics simulations and a random trap theory we found that initially the particle exhibits subdiffusional motion over several decades in time until it crosses over to pure diffusion in the long-time limit. We demonstrated that this subdiffusion is due to a temporally extended relaxation process towards thermal equilibrium. We compared the simulated behavior to Brownian motion in random potentials and developed a random trap model, from which we calculated the crossover time and the asymptotic diffusion constant analytically.

A big advantage of studying colloidal suspensions in quasicrystalline laser fields is that phasonic displacements, gradients, and drifts can be applied to the substrate potential by manipulating the phases of the laser beams in time accordingly. Phasons are unique to quasicrystals. Like phonons they are hydrodynamic modes, i.e., global excitations that do not change free energy in the long-wavelength limit. We demonstrated that phasonic drifts in the substrate potential induce phasonic flips in the colloidal monolayer. Secondly, a phasonic gradient or drift stabilizes the Archimedean-like tiling. Thirdly, if a constant phasonic drift is applied to a laser field while observing the Brownian motion of a single particle, the system never relaxes to thermal equilibrium. Instead, it reaches a non-equilibrium steady state which displays an enhanced diffusive transport. By varying the velocity of the phasonic drift, the non-equilibrium motion is controlled in a well-defined manner. Therefore, our system is very interesting for studying properties of the non-equilibrium. We presented some path-ensemble relations for future investigations.

In summary, a rich phase behavior was found for a colloidal monolayer on quasicrystalline substrates. New unexpected phases occur when the strengths of the colloidal interaction and the substrate potential are comparable. Studying dynamic aspects revealed novel phenomena such as a frustrated phase in a one-dimensional quasicrystalline potential or a subdiffusion to diffusion crossover for Brownian particles in laser fields with decagonal symmetry. We demonstrated how phasonic displacements, gradients, or drifts of the substrate affect the colloidal monolayer. This work also contributes to the understanding of the ordering and dynamics of adatoms on the surface of quasicrystals and therefore helps to establish the basis for many new applications such as the development of quasicrystalline catalysts or new wear-resistant materials.

List of Publications

Related to this work:

[A] M. Schmiedeberg, J. Roth, and H. Stark, *Freezing and Melting of a Colloidal Adsorbate on a 1D Quasicystalline Substrate*, Phys. Rev. Lett. **97**, 158304 (2006).

[B] M. Schmiedeberg, J. Roth, and H. Stark, *Brownian particles in random and quasicrystalline potentials: How they approach the equilibrium*, Eur. Phys. J. E **24**, 367 (2007).

[C] M. Schmiedeberg and H. Stark, *Comment on "Two-Dimensional Quasicrystals of Decagonal Order in One-Component Monolayer Films"*, Phys. Rev. Lett. **100**, 019601 (2008).

[D] M. Schmiedeberg and H. Stark, *Colloidal ordering on a 2D quasicrystalline substrate*, submitted to Phys. Rev. Lett. (2008).

Other publications:

[E] M. Schmiedeberg and H. Stark, *One-bead microrheology with rotating particles*, Eur. Phys. Lett. **69**, 629 (2005).

[F] M. Schmiedeberg, MF. Miri, and H. Stark, *Photon channelling in foams*, Eur. Phys. J. E **18**, 123 (2005).

[G] M. Schmiedeberg and H. Stark, *Superdiffusion in a honeycomb billiard*, Phys. Rev. E **73**, 031113 (2006).

[H] V. Yu. Zaburdaev, M. Schmiedeberg, and H. Stark, *Random Walks with random velocities*, Phys. Rev. E **78**, 011119 (2008).

In preparation:

[I] V. Yu. Zaburdaev, M. Schmiedeberg, and H. Stark, *On Moments and Scaling in anomalous random walks*, in preparation (2008).

Diploma thesis:

[J] M. Schmiedeberg, *Lichttransport in zellulären Strukturen*, Diplomarbeit, Universität Konstanz (2004).

Bibliography

[1] D. Shechtman, I. Blech, D. Gratias, and J. W. Cahn, *Metallic Phase with Long-Range Orientational Order and No Translational Symmetry*, Phys. Rev. Lett. **53**, 1951 (1984).

[2] D. Levine, T. C. Lubensky, S. Ostlund, S. Ramaswamym, P. J. Steinhardt, and J. Toner, *Elasticity and Dislocations in Pentagonal and Icosahedral quasicrystals*, Phys. Rev. Lett. **54**, 1520 (1985).

[3] J. E. S. Socolar, T. C. Lubensky, and P. J. Steinhardt, *Phonons phasons, and dislocations in quasicrystals*, Phys. Rev. B **34**, 3345 (1986).

[4] C. L. Henley, M. de Boissieu, and W. Steurer, *Discussion on clusters, phasons and quasicrystal stabilisation*, Phil. Mag. **86**, 1131 (2006).

[5] R. McGrath, J. Ledieu, E. J. Cox, and R. D. Diehl, *Quasicrystal surfaces: structure and potential as templates*, J. Phys.: Condens. Matter **14**, R119 (2002).

[6] N. Ferralis, K. Pussi, E. J. Cox, M. Gierer, J. Ledieu, I. R. Fisher, C. J. Jenks, M. Lindroos, R. McGrath, and R. D. Diehl, *Structure of the tenfold d-Al-Ni-Co quasicrystal surface*, Phys. Rev. B **69**, 153404 (2004).

[7] M. Shimoda, T. J. Sato, A. P. Tsai, and J. Q. Guo, *Epitaxial crystalline film with psuedo-tenfold symmetry formed by Au-deposition on a decagonal Al72-Ni12-Co16 quasicrystal*, Phys. Rev. B **62**, 11288 (2000).

[8] K. J. Franke, H. R. Sharma, W. Theis, P. Gille., P. Ebert, and K. H. Rieder, *Quasicrystalline Epitaxial Single Element Monolayers on Icosahedral Al-Pd-Mn and Decagonal Al-Ni-Co Quasicrystal Surfaces*, Phys. Rev. Lett. **89**, 156104 (2002).

[9] V. Fournée, T. C. Cai, A. R. Ross, T. A. Lograsso, J. W. Evans, and P. A. Thiel, *Nucleation and growth of Ag films on a quasicrystalline AlPdMn surface*, Phys. Rev. B **67**, 033406 (2003).

[10] N. Ferralis, R. D. Diehl, K. Pussi, M. Lindroos, I. Fisher, and C. J. Jenks, *Low-energy electron diffraction study of Xe adsorption on the ten-fold decagonal Al-Ni-Co quasicrystal surface*, Phys. Rev. B **69**, 075410 (2004).

[11] J. Ledieu, J. T. Hoeft, D. E. Reid, J. A. Smerdon, R. D. Diehl, T. A. Lograsso, A. R. Ross, and R. McGrath, *Pseudomorphic Growth of a Single Element Quasiperiodic Ultrathin Film on a Quasicrystal Substrate*, Phys. Rev. Lett. **92**, 135507 (2004).

[12] H. R. Sharma, M. Shimoda, A. R. Ross, T. A. Lograsso, and A. P. Tsai, *Real-space observation of quasicrystalline Sn monolayer formed on the fivefold surface of icosahedral Al-Cu-Fe quasicrystal*, Phys. Rev. B **72**, 045428 (2005).

[13] J. Ledieu, P. Unsworth, T. A. Lograsso, A. R. Ross, and R. McGrath, *Ordering of Si atoms on the fivefold Al-Pd-Mn quasicrystal surface*, Phys. Rev. B **73**, 012204 (2006).

[14] R. A. Tasca, N. Ferralis, R. D. Diehl, and M. W. Cole, *The adsorption of Xe and Ar on quasicrystalline AlNiCo*, J. Phys.: Condens. Matter **16**, (2004).

[15] S. Curtarolo, W. Setyawan, N. Ferralis, R. D. Diehl, and M. W. Cole, *Evolution of Topological Order in Xe Films on a Quasicrystal Surface*, Phys. Rev. Lett. **95**, 136104 (2005).

[16] W. Setyawan, N. Ferralis, R. D. Diehl, M. W. Cole, and S. Curtarolo, *Xe films on a decagonal Al-Ni-Co quasicrystalline surface*, Phys. Rev. B **74**, 125425 (2006).

[17] W. Setyawan, R. D. Diehl, N. Ferralis, M. W. Cole, and S. Curtarolo, *Noble gas films on a decagonal AlNiCo quasicrystal*, J. Phys.: Condens. Matter **19**, 016007 (2007).

[18] B. Bilki, M. Erbudak, M. Mungan, and Y. Weisskopf, *Structure formation of a layer of adatoms on a quasicrystalline substrate: Molecular dynamics study*, Phys. Rev. B **75**, 045437 (2007).

[19] M. Mungan, Y. Weisskopf, and M. Erbudak, *Deposition of atoms on a quasicrystalline substrate: Molecular dynamics study in three dimensions*, Phys. Rev. B **76**, 195443 (2007).

[20] J. Mikhael, L. Helden, and C. Bechinger, private communication .

[21] J. M. Kosterlitz and D. J. Thouless, *Ordering, metastability and phase transitions in two-dimensional systems*, J. Phys. C **6**, 1181 (1973).

[22] B. I. Halperin and D. R. Nelson, *Theory of Two-Dimensional Melting*, Phys. Rev. Lett. **41**, 121 (1978).

[23] D. R. Nelson, *Study of melting in two dimensions*, Phys. Rev. B **18**, 2318 (1978).

[24] D. R. Nelson and B. I. Halperin, *Dislocation-mediated melting in two dimensions*, Phys. Rev. B **19**, 2457 (1979).

[25] D. R. Nelson, *Defects and Geometry in Condensed Matter Physics*, Cambridge University Press, Cambridge (2002).

[26] A. P. Young, *On the theory of the phase transition in the two-dimensional planar spin model*, J. Phys. C: Solid State Phys. **11**, (1978).

[27] A. P. Young, *Melting and the vector Coulomb gas in two dimensions*, Phys. Rev. B **19**, 1855 (1979).

[28] A. Chowdhury, B. J. Ackerson, and N. A. Clark, *Laser-Induced Freezing*, Phys. Rev. Lett. **55**, 833 (1985).

[29] C. Bechinger, M. Brunner, and P. Leiderer, *Phase Behavior of Two-Dimensional Colloidal Systems in the Presence of Periodic Light Fields*, Phys. Rev. Lett. **86**, 930 (2001).

[30] C. Bechinger and E. Frey, *Phase behaviour of colloids in confining geometry*, J. Phys.: Condens. Matter **13**, (2001).

[31] W. Strepp, S. Sengupta, and P. Nielaba, *Phase transitions of hard disks in external periodic potentials: A Monte Carlo study*, Phys. Rev. E **63**, 046106 (2001).

[32] W. Strepp, S. Sengupta, and P. Nielaba, *Phase transitions of soft disks in external periodic potentials: A Monte Carlo study*, Phys. Rev. E **66**, 056109 (2002).

[33] M. M. Burns, J.-M. Fournier, and J. A. Golovchenko, *Optical Matter: Crystallization and Binding in Intense Optical Fields*, Science **249**, 749 (1990).

[34] B. V. Derjaguin and L. Landau, *Theory of stability of highly charged lyophobic sols and adhesion of highly charged particles in solutions of electrolytes*, Acta Physicochimica (USSR) **14**, 633 (1941).

[35] E. J. Verwey and J. T. G. Overbeek, *Theory of the Stability of Lyophobic Colloids*, Elsevier, Amsterdam (1948).

[36] A. Ashkin, *Acceleration and Trapping of Particles by Radiation Pressure*, Phys. Rev. Lett. **24**, 156 (1970).

[37] A. Ashkin, *Applications of Laser Radiation Pressure*, Science **210**, 1081 (1980).

[38] A. Ashkin, J. M. Dziedzic, J. E. Bjorkholm, and S. Chu, *Observation of a single-beam gradient force optical trap for dielectric particles*, Opt. Lett. **11**, 288 (1986).

[39] A. Ashkin and J. M. Dziedzic, *Optical trapping and manipulation of viruses and bacteria*, Science **235**, 1517 (1987).

[40] G. Gompper and M. Schick (editors), *Soft Matter, Volume 3: Colloidal Order: Entropic and Surface Forces*, Wiley-VCH, Weinheim (2007).

[41] K. Mangold, P. Leiderer, and C. Bechinger, *Phase Transitions of Colloidal Monolayers in Periodic Pinning Arrays*, Phys. Rev. Lett. **90**, 158302 (2003).

[42] M. Brunner and C. Bechinger, *Phase Behavior of Colloidal Molecular Crystals on Triangular Light Lattices*, Phys. Rev. Lett. **88**, 248302 (2002).

[43] C. Reichhardt and C. J. Olsen, *Novel Colloidal Crystalline States on Two-Dimensional Periodic Substrates*, Phys. Rev. Lett. **88**, 248301 (2002).

[44] C. Reichhardt and C. J. Olson Reichhardt, *Ordering and melting in colloidal molecular crystal mixtures*, Phys. Rev. E **71**, 062403 (200).

[45] A. Šarlah, T. Franosch, and E. Frey, *Melting of Colloidal Crystals on Triangular Lattices*, Phys. Rev. Lett. **95**, 088302 (2005).

[46] A. Šarlah, E. Frey, and T. Franosch, *Spin models for orientational ordering of colloidal molecular crystals*, Phys. Rev. E **75**, 021402 (2007).

[47] C. Reichhardt and C. J. Olsen, *Colloidal Dynamics on Disordered Substrates*, Phys. Rev. Lett. **89**, 078301 (2002).

[48] C. Reichhardt and C. J. Olsen Reichhardt, *Local Melting and Drag for a Particle Driven through a Colloidal Crystal*, Phys. Rev. Lett. **92**, 108301 (2004).

[49] C. Reichhardt and C. J. Olsen Reichhardt, *Dynamic regimes and spontaneous symmetry breaking for driven colloids on triangular substrates*, Eur. Phys. Lett. **68**, 303 (2004).

[50] C. Reichhardt and C. J. Olsen Reichhardt, *Pinning and dynamics of colloids on one-dimensional periodic potentials*, Phys. Rev. E **72**, 032401 (2005).

[51] Q.-H. Wei, C. Bechinger, and P. Leiderer, *Single-File Diffusion of Colloids in One-Dimensional Channels*, Science **287**, 625 (2000).

[52] C. Lutz, M. Kollmann, and C. Bechinger, *Single-file Diffusion of Colloids in One-Dimensional Channels*, Phys. Rev. Lett. **93**, 026001 (2004).

[53] C. Lutz, M. Kollmann, P. Leiderer, and C. Bechinger, *Diffusion of colloids in one-dimensional light channels*, J. Phys.: Condens. Matter **16**, S4075 (2004).

[54] S. H. Lee and D. G. Grier, *Giant Colloidal Diffusivity on Corrugated Optical Vortices*, Phys. Rev. Lett. **96**, 190601 (2006).

[55] M. Evstigneev, O. Zvyagolskaya, S. Bleil, R. Eichhorn, C. Bechinger, and P. Reimann, *Diffusion of colloidal particles in a tilted periodic potential: Theory versus experiment*, Phys. Rev. E **77**, 041107 (2008).

[56] C. Lutz, M. Reichert, H. Stark, and C. Bechinger, *Surmounting Barriers: The Benefit of Hydrodynamic Interactions*, Eur. Phys. Lett. **74**, 719 (2006).

[57] F. Scheffler, P. Maass, J. Roth, and H. Stark, *Quasicrystalline order in binary dipolar systems*, Eur. Phys. J. B **42**, 85 (2004).

[58] N. Hoffmann, F. Ebert, C. N. Likos, H. Löwen, and G. Maret, *Partial Clustering in Binary Two-Dimensional Colloidal Suspensions*, Phys. Rev. Lett. **97**, 078301 (2006).

[59] K. Franzrahe and P. Nielaba, *Entropy versus energy: The phase behavior of a hard-disk mixture in a periodic external potential*, Phys. Rev. E **76**, 061503 (2007).

[60] J. Baumgartl, R. P. A. Dullens, M. Dijkstra, R. Roth, and C. Bechinger, *Experimental Observation of Structural Crossover in Binary Mixtures of Colloidal Hard Spheres*, Phys. Rev. Lett. **98**, 198303 (2007).

[61] L. Assoud, R. Messina, and H. Löwen, *Stable crystalline lattices in two-dimensional binary mixtures of dipolar particles*, Eur. Phys. Lett. **80**, .

[62] F. Ebert, P. Keim, and G. Maret, *Local crystalline order in a 2D colloidal glass former*, Eur. Phys. J. E **26**, 161 (2008).

[63] J. Fornleitner, F. Lo Verso, G. Kahl, and C. N. Likos, *Genetic algorithms predict formation of exotic ordered configurations for two-component dipolar monolayers*, Soft Matter **4**, 480 (2008).

[64] D. J. W. Aastuen, N. A. Clark, L. K. Cotter, and B. J. Ackerson, *Nucleation and Growth of Colloidal Crystals*, Phys. Rev. Lett. **57**, 1733 (1986).

[65] A. van Blaaderen, R. Ruel, and P. Wiltzius, *Template-directed colloidal crystallization*, Nature **385**, 321 (1997).

[66] S. Auer and D. Frenkel, *Prediction of absolute crystal-nucleation rate in hard-sphere colloids*, Nature **409**, 1020 (2000).

[67] U. Gasser, E. R. Weeks, A. Schofield, P. N. Pusey, and D. A. Weitz, *Real space imaging of nucleation and growth in colloidal crystallization*, Science **292**, 258 (2001).

[68] S. van Teeffelen, C. N. Likos, N. Hoffmann, and H. Löwen, *Density functional theory of freezing for soft interactions in two dimensions*, Eur. Phys. Lett. **75**, 583 (2006).

[69] S. van Teeffelen, C. N. Likos, and H. Löwen, *Colloidal Crystal Growth at Externally Imposed Nucleation Clusters*, Phys. Rev. Lett. **100**, 108302 (2008).

[70] P. N. Pusey and W. van Megen, *Phase behaviour of concentrated suspensions of nearly hard colloidal spheres*, Nature **320**, 340 (1986).

[71] P. N. Pusey and W. van Megen, *Observation of a glass transition in suspensions of spherical colloidal particles*, Phys. Rev. Lett. **59**, 2083 (1987).

[72] W. Götze and L. Sjogren, *Relaxation processes in supercooled liquids*, Rep. Prog. Phys. **55**, 241 (1992).

[73] M. Fuchs, *MCT Results for a simple liquid at the glass transition*, Transport Theory and Statistical Physics **24**, 855 (1995).

[74] M. Fuchs, W. Götze, and M. R. Mayr, *Asymptotic laws for tagged-particle motion in glassy systems*, Phys. Rev. E **58**, 3384 (1998).

[75] W. Götze, *Recent tests of the mode-coupling theory for glassy dynamics*, J. Phys.: Condens. Matter **11**, A1 (1999).

[76] E. Zaccarelli, H. Löwen, P. P. F. Wessels, F. Sciortino, P. Tartaglia, and C. N. Likos, *Is There a Reentrant Glass in Binary Mixtures?*, Phys. Rev. Lett. **92**, 225703 (2004).

[77] T. G. Mason, K. Ganesan, J. H. van Zanten, D. Wirtz, and S. C. Kuo, *Particle Tracking Microrheology of Complex Fluids*, Phys. Rev. Lett. **79**, 3282 (1997).

[78] A. J. Levine and T. C. Lubensky, *One- and Two-Particle Microrheology*, Phys. Rev. Lett. **85**, 1774 (2000).

[79] A. I. Bishop, T. A. Nieminen, N. R. Heckenberg, and H. Rubinsztein-Dunlop, *Optical Microrheology Using Rotating Laser-Trapped Particles*, Phys. Rev. Lett. **92**, 198104 (2004).

[80] E. Andablo-Reyes, P. Diaz-Leyva, and J. L. Arauz-Lara, *Microrheology from Rotational Diffusion of Colloidal Particles*, Phys. Rev. Lett. **94**, 106001 (2005).

[81] S. Jabbari-Farouji, D. Mizuno, M. Atakhorrami, F. C. MacKintosh, C. F. Schmidt, E. Eiser, G. H. Wegdam, and D. Bonn, *Fluctuation-Dissipation Theorem in an Aging Colloidal Glass*, Phys. Rev. Lett. **98**, 108302 (2007).

[82] N. A. Clark and B. J. Ackerson, *Observation of the Coupling of Concentration Fluctuations to Steady-State Shear Flow*, Phys. Rev. Lett. **44**, 1005 (1980).

[83] B. J. Ackerson and N. A. Clark, Shear-Induced Melting, 1981.

[84] L. V. Woodcock, *Origins of Thixotropy*, Phys. Rev. Lett. **54**, 1513 (1985).

[85] S. Ramaswamy and S. R. Renn, *Theory of Shear-Induced Melting of Colloidal Crystals*, Phys. Rev. Lett. **56**, 945 (1986).

[86] B. J. Ackerson and N. A. Clark, *Shear-Induced Order in Suspensions of Hard Spheres*, Phys. Rev. Lett. **61**, 1033 (1988).

[87] D. J. Pine, J. P. Gollub, J. F. Brady, and A. M. Leshansky, *Chaos and threshold for irreversibility in sheared suspensions*, Nature **438**, 997 (2005).

[88] R. Besseling, E. R. Weeks, A. B. Schofield, and W. C. K. Poon, *Three-Dimensional Imaging of Colloidal Glasses under Steady Shear*, Phys. Rev. Lett. **99**, 028301 (2007).

[89] L. Corta, P. M. Chaikin, J. P. Gollub, and D. J. Pine, *Random organization in periodically driven systems*, Nature Physics **4**, 420 (2008).

[90] J. Dzubiella, G. P. Hoffmann, and H. Löwen, *Lane formation in colloidal mixtures driven by an external field*, Phys. Rev. E **65**, 021402 (2002).

[91] J. Chakrabarti, J. Dzubiella, and H. Löwen, *Reentrance effect in the lane formation of driven colloids*, Phys. Rev. E **70**, 012401 (2004).

[92] M. Köppl, P. Henseler, A. Erbe, P. Nielaba, and P. Leiderer, *Layer Reduction in Driven 2D-Colloidal Systems through Microchannels*, Phys. Rev. Lett. **97**, 208302 (2006).

[93] M. Rex and H. Löwen, *Lane formation in oppositely charged colloids driven by an electric field: Chaining and two-dimensional crystallization*, Phys. Rev. E **75**, 051402 (2007).

[94] J. Fornleitner and G. Kahl, *Lane formation vs. cluster formation in two-dimensional square-shoulder systems - A genetic algorithm approach*, Eur. Phys. Lett. **82**, 18001 (2008).

[95] P. E. Wolf and G. Maret, *Weak Localization and Coherent Backscattering of Photons in Disordered Media*, Phys. Rev. Lett. **55**, 2696 (1985).

[96] G. Maret and P. E. Wolf, *Multiple light scattering from disordered media. The effect of brownian motion of scatterers*, Zeitschrift fr Physik B Condensed Matter **65**, 409 (1986).

[97] S. Fraden and G. Maret, *Multiple Light Scattering from Concentrated Interacting Suspensions*, Phys. Rev. Lett. **65**, 515 (1990).

[98] G. Maret, *Multiple Light Scattering Illuminates Colloid Interaction*, Physics World **5**, 24 (1992).

[99] G. Maret, *Diffusing Wave Spectroscopy*, Current Opinion in Colloid and Interface Science **2**, 251 (1997).

[100] M. Störzer, P. Gross, C. Aegerter, and G. Maret, *Observation of the critical regime near Anderson localization of light*, Phys. Rev. Lett. **96**, 063904 (2006).

[101] D. Rudhardt, C. Bechinger, and P. Leiderer, *Direct measurement of depletion potentials in mixtures of colloids and non-ionic polymers*, Phys. Rev. Lett. **81**, 1330 (1989).

[102] C. Bechinger, D. Rudhardt, P. Leidererm, R. Roth, and S. Dietrich, *Understanding depletion forces beyond entropy*, Phys. Rev. Lett. **83**, 3960 (1999).

[103] H. H. von Gruünberg, L. Helden, P. Leiderer, and C. Bechinger, *Measurement of surface charge densities on Brownian particles using total internal reflection microscopy*, J. Chem. Phys. **114**, 10094 (2001).

[104] C. Hertlein, L. Helden, A. Gambassi, S. Dietrich, and C. Bechinger, *Direct measurement of critical Casimir forces*, Nature **451**, 172 (2008).

[105] K. Zahn, G. Maret, C. Ruß, and H. H. von Grünberg, *Three-Particle Correlations in Simple Liquids*, Phys. Rev. Lett. **91**, 115502 (2003).

[106] M. Brunner, J. Dobnikar, H. H. von Grünberg, and C. Bechinger, *Direct measurement of three-body interactions*, Phys. Rev. Lett. **92**, 078301 (2004).

[107] J. Dobnikar, M. Brunner, H. H. von Grünberg, and C. Bechinger, *Three-body interactions in colloidal systems*, Phys. Rev. E **69**, 031402 (2004).

[108] C. Bechinger and H. H. von Grünberg, *Wenn drei Körper mehr sind als drei Paare*, Physik Journal **11**, 33 (2004).

[109] C. Russ, M. Brunner, C. Bechinger, and H. H. von Grünberg, *Three-body forces at work:three-body potentials derived from triplet correlations in colloidal suspensions*, Eur. Phys. Lett. **69**, 468 (2005).

[110] D. Reinke, H. Stark, H. H. von Grünberg, A. B. Schofield, G. Maret, and U. Gasser, *Noncentral Forces in Crystals of Charged Colloids*, Phys. Rev. Lett. **038301**, 98 (2007).

[111] M. Reichert and H. Stark, *Hydrodynamic coupling of two rotating spheres trapped in harmonic potentials*, Phys. Rev. E **69**, 031407 (2004).

[112] S. Martin, M. Reichert, H. Stark, and T. Gisler, *Direct Observation of Hydrodynamic Rotation-Translation Coupling between Two Colloidal Spheres*, Phys. Rev. Lett. **97**, 248301 (2006).

[113] H. Stark, *Immer in Bewegung bleiben: Die sonderbare Welt der kleinen Reynolds-Zahlen*, Physik Journal **11**, 31 (2007).

[114] R. Dreyfus, J. Baudry, M. L. Roper, M. Fermigier, H. A. Stone, and J. Bibette, *Microscopic artificial swimmers*, Nature **437**, 862 (2005).

[115] E. Gauger and H. Stark, *Numerical study of a microscopic artificial swimmer*, Phys. Rev. E **74**, 021907 (2006).

[116] P. J. Lu and P. J. Steinhardt, *Decagonal and Quasi-Crystalline Tilings in Medieval Islamic Architecture*, Science **315**, 1106 (2007).

[117] M. A. Bravais, *Memoirs sur les systemes formes par des point distribues regulierement sur un plan ou dans l'espace*, J. Ec. Polytech. (Paris) **33**, 1 (1850).

[118] H. Wang, *Proving theorems by pattern recognition II*, Bell Systems Tech. J. **40**, 1 (1961).

[119] R. Berger, *The undecidability of the domino problem*, Memoirs Amer. Math. Soc **66**, 72 (1966).

[120] R. M. Robinson, *Undecidability and nonperiodicity of tilings in the plane*, Inv. Math. **12**, 177 (1971).

[121] R. Penrose, *The role of aesthetics in pure and applied mathematical research*, Bull. Inst. Math. Appl. **10**, 266 (1974).

[122] D. Levine and P. J. Steinhardt, *Quasicrystals: A New Class of Ordered Structures*, Phys. Rev. Lett. **53**, 2477 (1984).

[123] X. Zeng, G. Ungar, Y. Liu, V. Percec, A. E. Dulcey, and J. K. Hobbs, *Supramolecular dendritic liquid quasicrystals*, Nature **428**, 157 (2004).

[124] E. Macia, *The role of aperiodic order in science and technology*, Rep. Prog. Phys. **69**, 397 (2006).

[125] X. Wu, S. W. Kycia, C. G. Olson, P. J. Benning, A. I. Goldman, and D. W. Lynch, *Electronic Band Dispersion and Pseudogap in Quasicrystals: Angular-Resolved Photoemission Studies on Icosahedral* $Al_{70}Pd_{21.5}Mn_{8.5}$, Phys. Rev. Lett. **75**, 4540 (1995).

[126] P. A. Thiel and J. M. Dubois, *Quasicrystals: Electrons in a strange sea*, Nature **406**, 570 (2000).

[127] E. Rotenberg, W. Theis, K. Horn, and P. Gille, *Quasicrystalline valence bands in decagonal AlNiCo*, Nature **406**, 602 (2000).

[128] S. Martin, A. F. Hebard, A. R. Kortan, and F. A. Thiel, *Transport Properties of* $Al_{65}Cu_{15}Co_{20}$ *and* $Al_{70}Ni_{15}Co_{15}$ *Decagonal Quasicrystals*, Phys. Rev. Lett. **67**, 719 (1991).

[129] B. Passaro, C. Sire, and V. G. Benza, *Anomalous diffusion and conductivity in octagonal tiling models*, Phys. Rev. B **46**, 13751 (1992).

[130] S. Takeuchi, H. Iwanaga, and T. Shibuya, *Hardness of quasicrystals*, Jpn. J. Appl. Phys. **30**, 561 (1991).

[131] R. Mikulla, J. Stadler, F. Krul, H. R. Trebin, and P. Gumbsch, *Crack Propagation in Quasicrystals*, Phys. Rev. Lett. **81**, 3163 (1998).

[132] S. Takeuchi and T. Hashimoto, *Plastic Deformation of Al-Pd-Mn Icosahedral Quasicrystal*, Jpn. J. Appl. Phys. **32**, 2063 (1993).

[133] E. Yablonovitch, *Inhibited Spontaneous Emission in Solid-State Physics and Electronics*, Phys. Rev. Lett. **58**, 2059 (1987).

[134] Y. S. Chan, C. T. Chan, and Z. Y. Liu, *Photonic Band Gaps in Two Dimensional Photonic Quasicrystals*, Phys. Rev. Lett. **80**, 956 (1998).

[135] A. Della Villa, S. Enoch, G. Tayeb, V. Pierro, V. Galdi, and F. Capolino, *Band Gap Formation and Multiple Scattering in Photonic Quasicrystals with Penrose-Type Lattice*, Phys. Rev. Lett. **94**, 183903 (2005).

[136] W. Man, M. Megens, P. J. Steinhardt, and P. M. Chaikins, *Experimental measurement of the properties of icosahedral quasicrystals*, Nature **436**, 993 (2005).

[137] N. G. de Bruijn, *Algebraic theory of Penrose's nonperiodic tilings of the plane I*, Nederl. Akad. Wetensch. Indag. **43**, 39 (1981).

[138] N. G. de Bruijn, *Algebraic theory of Penrose's nonperiodic tilings of the plane II*, Nederl. Akad. Wetensch. Indag. **43**, 53 (1981).

[139] L. Levitov and J. Rhyner, *Crystallography of quasicrystals;application to icosahedral symmetry*, J. Phys. **49**, 1835 (1988).

[140] S. E. Burkov, *Enforcement of matching rules by chemical ordering in the decagonal AlCuCo quasicrytal*, Phys. Rev. B **47**, 12326 (1993).

[141] R. Klitzing, M. Schlottmann, and M. Baake, *Perfect matching rules for undecorates triangular tilings with 10-, 12- and 8-fold symmetry*, Int. J. Mod. Phys. B **7**, 1455 (1993).

[142] M. Duneau and A. Katz, *Quasiperiodic Patterns*, Phys. Rev. Lett. **54**, 2688 (1985).

[143] B. Grünbaum and G. C. Shepard, *Tilings and Patterns*, W.H. Freeman, New York (1987).

[144] T. Janssen, *Icosahedral Crystals, Quasi-Crystals: new Forms of Incommensurate crystal Phases*, J. Phys. **47**, 85 (1986).

[145] D. S. Rokhser, D. C. Wright, and N. D. Mermin, *The Two-Dimensional Quasicrystallographic Space Groups with Rotational Symmetries less than 23-Fold*, Acta Cryst. A **44**, 197 (1988).

[146] D. A. Rabson, N. D. Mermin, D. S. Rokhser, and D. C. Wright, *The space groups of axial crystals and quasicrystals*, Rev. Mod. Phys. **63**, 699 (1991).

[147] M. Livio, *The Golden Ratio: the story of phi, the world's most astonishing number*, Broadway Books, New York (2003).

[148] I. N. Bronstein, K. A. Semendjajew, G. Musiol, and H. Mühlig, *Taschenbuch der Mathematik*, Verlag Harry Deutsch, Frankfurt am Main (2000).

[149] S. P. Gorkhali, J. Qi, and G. P. Crawford, *Switchable quasi-crystal structures with five-, seven-, and ninefold symmetries*, J. Opt Soc. Am. B **23**, 149 (2006).

[150] A. A. Chernikow, R. Z. Sagdeev, D. A. Usikov, and G. M. Zaslavsky, *The Hamiltonian Method for Quasicrystal Symmetry*, Physics Lett. A **125**, 101 (1987).

[151] R. Collins, *A geometrical sum rule for two-dimensional fluid correlation functions*, J. Phys. C **1**, 1461 (1968).

[152] J. R. Shewchuk, *Triangle*, http://www-2.cs.cmu.edu/˜quake/triangle.html .

[153] J. L. Meijering, *Interface area, edge length, and number of vertices in crystal aggregates with random nucleation*, Philips Res. Rep. **8**, 270 (1953).

[154] K. Edagawa, K. Suzuki, and S. Takeuchi, *High Resolution Transmission Electron Microscopy Observation of Thermally Fluctuating Phasons in Decagonal Al-Cu-Co*, Phys. Rev. Lett. **85**, 1674 (2000).

[155] S. Francoual, F. Livet, M. de Boissieu, F. Yakhou, F. Bley, A. L'etoublon, R. Caudron, and J. Gastaldi, *Dynamics of Phason Fluctuations in the i-AlPdMn Quasicrystal*, Phys. Rev. Lett. **91**, 225501 (2003).

[156] M. Reichert, *Monte-Carlo-Simulationen zum Clustermodell der Quasikristalle*, Diplomarbeit, Universität Stuttgart (2001).

[157] F. Gähler and M. Reichert, *Cluster Models of Decagonal Tilings and Quasicrystals*, J. Alloys Compd. **342**, 180 (2002).

[158] M. Reichert and F. Gähler, *Cluster Model of Decagonal Tilings*, Phys. Rev. B **68**, 214202 (2003).

[159] U. Koschella, *Zur Phason-Phonon-Kopplung in dekagonalen Quasikristallen*, Diplomarbeit, Universität Stuttgart (2001).

[160] U. Koschella, F. Gähler, J. Roth, and H. R. Trebin, *Phason Elastic Constants of a Binary Tiling Quasicrystal*, J. Alloys Compd. **342**, 287 (2002).

[161] U. Koschella, *Phason-elastische Energie in dekagonalen Quasikristallen*, Dissertation, Universität Stuttgart (2005).

[162] V. Elser, *Indexing Problems in quasicrystal diffraction*, Phys. Rev. B **32**, 4892 (1985).

[163] F. Lancon, L. Billard, S. Burkov, and M. de Boissieu, *On choosing a proper basis for determining structures of quasicrystals*, J. Phys. I France **4**, 283 (1994).

[164] W. Steurer and T. Haibach, *The periodic average structure of particular quasicrystals*, Acta Cryst. A **55**, 48 (1999).

[165] A. Cervillino and W. Steurer, *General periodic average structures of decagonal quasicrystals*, Acta Cryst. A **58**, 180 (2001).

[166] F. Lancon and L. Billard, *Numerical simulation of quasicrystals*, Journal of Non-Crystalline Solids **117**, 836 (1990).

[167] F. Lancon and L. Billard, *Stability and atomic motifs of quasicrystalline models*, J. Phys. France **51**, 1099 (1990).

[168] R. V. Moody and J. Petera, *Dynamical Generation of Quasicrystals*, Letters in Mathematical Physics **36**, 291 (1996).

[169] M. Yoshimura and A. P. Tsai, *Quasicrystal application on catalyst*, Journal of Alloys and Compounds **342**, 451 (2002).

[170] J. M. Dubois, S. S. Kang, and J. Von Stebut, *Quasicrystalline low-friction coatings*, Journal of Materials Science Letters **10**, 537 (1991).

[171] R. P. Matthews, C. I. Lang, and D. Shechtman, *Sliding wear of quasicrystalline coatings*, Tribology Letters **7**, 179 (1999).

[172] J. Y. Park, D. F. Ogletree, M. Salmeron, R. A. Ribeiro, P. C. Canfield, C. J. Jenks, and P. A. Thiel, *Tribological properties of quasicrystals: Effect of aperiodic versus periodic surface order*, Phys. Rev. B **74**, 024203 (2006).

[173] M. H. Anderson, J. R. Ensher, M. R. Matthews, C. E. Wieman, and E. A. Cornell, *Observation of Bose-Einstein Condensation in a Dilute Atomic Vapor*, Science **269**, 198 (1995).

[174] L. Sanchez-Palencia and L. Santos, *Bose-Einstein condensates in optical quasicrystal lattices*, Phys. Rev. A **72**, 053607 (2005).

[175] L. Guidoni, B. Déebret, A. di Stefano, and P. Verkerk, *Atomic diffusion in an optical quasicrystal with five-fold symmetry*, Phys. Rev. A **60**, R4233 (1999).

[176] M. Greiner and S. Fölling, *Optical lattices*, Nature **453**, 736 (2008).

[177] B. Freedman, G. Bartal, M. Segev, R. Lifshitz, D. N. Christodoulides, and J. W. Fleischer, *Wave and defect dynamics in nonlinear photonic quasicrystals*, Nature **440**, 1166 (2006).

[178] B. Freedman, R. Lifshitz, J. W. Fleischer, and M. Segev, *Phason dynamics in nonlinear photonic quasicrystals*, Nat. Mat. **6**, 776 (2007).

[179] P. Langevin, *Sur la théorie du mouvement brownien*, C. R. Acad. Sci., Paris **146**, 530 (1908).

[180] W. Paul and J. Baschnagel, *Stochastic processes - from physics to finance*, Springer Verlag, Berlin, Heidelberg (1999).

[181] A. Einstein, *Über die von der molekularkinetischen Theorie der Wärme geforderte Bewegung von in ruhenden Flüssigkeiten suspendierten Teilchen*, Ann. Phys. (Leipzig) **17**, 549 (1905).

[182] M. Matsumoto and T. Nishimura, *Mersenne Twister: A 623-dimensionally equidistributed uniform pseudorandom number generator*, ACM Trans. on Modeling and Computer Simulation **8**, 3 (1998).

[183] K. Taketa, http://www.math.sci.hiroshima-u.ac.jp/~m-mat/MT/VERSIONS/C-LANG/mersennetwister.zip (2005).

[184] *Reference Manual of the GNU Scientific Library*, http://www.gnu.org/software/gsl/manual/html_node/Random-Number-Generation.html .

[185] N. Metropolis, A. W. Rosenbluth, M. N. Rosenbluth, A. H. Teller, and E. Teller, *Equation of State Calculations by fast Computing Machines*, J. Chem. Phys. **21**, 1087 (1953).

[186] K. Binder and D. W. Heermann, *Monte carlo simulations in Statistical Physics*, Springer, Berlin (1988).

[187] M. E. J. Newman and G. T. Barkema, *Monte Carlo Methods in Statistical Physics*, Oxford University Press, New York (1999).

[188] D. Gottwald, G. Kahl, and C. N. Likos, *Predicting equilibrium structures in freezing processes*, J. Chem. Phys. **122**, 204503 (2005).

[189] D.Gottwald, *Genetic Algorithms in Condensed Matter Theory*, Dissertation, Technische Universiät Wien (2005).

[190] J. H. Holland, *Adaptation in Natural and Artificial Systems*, The University of Michigan Press, Ann Arbor (1975).

[191] J. Mikhael, L. Helden, J. Roth, and C. Bechinger, *Archimedean Tiling Structures on Decagonal Quasicrystal Templates*, Nature **454**, 501 (2008).

[192] L. D. Landau, *Zur Theorie der Phasenumwandlungen I*, Phys. Z. Sowjet. **11**, 26 (1937).

[193] L. D. Landau, *Zur Theorie der Phasenumwandlungen II*, Phys. Z. Sowjet. **11**, 545 (1937).

[194] S. Alexander and J. McTague, *Should all Crystals Be bcc? Landau Theory of Solidification and Crystal Nucleation*, Phys. Rev. Lett. **41**, 702 (1978).

[195] T. V. Ramakrishnan and M. Yussouff, *Theory of the Liquid-Solid Transition*, Solid State Communications **21**, 389 (1977).

[196] T. V. Ramakrishnan and M. Yussouff, *First-principles order-parameter theory of freezing*, Phys. Rev. B **19**, 2775 (1979).

[197] Y. Singh, *Density-functional theory of freezing and properties of the ordered phase*, Phys. Rep. **207**, 351 (1991).

[198] H. Löwen, *Melting, freezing and colloidal suspensions*, Phys. Rep. **237**, 249 (1994).

[199] J. Wu and Z. Li, *Density-Functional Theory for Complex Fluids*, Annual Review of Physical Chemistry **58**, 85 (2007).

[200] T. V. Ramakrishnan, *Density wave theory of freezing and the solid*, Pramana **22**, 365 (1984).

[201] W. A. Curtin and N. W. Ashcroft, *Density-functional theory and freezing of simple liquids*, Phys. Rev. Lett. **56**, 2775 (1986).

[202] Y. Rosenfeld, *Free-energy model for the inhomogeneous hard-sphere fluid mixture and density-functional theory of freezing*, Phys. Rev. Lett. **63**, 980 (1989).

[203] S. Sengupta and A. K. Sood, *Theory of liquid-bcc-fcc coexistence in charge-stabilized colloidal systems*, Phys. Rev. A **44**, 1233 (1991).

[204] T. V. Ramakrishnan, *Density-Wave Theory of first-Order Freezing in Two dimensions*, Phys. Rev. Lett. **48**, 541 (1982).

[205] A. D. J. Haymet and D. W. Oxtoby, *A molecular theory for the solid-liquid interface*, J. Chem. Phys. **74**, 2559 (1981).

[206] W. Klein and F. Leyvraz, *Crystalline Nucleation in Deeply Quenched Liquids*, Phys. Rev. Lett. **57**, 2845 (1986).

[207] P. De and R. A. Pelcovits, *Linear elasticity theory of pentagonal quasicrystals*, Phys. Rev. B **35**, 8609 (1987).

[208] P. De and R. A. Pelcovits, *Disclinations in pentagonal quasicrystals*, Phys. Rev. B **36**, 9304 (1987).

[209] P. De and R. A. Pelcovits, *Interaction energy of disclinations in pentagonal quasicrystals*, Phys. Rev. B **38**, 5042 (1988).

[210] P. De and R. A. Pelcovits, *Defect-mediated meling of pentagonnal quasicrystals*, J. Phys. A **22**, 1167 (1989).

[211] C. A. Murray and d. H. Van Winkle, *Experimental observation of two-stage melting in a classical two-dimensional screened Coulomb system*, Phys. Rev. Lett. **58**, 1200 (1988).

[212] C. A. Murray and R. A. Wenk, *Microscopic particle motions and topological defects in two-dimensional hexatics and dense fluids*, Phys. Rev. Lett. **62**, 1643 (1989).

[213] C. A. Murray, W. O. Sprenger, and R. A. Wenk, *Comparison of melting in three and two dimensions: Microscopy of colloidal spheres*, Phys. Rev. B **42**, 688 (1990).

[214] O. S. Vaulina, I. E. Drangevski, X. G. Adamovich, O. F. Petrov, and V. E. Fortov, *Two-Stage Melting in Quasi-Two-Dimensional Dissipative Yukawa Systems*, Phys. Rev. Lett. **97**, 195001 (2006).

[215] K. Zahn, R. Lenke, and G. Maret, *Two-Stage Melting of Paramagnetic Colloidal Crystals in Two Dimensions*, Phys. Rev. Lett. **82**, 2721 (1999).

[216] K. Zahn, A. Wille, G. Maret, S. Sengupta, and P. Nielaba, *Elastic Properties of 2D Colloidal Crystals from Video Microscopy*, Phys. Rev. Lett. **90**, 155506 (2003).

[217] P. Keim, G. Maret, U. Herz, and H. H. von Grünberg, *Harmonic Lattice Behavior of Two-Dimensional Colloidal Crystals*, Phys. Rev. Lett. **92**, 215504 (2004).

[218] H. H. von Grünberg, P. Keim, G. Maret, and U. Herz, *Elastic Behavior of a Two-Dimensional Crystal Near Melting*, Phys. Rev. Lett. **93**, 255703 (2004).

[219] P. Keim, *Schmelzen und Erstarren in zwei Dimensionen*, Dissertation, Universität Konstanz (2005).

[220] P. Keim, G. Maret, and H. H. von Gruünberg, *Frank's constant in the hexatic phase*, Phys. Rev. E **75**, 031402 (2007).

[221] K. Loudiyi and B. J. Ackerson, *Direct observation of laser induced freezing*, Physica A **184**, 1 (1992).

[222] K. Loudiyi and B. J. Ackerson, *Monte carlo simulation of laser induced freezing*, Physica A **184**, 26 (1992).

[223] J. Chakrabarti, H. R. Krishnamurthy, and A. K. Sood, *Density Functional Theory of Laser-Induced Freezing in Colloidal Suspensions*, Phys. Rev. Lett. **73**, 2923 (1994).

[224] J. Chakrabarti, H. R. Krishnamurthy, A. K. Sood, and S. Sengupta, *Reentrant Melting in Laser Fields Modulated Colloidal Suspensions*, Phys. Rev. Lett. **75**, 2232 (1995).

[225] Q.-H. Wei, C. Bechinger, D. Rudhardt, and P. Leiderer, *Experimental Study of Laser-Induced Melting in Two-Dimensional Colloids*, Phys. Rev. Lett. **81**, 2606 (1998).

[226] C. Das, P. Chaudhuri, A. K. Sood, and H. R. Krishnamurthy, *Laser-induced freezing in 2-d colloids*, Current Science **80**, 959 (2001).

[227] F. Bürzle and P. Nielaba, *Phase transitions in two-dimensional model colloids in a one-dimensional external potential*, Phys. Rev. E **76**, 051112 (2007).

[228] J. Chakrabarti and S. Sinha, *Effect of Fluctuations on the Freezing of a Colloidal Suspension in an External Periodic Potential*, J. Phys. II **7**, 729 (1997).

[229] E. Frey, D. R. Nelson, and L. Radzihovsky, *Light-Induced Melting of Colloidal Crystals in Two Dimensions*, Phys. Rev. Lett. **83**, 2977 (1999).

[230] L. Radzihovsky, E. Frey, and D. R. Nelson, *Novel phases and reentrant melting of two-dimensional colloidal crystals*, Phys. Rev. E **63**, 031503 (2001).

[231] C. Das and H. R. Krishnamurthy, *Laser-induced quasicrystalline order in charge-stabilized colloidal systems*, Phys. Rev. B **58**, (1998).

[232] C. Das, A. K. Sood, and H. R. Krishnamurthy, *Bond-orientational ordering and shear rigidity in modulated colloidal liquids*, Physica A **270**, 237 (1999).

[233] D. G. Levitt, *Dynamics of a Single-File Pore: Non-Fickian Behavior*, Phys. Rev. A **8**, 3050 (1973).

[234] M. Kollmann, *Single-file Diffusion of Atomic and Colloidal Systems: Asymptotic Laws*, Phys. Rev. Lett. **90**, 180602 (2003).

[235] V. M. Bedanov, G. V. Gadiyak, and Y. E. Lozovik, *On a modified Lindemann-like criterion for 2D melting*, Phys. Lett. A **109**, 289 (1989).

[236] K. Zahn and G. Maret, *Dynamic Criteria for Melting in Two Dimensions*, Phys. Rev. Lett. **85**, 3656 (2000).

[237] G. H. Wannier, *Antiferromagnetism. The Triangular Ising Net*, Phys. Rev. **79**, 357 (1950).

[238] C. D. Modes and R. D. Kamien, *Geometrical frustration in two dimensions: Idealizations and realizations of a hard-disk fluid in negative curvature*, Phys. Rev. E **77**, 041125 (2008).

[239] J. Baumgartl and C. Bechinger, private communication .

[240] J. Baumgartl, M. Brunner, and C. Bechinger, *Locked-Floating-Solid to Locked-Smectic Transition in Colloidal Systems*, Phys. Rev. Lett. **93**, 168301 (2004).

[241] A. Patrykiejew and S. Sokołowski, *Two-Dimensional Quasicrystals of Decagonal Order in One-Component Monolayer Films*, Phys. Rev. Lett. **99**, 156101 (2007).

[242] A. Patrykiejew and S. Sokołowski, *Reply*, Phys. Rev. Lett. **100**, 019602 (2008).

[243] H. H. von Grünberg and J. Baumgartl, *Lattice dynamics of two-dimensional colloidal crystals subject to external light potentials*, Phys. Rev. E **75**, 051406 (2007).

[244] J. Baumgartl, M. Zvyagolskaya, and C. Bechinger, *Tailoring of Phononic Band Structures in Colloidal Crystals*, Phys. Rev. Lett. **99**, 205503 (2007).

[245] C. Wöll, *Phonons on Surfaces: The Importance of Structure and Adsorbates*, Appl. Phys. A **53**, 377 (1991).

[246] Y. N. Ohshima and I. Nishio, *Colloidal crystal: bead-spring lattice immersed in viscous media*, J. Chem. Phys. **114**, 8649 (2001).

[247] U. Herz, *Berechnungenvon Kompressibilitäten zweidimensionaler, geladener Kolloidsysteme*, Dissertation, Universität Konstanz (2004).

[248] M. Engel, S. Sonntag, H. Lipp, and h. R. Trebin, *Structure factors of harmonic and anharmonic Fibonacci chains by molecular dynamics simulations*, Phys. Rev. B **75**, 144203 (2007).

[249] A. R. Denton and H. Löwen, *Stability of Colloidal Quasicrystals*, Phys. Rev. Lett. **81**, 469 (1998).

[250] M. Engel and H. R. Trebin, *Self-assembly of monatomic complex crystals and quasicrystals with a double-well interaction potential*, Phys. Rev. Lett. **98**, 225505 (2007).

[251] H. K. Lee, R. H. Swendsen, and M. Widom, *Crystalline ground states of an entropically stabilized quasicrystal model*, Phys. Rev. B **64**, 224201 (2001).

[252] J. Roth, submitted to Philosophical Magazine (2008).

[253] S. Bleil, H. H. von Grünberg, J. Dobnikar, R. Castaneda-Priego, and C. Bechinger, *Strain-induced domain formation in two-dimensional colloidal systems*, Eur. Phys. Lett. **73**, 450 (2006).

[254] T. Geisel, J. Nierwetberg, and A. Zacherl, *Accelerated Diffusion in Josephson Junctions and Related Chaotic Systems*, Phys. Rev. Lett. **54**, 616 (1985).

[255] J. Klafter, A. Blumen, and M. F. Shlesinger, *Stochastic pathway to anomalous diffusion*, Phys. Rev. E **35**, 3081 (1987).

[256] M. F. Shlesinger, B. J. West, and J. Klafter, *Lévy Dynamics of Enhanced Diffusion: Application to Turbulence*, Phys. Rev. Lett. **58**, 1100 (1987).

[257] A. Blumen, G. Zumofen, and J. Klafter, *Transport aspects in anomalous diffusion: Lévy Walks*, Phys. Rev. A **40**, 3964 (1989).

[258] G. Zumofen and J. Klafter, *Scale-invariant motion in intermittent chaotic systems*, Phys. Rev. E **47**, 851 (1993).

[259] E. Barkai and J. Klafter, *Anomalous Diffusion in the Strong Scattering Limit: A Lévy Walk Approach*, Lecture notes in physics **511**, 373 (1988).

[260] R. Metzler and J. Klafter, *The random walk's guide to anomalous diffusion: a fractional dynamics approach*, Phys. Rep. **339**, 1 (2000).

[261] R. Metzler and J. Klafter, *The restaurant at the end of the random walk: recent developments in the description of anomalous transport by fractional dynamics*, J. of Physics A **37**, 161 (2004).

[262] J. Machta and R. Zwanzig, *Diffusion in a Periodic Lorentz Gas*, Phys. Rev. Lett. **50**, 1959 (1983).

[263] G. Zumofen and J. Klafter, *Power spectra for anomalous diffusion in the extended Sinai billiard*, Phys. Lett. A **114**, 317 (1986).

[264] D. N. Armstead, B. R. Hunt, and E. Ott, *Anomalous diffusion in infinite horizon billiards*, Phys. Rev. E **67**, 021110 (2003).

[265] D. P. Sanders and H. Larralde, *Occurrence of normal and anomalous diffusion in polygonal billiard channels*, Phys. Rev. E **73**, 026205 (2006).

[266] A. V. Indrani and S. Ramaswamy, *Universal self-diffusion and subdiffusion in colloids at freezing*, Phys. Rev. Lett. **73**, 360 (1994).

[267] F. H. Stillinger, *A Topographic View of Supercooled Liquids and Glass Formation*, Science **267**, 1935 (1995).

[268] C. A. Angell, *Formation of Glasses from Liquids and Biopolymers*, Science **267**, 1924 (1995).

[269] C. A. Angell and S. R. Nagel, *Supercooled Liquids and Glasses*, J. Phys. Chem. **100**, 13200 (1996).

[270] E. R. Weeks, J. C. Crocker, A. C. Levitt, A. Schofield, and D. A. Weitz, *Three-Dimensional Direct Imaging of Structural Relaxation Near the Colloidal Glass Transition*, Science **287**, 627 (2000).

[271] E. R. Weeks and D. A. Weitz, *Properties of Cage Rearrangements Observed near the Colloidal Glass Transition*, Phys. Rev. Lett. **89**, 095704 (2002).

[272] E. R. Weeks and D. A. Weitz, *Subdiffusion and the cage effect studied near the colloidal glass transition*, Chem. Phys. **284**, 361 (2002).

[273] F. Höfling, T. Franosch, and E. Frey, *Localization Transition of the Three-Dimensional Lorentz Model and Continuum Percolation*, Phys. Rev. Lett. **96**, 165901 (2006).

[274] Y. Kafri, D. K. Lubensky, and D. R. Nelson, *Dynamics of Molecular Motors and Polymer Translocation with Sequence Heterogeneity*, Biophys. J. **86**, 3373 (2004).

[275] P. Dieterich, R. Klages, R. Preuss, and A. Schwab, *Anomalous dynamics of cell migration*, PNAS **105**, 459 (2008).

[276] M. Weiss, M. Elsner, F. Kartberg, and T. Nilsson, *Anomalous Subdiffusion Is a Measure for Cytoplasmic Crowding in Living Cells*, Biophys. J. **87**, 3518 (2004).

[277] F. Amblard, *Subdiffusion and Anomalous Local Viscoelasticity in Actin Networks*, Phys. Rev. Lett. **77**, 4470 (1996).

[278] P. Bursac, G. Lenormand, B. Fabry, M. Oliver, D. A. Weitz, V. Viasnoff, J. P. Butler, and J. J. Fredberg, *Cytoskeletal remodeling and slow dynamics in the living cell*, Nat. Mat. **4**, 557 (2005).

[279] P. R. Smith, I. E. Morrison, K. M. Wilson, N. Fernandez, and R. J. Cherry, *Anomalous diffusion of major histocompatibility complex class I molecules on HeLa cells determined by single particle tracking*, Biophys. J. **76**, 3331 (1999).

[280] P. Schwille, U. Haupts, S. Maiti, and W. W. Webb, *Molecular dynamics in living cells observed by fluorescence correlation spectroscopy with one- and two-photon excitation*, Biophys. J. **77**, 2251 (1999).

[281] I. Golding and E. C. Cox, *Physical Nature of Bacterial Cytoplasm*, Phys. Rev. Lett. **96**, 098102 (2006).

[282] T. J. Feder, I. Brust-Mascher, J. P. Slattery, B. Baird, and W. W. Webb, *Constrained diffusion or immobile fraction on cell surfaces: a new interpretation*, Biophys. J. **70**, 2767 (1996).

[283] J. Honkonen and Y. M. Pis'mak, *Exact calculation of the anaomalous dimension of the diffusion coefficient for a model of a random walk in a random potential*, J. Phys. A **22**, (1989).

[284] A. H. Romero and J. M. Sancho, *Brownian motion in short range random potentials*, Phys. Rev. E **58**, 2833 (1998).

[285] J. M. Sancho, A. M. Lacasta, K. Lindenberg, I. M. Sokolov, and A. H. Romero, *Diffusion on a Solid Surface: Anomalous is Normal*, Phys. Rev. Lett. **92**, 250601 (2004).

[286] A. M. Lacasta, J. M. Sancho, A. H. Romero, I. M. Sokolov, and K. Lindenberg, *From subdiffusion to superdiffusion of particles on solid surfaces*, Phys. Rev. E **70**, 051104 (2004).

[287] J.-D. Bao and Y. Zhou, *Comment on ¨Diffusion on a Solid Surface: Anomalous is Normal¨*, Phys. Rev. Lett. **94**, 188901 (2005).

[288] J. M. Sancho, A. M. Lacasta, K. Lindenberg, I. M. Sokolov, and A. H. Romero, *Reply*, Phys. Rev. Lett. **94**, 188902 (2005).

[289] Y. Zhou and J.-D. Bao, *Time-dependent diffusion in a random correlated potential*, Phys. Rev. E **73**, 031103 (2006).

[290] J. W. Haus, K. W. Kehr, and J. W. Lyklema, *Diffusion in a disordered medium*, Phys. Rev. B **25**, 2905 (1982).

[291] J. W. Haus and K. W. Kehr, *Diffusion in regular and disordered lattices*, Phys. Rep. **150**, 263 (1987).

[292] J.-P. Bouchard and A. Georges, *Anomalous Diffusion in Disordered Media: Statistical Mechanisms, Models and Physical Aplications*, Phys. Rep. **195**, 127 (1990).

[293] P. Hänggi, P. Talkner, and M. Borkovec, *Reaction-rate theory: fifty years after Kramers*, Rev. Mod. Phys. **62**, 251 (1990).

[294] G. E. Crooks, *Path-ensemble averages in systems driven far from equilibrium*, Phys. Rev. E **61**, 2361 (2000).

[295] C. Jarzynski, *Nonequilibrium Equality for Free Energy Differences*, Phys. Rev. Lett. **78**, 2690 (1997).

[296] U. Seifert, *Entropy Production along a Stochastic Trajectory and an Integral Fluctuation Theorem*, Phys. Rev. Lett. **95**, 040602 (2005).

[297] J. Liphardt, S. Dumont, S. B. Smith, I. Tinoco Jr., and C. Bustamante, *Equilibrium Information from Nonequilibrium Measurements in an Experimental Test of Jarzynski's Equality*, Science **296**, 1832 (2002).

[298] O. Braun, A. Hanke, and U. Seifert, *Probing Molecular Free Energy Landscapes by Periodic Loading*, Phys. Rev. Lett. **93**, 158105 (2004).

[299] V. Blickle, T. Speck, L. Helden, U. Seifert, and C. Bechinger, *Thermodynamics of a Colloidal Particle in a Time-Dependent Nonharmonic Potential*, Phys. Rev. Lett. **96**, 070603 (2006).

[300] E. G. D. Cohen and D. Mauzerall, *A note on the Jarzynski equality*, J. Stat. Mech. P07006 (2004).

[301] C. Jarzynski, *Nonequilibrium work theorem for a system strongly coupled to a thermal environment*, J. Stat. Mech. P09005 (2004).

[302] D. J. Evans, E. G. D. Cohen, and G. P. Morriss, *Probability of Second Law Violations in Shering Steady States*, Phys. Rev. Lett. **71**, 2401 (1993).

[303] D. J. Evans and D. J. Searles, *Equilibrium microstates which generate second law violating steady states*, Phys. Rev. E **50**, 1645 (1994).

[304] G. Gallavotti and E. G. D. Cohen, *Dynamical ensembles in Nonequilibrium Statistical Mechanics*, Phys. Rev. Lett. **74**, 2694 (1995).

[305] D. J. Searles and D. J. Evans, *Fluctuation theorem for stochastic systems*, Phys. Rev. E **60**, 159 (1999).

[306] G. E. Crooks, *Entropy production fluctuation theorem and the nonequilibrium work relation for free energy differences*, Phys. Rev. E **60**, 2721 (1999).

[307] T. Speck, V. Blickle, C. Bechinger, and U. Seifert, *Distribution of entropy production for a colloidal particle in a nonequilibrium steady state*, Eur. Phys. Lett. **79**, 30002 (2007).

[308] G. M. Wang, E. M. Sevick, E. Mittag, D. J. Searles, and D. J. Evans, *Experimental Demonstration of Violations of the Second Law of Thermodynamics for Small Systems and Short Time Scales*, Phys. Rev. Lett. **89**, 050601 (2002).

[309] D. M. Carberry, J. C. Reid, G. M. Wang, E. M. Sevick, D. J. Searles, and D. J. Evans, *Fluctuations and Irreversibility: An Experimental Demonstration of a Second-Law-Like Theorem Using a Colloidal Particle Held in an Optical Trap*, Phys. Rev. Lett. **92**, 140601 (2004).

[310] D. Collin, F. Ritort, C. Jarzynski, S. B. Smith, I. Tinoco Jr., and C. Bustamante, *Verification of the Crooks fluctuation theorem and recovery of RNA folding free energies*, Nature **437**, 231 (2005).

[311] J. Tekic, O. M. Braun, and B. Hu, *Dynamic phases in the two-dimensional underdamped driven Frenkel-Kontorova model*, Phys. Rev. E **71**, 026104 (2005).

[312] A. S. Keys and S. C. Glotzer, *How do Quasicrystals Grow?*, Phys. Rev. Lett. **99**, 235503 (2007).

[313] P. J. Steinhardt, *Solid-state physics: How does your quasicrystal grow?*, Nature **452**, 43 (2008).

References [A] to [J] are listed in the List of Publications on page 139.

Index

Zusammenfassung

Quasikristalle sind nicht periodische Festkörper, die trotzdem eine weitreichende Ordnung besitzen. In einige Eigenschaften unterscheiden sich Quasikristalle wesentlich von periodischen Kristallen. So sind in zweidimensonalen periodischen Strukturen nur 1-, 2-, 3-, 4- oder 6-zählige Rotations-Symmetrieachsen erlaubt, wo hingen in Quasikristallen zum Beispiel auch 5- oder 10-fache Symmetrien vorkommen können. Eine andere Besonderheit von Quasikristallen sind die sogenannten Phasonen. Dabei handelt es sich wie bei Phononen um hydrodynamische Moden, d.h. globale Umordnungen, die im Grenzfall langer Wellenlängen nicht mit einer Erhöhung der freien Energie einhergehen [2, 3]. Die Fragen, wie Phasonen tatsächlich in Erscheinung treten und welche Eigenschaften oder Auswirkungen sie haben, sind Gegenstand der aktuellen Forschung und vieler Diskussionen [4]. Seit einigen Jahren wird zunehmend auch die Anlagerung von Atomen an quasikristallinen Oberflächen erforscht. Insbesondere die Struktur der sich bildenden Monolagen wird intensiv untersucht [5–19]. Ziel dieser Arbeiten ist es, den Wachstumsprozess sowie die einzigartigen Materialeigenschaften von Quasikristallen verstehen und beeinflussen zu können.

Kolloidale Suspensionen bestehen aus Teilchen mit einem Durchmesser im Mikometer-Bereich, die in einer Flüssigkeit dispergiert sind. Da die Teilchenwechselwirkung sehr genau gesteuert werden kann und da es möglich ist, die Positionen sowie die Bewegungen der Teilchen per Video-Mikroskopie experimentell zu beobachten, sind Kolloide ein sehr beliebtes Modellsystem zur Erforschung und Beschreibung atomarer Prozesse. In einem Laserfeld wirkt auf Kolloide eine Kraft in Richtung der höchsten Intensität. Deshalb lassen sich mit Laserstrahlen ausgezeichnet äußere Potentiale für Kolloidsysteme erzeugen. Interessiert man sich also, unabhängig von chemischen Details, für Strukturen und Bewegungen von Teilchen auf Substraten, so eignen sich kolloidale Suspensionen in Laserfeldern sehr gut als Modellsystem. Im Falle von quasikristallinen Laserfeldern lassen sich außerdem durch Veränderung der Phasen der Laserstrahlen phasonische Verschiebungen oder Gradienten erzeugen und deren Auswirkungen auf die Teilchen untersuchen.

In dieser Arbeit betrachten wir die Struktur und Dynamik von Kolloiden in quasikristallinen Potentialen. Die Bewegung der Kolloide ist dabei auf eine Ebene begrenzt. Schmelzen in zwei Dimensionen ist besonders interessant, da es in einem zweistufigen Prozess stattfindet, bei dem schrittweise erst die Positionsordnung und dann die Orientierungsordnung verschwindet [21–27]. In externen Potentialen kann ein sehr komplexes Phasenverhalten beobachtet werden. So kann mit einem Potential, welches in eine Richtung konstant und in die andere Richtung kommensurabel periodisch moduliert ist, eine stabile zwei dimen-

sionale Dreiecksordnung induziert werden [28]. Wie wir in dieser Arbeit zeigen, tauchen in quasikristallinen Laserfeldern weitere, unerwartete Phasen auf, wobei sich auch das Phasenverhalten allgemein von dem in periodischen Potentialen unterscheidet.
Zunächst untersuchen wir Kolloide in einem eindimensional quasikristallinen Potential, welches in eine Richtung konstant und in die andere Richtung durch zwei Modulationen, deren Wellenlängen sich um τ^2 unterscheiden, geben ist. Dabei ist $\tau = (1+\sqrt{5})/2 \approx 1,618$ die Zahl des goldenen Schnittes. Mit Monte-Carlo-Simulationen finden wir, abhängig von der Stärke der Teilchenwechselwirkung, eine Dreiecksphase oder eine flüssige Phase in einem schwachen Potential. Bei mittlerer Laserintensität beobachten wir eine rhombische Phase, bei der die Kolloide sich gemäß einer Modulation periodisch anordnen und gleichzeitig die zweite Modulation ignorieren. Mit einer speziell entwickelten Variante der Landau-Alexander-McTague-Theorie kommen wir zu den gleichen Ergebnissen wie in den Simulationen. In sehr starken Potentialen ist keine periodische Struktur mehr vorhanden. Dann befinden sich alle Teilchen auf Linien in den Potentialminima. Da diese unterschiedliche Tiefen und Abstände haben, kann das Verhältnis der Teilchendichten in benachbarten Minima irrational sein, womit eine periodische Anordnung ausgeschlossen ist. Durch Bown'sche Dynamik-Simulationen weisen wir einen Phasenübergang von einer modulierten Flüssigkeit bei schwachen Teilchenwechselwirkungen in eine frustrierte, nicht periodische, feste Phase bei starken Wechselwirkungen nach.
Das zweidimensional quasikristalline Potential, kann experimentell als Interferenzmuster von fünf Laserstrahlen erzeugt werden. Es hat somit dekagonale Symmetrie. Monte-Carlo-Simulationen ergeben einen Dreiecksphase oder Flüssigkeit in schwachen Potentialen und dekagonale Ordnung bei hohen Laserintensitäten. Überraschenderweise gibt es für mittlere Potentialstärken eine quasikristalline Phase, die sich durch zwanzig Verbindungsrichtungen zwischen nächsten Nachbarn auszeichnet. Im Falle sehr hoher Dichten jedoch, wenn also insbesondere mehr Kolloide als lokale Minima vorhanden sind, geht für mittlere Laserintensitäten jegliche Orientierungsordnung verloren. Außerdem tritt in zwei eng begrenzten Dichtebereichen eine Phase auf, deren Struktur sich durch Archimedische Parketierungen beschreiben lässt. Desweiteren untersuchen wir den Einfluss von phasonischen Verschiebungen und Gradienten und beobachten insbesondere die dadurch erzeugte Umordnung der Teilchen.
Die Bewegung von einzelnen Teilchen in einem dekagonalen Potential untersuchen wir mit Hilfe von Brown'schen Dynamik-Simulationen und einer analytischen Theorie, die auf einer Ratengleichung für die Besetzungswahrscheinlichkeit für Minima einer speziellen Tiefe basiert. Im asymptotischen Grenzfall sehr langer Zeiten ist die Bewegung immer diffusiv, für mittlere Zeit jedoch kann sie subdiffusiv sein. Wir zeigen, dass der Übergang von der Subdiffusion zur Difussion direkt in Zusammenhang mit dem Relaxationsprozess ins thermische Gleichgewicht steht. Verwendet man ein Potential mit einer mit konstanter Rate anwachsender phasonischen Verschiebung, so tritt der Übergang zur Diffusion früher ein und die Diffusionskonstante ist wesentlich erhöht. Das System relaxiert nicht mehr ins thermische Gleichgewicht sondern gelangt in einen stationären Nichtgleichgewichtszustand. Wir zeigen, dass dieses System deshalb auch als Modellsystem zum Erforschen von Nichtgleichgewichts-Relationen geeignet ist.

Teilchen auf quasikristallinen Substraten haben eine interessante Dynamik und ein in vielerlei Hinsicht unerwartetes Phasenverhalten. Wie diese Arbeit zeigt, eignen sich Kolloide in quasikristallinen Laserfeldern sehr gut um dies genauer zu untersuchen.

Danksagung

Mein ganz besonderer Dank gilt Prof. Dr. Holger Stark, der mit viel Rat und einer Menge Ideen die Forschung an diesem Projekt ermöglicht und unterstützt hat. Seine Anmerkungen und kritischen Fragen, sowie viele Korrektur- und Verbesserungsvorschläge haben entscheidend beim Erstellen dieser Arbeit geholfen. Er stand jederzeit für alle Fragen oder Diskussionen zur Verfügung und verstand es, für eine anhaltend hohe Motivation zu sorgen. Ich habe die Zusammenarbeit mit ihm immer sehr genossen. Auch wenn ich mehr Wissenschaftsstandorte kennenlernen durfte, als ursprünglich gedacht, habe ich es nie bereut, als Teil seiner "Wanderarbeitsgruppe" quer durch Deutschland gezogen zu sein.

Prof. Dr. Sabine Klapp und Prof. Dr. Hartmut Löwen danke ich dafür, dass Sie sich sofort bereit erklärt haben, die weiteren Gutachten zu dieser Arbeit anzufertigen. Mein Dank gilt auch Prof. Dr. Martin Schoen, der einverstanden war, den Vorsitz des Promotionsausschusses zu übernehmen.

Ich bedanke mich ebenfalls bei unseren Kooperationspartnern an der Universität Stuttgart. Experimente an Kolloiden in quasikristallinen Laserfeldern wurden am 2. Physikalischen Institut in der Gruppe von Prof. Dr. Clemens Bechinger durchgeführt, zunächst von Dr. Jörg Baumgartl, später von Dr. Laurent Helden und Jules Mikhael. Ich verdanke dieser Zusammenarbeit viele neue Ideen und zahlreiche anregende Diskussionen. Es war ein Glücksfall für diese Arbeit, dass theoretische und experimentelle Ergebnisse direkt miteinander verglichen werden konnten.

Desweiteren danke ich Dr. Johannes Roth vom Institut für Theoretische und Angewandte Physik der Universität Stuttgart, ohne den es wahrscheinlich nie zu diesem Projekt gekommen wäre. Mit seinem großem Wissen im Gebiet der Quasikristalle war er außerdem immer zur Stelle, wenn es darum ging, spezifisch quasikristalline Probleme zu lösen. Seine zahlreichen Hinweise und Korrekturvorschläge zu dieser Arbeit haben mir sehr geholfen.

Diese Arbeit wurde am Fachbereich Physik der Universität Konstanz, in der Abteilung komplexe Fluide des Max-Planck-Institutes für Dynamik und Selbstorganisation in Göttingen und am Institut für Theoretische Physik der Technischen Universität Berlin angefertigt. An all diesen Standorten habe ich ausgezeichnete Arbeitsbedingungen vorgefunden und bin den entsprechenden Gruppen zu großem Dank für die Unterstützung aber auch die gute Arbeitsatmosphäre dankbar.

An der Universität Konstanz gilt mein Dank insbesondere Prof. Dr. Georg Maret, mit dessen Lehrstuhl unsere Arbeitsgruppe assoziiert war. Insbesondere der von ihm geleiteten "International Research Training Group" zum Thema "Soft Condensed Matter Physics of

Model Systems" verdanke ich unter anderem viele sehr interessante Seminare und Kontakte. In diesem Zusammenhang möchte ich mich bei Prof. Dr. Nicolas Rivier und Prof. Dr. Jörg Baschnagel für die hilfreichen Diskussionen bedanken. Den Start in Konstanz, sowohl bei meiner Diplom- wie auch bei der Doktorarbeit, insbesondere in Bezug auf des Computersystem und der Simulation Brown'scher Dynamik, wurde mir von Dr. Michael Reichert sehr erleichtert. Matthias Huber, Erik Gauger und Andrej Grimm sorgten für eine angenehme und nie langweilige Arbeitsatmosphäre. Den Mitgliedern des Lehrstuhles von Prof. Dr. Nielaba verdanke ich viele interessante Diskussionen sowie Hilfestellungen zu Programmiertechniken, insbesondere möchte ich Kerstin Franzrahe, Peter Henseler, Christine Kircher und Jörg Neder danken.
In Göttingen bin ich Prof. Dr. Stephan Herminghaus und der gesamten Abteilung komplexe Fluide zu großem Dank verpflichtet. Ich habe die Zeit am Max-Planck-Institut und insbesondere die sehr internationale Atmosphäre dort sehr genossen. Besonders danke ich Dr. Axel Fingerle für viele Hinweise in Bezug auf Fluktuationstheoreme. Dr. Martin Brinkmann und Marcus Schwamberger kümmerten sich um das Computersystem und richteten den Rechnercluster ein, der viele Simulationen zu meiner Arbeit wesentlich beschleunigt hat. Prof. Dr. MirFaez Miri war, wie schon in Konstanz, kurzzeitig Gast unserer Arbeitsgruppe und ich danke ihm für die vielen sehr anregenden Diskussionen insbesondere über die Brown'sche Bewegung in externen Potentialen.
In Berlin bedanke ich mich bei allen Mitgliedern des hervorragend organisierten Institutes für Theoretische Physik. Neben Prof. Dr. Holger Stark danke ich Dr. Vasily Zaburdaev, der ebenfalls von Göttingen nach Berlin umzog, für viele hilfreiche Diskussionen und für die interessante und erfolgreiche Abwechslung durch das Projekt zu "Random Walks with Random Velocities". Für die ausgezeichnete und produktive Arbeitsatmosphäre danke ich außerdem Dr. Mathew Downton, Sebastian Heidenreich, Sareh Nakaie, Dr. Arthur Straube und Reinhard Vogel. Prof. Dr. Hess verdanke ich einige Ideen und Hinweise. Peter Orlowski sorgt am Institut für ein immer perfekt funktionierendes Computersystem.
Schließlich bedanke ich mich noch bei Prof. Dr. von Grünberg und Prof. Dr. Trebin für interessante und hilfreiche Diskussionen.

Finanziell unterstützt wurde diese Arbeit von der "International Research Training Group" an der Universität Konstanz sowie der Deutschen Forschungsgemeinschaft im Rahmen des Projektes Ro 924/5-1.